

Electronic Thesis and Dissertation Repository

11-4-2011 12:00 AM

Seismic Microzonation of Great Toronto Area and Influence of Building Resonances on Measured Soil Responses

Dimitar Genchev Mihaylov, *The University of Western Ontario*

Supervisor: Dr. Hesham El Naggar, *The University of Western Ontario*

A thesis submitted in partial fulfillment of the requirements for the Doctor of Philosophy degree in Civil and Environmental Engineering

© Dimitar Genchev Mihaylov 2011

Follow this and additional works at: <https://ir.lib.uwo.ca/etd>



Part of the [Civil Engineering Commons](#), [Geophysics and Seismology Commons](#), [Geotechnical Engineering Commons](#), [Soil Science Commons](#), and the [Structural Engineering Commons](#)

Recommended Citation

Mihaylov, Dimitar Genchev, "Seismic Microzonation of Great Toronto Area and Influence of Building Resonances on Measured Soil Responses" (2011). *Electronic Thesis and Dissertation Repository*. 306. <https://ir.lib.uwo.ca/etd/306>

This Dissertation/Thesis is brought to you for free and open access by Scholarship@Western. It has been accepted for inclusion in Electronic Thesis and Dissertation Repository by an authorized administrator of Scholarship@Western. For more information, please contact wlsadmin@uwo.ca.

SEISMIC MICROZONATION OF GREAT TORONTO AREA AND INFLUENCE OF
BUILDING RESONANCES ON MEASURED SOIL RESPONSES

(Spine title: Seismic microzonation of GTA)

(Thesis format: Monograph)

by

Dimitar Mihaylov

Graduate Program in Engineering Science

Department of Civil and Environmental Engineering

A thesis submitted in partial fulfillment

of the requirements for the degree of

Doctor of Philosophy

The School of Graduate and Postdoctoral Studies

The University of Western Ontario

London, Ontario, Canada

© Dimitar G. Mihaylov 2011

THE UNIVERSITY OF WESTERN ONTARIO
School of Graduate and Postdoctoral Studies

CERTIFICATE OF EXAMINATION

Supervisor

Examiners

Dr. M. Hesham El Naggar

Dr. Horia Hangan

Dr. Ashraf El Damatty

Dr. Gail Atkinson.

Dr. Miroslav Nastev

The thesis by

Dimitar Mihaylov

entitled:

**Seismic microzonation of Great Toronto Area and influence of
building resonances on measured soil responses**

is accepted in partial fulfillment of the
requirements for the degree of
Doctor of Philosophy

Date

Chair of the Thesis Examination Board

Abstract

A pilot seismic microzonation of the Greater Toronto Area (GTA) is used to establish the conditions and limitations of geophysical methods for site response investigations in city conditions. Maps of fundamental soil resonant frequencies, amplifications at these frequencies and interpolated average shear wave velocity of top 30 m of soil profile (VS-30) used in soil classification were compared to the maps of drift thickness and surficial geology for the GTA. The non-applicability of the interpolated VS-30 map for site classification between measured test points is indicated. It is also shown that the soil response cannot be estimated properly using VS-30 values only.

In order to enhance the capability of the horizontal-to-vertical-spectral-ratio (HVSr) method to resolve the fundamental soil resonances, a procedure and a computer program were developed for separation of ambient vibrations from nearby traffic as well as distant sources using the recorded waveforms before calculating the HVSr. A portable seismic station was developed for field HVSr waveforms recordings. It was also used for identification of building vibration modes. The influence of building vibrations on the HVSr result was investigated considering a benchmark building before construction started and after its completion. This influence is expressed as suppression or split-up of HVSr resonance if the building and soil resonances are close. This effect spreads out to distances comparable to the maximum dimension of the building. The experimentally obtained building resonant frequency at first vibration mode was found to be significantly higher than that calculated using empirical equations proposed by building codes, while the damping factor was less than the prescribed value. Additionally, the concept of using the HVSr inside a building to identify its resonances was examined using recorded waveforms, but the results did not confirm applicability of the HVSr for this purpose.

The limitations and initial conditions that are necessary for successful implementation of refracted shear wave seismic profiling (SH-profiling) and multi-channel-analysis-of-surface-waves (MASW) methods for application in urban areas are discussed. The problems with interlaying low velocity soil layer are pointed out. The soil response functions obtained from the microzonation studies using low intensity seismic sources differ from the response during an earthquake. An approach to estimate the changes of

soil response in relation with expected Peak Ground Velocity (PGV) and Intensity of Modified Mercalli Scale (IMM) is proposed. The results were found to be in agreement with strong motion data from the epicentral area of a strong earthquake.

It was concluded that the results from seismic microzonation studies should be considered in conjunction with models that simulate the change in dynamic characteristics of soil and buildings during expected earthquake events.

Keywords:

Earthquake, Ambient vibration, Seismic microzonation, Soil resonant frequencies, Soil resonance map, Soil classification, VS-30, HVSR, MASW, Shear wave velocity, PGV, IMM, Portable seismic station, Sallen-Key filter, Benchmark building, Soil-bedrock boundary, Cyclic load, Stiffness degradation, Building resonance.

Co-Authorship Statement

This thesis has been prepared in accordance with the specifications of Manuscript format stipulated by the Faculty of Graduate Studies at The University of Western Ontario.

All the experimental works were conducted at the University of Western Ontario and in Great Toronto Area by the author under the supervision of Prof. M. Hesham El Naggar.

The author carried out all experimental work, data analysis, interpretation, and writing of the initial draft of the thesis.

The contribution of his research advisor consisted of providing guidance and supervision, and helping in the development of the final versions of the thesis.

The test measurements in and around the benchmark building on Richmond St. are conducted together with Richard Oskirko who negotiated with owner access to the building and obtaining the necessary technical documentation as well as technical assistance during the experiment. Richard Oskirko has made his own processing of the experimental data. The peculiarities ascertain in his work are explained in this thesis.

Acknowledgments

This research project has been partially funded by a grant from the Institute for Catastrophic Loss Reduction, ICLR. The author would like to express his appreciation to ICLR and Mr. Paul Kovacs, Executive Director, ICLR, for their support to this project.

The project is also partially funded by ORDCF grant for Ontario Research Centres in Earthquake Hazards. This support is much appreciated.

This study was possible owing to kindness shown by Tricar Corp. and essential assistance from Richard Oskirko with field data acquisition, negotiating access to the building and collecting the necessary design documentation.

I would like to thank also my supervisor Hesham El Naggar for giving me the opportunity to do this interesting work. I appreciate very much his excellent supervision, help and support. I have learned a lot from him. I would like to thank him also for his patience.

Dr. Savka Dineva has been a great support and help for me during the years. The descriptions of the geological and seismological conditions in GTA are made with her assistance. She helped me also with the editing of the thesis. Thanks to her persistence this thesis is completed.

I would like to thank also Mohammad El Naggar and Aleksandar Mihaylov for their assistance with the field measurements in Toronto.

Table of Contents

Certificate of examination	ii
Abstract	iii
Copyright and co-authorship	v
Acknowledgements.....	vi
Table of content	vii
List of tables	x
List of figures	xi
List of abbreviations and notations	xvi
Chapter 1. Introduction.....	1
1.1. Introduction	1
1.2. Objective and Methods of the Study	3
1.3. Organization of the Dissertation	5
1.4. Original Contributions of the Thesis	7
1.5. Seismic microzonation - methodologies	8
1.6. Description of the study area	9
1.6.1. Location and population	9
1.6.2. Geological conditions in the GTA	10
1.7. Earthquakes and faults around GTA	16
1.8. NBCC 2005/2010 and microzonation	18
Chapter 2. Soil response to seismic vibrations	20
2.1. Introduction	20
2.2. Evaluation of linear soil response to weak seismic impact	21
2.3. Modeling of soil resonance changes during moderate and strong earthquakes... ..	24
Chapter 3. Geophysical methods for seismic microzonation in a city	33
3.1. Horizontal to Vertical Spectral Ratio (HVSr) Methods	34
3.1.1. Assumptions behind HVSr method	34
3.1.2. Application of HVSr in city conditions	36
3.1.3. Noise separation from close and distant sources	37
3.2. Shear-Wave Seismic Refraction Profiling (SH refraction profiling)... ..	41
3.3. Surface-Wave Methods for Phase Velocity estimation	48
3.3.1. Spectral analysis of surface waves (SASW)	48
3.3.2. Multi-Channel Analysis of Surface Waves (MASW)	50
3.4. Application of SH velocity profiling, SASW and MASW in city conditions....	51
Chapter 4. Equipment for field measurements.....	52
4.1. Seismic station GEODE, geophones, seismometers and cables	52
4.1.1. Settings for SH refraction profiling in GTA	53
4.1.2. Settings for MASW survey in GTA	55
4.1.3. Settings for building resonances test	56
4.2. Portable three-component 1-40 Hz seismic station	57
4.2.1. Electronic moduli	57
4.2.2. Seismometer L4-3D - correction of the transfer function	60

Chapter 5. Geophysical field investigations	63
5.1. Introduction	63
5.2. Seismic SH refraction profiling	64
5.2.1. Refraction survey data acquisition	64
5.2.2. Refraction survey data processing	65
5.3. MASW estimation of the velocity model for shallow soil profile	66
5.3.1. MASW field measurements	66
5.3.2. MASW data processing	67
5.4. Comparison between VS-30 from SH refraction profiling and MASW survey..	72
5.5. HVSr data acquisition and processing	74
5.5.1. Field data acquisition	74
5.5.2. HVSr data processing	74
5.6. Comparing HVSr results with theoretical response functions using data from SH refraction profiling	84
 Chapter 6. Results from geophysical study for GTA microzonation	 89
6.1. Summary of the results for the GTA microzonation	89
6.2. Maps using GIS and Surfer software	95
 Chapter 7. Influence of Building Resonances on HVSr Results	 101
7.1. Introduction	101
7.2. Some techniques for modal identification using wind and ambient vibrations ..	102
7.2.1. Basic Frequency Domain Decomposition versus some other techniques for identification of the structural vibration modes	103
7.2.2. Mode shapes derived for a building approximation	105
7.3. Experimental study of the effects of building vibration on the soil resonances obtained by HVSr technique	110
7.3.1. Short description of the studied building	110
7.3.2. Test points locations	112
7.3.3. Building resonant frequencies at dominant vibration mode from three-component waveforms recorded at the center test point on the 13-th floor.....	114
7.3.4. Separation of the vibration modes of the building using resonant frequencies from three-component waveforms recorded simultaneously at five test points distributed vertically along the northern staircase	117
7.3.5. Separation of the torsional vibration modes from deflection of the building using the resonant frequencies from two-component waveforms recorded simultaneously at five test points distributed horizontally along the corridor on the twelfth floor	120
7.4. Application of the Horizontal to Vertical Spectral Ratio (HVSr) for determination of the building resonances	124
7.5. Influence of the building vibrations on the results from HVSr used for estimation of the soil resonances	127
7.5.1. Discovering of the hinge point from collected data set	128
7.5.2. Comparison of HVSr results before and after completion of the building	131

7.5.3. Seismic wave excitation from building vibrations and wave propagation through the soil below and around building foundation	134
7.5.4. Influence of the first vibration mode of the building on the HVSR results	136
Chapter 8. Difference between building resonances estimated by empirical relations from Building Codes and obtained experimentally	137
8.1. Introduction	137
8.2. Building resonant frequencies estimated by commonly accepted empirical relations and finite element modeling	137
8.3. Building RC framed construction under dynamic loading	138
8.4. RC structure under dynamic lateral load	140
8.5. Change of resonant frequencies of the studied building 2.5 years after construction	143
8.6. Relation between resonant frequencies and damping ratios obtained from direct measurement and from empirical calculation	147
8.7. Implementation of stiffness reduction and increase of resonant period and damping ratio of a building during strong earthquake	147
Chapter 9. Summary and conclusions	155
9.1. Summary of the results and discussion	158
9.2. Conclusions	161
9.3. Recommendations for future research	163
References	165
Appendix: Geophysical results for the referent test points	179
Curriculum Vita	243

List of Tables

Table 1.1.	Seismic provisions of the NBCC 2005 (Adams and Halchuk, 2003) Sa(0.2) to Sa(2.0) - spectral acceleration, (g) for periods 0.2 to 2 seconds, PGA - peak ground acceleration (g)	2
Table 1.2.	NBCC 2005 Site Classification for Seismic Site Response	19
Table 5.1.	Results for VS -30 from SH profiling and MASW models	72
Table 6.1.	Results from geophysical field investigations and soil classification	92
Table 7.1.	Vibration modes – coefficients	108
Table 8.1.	Empirical building resonances	138
Table 8.2.	Changes of the building first and torsional resonances (Hz) with years	144

List of Figures

Figure 1.1.	Uniform Hazard Spectra for median 2%/50 year ground motions on Site Class C for key cities (NBCC 2005)	2
Figure 1.2.	Study area (enclosed by black line) of Great Toronto Area. Map base @ 2011 Google	9
Figure 1.3.	Illustration of major stratigraphic layers in the GTA. (from Eyles, 2004)	10
Figure 1.4.	Distribution of Paleozoic bedrock formations in the Toronto area (from Baker et al., 1998)	11
Figure 1.5.	Paleozoic Geology (layer II) of GTA region (Ontario Geological Survey, Map 2544)	12
Figure 1.6.	The surface of rocks making up Layer II, ‘stripped’ of its glacial sediments. (from Eyles, 2004)	13
Figure 1.7.	Quaternary geology of GTA (from Baker, 1998)	14
Figure 1.8.	Cross section through Layer III: Oak Ridge’s Moraine to Lake Ontario (from Eyles, 2004)	14
Figure 1.9.	Landfill in downtown Toronto (acc. to Eyles, 2004)	15
Figure 1.10.	Earthquakes after 1900 with $m_N > 5$ in 500-km area around Toronto labeled with its accepted name. (Data: NRC, Earthquakes Canada, GSC (On-line Bulletin), http://seismo.nrcan.gc.ca/stnsdata/nedb/bull_e.php)	16
Figure 1.11.	Seismicity around GTA (1990-2001) (acc. to Dineva et al., 2004)	17
Figure 1.12.	Earthquakes around GTA (2007-2011) (from http://earthquakescanada.nrcan.gc.ca)	17
Figure 1.13.	Spectral acceleration for a period of 0.2 seconds at a probability of 2%/50 years for firm ground conditions (NBCC 2005 soil class C, NBCC 2010)	18
Figure 2.1.	Example of changes in the shear modulus and damping factor vs. shear strain (from Studer and Ziegler, 1986)	25
Figure 2.2.	Changes in a) the shear modulus G/G_0 and b) damping factor D [%] vs. effective shear strain averaged in this study (from Kokusho, 2004)	26
Figure 2.3.	Changes in the shear modulus and damping factor vs. shear strain assuming degradation of soil with $V_{S0} = 200$ m/s.	27
Figure 2.4.	Some MMI vs. PGV regressions	28
Figure 2.5.	Nomogram from eq. 2.17 to 2.19 connecting PGV with MM Intensity (red line) and with Effective Shear stain γ_{eff} for different values of V_{S0} (blue lines)	29
Figure 2.6.	Normalized soil resonances at different Intensity MM (I_{MM}) ..	30
Figure 2.7.	Modified hypothetical flat velocity spectra for different I_{MM} with normalized soil transfer functions shown on Figure 2.6. ...	31
Figure 2.8.	Soil resonances from H/V ratio during the earthquakes with different magnitudes in North Anatolian Turkey recorded at station Duzce DUZ (DZC) (from Lang et al., 2002)	32

Figure 3.1.	Data separation for HVSR calculations. FFT-10.24s - running time interval for individual FFT spectrum: a) Average modulus of all 3 components and threshold levels H-level and L-level; b) Windows with low and high level of vibration and starting time for each individual FFT spectrum: H-start and L-start	39
Figure 3.2.	HVSR from the original records and from separated Low and High Level time windows, σ - standard deviation ...	40
Figure 3.3.	Raypath diagram for direct, reflected and refracted rays	42
Figure 3.4.	Example of 12-channel seismic refraction record	42
Figure 3.5.	Time-distance plot for seismic refraction/reflection survey	43
Figure 3.6.	Travel time curves for three layer soil profile with increasing velocity with depth	44
Figure 3.7.	Example of hidden second layer due to absence of head wave from h1 boundary in first arrival	45
Figure 3.8.	Example of refracted wave travel times for a dipping second layer.....	47
Figure 3.9.	Arrangement of SASW test	49
Figure 3.10.	Example of MASW - CMPCC data and their interpretation	51
Figure 4.1.	A simplified scheme of the equipment for HVSR field measurements.	57
Figure 4.2.	a) Instrumental differential amplifier R_G - gain control; b) Schematic of Sallen-Key topology for a second order low-pass filter	58
Figure 4.3.	Excel worksheet for calculation of the 8 th order low-pass filter.	59
Figure 4.4.	Schematic of the 8 th order Bessel low-pass filter at 40 Hz	60
Figure 4.5.	Normalized transfer function of L4-3D and the 8 th order Bessel low-pass filter at 40 Hz	62
Figure 5.1.	Test points over studied part of GTA	63
Figure 5.2.	Geometry of the SH refraction seismic profiles	65
Figure 5.3.	Example of seismic records and travel-time lines from all shot points for SH refraction seismic profiles	65
Figure 5.4.	Geometry of the MASW field profiles	67
Figure 5.5a.	MASW field records at referent Test point #4 and dispersion curves	69
Figure 5.5b.	MASW inversion with different starting models for Test point #4	70
Figure 5.6.	Comparison between VS-30 from SH profiling and from MASW inversions for four initial soil models	73
Figure 5.7.	INPUT worksheet for HVSR calculations.	75
Figure 5.8.	Hann window effect. a)The Hann window; b), c), d) - 3 components time series subjected to hanning (black lines) over the original waveforms (grey lines)	77
Figure 5.9.	HVSR smoothed by triangle function with different width Δf_{AVE} a) without applying of Hann window; b) using Hann window.	78

Figure 5.10.	Examples of Fundamental (F) and Dominant (D) HVSR resonances: a, b, c - fundamental resonances are dominant in HVSR; d, e, f - fundamental resonance has smaller amplitude than the dominant ones.	79
Figure 5.11.	Example of separation of the waveforms and HVSR into low and high levels of the ambient vibrations. Modulus is the sum of the absolute values of all components for each time increment (sample), L/H - the hysteretic thresholds.	80
Figure 5.12.	Example of separation of the waveforms and HVSR into low and high levels of the ambient vibrations.	81
Figure 5.13.	HVSR for low and high level of vibrations shown on Figure 5.11. The resonance is from the Low level of the ambient vibrations	82
Figure 5.14.	HVSR for low and high level of vibrations shown on Figure 5.12. The fundamental resonance is from the High level of the ambient vibrations	82
Figure 5.15.	HVSR data processing of two field records for test point 4: a) field records, b) separation of the signal for Low and High vibration levels, c) start of the windows for the time series, d) HVSR for Low and High levels	83
Figure 5.16.	Spreadsheet for calculation theoretical site response of two soil layers over bedrock using velocities and depth to the first boundary from SH refraction profiling.	85
Figure 5.17a.	Comparison between HVSR and calculated response for the referent test point #4	86
Figure 5.17b.	Comparison between HVSR and calculated response for the referent test point #17.	86
Figure 5.17c.	Comparison between HVSR and calculated response for the referent test point #27.	87
Figure 5.17d.	Comparison between HVSR and calculated response for the referent test point #31.	87
Figure 6.1.	Classification of the soil deposits according to NBCC 2005 against the legend to the GSC map (Surficial Geology of the Greater Toronto and Oak Ridges Moraine Area, Southern Ontario) (Sharpe et al., 1997)	90
Figure 6.2.	Fundamental soil resonant frequencies in GTA (this study)	96
Figure 6.3.	Drift Thickness in GTA (from Gao et al., 2006)	96
Figure 6.4.	Relative amplification at the fundamental resonances (this study)	97
Figure 6.5.	Fundamental resonances with relative amplification ≥ 3 (this study).	97
Figure 6.6.	Surficial geology of the GTA (from Sharpe et al., 1997).	99
Figure 6.7.	Interpolated NBCC 2005 soil classes for GTA (this study)	99
Figure 6.8.	Applicable NBCC 2005 soil classes for GTA (this study)	100
Figure 7.1.	Simplified approximation of a tall building as a column	105
Figure 7.2.	Plot of the equation (7.19).	108

Figure 7.3.	Plots of the first three mode shapes from normalized eigenvectors	109
Figure 7.4.	Torsional mode-1	110
Figure 7.5.	Photo of the studied building after completion.	111
Figure 7.6.	Sketch of the shear resistant elements at the base of the building.	111
Figure 7.7.	Locations of the measurement points around the building and at the base (ground) level of the building	113
Figure 7.8.	Wireframe sketch of the building, parking-garage and the test points	114
Figure 7.9.	TOP-CENTER test point on the 13-th floor of the building ...	115
Figure 7.10.	Averaged velocity spectra at the building TOP-CENTER test point	116
Figure 7.11.	Normalized velocity spectra at dominant vibration mode at the building TOP-CENTER test point.	116
Figure 7.12.	Changes of the spectra in different azimuths - normalized velocity spectra at the dominant vibration mode at the building TOP-CENTER test point.	117
Figure 7.13.	Locations of the test points along the northern staircase	118
Figure 7.14.	Example of the raw and filtered from 1.8 to 2.4 Hz signals.....	118
Figure 7.15.	First and second mode shapes - each with 20 positions in time	119
Figure 7.16.	Locations of the test points on the twelfth floor	120
Figure 7.17.	Cross-spectra between parallel and orthogonal components.....	121
Figure 7.18.	The filter sets for the torsional and first three vibration modes for both primary axes of the structure.	122
Figure 7.19.	Screen-shots of the animated movements from the test points on the 12-th floor used for animation a) and filtered horizontal waveforms b).	123
Figure 7.20.	Test points used for comparison between building first vibration modes obtained directly from spectra and from HVSR are marked in yellow	124
Figure 7.21.	Comparison between the original spectra from horizontal (N-S and E-W) and vertical (VERT.) movements (left) and HVSR (right) from the same waveforms at six test point in the building	126
Figure 7.22.	Test points (marked in yellow/red) used for polarization analysis to find a potential hinge point	128
Figure 7.23.	Snap-shot of the EXCEL animation for test point BASE-N. Polarization of vibrations and movement trajectory.	129
Figure 7.24.	Trajectories of vibration in two vertical projections at basement edges, marked in the same way as the test points on Figure 7.22.	130
Figure 7.25.	Tilting (rocking) of the basement floor of the building and hinge point established from the main movement directions (major axes of the elliptical trajectories)	131

Figure 7.26.	Comparison between HVSR before and after building completion	133
Figure 7.27.	Sketch of the propagation of the seismic waves generated due to rocking of the building around hinge point S	135
Figure 8.1.	Deformation of RC frame buildings with different stiffness of the columns and beams.	139
Figure 8.2.	Segment of a RC column under static and dynamic loads	135
Figure 8.3.	Velocity spectra from the waveforms recorded in 2009 and 2011 at the top floor of the building smoothed with triangle window +/- 0.01 Hz	143
Figure 8.4.	Reference SDOFs over transfer function calculated from NS unfiltered velocity waveform recorded at the Top-Center test point of the building and calculated from equations in the building codes	145
Figure 8.5.	Velocity waveform at the top of building and time windows after wind gusts used for approximating the free oscillations with damped sinusoid. DATA NS - velocity waveform NS component	146
Figure 8.6.	Approximation of the free oscillations at the first vibration mode in NS direction for the TOP-CENTER test point	147
Figure 8.7.	Acceleration waveforms, Vina Del Mar, Chile Mw=8.8 February 27, 2010 (source: Boroschek et al., 2010)	150
Figure 8.8.	Earthquake response spectra for Vina Del Mar, Chile Mw=8.8 February 27, 2010 (source: Boroschek, 2010).	150
Figure 8.9.	Earthquake response spectra with 5% damping for Vina Del Mar, Chile Mw=8.8 February 27, 2010 for the site of registration (Source: Boroschek et al, 2010). RP-1 and RP-2 - referent points.	152
Figure 8.10.	The amplification factor, α , for the four soil types in the Chilean code (modified from Ene and Craifaleanu, 2010). RP-1 and RP-2 - referent points.	152

List of Abbreviations and Notations

Abbreviations

ASCE	American Society of Civil Engineers
ASCE/SEI 7-05	ASCE Minimum Design Loads for Buildings and Other Structures
BFD	Basic Frequency Domain Decomposition
DFT	Discrete Fourier Transform
CG	Centre of Gravity
CMPPC	Common Mid-Point Cross-Correlation Analysis
CTR	
FEM	Finite Element Model
FEMA	Federal Emergency Management Agency U.S.A.
FFT	Fast Fourier Transform
GSC	Geological Survey of Canada
GTA	Great Toronto Area
HVSR	Horizontal-to-Vertical Spectral Ratio
H/V	Horizontal-to-Vertical Spectral Ratio
IFFT	Inverse Fast Fourier Transform
I_{MM}	Macroseismic Intensity, MM scale
MASW	Multi-channel analysis of surface waves
NAD83	North American Datum 83
NBCC	National Building Code of Canada
NEHRP	National Earthquake Hazards Reduction Program U.S.A.
MGOS	Multiple Geode Operating Software
OA	Operational Amplifier
PGA	Peak Ground Acceleration
PGV	Peak Ground Velocity
QTS	Quasi-Transfer Spectrum
RC	Reinforced Concrete
RP	Referent Point
S_a	Spectral Acceleration
SASW	Spectral analysis of surface waves
SDOF	Single Degree Of Freedom
SH	Horizontally polarized shear wave
SSR	Standard Spectral Ratio
SVD	Singular Value Decomposition
SWSP	Shear-Wave Seismic Profiling
UHS	Uniform Hazard Spectra
UWO	University of Western Ontario
VSP	Vertical Seismic Profiling

Notations

A	Amplification factor
$A(f)$	Soil amplification (SDOF)
A_i	Amplitudes of the upward propagated shear waves in layer i
A_0	HVSR amplification facto related to the impedance ratio.
α	Soil amplification factor in the Chilean building code
α_m^*	Complex impedance ratio
B	Amplitude of shear wave
B_i	Amplitudes of the downward propagated shear waves in layer i
D	Damping ratio
C_i	Capacitance
D_o	Initial damping ratio for undisturbed soil
D_{IMM}	Damping ratio for intensity I_{MM}
E	Energy in shear wave
E	Young modulus (Chapter 7)
f	Frequency
f_{0IMM}	Resonant frequency for intensity I_{MM}
f_c	Filter frequency
$F(\omega)$	Transfer function for shear waves
F_a	Soil modification factor for acceleration
F_V	Soil modification factor for velocity
ϕ_R	Phase shift
G	Shear modulus
G^*	Complex shear modulus
G_0	Maximum shear modulus of undisturbed soil
γ_{eff}	Effective shear strain
h	Depth to the basement or refractor
I	Areal moment of inertia
I_{MM}	Modified Mercalli Intensity
i_c	Critical angle
J	Torsion constant (torsional stiffness)
k	Wave number
k^*	Complex wave number
ζ	Damping ratio
M_L	Local Richter magnitude
M_W	Moment magnitude
M_S	Surface magnitude
m	Slope of the travel-time graphs from a seismic refraction profile
\bar{N}_{60}	Standard penetration resistance
ω	Angular frequency
Q	Quality factor
R_i	Resistance

R_G	Gain control resistor
ρ	Density
S_a	Spectral acceleration
s_u	Soil undrained shear strength
σ'_0	Effective stress
T	Fundamental period
T_d	Travel time downhill slope
T_u	Travel time uphill slope
t_i	Intercept time of refracted wave on the travel-time graphs
t_d	Intercept time downhill slope
t_u	Intercept time uphill slope
$\tau(z,t)$	Shear stress
$u(z,t)$	Horizontal displacement along the vertical axis
V_R	Velocity of Rayleigh wave
V_S	Shear-wave velocity
V_{SSurf}	Shear wave velocity in a subsurface layer
V_{SBase}	Shear wave velocity in the base (bedrock)
V_{S0}	Shear wave velocity in the uppermost soil layer
$VS-30$	Average shear-wave velocity in the upper 30 m
V_d	Apparent velocity down slope
V_{pp}	Voltage amplitude peak-to-peak
V_u	Apparent velocity uphill
x_{cross}	Crossover distance on of the travel-time graphs
Δx	Spacing between two receivers
Z_m	Vertical coordinate
θ	Dip angle
λ_R	Wavelength of Rayleigh wave
λ_{Rmin}	Shortest wavelength of interest
$\Delta\phi$	Phase angle difference between two receivers
ν	Poisson's ratio

Chapter 1

Introduction

1.1. Introduction

The national seismic hazard map of Canada forms the fundamental basis of the most effective way to reduce casualties and economic losses from future earthquakes. According to the 2005 National Building Code of Canada (NBCC 2005), the region of Great Toronto Area (GTA) is located in the more “stable” eastern part of Canada, but it can experience peak ground accelerations (PGA) of up to 0.24 g from local sources (earthquakes). The level of 5% damped Spectral Acceleration, for the City of Toronto is lower than that for Montreal, but higher than that for Calgary and Winnipeg (Adams and Halchuck, 2003, 2004). The estimated PGA and spectral levels in the NBCC 2005 are defined for a “reference” ground conditions.

Damages caused by the recent earthquakes are exacerbated as a direct result of ground motion amplification due to local geological conditions. Amplified motions have a much stronger effect on structures when the soil resonances and the resonant frequencies of seismic waves are in the range of the dominant periods of structures. Seismic microzonation is a process for determining the necessary adjustment to seismic hazard due to effects in soils under dynamic loads such as amplification of ground motion, slope instability and liquefaction.

Seismic microzonation involves specification in details of soil resonances and its results are useful in the planning of urban areas and individual structures.

Uniform Hazard Spectra (UHS) constructed for 2005 NBCC is based on five spectral values. UHS for a few major cities illustrate the range and period dependence of seismic hazard across Canada (Figure 1.1 and Table 1.1). Each populated area, however, has a unique site-specific response spectrum with resonant frequencies generally different from those used for UHS. The soil classification is limited to only five site classes in 2005 NBCC. These classes are based on averaged values of shear wave velocity to depth 30 m below ground surface.

The available geological and geotechnical information for the GTA area at present is sparse. It is not easy to define where and how the original soil profile has been altered during land reclaim and construction of the underground infrastructure, buildings, etc.

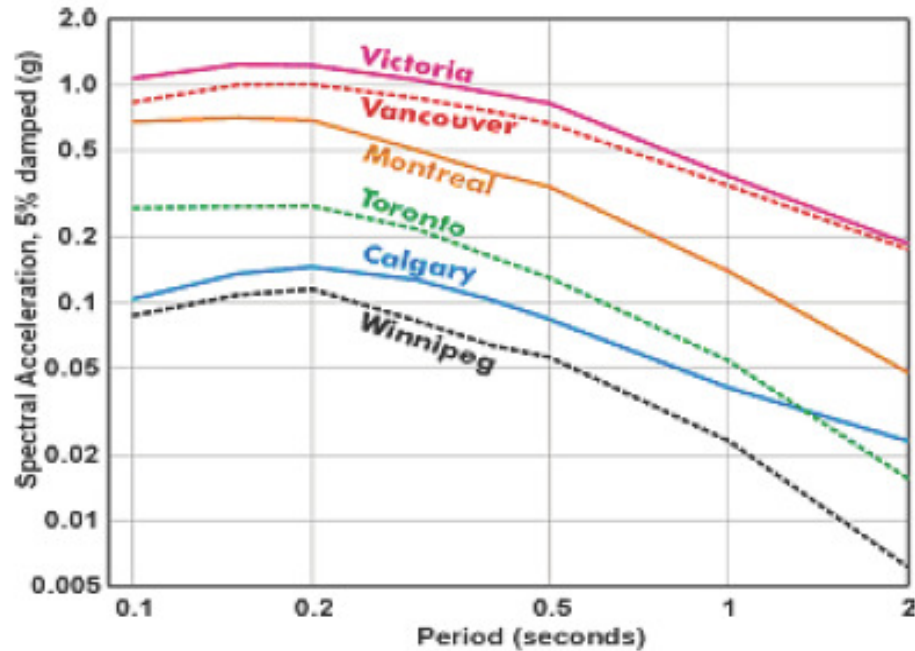


Figure 1.1. Uniform Hazard Spectra for median 2%/50 year ground motions on Site Class C for key cities (NBCC 2005).

Table 1.1.

City	Sa(0.2)	Sa(0.5)	Sa(1.0)	Sa(2.0)	PGA
Burlington	0.36	0.18	0.063	0.020	0.27
Hamilton	0.33	0.16	0.58	0.018	0.24
Mississauga	0.31	0.15	0.055	0.017	0.22
North York	0.24	0.12	0.054	0.015	0.15
Oakville	0.35	0.17	0.062	0.020	0.26
Port Credit	0.32	0.16	0.058	0.018	0.24
Toronto	0.26	0.13	0.055	0.015	0.17
Scarborough	0.24	0.12	0.056	0.015	0.15

Seismic provisions of the NBCC 2005 (Adams and Halchuk, 2003)

Sa(0.2) to Sa(2.0) - spectral acceleration, (g) for periods 0.2 to 2 seconds,

PGA - peak ground acceleration (g)

Significant engineering problems in Toronto are associated mainly with some of the following factors (Baker et al., 1998): weak glacial lake deposits; ‘running’ sand; slope stability; variable soil conditions, including artificial landfills, buried valleys etc.

For urban areas, the site response evaluation is also complicated by the influence of building loads, soil improvement, pile foundation, densification, etc. In these areas, the soil resonances can be found using Horizontal-to-Vertical Spectral Ratio (HVSr) (Nakamura, 1989, 2000) or other geophysical methods only on the free surface between buildings. In the built-up areas of the cities the soil response determination has primarily informative value. In case of new construction, the soil classification and soil transfer function should be specified at the design stage. Additionally, the geophysical methods using ambient noise and active vibration sources give information about the soil response at very low dynamic loading which is not the case during an earthquake.

A common problem in city conditions is how to evaluate the influence of building vibrations on the results from the geophysical methods that use the ambient vibrations as a seismic source. The evaluation of the site response is important when evaluating the building behaviour during an earthquake. Both soil and building resonances change if a strong dynamic load is applied. An attempt is made here to create a generic model of the ground motion amplification and non-elastic effects due to strong ground shaking. Similarly a simplified hypothetical model of building resonances is created to explain the changes of the building resonances during and after strong shaking.

1.2. Objective and Methods of the Study

The objectives of this study are to establish and verify a methodology of seismic microzonation suitable for urban areas through the comparison of field measurements with theoretical predictions, and apply this methodology for the Greater Toronto Area (GTA). To achieve these objectives, a pilot field microzonation study of the GTA was undertaken involving the following tasks: selection and assembly of equipment suitable for the measurements using the chosen microzonation methodology, including digital data acquisition for recording ambient noise; gathering and analyzing of field data for the purpose of the microzonation; comparison of the field results with theoretical calculations in order to examine the validity of the theoretical approach; verification of the

applicability of the chosen microzonation methodology for the study area; verification of the influence of building vibrations on the site response obtained by HVSR which uses the ambient vibration as seismic source; establishment of a connection between the changes in building and soil resonances during moderate and strong earthquakes; and preparation of recommendation for future work on the microzonation of the GTA.

The activities and methods to attain the objectives of this study are provided below:

1. To summarize geological and seismological data for the GTA from recognized sources.
2. To develop an automatic procedure to simplify calculation of the Horizontal to Vertical Spectral ratio (HVSR) from ambient vibrations in city conditions separating the waveforms from near-by and distant vibration sources.
3. To perform mass field measurements of ambient vibrations using the HVSR method to establish the distribution of soil resonances in the GTA.
4. To perform SH refraction seismic profiling and Multichannel Analysis of Surface Waves (MASW) at some reference test point in the GTA in order to correlate the obtained velocity soil profiles with HVSR results and surface geology in the GTA.
5. To evaluate the applicability of geophysical methods for seismic microzonation in urban areas.
6. To develop a simplified, portable, 3-component seismic station for HVSR field measurement.
7. To develop a program for the calculation of soil resonances applicable for n-layer soil structure and to compare the program's outputs with the results from field measurements.
8. To develop maps for the distribution of fundamental soil resonances, relative amplification factors and soil classification according to NBCC 2005 requirements using standard mapping software (ArcGIS, SURFER, etc.).
9. To establish the dynamic changes of soil properties during earthquake shaking using published data for soils similar to those found in the GTA.

10. To estimate from experimental data the influence of building vibrations on the results of HVSR measurements using a benchmark building.

11. To evaluate the changes in building resonances during moderate or strong earthquakes in conjunction with the earthquake spectra and soil response obtained from seismic microzonation.

1.3. Organization of the Dissertation

This thesis has been prepared according to the guidelines specified by the Faculty of Graduate Studies at the University of Western Ontario for Monograph format. It has been divided into nine chapters. Related literature and necessary background to each subject have been included in the References. The subsequent sections provide in sequence a concise description of the contents of each chapter in order to address the objectives of the study presented in Section 1.2.

Chapter 1

The introduction includes the general seismic provisions of the NBCC 2005, objectives and scope of this study, organization of the dissertation and some original contributions of the thesis.

Chapter 2

The basic concepts of soil response during seismic vibrations are applied along with an Excel program for the calculation of linear soil response to weak seismic impact. Included are the modeling and evaluation of changes in the soil resonance during strong earthquakes.

Chapter 3

This chapter describes geophysical methods for seismic microzonation in urbanized areas including Horizontal to Vertical Spectral Ratio (HVSR) for estimation of soil resonances and SH refraction velocity profiling (SH profiling), Spectral Analysis of Surface Waves (SASW), and Multi-Channel Analysis of Surface Waves (MASW) for shear wave velocity estimation. The background behind the idea of noise separation from nearby and

distant sources and a VBA/Excel program for HVSR calculation are presented. The limitations for geophysical methods in city conditions are discussed.

Chapter 4

Equipment required for the field measurements is specified including setup of the seismic station GEODE, geophones, seismometers and cables for different geophysical measurements.

The schematics of the designed three-component portable seismic station and electronic modules are described. An Excel spreadsheet for calculation of adjustable 8-th order low pass filters is made for the prototyping. The equation for correction of the transfer function of seismometer L4-3D is derived.

Chapter 5

Geophysical field investigations are described: SH profiling data acquisition and processing; MASW measurements, data processing and estimation of the velocity model for shallow soil profile; Comparison between VS-30 from SH and MASW is presented; HVSR data acquisition and processing are described; comparison between HVSR results and theoretical soil response functions based on the data from SH profiling is presented.

Chapter 6

The results of the geophysical study for the GTA seismic microzonation are presented including soil resonances and classification of the test sites. The results are presented in table form and with maps of soil fundamental resonances, amplifications and interpolated soil classification using ArcGIS and Surfer software.

Chapter 7

Some techniques for modal identification using wind and ambient vibrations are described. For structural vibration modes, basic frequency domain decomposition is preferred versus other identification techniques. Mode shapes are derived for an approximation of the building with a vertical cantilever. Short descriptions of the studied benchmark building and test point locations are given. Building resonant frequencies for

the first three and the torsional vibration modes are established from three-component waveforms recorded consecutively or simultaneously at different test points. The center of rotation (hinge point) below the building is identified using the collected data set. Application of the Horizontal to Vertical Spectral Ratio (HVSR) for the determination of building resonances is examined. The influence of the first vibration mode of the building on the HVSR results is established by comparing the collected HVSR data sets before and after completion of the building. The excitation of seismic waves from building vibrations and wave propagation through soil below and around the building foundation is presented.

Chapter 8

An explanation is proposed for why building resonances estimated by empirical correlations and finite element modeling differ from those obtained by field measurements.

Stiffness reduction and probably short initial resonant period and low damping ratio for the first vibration mode of a building during a strong earthquake is proposed as a possible explanation of the phenomenon where some new RC buildings were damaged during the Chilean earthquake 2010, while the older ones were intact.

Chapter 9

Chapter 9 presents a summary and conclusions for this study chapter by chapter as well as recommendations for future research.

1.4. Original Contributions of the Thesis

This thesis provides a pilot study on the seismic microzonation for the GTA.

The results are original maps of soil fundamental resonance, amplification factors and interpolated soil classification.

An unknown until now depression in the bedrock surface is outlined.

A program for separate calculation of the HVSR resonances from ambient vibrations with low and high levels is developed.

An Excel program for calculating the theoretical soil resonances in case of multilayered strata is developed.

A portable 3-component seismic station for HVSR measurements is designed. It is easy to use in urban areas comparable to the existing commercial equipment.

A relationship between shaking intensity IMM, peak ground velocity (PGV) and soil elastic moduli is used to establish an example of nomogram for calculating of the effective soil strain and elastic moduli during intense earthquake shaking.

The influence of the building resonances at first mode on the HVSR results is explained by establishing the ray-paths and polarizations of seismic waves generated by the building vibrations.

The center of the rocking of the building (hinge point) is determined using polarogram from asynchronously recorded 3-component waveforms at the edges of the basement.

A change of resonant frequency of the studied building 2.5 years after construction is observed. A proposed explanation for the differences between fundamental resonances of buildings calculated using empirical equations from building codes and those obtained from direct measurements. The nonlinear effects during intense dynamic loading reduce the stiffness of the structure and increase fundamental periods and damping ratios.

The nonlinear change of building resonances is employed to illustrate why new RC buildings with probably short resonant period and low damping were more vulnerable than older ones during the Chilean earthquake (M8.8, 2010).

1.5. Seismic microzonation - methodologies:

Geological methods applicable for study of shallow sediments and their association with soil classification suggested by NBCC 2005;

Geomorphologic methods for investigation of slope distribution, their topology and stability under earthquake shaking;

Theoretical and numerical modeling of site response during dynamic loading and earthquake shaking;

Geophysical methods for investigation of sediments covering the bedrock surface and for determining of local shear wave vertical soil profile;

This study involves mainly seismic geophysical methods in conjunction with available geological information and theoretical modeling of site response spectra and for determination of shear wave velocity in the upper 30 m of the sediment cover (V_{s30m} suggested by NBCC 2005).

1.6. Description of the study area

1.6.1. Location and population

The GTA is part of a larger urban area, extending from Niagara Falls to Kingston, called ‘Golden Horseshoe’. This area is the most heavily populated area in Canada. It is home for almost 20% of the nation’s population and is considered to be its economic engine. The study area covers the most populated part of the Greater Toronto Area (GTA) (Figure 1.2). The total area included in this study is approximately 2500 km².

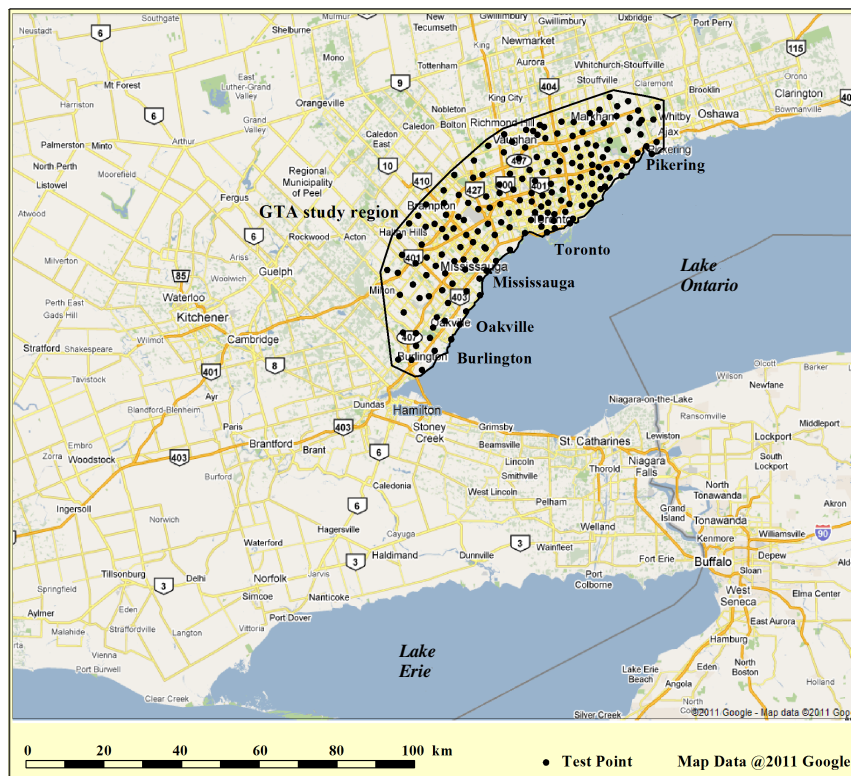


Figure 1.2. Study area (enclosed by black line) of Great Toronto Area.
Map base @ 2011 Google

1.6.2. Geological Conditions in the GTA

The geology of Toronto can be divided in four different layers (Figure 1.3, Eyles, 2004):

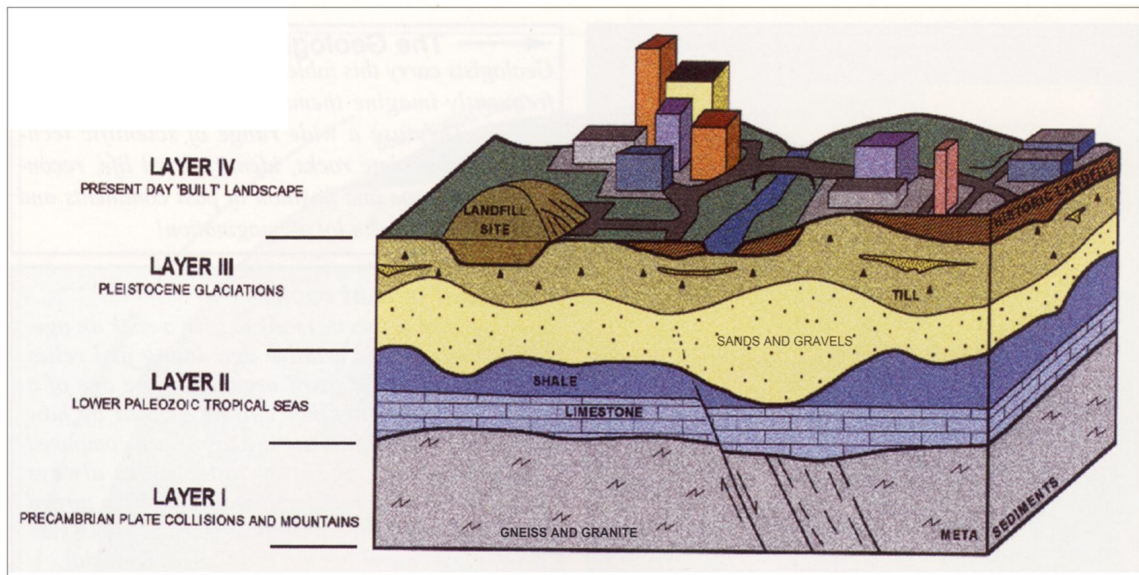


Figure 1.3. Illustration of major stratigraphic layers in the GTA. (from Eyles, 2004)

Layer I (the oldest) – Precambrian Canadian Shield rocks 35-40 km thick, 1.1 to 1.45 billion years old.

The three upper (younger) layers, i.e. Paleozoic (bedrock) sediments, Pleistocene (glacial) sediments and the natural landscape (glacial) sediments, play the most important role for the earthquake ground motion amplification / deamplification.

Layer II – Paleozoic age sedimentary rocks up to 500 m thick, deposited between 600 and 400 million years ago in an ancient sea.

Layer III – Pleistocene glacial sediments formed within the last 135,000 years, up to 200 m thick. These sediments were deposited by continent-wide ice sheets during several ice ages. They consist of warm-climate ‘interglacial’ deposits sandwiched between the glacial deposits.

Layer IV (the youngest) – Natural landscape, created and sculpted by the last glaciations. This landscape has been smoothed by the city streets and artificially built landscape or landfill up to 15 m thick, consisting of waste materials, used to ‘reclaim’ new land from Lake Ontario, marshes and ravines.

Layer II

The oldest rocks in Layer II seen in the Toronto region are limestones of Simcoe Group (Eyles, 2004). They are overlaid by three shale-dominated units of Late Ordovician age – the Blue Mountain, Georgian Bay and Queenston formations as shown in Figure 1.4 (Baker et al., 1998). Thick Silurian sandstone, shale and limestone layers are deposited on top of Ordovician layers. The Paleozoic bedrock formations and Paleozoic geology (Layer II) of GTA are shown in Figures 1.2, 1.4 and Figure 1.5.

The Blue Mountain Formation in Toronto consists predominantly of brown-grey shales termed the Rouge River Member. The Blue Mountain Formation subcrops in the eastern third of the area with small outcrops present along the valley floors of Rouge River and Little Rouge Creek. The formation is interpreted to be deposited in a shelf environment below storm wave base.

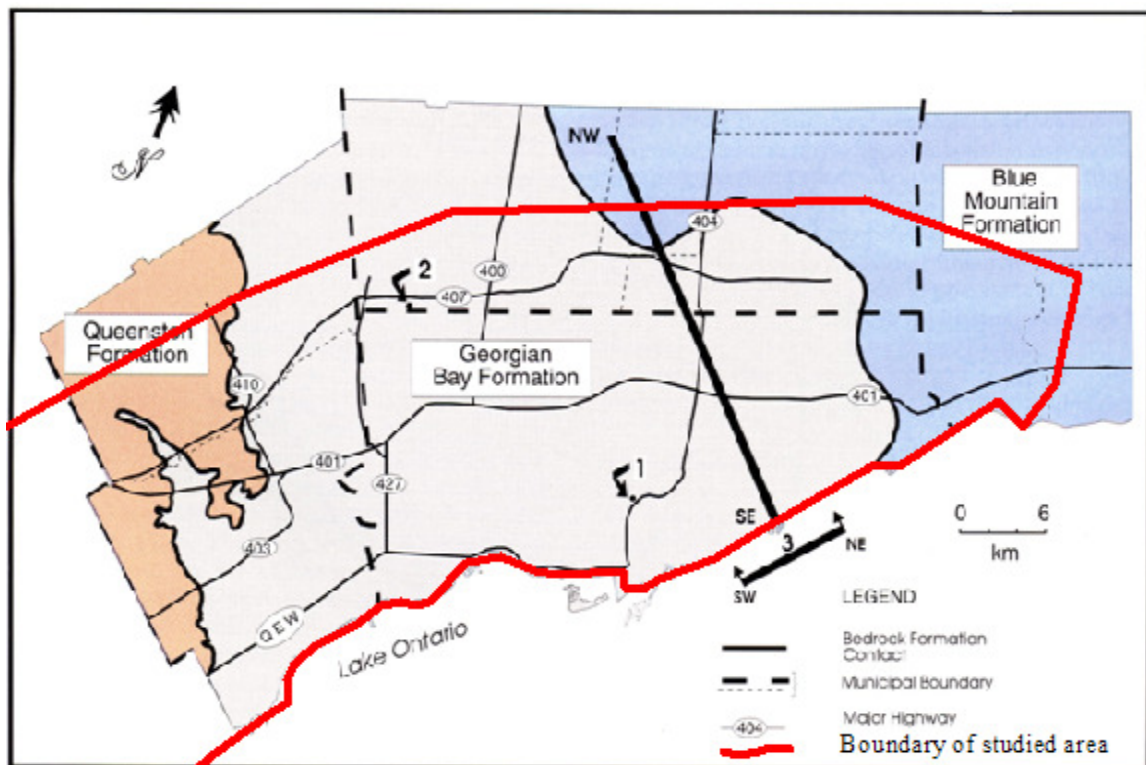


Figure 1.4. Distribution of Paleozoic bedrock formations in the Toronto area (from Baker et al., 1998)

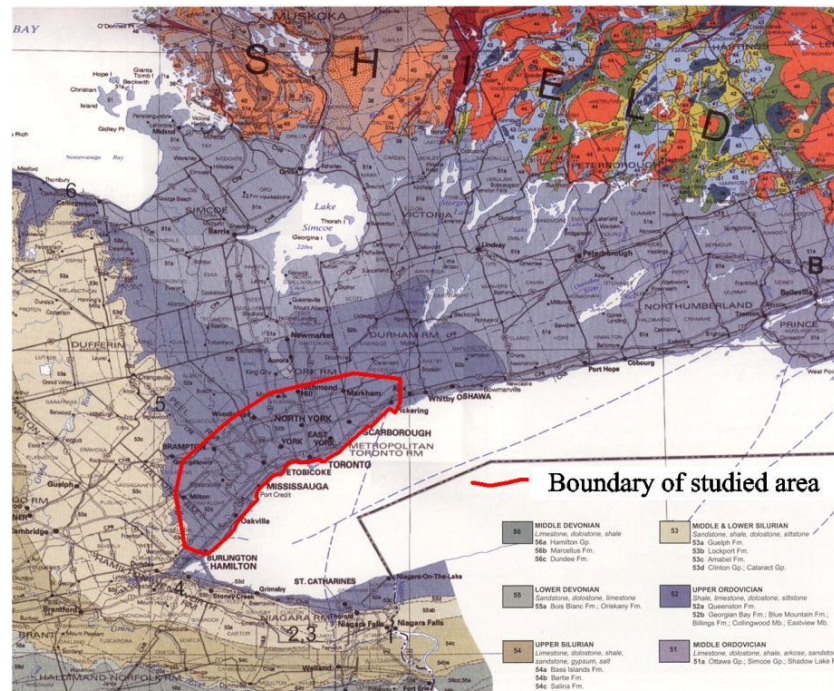


Figure 1.5. Paleozoic Geology (layer II) of GTA region (Ontario Geological Survey, Map 2544).

The Georgian Bay Formation underlies the central portion of the Toronto area. The formation consists of blue-grey shale with minor siltstone, sandstone and limestone interbeds. The Georgian Bay Formation is interpreted to represent shallowing upward, storm-dominated shelf succession. Outcrops of the Georgian Bay Formation are common along water courses in the western portion of Toronto area, e.g. Humber River, Mimico Creek, Etobicoke Creek and the Credit River. Construction excavations in downtown Toronto commonly intersect and expose this formation.

The Queenston Formation, found along the western margin of Toronto area, is a maroon shale containing some interbeds of grey-green shale, bioclastic limestone and calcereous siltstone. The Queenston Formation is believed to be deposited as part of a large, northward-prograding, deltaic complex.

Post-depositional erosion of the bedrock surface in the Toronto area has resulted in the formation of a series of poorly defined bedrock valleys, the largest of which is the south-trending Laurentian River valley. Figure 1.6 shows the surface of rocks making up Layer II deeply eroded prior to the Pleistocene glaciation, 'stripped' of its glacial sediment cover.

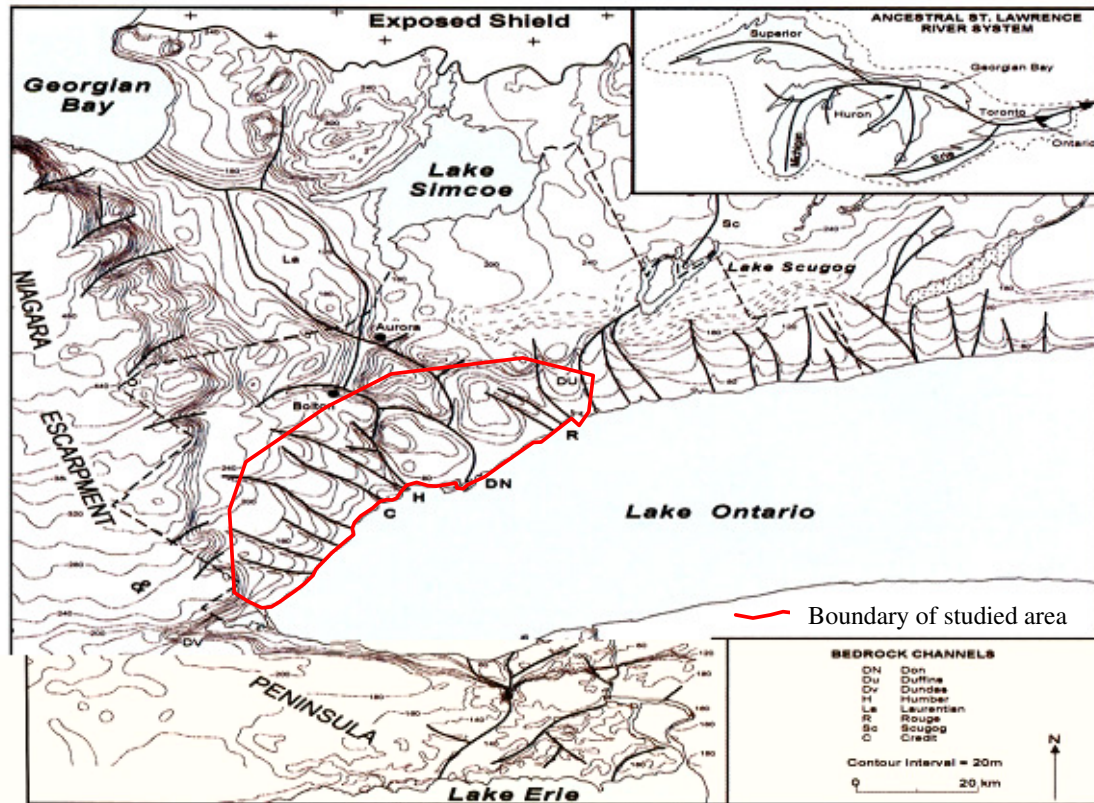


Figure 1.6. The surface of rocks making up Layer II, ‘stripped’ of its glacial sediments. (from Eyles, 2004).

Layer III

The Pleistocene glacial sediments are poorly graded deposits, containing a mixture of boulders, gravel, sand and mud called till. Boulders were transported over long distances by glaciers from the Canadian Shield to the north. Till pushed in front of the ice sheet formed moraine ridges or was overrun to leave drumlins (Eyles, 2004). The most prominent features in these layers are the Scarborough Bluffs, the Don Valley Brickyards (Brick Works) and the Woodbridge Cut (Figure 1.4). Just on the northern edge of GTA, the Oak Ridge’s Moraine is 20 km wide belt of hilly topography extending over 150 km. The moraine is composed of sand and gravel deposited in a deep interlobate lake. Large blocks of the ice sheet were buried below sediments (Eyles, 2004).

A Quaternary geology map is shown in Figure 1.7. A cross section through Oak Ridge’s Moraine to Lake Ontario is shown in Figure 1.8.

Layer IV (Artificial Landscape)

More than 50% of downtown Toronto is landfill, resulting from infilling of marshes and bays with waste materials. Current Front Street was the former lake shore.

Starting initially with disposal of 'night soil' and ash from houses, after 1912 landfiling became a systematic policy on a grand scale.

Entire ravines have been filled with waste and creeks disappeared from the surface to flow trough pipes underground (Eyles, 2004).

Figure 1.9 shows the progressing of the landfill in downtown Toronto.

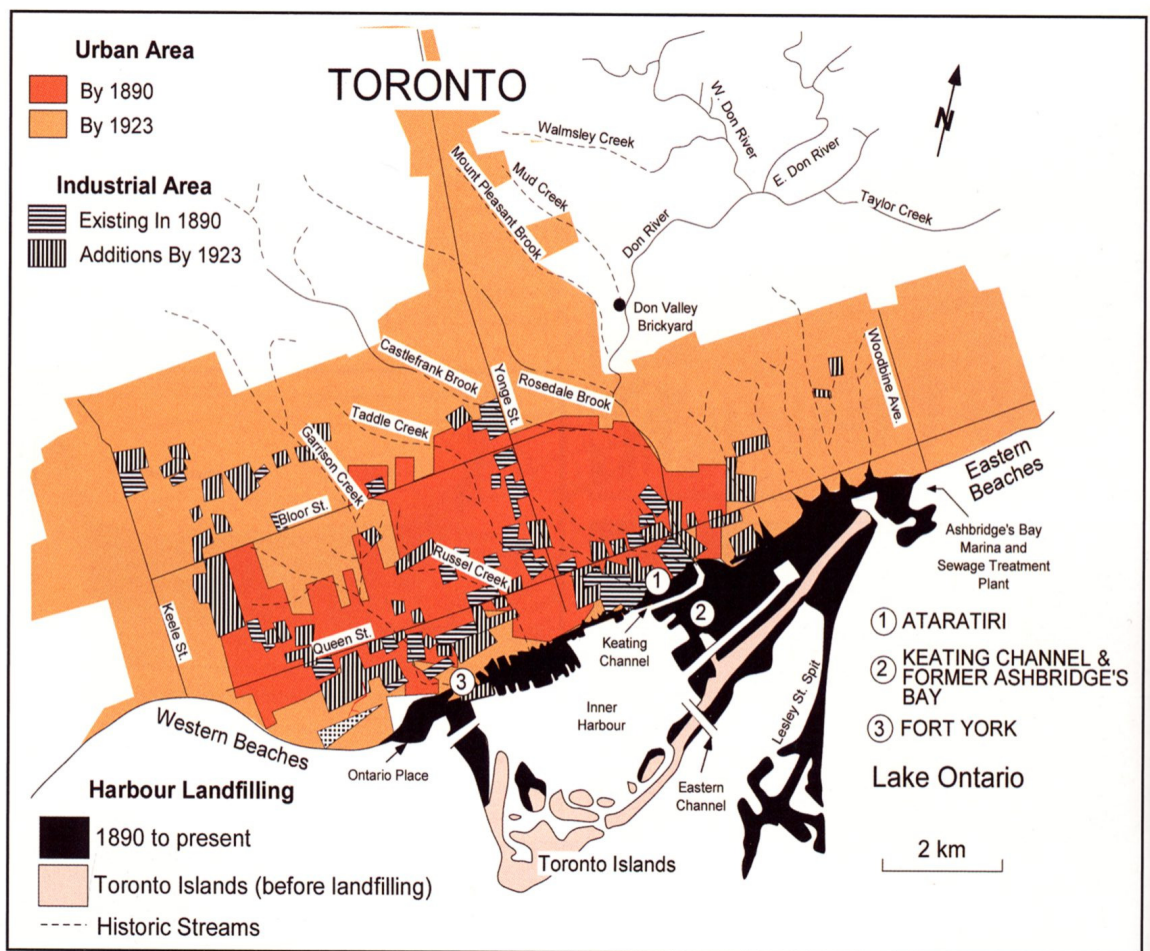


Figure 1.9. Landfill in downtown Toronto (acc. to Eyles, 2004).

1.7. Earthquakes and Faults Around GTA

The area around GTA is characterized by moderate, ‘intraplate’ seismicity. The maximum observed earthquake in the last century in 500-km area around GTA was the Temiskaming earthquake (1935/11/01, M_L 6.2), around 340 km from Toronto. Other earthquakes with magnitude around 5.5 occurred near Attica, NY, USA (1929/08/12, M_L 5.5), 125 km from Toronto; Cornwall earthquake (1944/09/05, M_L 5.6), 390 km from Toronto; Pymatuning earthquake (1998/09/28, M_L 5.4), 250 km from Toronto (and felt in Toronto); Plattsburgh earthquake (2002/04/20, M_L 5.5), 460 km from Toronto, and Val-des-Bois earthquake in Quebec (2010/06/23, M_w 5.0), the biggest recent earthquake in Eastern Canada, around 350 km from Toronto (Figure 1.10).



Figure 1.10. Earthquakes after 1900 with $m_N > 5$ in 500-km area around Toronto labeled with its accepted name. (Data: NRC, Earthquakes Canada, GSC (On-line Bulletin), http://seismo.nrcan.gc.ca/stnsdata/nedb/bull_e.php)

Some concentration of small events is observed in western Lake Ontario (Mereu et al., 2002; Dineva et al., 2004, 2007; Kim et al., 2006, etc.). The locations of these earthquakes and the proposed seismic lineaments are shown on Figure 1.11. However, there is no evidence for seismogenic faults observed on the earth surface.

The earthquakes around GTA in the last years are shown on Figure 1.12 (from <http://earthquakescanada.nrcan.gc.ca/recent/>)

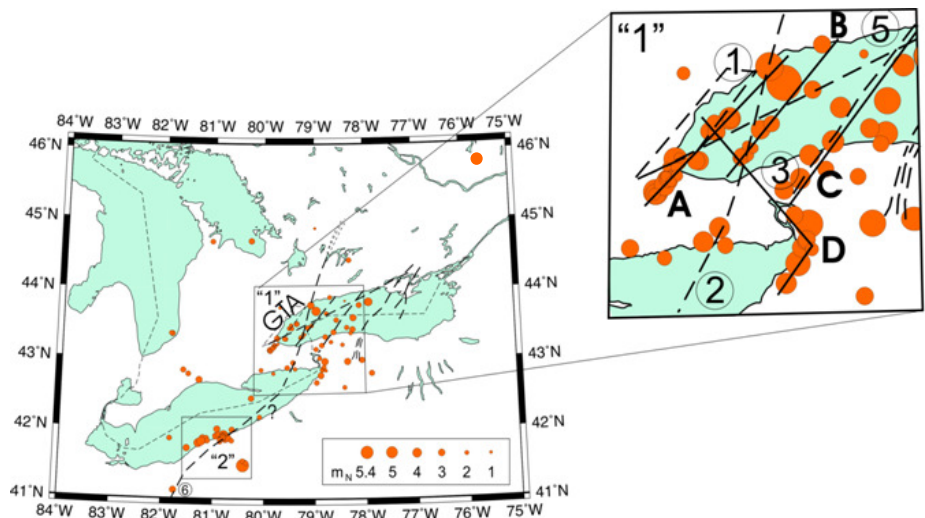


Figure 1.11. Seismicity around GTA (1990-2001) acc. to Dineva et al., 2004.

(The circles proportional to the magnitudes show the epicenters. The lines are the possible seismic lineaments, postulated in Dineva et al., 2004; Mohajer et al., 1992; McQuest Marine, 1995; Geomatrix, 1997. Squares numbered “1” and “2” outline two seismicity clusters called ‘Lake Ontario-Niagara seismic zone (“1”) and Ohio-Pennsylvania seismic zone (“2”), identified in Dineva et al., 2004.)

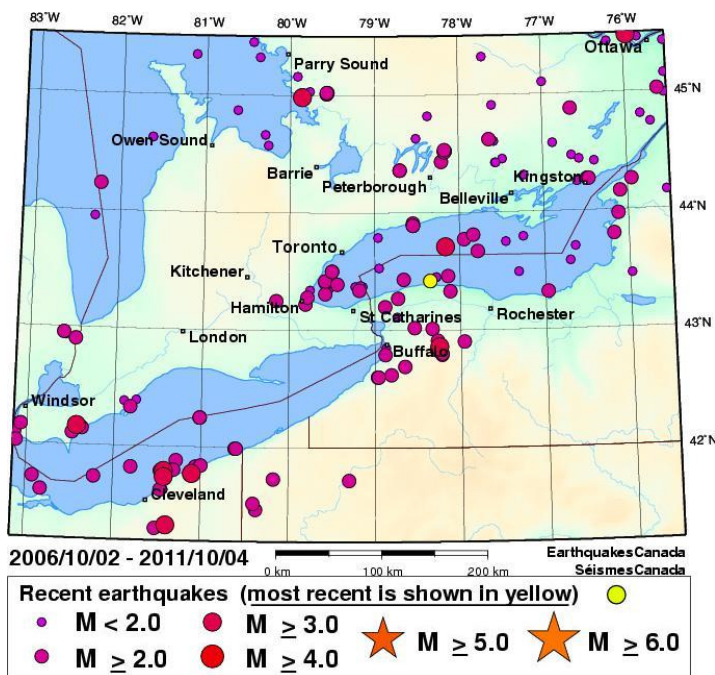


Figure 1.12. Earthquakes around GTA (2007-2011)

(from <http://earthquakescanada.nrcan.gc.ca>)

1.8. NBCC 2005/2010 and Microzonation

The probability of earthquake ground shaking can be predicted based on regional seismicity and the local geological site conditions. The national seismic hazard map of Canada gives the basis to reduce casualties, social and economic losses from future earthquakes (Adams and Halchuk, 2005). The results are maps of median values of 5% damped spectral acceleration for a reference site and for probability of exceeding 2%/50 years. This hazard estimation is included in the National Building Code of Canada (NBCC 2005). A map of spectral acceleration for 0.2 s period $S_a(0.2)$ for Canada (median values of 5% damped spectral acceleration for Site Class C and a probability of 2%/50 years) is shown in Figure 1.13 (NBCC 2010).

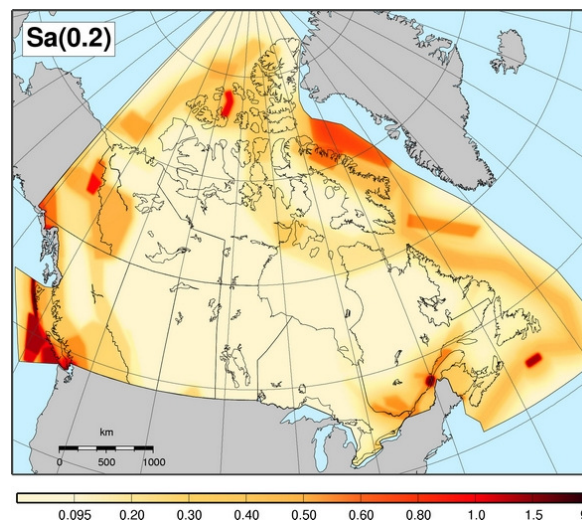


Figure 1.13. Spectral acceleration for a period of 0.2 seconds at a probability of 2%/50 years for firm ground conditions (NBCC 2005 soil class C), (NBCC 2010)

NBCC 2005 suggests five classes of soil conditions (Table 1.2) (Finn and Wightman, 2003). "Site Class C" has been adopted as a "reference" class, with average shear wave velocity in the uppermost 30 m from 360 to 750 m/s (Finn and Wightman 2003).

For most Canadian cities, the spectral accelerations are calculated as Uniform Hazard Spectra for median 2%/50 year. Uniform Hazard Spectra for median 2%/50 year ground motions on Site Class C for key cities are shown in Figure 1.1 (NBCC 2005). Soil classes, as defined in Table 1.2, involve site modification factors F_a and F_v for acceleration and velocity at frequencies 0.2 Hz and 1 Hz for each class.

Adams and Halchuk (2007) wrote for Vancouver but it applicable in general: "An earlier generation of strong motion instruments has already given some sparse information about soil amplification in Vancouver..., but while we wait for strong, damaging earthquakes, the current instruments will provide many more weak ground motion records on a variety of soil sites and hence direct measurements of soil amplification. These will provide ground truth for other microzoning methods such as those using ambient noise that provide a more finely-detailed picture of ground conditions on a block-by-block basis".

Table 1.2.

Site Class	Soil Profile Name	Average Properties in Top 30 m as per Appendix A (NBCC)		
		Soil Shear Wave Average Velocity, \bar{V}_s (m/s)	Standard Penetration Resistance, \bar{N}_{60}	Soil Undrained Shear Strength, s_u
A	Hard Rock	$\bar{V}_s > 1500$	Not applicable	Not applicable
B	Rock	$760 < \bar{V}_s \leq 1500$	Not applicable	Not applicable
C	Very Dense Soil and Soft Rock	$360 < \bar{V}_s < 760$	$\bar{N}_{60} > 50$	$s_u > 100\text{kPa}$
D	Stiff Soil	$180 < \bar{V}_s < 360$	$15 \leq \bar{N}_{60} \leq 50$	$50 < s_u \leq 100\text{kPa}$
E	Soft Soil	$\bar{V}_s < 180$	$\bar{N}_{60} < 15$	$s_u < 50\text{kPa}$
E		Any profile with more than 3 m of <i>soil</i> with the following characteristics: Plastic index $PI > 20$, Moisture content $w \geq 40\%$, and Undrained shear strength $s_u < 25\text{ kPa}$		
F	⁽¹⁾ Others	Site Specific Evaluation Required		

NBCC 2005 Site Classification for Seismic Site Response

Note ⁽¹⁾: other soils include: liquefiable soils, quick and highly sensitive clays, collapsible weakly cemented soils, and other soils susceptible to failure or collapse under seismic loading. Peat and/or highly organic clays greater than 3 m in thickness.

Highly plastic clays ($PI > 75$) with thickness greater than 8 m.

Soft to medium stiff clays with thickness greater than 30 m.

Seismic microzonation studies for other Canadian cities include: Montreal (Chouinard et al., 2004), Vancouver (Ventura et al., 2004; Molnar et al., 2007), Ottawa (Hunter and Motazedian, 2006; Hunter et al. 2010; Motazedian et al., 2011), and Quebec City (Nastev et al., 2007).

Chapter 2

Soil Response to Seismic Vibrations

2.1. Introduction

There are three main mechanisms that influence the ground response during an earthquake shaking:

1 - Conservation of energy of seismic waves is another mechanism that causes amplification or attenuation of surface ground shaking.

The energy of a seismic shear wave at a given point (Reynolds, 1997) is:

$$E \approx B^2 \omega^2 \rho V_S, \quad (2.1)$$

where: B and ω are amplitude and angular frequency of the shear-wave, ρ is rock or soil density and V_S is shear-wave velocity.

Generally, values of both density and shear-wave velocity decrease close to the surface (due to decreased overburden and less compacted soils). Amplitude B increases in order to preserve $E = \text{const}$. This amplification effect takes place at all boundaries between layers with different V_S in sedimentary basins.

2 - During strong shaking, the soil parameters can change dynamically and as a result, the soil resonances will vary from their frequencies and amplifications obtained from weak earthquakes or ambient vibrations. Seismic waves from strong earthquakes can produce localized damaged volumes in the soil structure with lower elastic moduli than the surrounding rocks (e.g. Ben-Zion and Sammis, 2003). This process affects the relatively shallow layers of the Earth crust, because the increasing normal stress with depth restrains the generation of new cracks and contributes to the damage recovery (e.g. Finzi et al., 2009; Ben-Zion and Shi, 2005). Many field observations point at rheological restoration of soil properties after a short time period (e.g Peng and Ben-Zion, 2006). Understanding the changes of properties of the near-surface soil layers is important for estimating the strong ground motion in epicentral zone during moderate and strong earthquakes.

3 - Deep basin topology: can be an important factor for amplification or attenuation at sites on sedimentary basins (e.g. Gao et al., 1996; Hartzell et al., 1997). Focusing and scattering of seismic wave energy propagating through velocity contrasts at basin margins is the dominant mechanism for these effects (Davis et al., 2000). In NBCC 2005, these site effects are partially included through processing macroseismic maps from populated areas. At present, there are no any specific requirements on how to incorporate basin geometry in site response investigation.

NBCC 2005 specifies that subsurface average of shear wave velocity of soil layers to the depth of 30 m is a key parameter for soil classification (Table 1.2). The averaged shear wave velocity to this depth is not sufficient to allow accurate calculation of the soil response to earthquake and possible resonances. The main task of seismic site response investigations is to obtain valuable evidences for categorization of given area to the nearest class in reference to class "C" (Table 1.2). The layered soil responds to an incident seismic wave with broad frequency spectrum converting the energy selectively into a resonant spectrum according to its transfer function. This transfer function is determined by the geometry and material properties of the soil structure.

2.2. Evaluation of linear soil response to weak seismic impact.

The experimental HVSR data can be compared with results of a theoretical site response analysis considering vertically propagating, horizontally polarized shear waves. An analytical model is developed after Kramer (Kramer, 1996) to analyze the site response of soil profiles with up to three layers. The derivation of the model is described below.

The horizontal displacement at a distance z from the origin due to a shear wave vertically propagating from the bedrock to the free surface is (Kramer, 1996):

$$u(z, t) = Ae^{i(\omega t + k^* z)} + Be^{i(\omega t - k^* z)} \quad (2.2)$$

where V_s is wave number; $k^* = \omega/V_s^* = \omega/[V_s(1+i\xi)] = k(1-i\xi)$ is complex wave number; ω is angular frequency; V_s is shear wave velocity; ξ is damping ratio;

$V_s^* = \sqrt{G^*/\rho} = V_s(1+i\xi)$; and finally $G^* = G(1+i2\xi)$ is the complex shear modulus.

The first term in Eq. (2.2) describes the upward shear wave and the second term describes a downward wave. The shear stress is given as the product of complex shear modulus

G^* and shear strain $\frac{\partial u}{\partial z}$, i.e.

$$\tau(z, t) = G^* \frac{\partial u}{\partial z} = G(1 + 2i\xi) \frac{\partial u}{\partial z} \quad (2.3)$$

In local coordinate system (Z_m), displacements at the top and the bottom of each layer are:

$$u_m(Z_m = 0, t) = (A_m + B_m) e^{i\omega t} \quad (2.4a)$$

$$u_m(Z_m = H_m, t) = \left(A_m e^{ik_m^* H_m} + B_m e^{-ik_m^* H_m} \right) e^{i\omega t} \quad (2.4b)$$

Enforcing compatibility of the displacement at the boundary between every two layers gives:

$$u_m(Z_m = H_m, t) = u_{m+1}(Z_{m+1} = 0, t) \quad (2.5a)$$

$$A_{m+1} + B_{m+1} = A_m e^{ik_m^* H_m} + B_m e^{-ik_m^* H_m} \quad (2.5b)$$

The shear stresses at the top and the bottom of the m -th layer are:

$$\tau_m(Z_m = 0, t) = ik_m^* G_m^* (A_m - B_m) e^{i\omega t} \quad (2.6a)$$

$$\tau_m(Z_m = H_m, t) = ik_m^* G_m^* \left(A_m e^{ik_m^* H_m} - B_m e^{-ik_m^* H_m} \right) e^{i\omega t} \quad (2.6b)$$

Considering equilibrium at the boundary between layers yields:

$$\tau_m(Z_m = H_m, t) = \tau_{m+1}(Z_{m+1} = 0, t) \quad (2.7a)$$

$$A_{m+1} - B_{m+1} = \frac{k_m^* G_m^*}{k_{m+1}^* G_{m+1}^*} \left(A_m e^{ik_m^* H_m} - B_m e^{-ik_m^* H_m} \right) \quad (2.7b)$$

Defining the complex impedance ratio as:

$$\alpha_m^* = \frac{k_m^* G_m^*}{k_{m+1}^* G_{m+1}^*} = \frac{\rho_m (V_S^*)_m}{\rho_{m+1} (V_S^*)_{m+1}} \quad (2.8)$$

Then the amplitudes of the upward and downward propagating shear waves can be written as:

$$A_{m+1} = 0.5A_m(1 + \alpha_m^*) e^{ik_m^* H_m} + 0.5B_m(1 - \alpha_m^*) e^{-ik_m^* H_m} \quad (2.9a)$$

$$B_{m+1} = 0.5A_m(1 - \alpha_m^*) e^{ik_m^* H_m} + 0.5B_m(1 + \alpha_m^*) e^{-ik_m^* H_m} \quad (2.9b)$$

At the ground surface, the shear stress $\tau_1 = 0$ and

$$\tau_1(Z_1 = 0, t) = ik_1^* G_1^* (A_1 - B_1) e^{i\omega t} = 0 \quad \text{or} \quad A_1 = B_1 \quad (2.10)$$

At the boundary between the first and the second layers:

$$A_2 = 0.5A_1 \left[(1 + \alpha_1^*) e^{ik_1^* H_1} + (1 - \alpha_1^*) e^{-ik_1^* H_1} \right] \quad (2.11a)$$

$$B_2 = 0.5A_1 \left[(1 - \alpha_1^*) e^{ik_1^* H_1} + (1 + \alpha_1^*) e^{-ik_1^* H_1} \right] \quad (2.11b)$$

At the boundary between the second soil layer and the bedrock:

$$A_3 = 0.25A_1 \left\{ \left[(1 + \alpha_1^*) e^{ik_1^* H_1} + (1 - \alpha_1^*) e^{-ik_1^* H_1} \right] (1 + \alpha_2^*) e^{ik_2^* H_2} + \left[(1 - \alpha_1^*) e^{ik_1^* H_1} + (1 + \alpha_1^*) e^{-ik_1^* H_1} \right] (1 - \alpha_2^*) e^{-ik_2^* H_2} \right\} \quad (2.12a)$$

$$B_3 = 0.25A_1 \left\{ \left[(1 + \alpha_1^*) e^{ik_1^* H_1} + (1 - \alpha_1^*) e^{-ik_1^* H_1} \right] (1 - \alpha_2^*) e^{ik_2^* H_2} + \left[(1 - \alpha_1^*) e^{ik_1^* H_1} + (1 + \alpha_1^*) e^{-ik_1^* H_1} \right] (1 + \alpha_2^*) e^{-ik_2^* H_2} \right\} \quad (2.12b)$$

Assuming for bedrock, $G_3 = \infty$ leads to $\alpha_2^* = \frac{k_2^* G_2^*}{k_3^* G_3^*} = 0$ and

$$A_3 = 0.25A_1 \left\{ \left[(1 + \alpha_1^*) e^{ik_1^* H_1} + (1 - \alpha_1^*) e^{-ik_1^* H_1} \right] e^{ik_2^* H_2} + \left[(1 - \alpha_1^*) e^{ik_1^* H_1} + (1 + \alpha_1^*) e^{-ik_1^* H_1} \right] e^{-ik_2^* H_2} \right\} \quad (2.13a)$$

$$B_3 = 0.25A_1 \left\{ \left[(1 + \alpha_1^*) e^{ik_1^* H_1} + (1 - \alpha_1^*) e^{-ik_1^* H_1} \right] e^{ik_2^* H_2} + \left[(1 - \alpha_1^*) e^{ik_1^* H_1} + (1 + \alpha_1^*) e^{-ik_1^* H_1} \right] e^{-ik_2^* H_2} \right\} \quad (2.13b)$$

and consequently:

$$A_3 = B_3 = 0.25A_1 \left[(1 + \alpha_1^*) e^{i(k_1^* H_1 + k_2^* H_2)} + (1 - \alpha_1^*) e^{-i(k_1^* H_1 - k_2^* H_2)} + (1 - \alpha_1^*) e^{i(k_1^* H_1 - k_2^* H_2)} + (1 + \alpha_1^*) e^{-i(k_1^* H_1 + k_2^* H_2)} \right] \quad (2.13c)$$

Re-arranging and combining the terms gives:

$$A_3 = B_3 = 0.25A_1 \left[(1 + \alpha_1^*) \left(e^{i(k_1^* H_1 + k_2^* H_2)} + e^{-i(k_1^* H_1 + k_2^* H_2)} \right) + (1 - \alpha_1^*) \left(e^{i(k_1^* H_1 - k_2^* H_2)} + e^{-i(k_1^* H_1 - k_2^* H_2)} \right) \right] \quad (2.14)$$

Applying Euler's rules to the upward and downward coefficients at the bedrock surface gives:

$$A_3 = B_3 = 0.5A_1 \left[(1 + \alpha_1^*) \cos(k_1^* H_1 + k_2^* H_2) + (1 - \alpha_1^*) i \cos(k_1^* H_1 - k_2^* H_2) \right] \quad (2.15)$$

The transfer function for shear waves propagating vertically from bedrock to the free surface is:

$$F(\omega) = \frac{A_1 + B_1}{A_3(\omega) + B_3(\omega)} = \frac{2}{(1 + \alpha_1^*) \cos(k_1^* H_1 + k_2^* H_2) + (1 - \alpha_1^*) i \cos(k_1^* H_1 - k_2^* H_2)},$$

where:

$$\alpha_1^* = \frac{k_1^* G_1^*}{k_2^* G_2^*} = \frac{\rho_1 (V_{S1}^*)}{\rho_2 (V_{S2}^*)} = \frac{\rho_1 V_{S1} (1 + i\xi_1)}{\rho_2 V_{S2} (1 + i\xi_2)}; \quad k_m^* = \omega / [V_{Sm} (1 + i\xi_m)] = k_m (1 - i\xi_m);$$

$$G_m^* = G_m (1 + i2\xi_m) \quad \text{for } m = 1 \text{ or } 2; \quad k_1^* = \omega / [V_{S1} (1 + i\xi_1)] = k_1 (1 - i\xi_1);$$

$$k_2^* = \omega / [V_{S2} (1 + i\xi_2)] = k_2 (1 - i\xi_2).$$

This analytical model was developed in Excel environment and was used to approximate the observed HVSR response. An Excel example with real data is shown in Figure 5.16

The input parameters include the shear modulus (or shear wave velocity), damping ratio and thickness for each layer within the profile. The parameters of layers are varied until a reasonable match with the HVSR is achieved.

2.3. Modeling of soil resonance changes during strong earthquakes

The results from seismic microzonation comprise predominant soil resonances and site resonances, particularly those obtained from ambient seismic noise or small earthquakes, reflect only the elastic soil behavior.

The problem with soil resonances from microzonation study is how to predict changes of their frequencies and particularly amplifications when the soil layers are affected by strong shaking.

Spectral ratios from strong ground motion tend to “suppress” the resonances in the soil layers. The application of weak-motion ground-shaking (such as small earthquakes or seismic noise) for estimation of ground shaking from stronger earthquakes needs also an assessment of possible nonlinear effects and degradation of soil parameters.

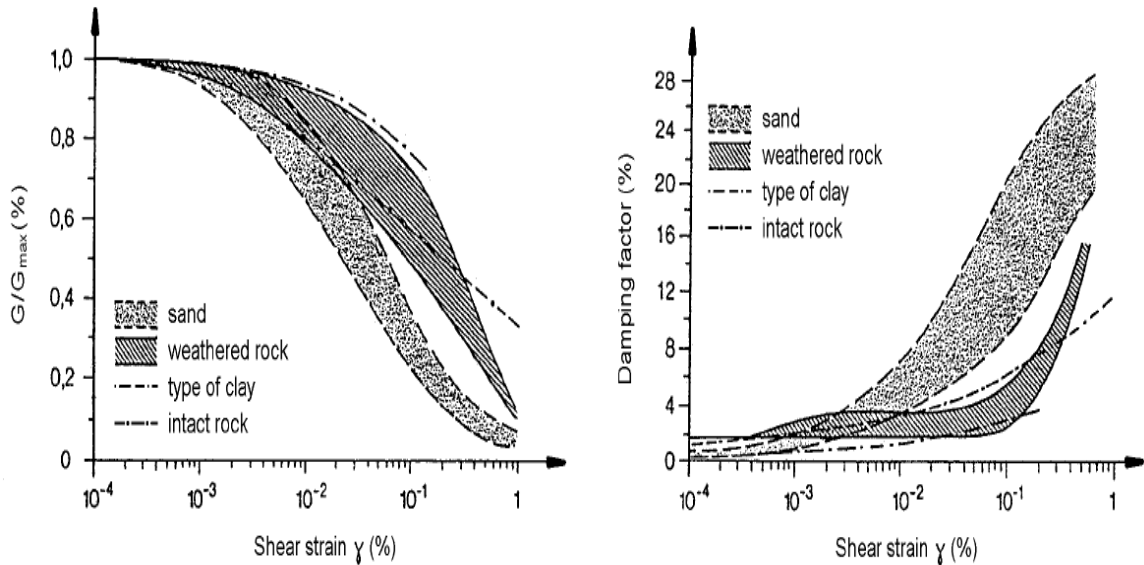


Figure 2.1. Example of changes in the shear modulus and damping factor vs. shear strain (from Studer and Ziegler, 1986).

The determination of the threshold ground shaking or shear strain, beyond which soil nonlinearity becomes noticeable, is quite difficult. In Figure 2.1 is shown nonlinear behavior of different soils. (This example is taken from Studer and Ziegler (1986) fundamental monograph).

The factors which define soil resonances and amplification/attenuation of earthquake shaking can be estimated by modeling using lab and field data. The obtained empirical models can be used for prediction of soil response during intense shaking.

Many observations, ideas and models for predicting soil nonlinearity are available in the literature (e.g. Paz, 1994; Field et al., 1997; Beresnev and Wen, 1996; Kausel et al, 2002; Pavlenko and Irikura 2003; Hartzell et al., 2004). Some of the proposed nonlinear models consider pore-water pressure (effective stress calculation) or assume dry conditions (total stress calculation).

A simplified model can describe these effects if the changes in soil shear strength and damping at different level of shear strain are known from laboratory tests. Degradation of soil shear modulus and damping ratio versus effective shear strain can be averaged over data for soft soils taken from Kokusho (2004) as shown in Figure 2.2.

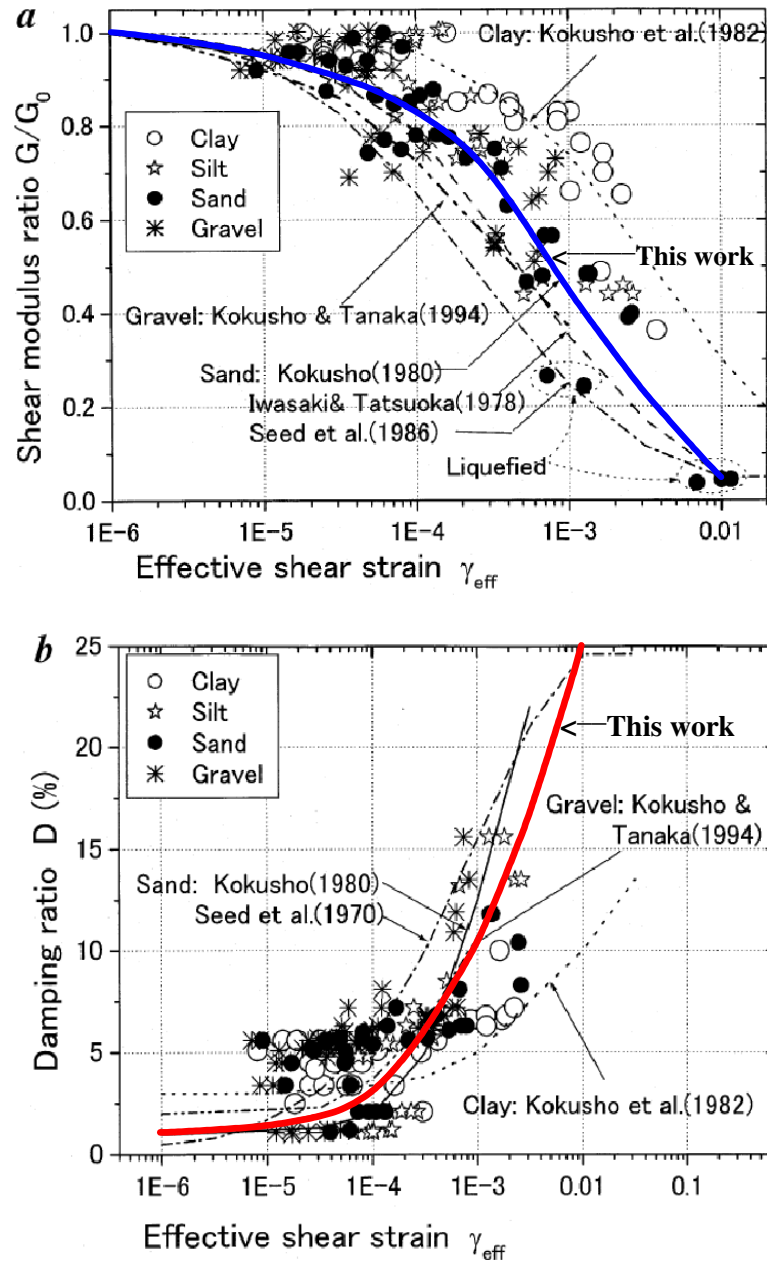


Figure 2.2. Changes in a) the shear modulus G/G_0 and b) damping factor D [%] vs. effective shear strain averaged in this study (from Kokusho, 2004). The blue line represents averaged reduction of the shear modulus. The red line gives the increase of the damping factor with increase of the soil strain.

The references for the data are given on the figures.

Supposed degradation of soil with $V_{s0} = 200$ m/s due to changes of shear modulus and damping factor vs. shear strain is presented in Figure 2.3.

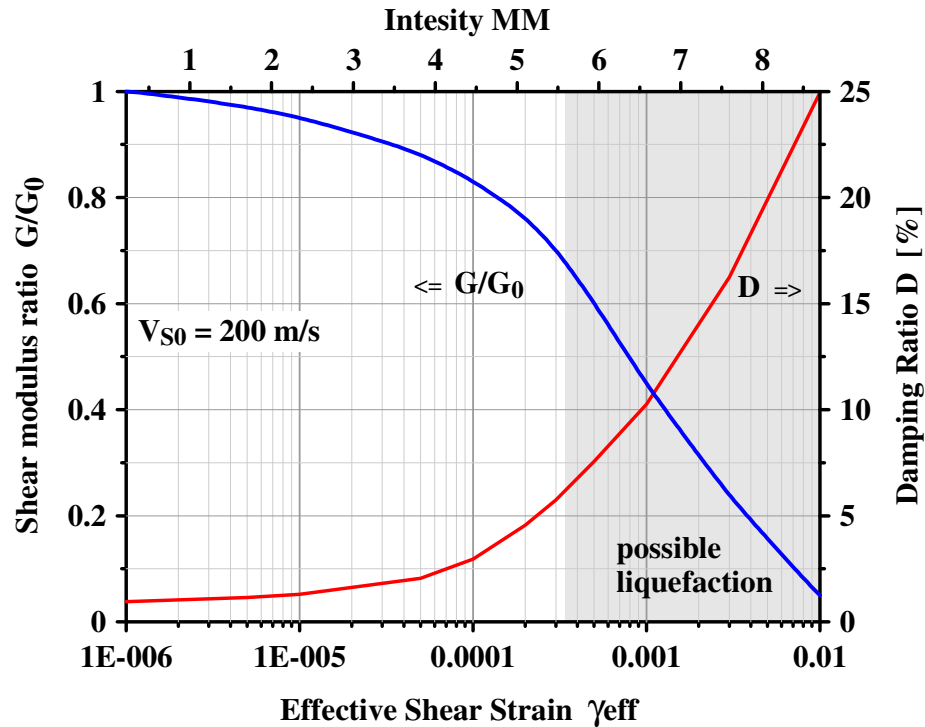


Figure 2.3. Changes in the shear modulus and damping factor vs. shear strain assuming degradation of soil with $V_{S0} = 200$ m/s.

The blue line represents smoothed reduction of the shear modulus and the red line gives the increase of the damping factor with increase of the soil strain.

Macroseismic scales describe adequately damages related to the ground shaking velocity during earthquakes. Numerous relations between Peak Ground Acceleration (*PGA*), Peak Ground Velocity (*PGV*) and Modified Mercalli scale Intensity (I_{MM}) are proposed (e.g. Wald et al., 1999a,b; Atkinson and Sonley, 2000; Kaka and Atkinson, 2004; Atkinson, and Kaka, 2007; Boore and Atkinson, 2008). The *PGV* is chosen here because it shows less sensitivity to the local geology (Trifunac and Brady, 1975) and because the damages of buildings (weighty element for MMI estimation) are proportional to the dissipated energy in the structures.

The determination of representative relationships between *PGV* and MMI depends on sophisticated regression techniques because of the scattered observations and the descriptive nature of MMI intensities. The problem is additionally complicated by the relatively small amount of instrumental data along with intensity observations for very

low and for very high intensity ranges. Figure 2.4 illustrates the diversity of proposed relations between PGV and MMI.

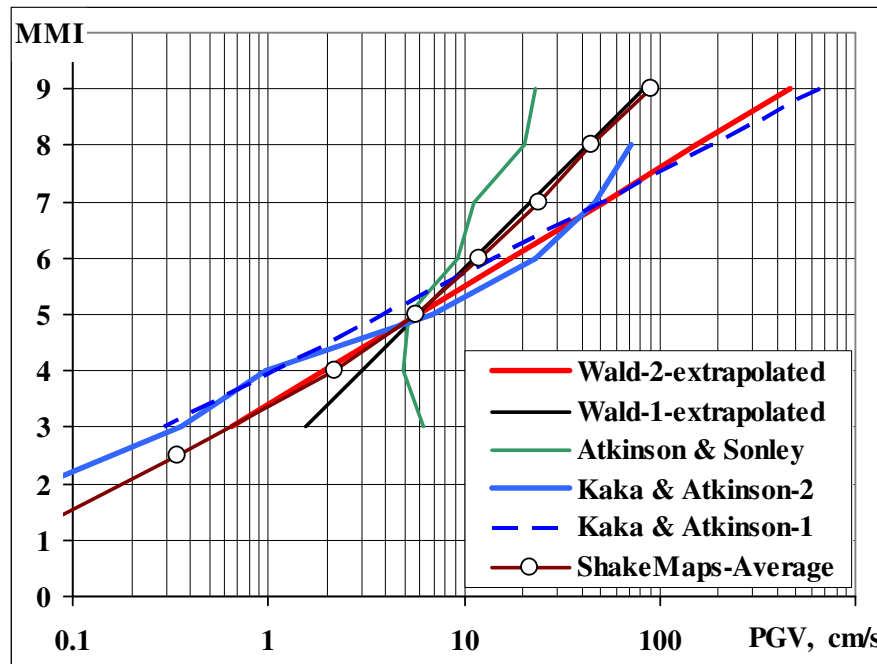


Figure 2.4. Some MMI vs. PGV regressions:

Wald-2 -extrapolated $I_{MM} = 2.10\log(PGV) + 3.40$ (Wald et al., 1999)

Wald-1 -extrapolated $I_{MM} = 3.47\log(PGV) + 2.35$ (Wald et al., 1999)

Atkinson&Sonley - from corrected data (Atkinson and Sonley, 2000)

Kaka & Atkinson-2 - from averaged data (Kaka and Atkinson, 2004)

Kaka & Atkinson-1 $I_{MM} = 1.79\log(PGV) + 1.96$ (Kaka and Atkinson, 2004)

ShakeMap-Average <http://www.cisn.org/shakemap/sc/shake/about.html#intmapshttp>

In our case, only a simple equation is necessary to illustrate the relation between intensity of ground shaking and soil nonlinearity. Modified Mercalli Intensity (I_{MM}) obtained from PGV (Wald et al., 1999a) is:

$$I_{MM} = 2.10\log(PGV) + 3.40, \quad (2.17)$$

where PGV is in cm/s. PGV can be expressed as:

$$PGV = 10^{(I_{MM} - 3.4)/2.1} \text{ [cm/s]}. \quad (2.18)$$

Equations 2.17 and 2.18 are initially valid for the range V < IMM < IX. They are extrapolated here to I < IMM < IX to simplify the demonstration of dynamic changes of

soil properties. The effective shear strain is proportional to PGV and can be calculated for

$$\text{a soil layer as: } \gamma_{eff} = k_{\gamma} \frac{PGV}{V_{S0}}, \quad (2.19)$$

where: V_{S0} is the shear wave velocity in the uppermost soil layer, obtained by field site response technique; k_{γ} - theoretically is 0.5, but from different sources varies from 0.4 to 0.7. Here $k_{\gamma} = 0.63$ assuming average $G/G_0 = 0.8$ before liquefaction (Figure 2.3).

Relations between IMM, PGV and effective Shear stain γ_{eff} using eq. (2.17 - 2.19) for different values of V_{S0} are shown on Figure 2.5. This figure can be used as a nomogram to estimate γ_{eff} from PGV through MM Intensity scale.

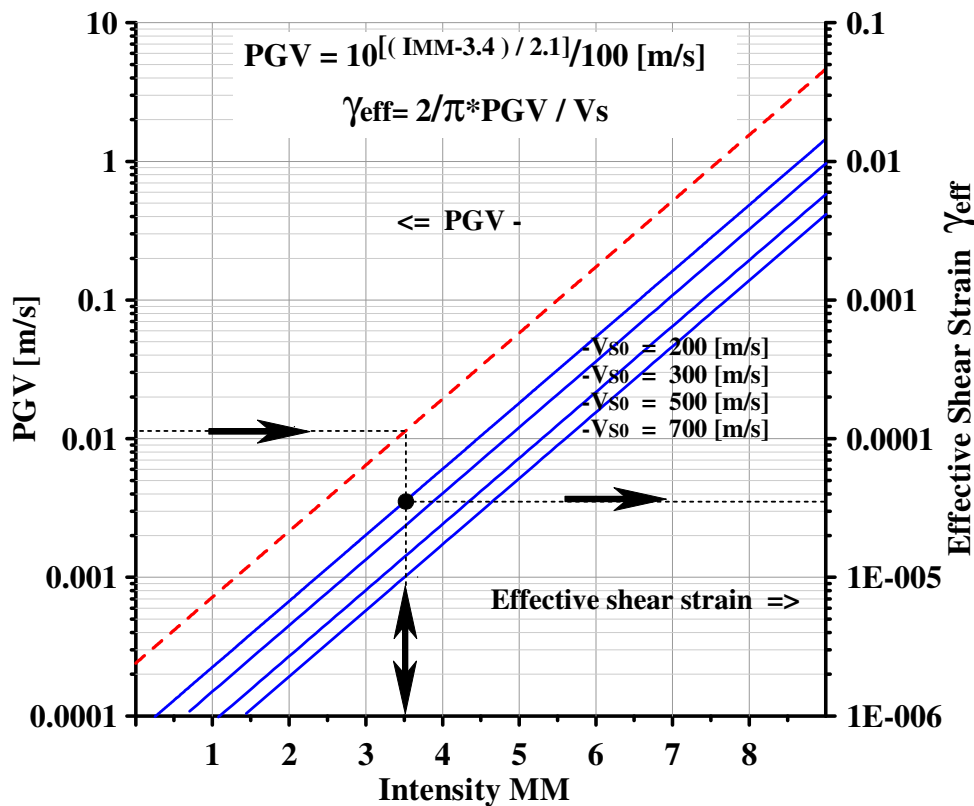


Figure 2.5. Nomogram from eq. 2.17 to 2.19 connecting PGV with MM Intensity (red line) and with Effective Shear strain γ_{eff} for different values of V_{S0} (blue lines).

The diversity of soil structures allows only a very simplified modeling of changes in soil dynamic properties with the increase of dynamic strain. A homogeneous subsurface layer over half-space can be approximated as a Single Degree Of Freedom (SDOF) oscillator:

$$A(f) = \frac{1}{\sqrt{\left(1 - \left(\frac{f}{f_{0IMM}}\right)^2\right)^2 + 4D_{IMM}^2 \left(\frac{f}{f_{0IMM}}\right)^2}}, \quad (2.20)$$

where the resonant frequency f_{0IMM} and the damping ratio D_{IMM} are dependent on the Effective Shear Strain related to the MM Intensity. f_{0IMM} and D_{IMM} can be calculated for different MM Intensities taking into account degradation ratio of shear modulus G/G_0 versus effective shear strain γ_{eff} from Figure 2.3 starting with:

$$f_{0IMM} = f_0 \sqrt{\frac{G}{G_0}}, \text{ and } D_0 = 1\%, \quad (2.21)$$

where f_0 is the natural frequency, G is the shear modulus of the soil layer under intense ground vibration, G_0 is the maximum shear modulus and D_0 is the damping factor for undisturbed soil layers. Changes of resonance with IMM shown in Figure 2.6 are modeled as a SDOF oscillator.

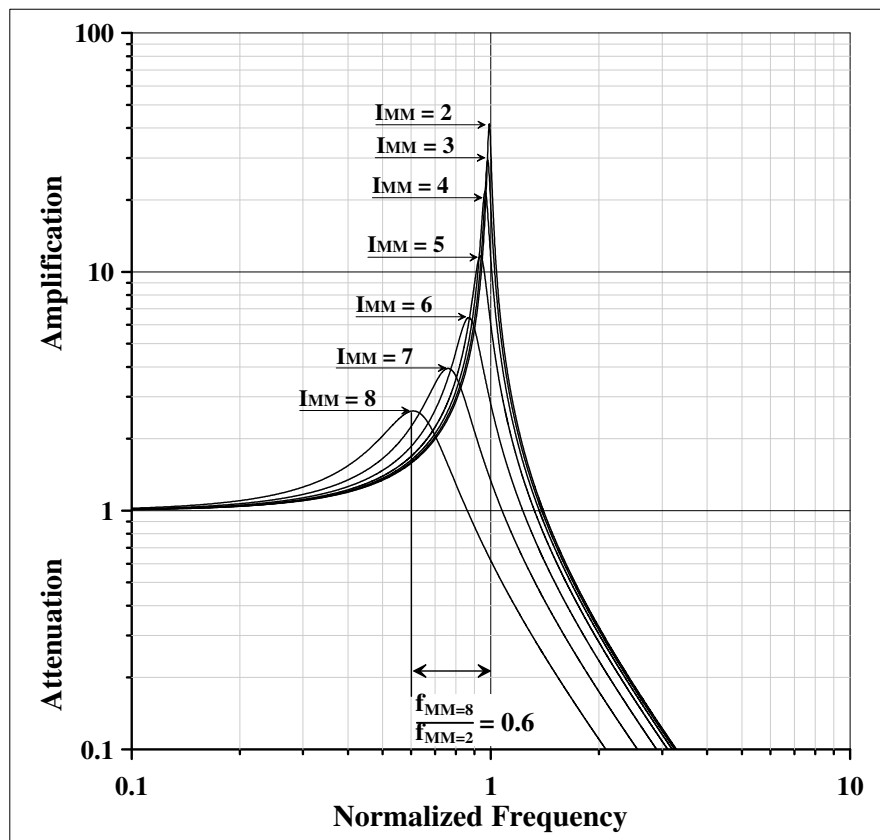


Figure 2.6. Normalized soil resonances at different Intensity MM (I_{MM})

The transfer function on figure 2.6 is normalized to the spectra at the bedrock-soil boundary.

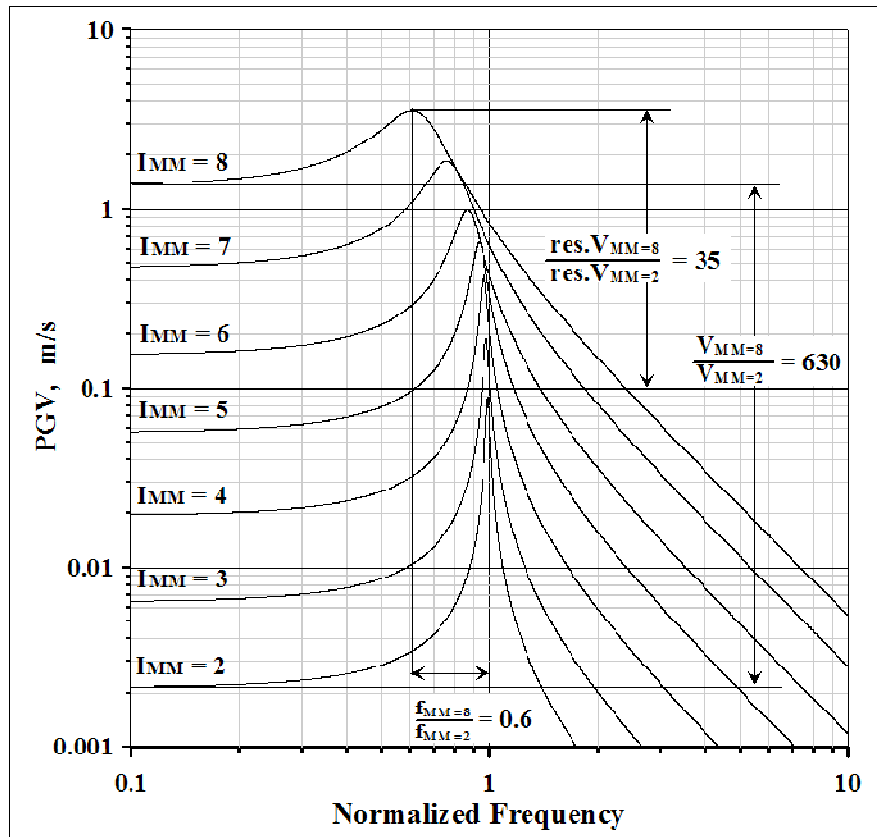


Figure 2.7. Modified hypothetical flat velocity spectra for different I_{MM} with normalized soil transfer functions shown on Figure 2.6.

This simplified SDOF model involves changes in site response amplification-attenuation curves when surface layer is subjected to shaking with different MM Intensities as is shown on Figures 2.6 and 2.7. Predominant frequency and amplification factor decrease but the frequency band with amplification expands.

Despite of its simplicity, this SDOF model provided a comparatively good tool to explain changes in the shape of HVSr, resonant frequencies and damping factors during the strong earthquake in North Anatolian Turkey, recorded at station Duzce Duz (DZC) (Lang et al., 2002), which is shown in Figure 2.8. About 20 to 40 % reduction of peak frequency (frequency of maximum spectral ratio amplitude), which was found to be

consistent with the approximately 45 % reduction in S-wave velocity following the Duzce main shock (Karabulut and Bouchon, 2007).

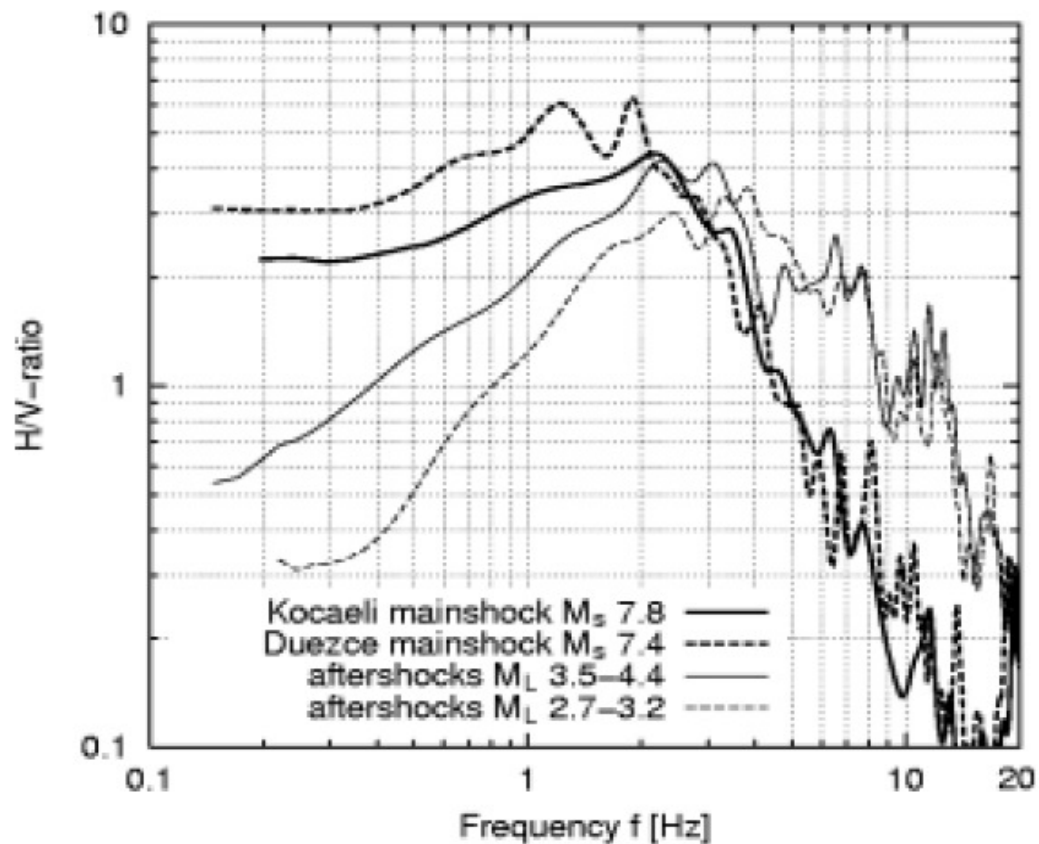


Figure 2.8. Soil resonances from H/V ratio during the earthquakes with different magnitudes in North Anatolian Turkey recorded at station Duzce DUZ (DZC) (from Lang et al., 2002).

The epicentral distances for this example were below 30 km and macroseismic intensities were between 3 and 11 IMM. The H/V ratio keeps its shape for all shown magnitudes. Decreasing of the dominant frequencies and expanding of frequency band are obvious and similar to those of the idealized model, shown in Figure 2.7. Similar comparison between site response to strong and weak motion can be found in many other publications (e.g. Ozel et al, 2002).

The simplified SDOF model illustrates how to apply soil transfer function, amplification-attenuation and resonances obtained from site response investigation with low intensity seismic sources in order to make the geophysical results more suitable for extrapolation to strong earthquake shaking.

Chapter 3

Geophysical Methods for Seismic Microzonation in a City

A key parameter for seismic microzonation is the shear wave velocity (V_s) in shallow layers, which is used to define the variable ground motion amplification and to evaluate the site response in sedimentary basins (e.g. Borchardt, 1970). Accordingly, V_s is an important parameter in building codes (e.g. NBCC 2005 and NEHRP 1997). The soil shear wave velocity, V_s , is widely used in the earthquake engineering community in design applications (Kramer, 1996).

The current trend in advancing hazard-mapping methodology is to incorporate more accurately local V_s information into the hazard calculation, particularly in urbanized areas (Cramer, 2003; Cramer et al., 2004). This trend is expected to accelerate with future expansion of these ideas (e.g. Applegate, 2004). Consequently, the need for rapid and inexpensive determination of shallow shear wave velocity over large urbanized sedimentary basins is important for site response estimation in the future urban hazard maps. The aim of the seismic microzonation is to define not only the shear wave velocity (V_s) profile but also the soil transfer function and resonances.

Different geophysical methods can be used for seismic microzonation, including: microtremor and ambient vibrations measurements for Nakamura's method (H/V or HVSR method) (Nakamura, 1989, 2000), spectral analysis of surface waves (SASW) (Park, 1999a), multichannel analysis of surface waves (MASW) (Park, 1999b; Miller, 1999), earthquake response (ER), vertical seismic profiling (VSP), surface-to-surface spectral ratio based on earthquake data (Borchardt, 1970), and surface-to-borehole spectral ratio on earthquake data (e.g. Enomoto et al., 2000; Tsuboi et al., 2001).

Conventional active-source seismic reflection/refraction profiling has also been used widely for characterization of the shear wave velocity down to 50-70 m. Some of these methods are cost-effective and non-invasive and, therefore, are suitable for urban areas (e.g. Hunter and Motazedian, 2006).

3.1. Horizontal to Vertical Spectral Ratio (HVSr) Method

The best approach to evaluate the characteristics of the local site response is through direct observation of seismic ground motion during local and regional earthquakes. However, such studies are generally restricted to areas with high seismicity. In areas with low seismicity, methods utilizing Horizontal to Vertical Spectral Ratio (HVSr) of ground vibration from small earthquakes and ambient seismic noise are convenient tools to estimate the effect of surface geology on seismic motion.

3.1.1. Assumptions behind HVSr method

A method initially proposed by Nogoshi and Igarashi (1971), and updated by Nakamura (1989, 2000), uses measurements from one 3-component seismic station to evaluate the local site effect. Nakamura (1989) suggested that H/V- spectral ratios from microtremors (HVSr) represent the “Quasi-Transfer Spectrum (QTS)” of the recording site. He assumed that the vertical spectrum of ground motion is unaffected by sedimentary layers and carries uncontaminated information about the seismic source. On the other hand, the horizontal spectrum is changed due to sedimentary layers. The vertical vibrations could be used to deconvolve the source effects from the site effects affecting the horizontal motion. In Nakamura’s HVSr method, short duration records of microtremors of the ground surface are used to find QTS in the frequency domain. The QTS is obtained through normalizing the horizontal spectrum of each site by its vertical spectrum (H/V). The resulting curve generally shows some peaks at the resonant frequencies of the site. The technique has proved successful in predicting resonance frequencies of sediments using ambient noise as a source (e.g. Lermo and Chavez-Garcia, 1992, 1994; Field et al., 1990; and Lachet and Bard, 1994).

According to Nakamura (2000), the resonance frequency peak of QTS is caused by multiple refractions of S-waves and QTS represents the soil transfer function. The predominant frequency, f_0 , of QTS is related to the depth h to the basement or to the boundary with sharp acoustic impedance between layers:

$$f_0 = \frac{V_{SSurf}}{4h}, \quad (3.1)$$

where V_{SSurf} is the shear wave velocity in the subsurface layer.

The amplification factor A_0 at this frequency is related to the impedance ratio. If the densities for basement and surface layers are the same, then:

$$A_0 = \frac{V_{SBase}}{V_{SSurf}}, \quad (3.2)$$

where V_{SBase} is the shear wave velocity in the basement or in the layer below the impedance margin. The depth to the basement or to the impedance discontinuity in this case can be estimated as:

$$h = \frac{V_{SBase}}{4A_0 f_0} \quad (3.3)$$

Nakamura's qualitative explanations regarding the type of seismic waves recorded at the ground surface seem to be questionable (Kudo, 1996; Nakamura, 2000). In spite of this, various sets of experimental data (e.g. Lachet and Bard, 1994; Duval et al., 1994; Duval et al., 1998; Kudo et al., 2002) confirmed that HVSR is much more stable than the raw noise spectra. For soft soil sites, the HVSR usually provides a clear peak that is correlated with the fundamental S-wave resonant frequency for the uppermost layer.

Lermo and Chavez-Garcia (1993) reported good agreement between the HVSR technique and standard spectral ratios. Other researchers (e.g. Field and Jacob, 1995; Lachet et al., 1996) found that the H/V method gives results close to the standard spectral ratio (SSR) technique for the fundamental frequency of the near surface sediments. "However Nakamura's method does not seem to be able to give all information required for a reliable estimation of the amplification of surface ground motion" (Bour et al., 1998). An important limitation to HVSR application is the requirement of a strong impedance contrast between the overlying soil layers and the half space below in order to obtain reliable estimations of the resonant frequencies and site characteristics. Despite of its limitations, the Nakamura's technique is considered to be a suitable method for investigating specific site response changes in large urban areas.

The HVSR technique allows obtaining the fundamental resonant frequency of the soil deposit, but fails to accurately predict the higher harmonics, and the peak amplitude is

often somewhat different from the amplification measured on SSR or VSP spectral ratios (Murphy and Eaton, 2005).

Langston et al. (2009) proposed a complicated explanation for HVSR phenomena: “The low-velocity embayment sediments cause inhomogeneous shear waves from the incident Rayleigh- and Love-wave trains to convert to homogeneous, near-vertically propagating shear waves within the sediments that then constructively interfere to produce a resonant peak in both horizontal and vertical motions but destructively interfere at a different frequency for vertical motions. The overall amplification is due to the fact that incident waves are inhomogeneous and that the converted homogeneous shear waves become completely trapped in the sediment layer. Amplification can be expected to be much less for higher phase velocity shear waves from local earthquakes.” Nevertheless they made a conclusion that: “Nakamura’s method appears to be a robust technique that can be used to perform an inexpensive study of the average velocity structure of the entire Mississippi embayment given previous knowledge of sediment thickness.”

Motazedian et al. (2011) presented a comparison between the resonant periods obtained experimentally using HVSR technique and calculated from average shear wave velocity knowing the thicknesses of soil layers from SH refraction/reflection seismic profiling. The relation between both resonant periods appears to be non-linear. This comparison makes questionable the correctness of the equation (3.1) and its derivatives to establish the drift thickness knowing the shear wave velocity or vice versa from the HVSR resonance.

3.1.2. Application of HVSR in city conditions.

In spite of its uncertain physical background and in some cases questionable results, the Nakamura’s HVSR was used to estimate the potential resonances of the soil structure in GTA. This decision is based on two reasons:

1. Most researchers agree that HVSR gives the frequencies of the soil resonances comparable with those obtained by other geophysical methods.
2. HVSR is the cheapest and easy applicable technique for field investigation in city conditions.

In order to obtain the fundamental soil resonance, the lowest resonant frequency has to be resolved. Only this resonance depends on the depth to the bedrock. In many cases, there are different dominant resonances due to the existence of seismic boundary in the sedimentary strata with higher impedance ratio than that between overburden and bedrock.

In general, the HVSR method assumes near vertical incident seismic waves. This can be true if the vibration sources are located far from the measurement point, so that the waves refracted from the bedrock can be recorded without interference with direct body waves. This may not be the case in urban areas where recorded ground vibrations are mainly from industrial and traffic sources. These sources can be located at any distance from the measurement point, and at times in its close vicinity. If the sources are close to the measurement point, the records will contain a mixture of surface waves and reflected, refracted and direct body waves. The HVSR technique usually employs the record from only one 3-component seismometer. This complicates the separation of different seismic waves using only one 3-component record, which is a standard practice.

3.1.3. Noise separation from close and distant sources

Seismic waves from nearby traffic in cities propagate mostly in soft soil sediments as direct and reflected waves, and thus seismic rays at the measurement point are not vertical. In this case some refracted waves from shallower soil layers may be recorded, but usually the first refracted wave from the bedrock emerges behind the measurement point. The direct waves from close sources usually have high intensity and can ‘mask’ the refracted and reflected waves from more distant sources. As a result, the resonance in the HVSR at the fundamental frequency may be suppressed, and resonances with higher frequencies are more prominent due to the stronger refracted waves from shallower boundaries and the lack of refracted waves from the bedrock.

The hypothesis that vibrations from nearby sources ‘mask’ the amplitude of the fundamental resonant frequency is examined herein using data collected as part of the measurements for the microzonation of GTA. A technique is developed to separate the seismic noise into ‘strong’ and ‘weak’ signals for two reasons:

1. To detect the contribution of the nearby sources on HVSR;
2. To distinguish the fundamental frequency from high frequency resonances.

The main assumptions adopted in such conditions are:

1. The vibrations from nearby traffic are much stronger than those from distant sources. In the case of thick overburden, the refracted waves from the bedrock do not reach the measurement point. Thus, seismic waves from nearby traffic can be body waves - direct or refracted, from shallower boundaries in the soil deposits, as well as surface waves;

2. The seismic waves from distant sources arrive at the registration point as refracted waves from the bedrock and have lower attenuation compared to the direct body waves from the neighboring sources due to the higher attenuation in shallower soil layers;

3. As the 3-component seismometer reacts to the movements in 3 orthogonal directions, it is not necessary that only shear (SH) waves are registered on the horizontal components. If the source is close to the seismometer, the records on the horizontal components can contain intense direct compressional waves. All 3 components will register the surface waves (mainly Rayleigh waves) produced by close-by moving sources. These waves have elliptical polarization with significant vertical component in a broad spectral range.

A procedure is developed in Excel for automatic separation of the ambient vibration signal depending on its intensity (amplitude). The procedure is as follows:

1. In order to eliminate the irregularity of the traffic vibrations, the modulus of the ground vibration is smoothed by averaging of the sum of the moduli of the recorded waveforms in the time domain with a triangular function. The width of this function (time interval for averaging) is obtained by trial-and-error. It depends on the traffic regime and is proportional to the dominant time periods of the traffic pulsations. For the measurements in the GTA, the suitable time interval is 13 seconds.

2. The average value of the entire records (mean value of the 3-component vector moduli) is calculated. It is then multiplied by a safety factor to avoid “contamination” of low-level signals with high-level tails. This safety factor was found to be 0.9 by trial-and-

error. This ensures the separation between strong and weak vibrations to be at a level which is low enough to reduce significantly the mixing of high and low intensity signals. Thus the time intervals with high and low level vibration are separated into different time windows. The separation of data is shown on Figure 3.1.

3. To avoid flickering (jumping between high and low levels), a 10% hysteretic threshold with two levels is used around the separation level. This allows discriminating of the vibrations between threshold levels as ‘undetermined’.

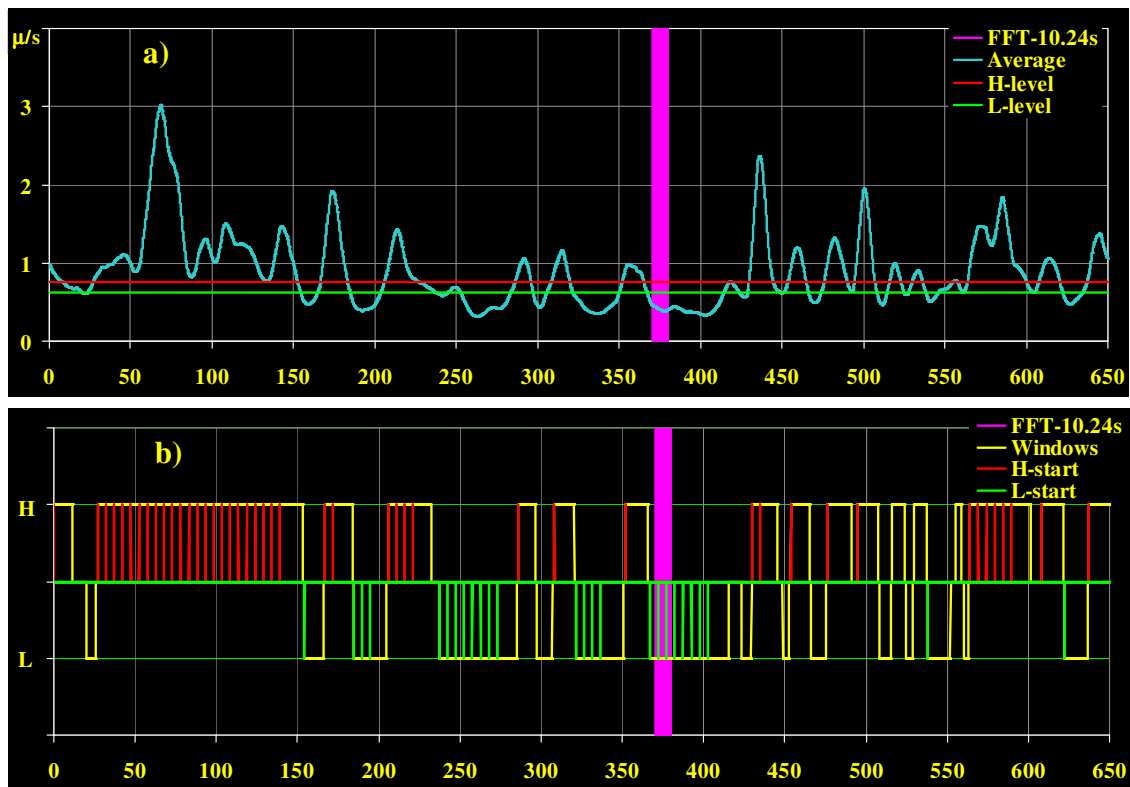


Figure 3.1. Data separation for HVSR calculations. FFT-10.24s - running time interval for individual FFT spectrum:

- a) Average modulus of all 3 components and threshold levels H-level and L-level;**
- b) Windows with low and high level of vibration and starting time for each individual FFT spectrum: H-start and L-start.**

4. Finally, the signal is divided into three different time windows as ‘strong’, ‘weak’, and ‘undetermined’. The strong signal is defined to be above the upper hysteretic threshold level. The weak signal is defined to be under the lower hysteretic threshold level. The undetermined signal is between the two threshold levels. The FFT spectral

analysis of the records of horizontal and vertical components is performed separately over the partitions with strong and weak signals separated by a hysteretic threshold level (Figure 3.1).

In the current study, 50 % overlapping time intervals of 10.24 s multiplied by a standard Hanning window are used. The separation of each record into short time series is applied to the records of the horizontal and vertical components and used for calculating of all individual FFT spectra. Each individual spectrum is smoothed using a triangle function with linearly increasing-decreasing weights (e.g. 0.25, 0.50, 0.75, 1.00, 0.75, 0.50, 0.25). The resulting smoothed individual horizontal and vertical spectra in each time window are used to compute the individual HVSR, as a ratio of the vector sum of the horizontal spectra to the vertical spectrum. The ensembles (Bendat and Piersol, 2000) of the individual HVSR - for strong and weak vibrations are averaged separately. Calculated two HVSR represent QTS in the frequency domain for strong and weak vibrations. The validity of the averaged HVSR is established using the standard deviation. An example of the HVSR calculated from the entire 3-component records and from separated into Low and High Level time windows are shown on Figure 3.2.

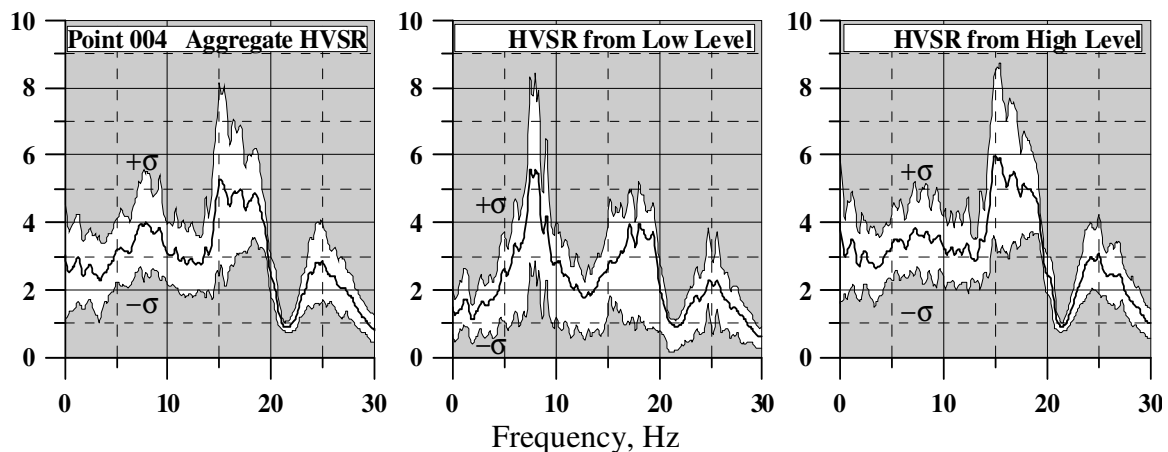


Figure 3.2. HVSR from the original records and from separated Low and High Level time windows, σ - standard deviation

The above treatment of the problem with the vibration sources close to the measurement point implied that the local source excites more intense vibrations than the distant sources. The separation allows establishing of low frequency fundamental soil resonance from low level ambient vibrations reliably, as it is shown on Figure 3.2.

In many cases an accidental powerful distant source (for example a heavy fast moving vehicle) can excite strong ground vibrations, which propagate through soil structure to the bedrock and arrive at the measured point as refracted or reflected wave. This source doesn't exist for long time but it can produce HVSR resonance at fundamental frequency. If the other distant sources, which act continuously are very weak, their energy may be insufficient to produce the refracted seismic waves above the instrumental noise. If the time when the accidental source works is short relatively to the duration of the field record, it will result in a suppression of the fundamental resonance. In this case, it is expedient to use the HVSR resonance obtained from the high level vibrations.

In most cases, the high and low level give the same fundamental resonant frequency. Nevertheless the utilization of the separation of the recorded waveforms gives an additional assurance during the data processing.

3.2. Shear-Wave Seismic Refraction Profiling (SH refraction profiling)

Refraction and reflection surveys are widely used for near-surface (engineering) applications. In this study, the refraction method (Reynolds, 1997) is used and is described herein.

The refraction surveying can be used for resolving the wave velocity with depth. The most commonly derived parameter is the shear wave velocity of the layers. The seismic refraction method is accurate for profiles characterized by high-wave velocity bed overlain by formations that have lower seismic velocity. This allows observing the so called 'critical refraction'. In the case of a lower seismic velocity in the lower layer than in the upper layer (i.e. velocity inversion), there will be no critical refraction and this layer will not be detected. This situation is known as 'hidden layer'.

The following assumptions are implied in the refraction method:

- The thickness of each layer within the profile is greater than the quarter of the wavelength of the incident wave.
- Raypaths lie in the vertical plane of the refraction profile line such that there is no seismic waves (refracted or reflected) arising from out of plane boundaries.

- Soil layers are either horizontal or slightly sloped;
- The layers' interfaces are planar.

For the refraction field measurements, a set of geophones (usually 12 or 24) are placed at equal distances along a straight line as shown in Figure 3.3. The figure also shows the raypaths for different types of waves observed along a simple seismic profile. A sledge hammer is used to produce the seismic waves. The seismic source has to be along the same line as the geophones. Figure 3.4 shows an example of the recorded seismograms. The basic components of a seismic refraction experiment are shown on Figure 3.5.

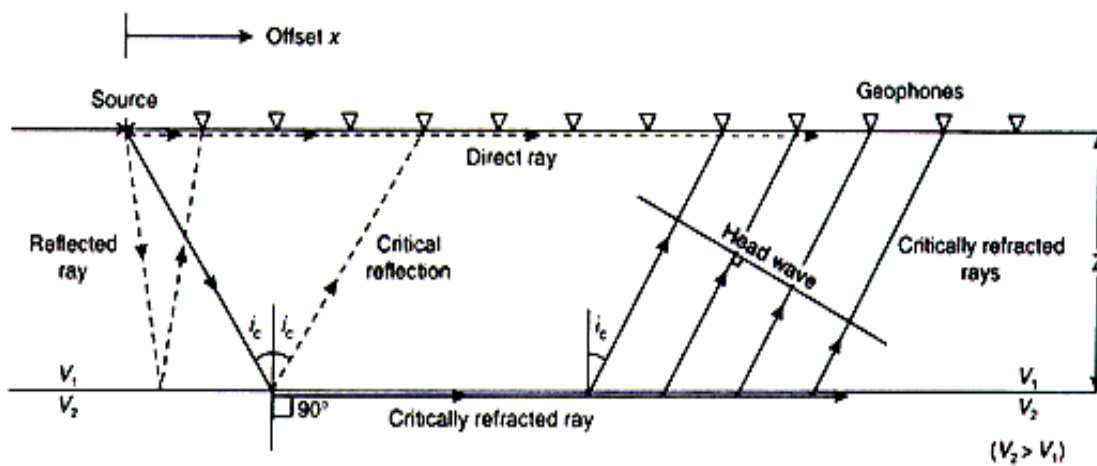


Figure 3.3. Raypaths for direct, reflected and refracted rays (from Reynolds, 1997)

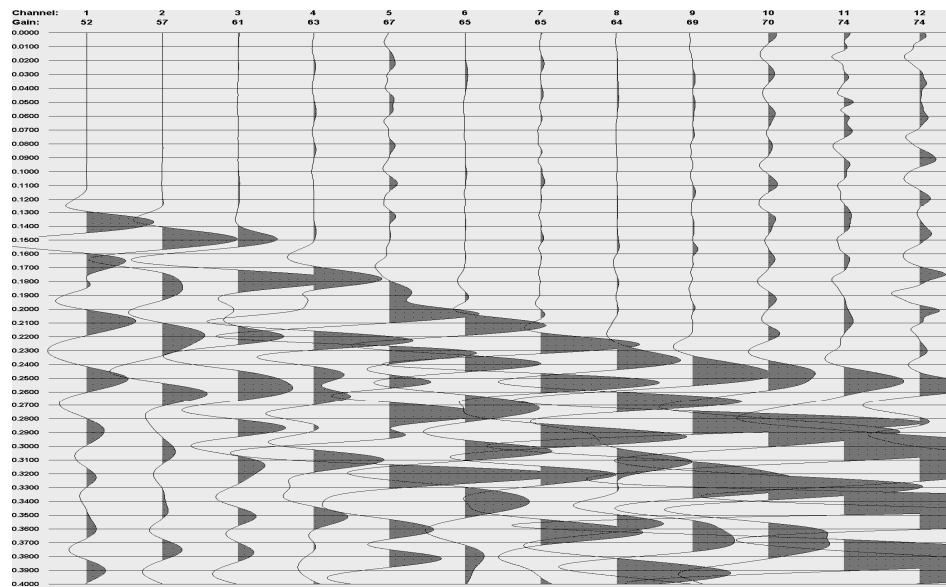


Figure 3.4. Example of 12 channel seismic refraction record

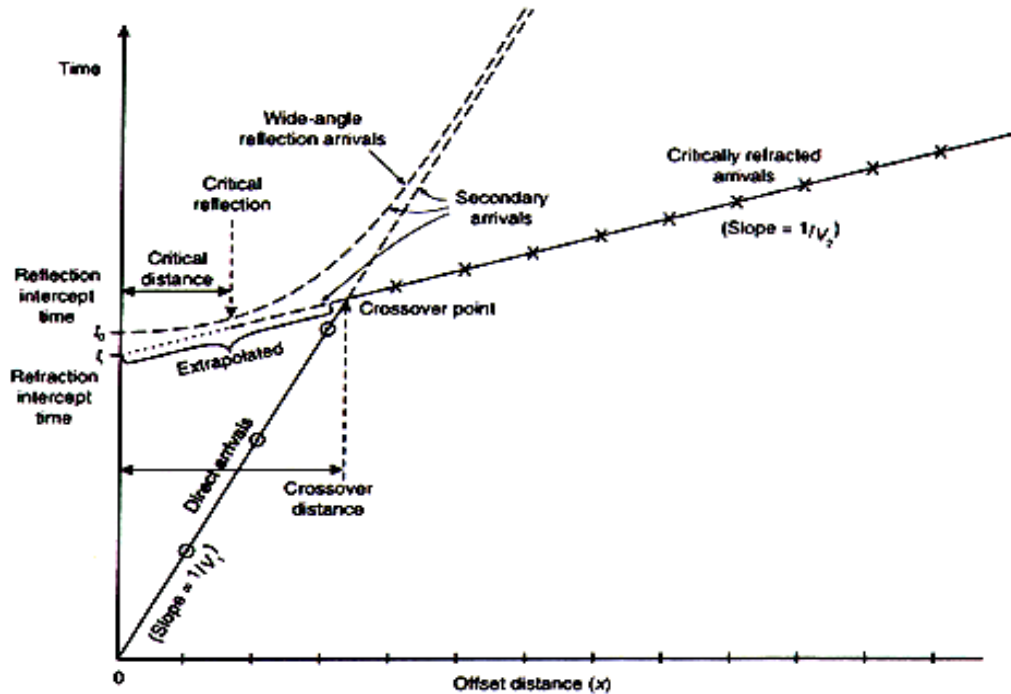


Figure 3.5. Time-distance plot for seismic refraction survey (Reynolds, 1997)

Assuming that the travel-time graphs of the direct and refracted waves are straight lines, simple equations are derived to obtain the velocities and depths to the refractors.

In case of two-layer structure (Reynolds, 1997), the velocity of the direct and refracted waves (the velocity in the second layer) can be obtained from the slope, m , and intercept time t_i :

$$m = 1/V_2 \text{ is the gradient (slope)} \quad (3.4)$$

$$t_i = 2h\cos(i_c)/V_1 \text{ is the intercept} \quad (3.5)$$

In Eq. (3.5), i_c is the critical angle of the refraction from layer 2. The depth of the refractor can then be obtained as:

$$h = t_i V_1 V_2 / 2(V_2^2 - V_1^2)^{1/2} \quad (3.6)$$

or the depth can be obtained from the crossover distance:

$$h = \frac{1}{2} x_{cross} [(V_2 - V_1)/(V_2 + V_1)]^{1/2} \quad (3.7)$$

where x_{cross} is the crossover distance.

For a soil profile with three horizontal layers (Figure 3.6), with velocities V_1 , V_2 and V_3 ($V_2 > V_1$, $V_3 > V_2$), the velocities are calculated from the slopes of the travel-time graphs, then the depths to the refractors, can be calculated using equations:

$$h_1 = t_{i2} V_1 V_2 / 2(V_2^2 - V_1^2)^{1/2} \quad (3.8)$$

$$h_2 = t_{i3} V_1 V_2 / 2(V_3^2 - V_2^2)^{1/2} - h_1 V_2 (V_3^2 - V_1^2)^{1/2} / V_1 (V_3^2 - V_2^2)^{1/2} \quad (3.9)$$

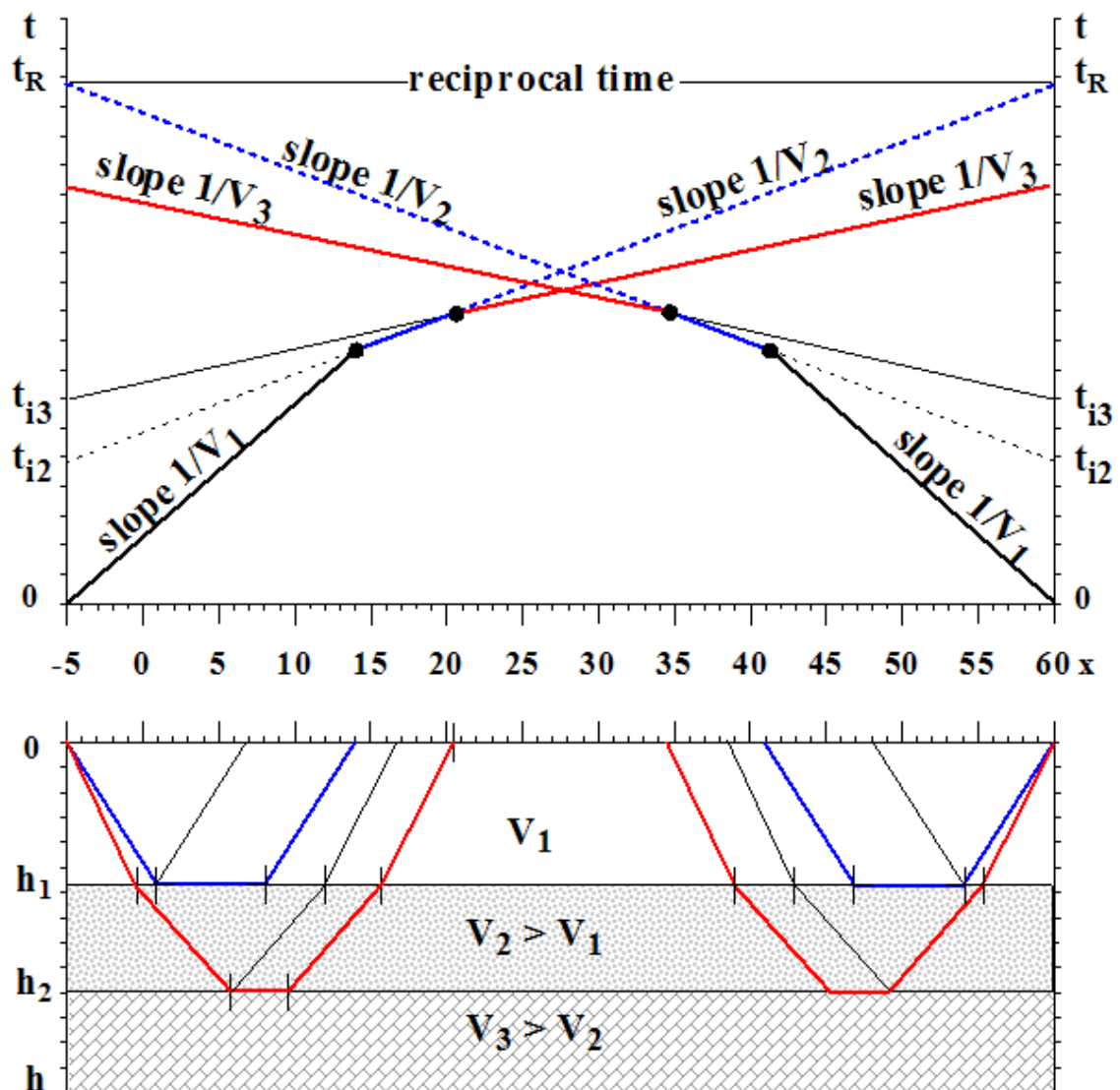


Figure 3.6. Travel time curves for three layer soil profile with increasing velocity with depth.

t_{i2} and t_{i3} are the intercept times for the second and third layers.

In the case of a thin intermediate soil layer with velocity $V_2 > V_1$ and $V_2 < V_3$, it is possible not to have refracted wave from the bottom of this layer in first arrivals. This layer will be “hidden” in the refraction profiling. This case is illustrated on Figure 3.7, which shows the travel time curves of refracted head waves with bold lines only for the first arrivals. The dashed lines show the travel time for the refracted waves from the boundary between second and third soil layers.

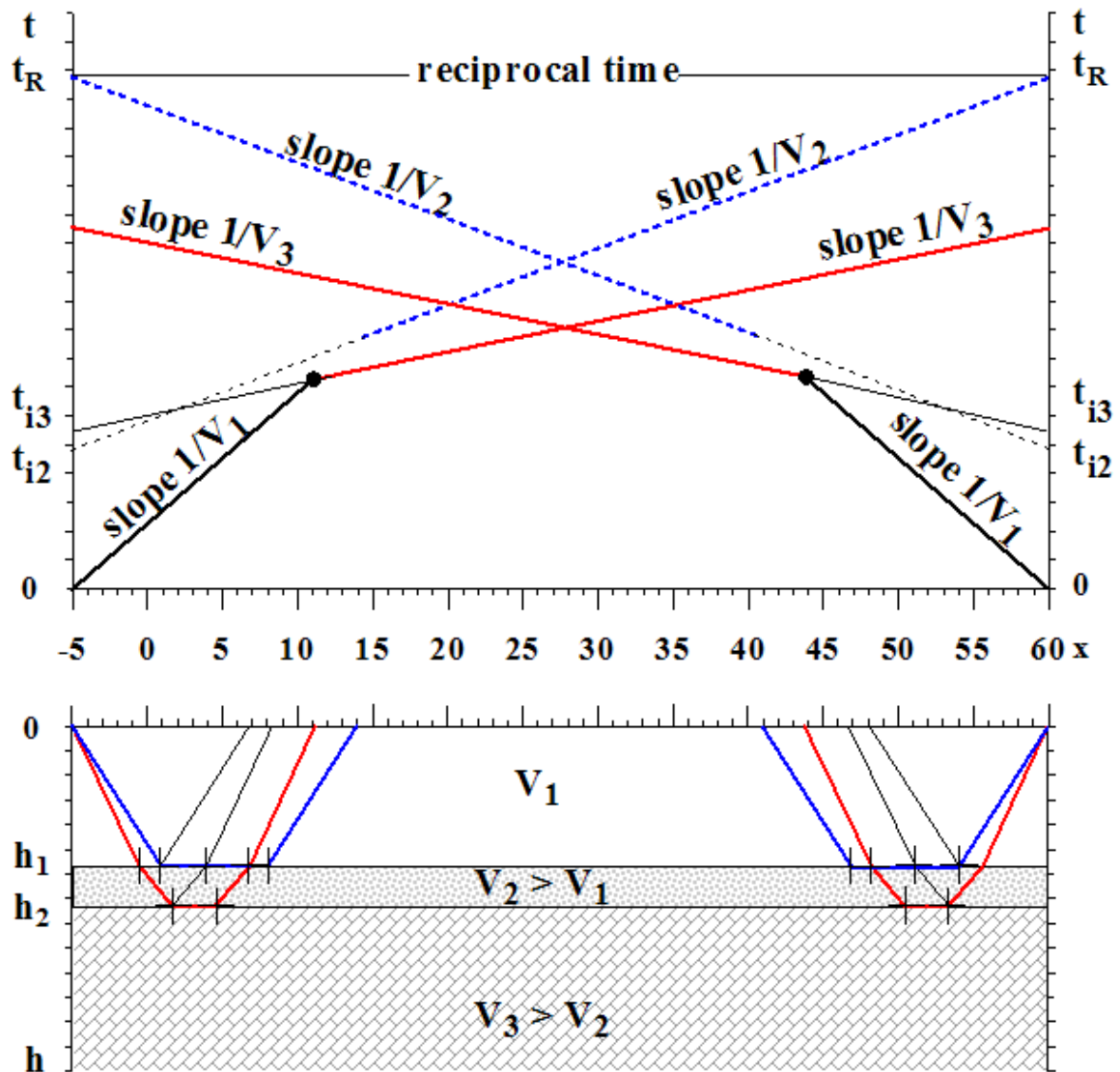


Figure 3.7. Example of hidden second layer due to absence of head wave from h_1 boundary in first arrival. t_{i2} and t_{i3} are the intercept times for the second and third layers. Travel time from the second layer (blue dashed line) is not in first arrival.

A blind zone similar to Figure 3.7 exists as a rule if a deeper layer has velocity less than that in overlaying layers. The SH profiling with refracted waves can't resolve the blind zones due to thin layer or in case of the low velocity intermediate layer.

Two seismic sources on both ends of the profiles are required to define the dipping angle θ for the case of dipping boundaries (Figure 3.8). The travel time from a source at point A to a receiver at point D is:

$$T_d = x / V_d + t_d \quad (3.10)$$

Where index "d" indicates the seismic wave traveling down slope.

The travel time from a source at point B to a geophone at point A is:

$$T_u = x / V_u + t_u \quad (3.11)$$

Where index "u" indicates the seismic wave traveling uphill.

V_d and V_u are apparent velocities which correspond to the slopes of the head wave travel time curves. They are;

$$V_u = V_1 / \sin(i_c - \theta) \text{ and } V_d = V_1 / \sin(i_c + \theta) \quad (3.12)$$

Where i_c is the critical angle.

t_d and t_u are the interception times for each source-receiver direction. They are:

$$t_u = 2h \cos(i_c) / V_1 \text{ and } t_d = 2h' \cos(i_c) / V_1, \quad (3.13)$$

h and h' are the perpendicular distances from points A and D respectively to the interface between two layers.

The slope of the direct wave is the same in both directions.

The slopes of the direct and refracted travel time lines are used for calculation of the dip angle θ and critical angle i_c :

$$\theta = 0.5 [\text{asin}(V_1 / V_d) - \text{asin}(V_1 / V_u)] \quad (3.14)$$

$$i_c = 0.5 [\text{asin}(V_1 / V_d) + \text{asin}(V_1 / V_u)] \quad (3.15)$$

The half-space velocity is:

$$V_2 = V_1 / \sin(i_c) \quad (3.16)$$

In a case of two-layer soil profile the average thickness of the first layer is:

$$H = (h + h') / [2\cos(\theta)] \quad (3.17)$$

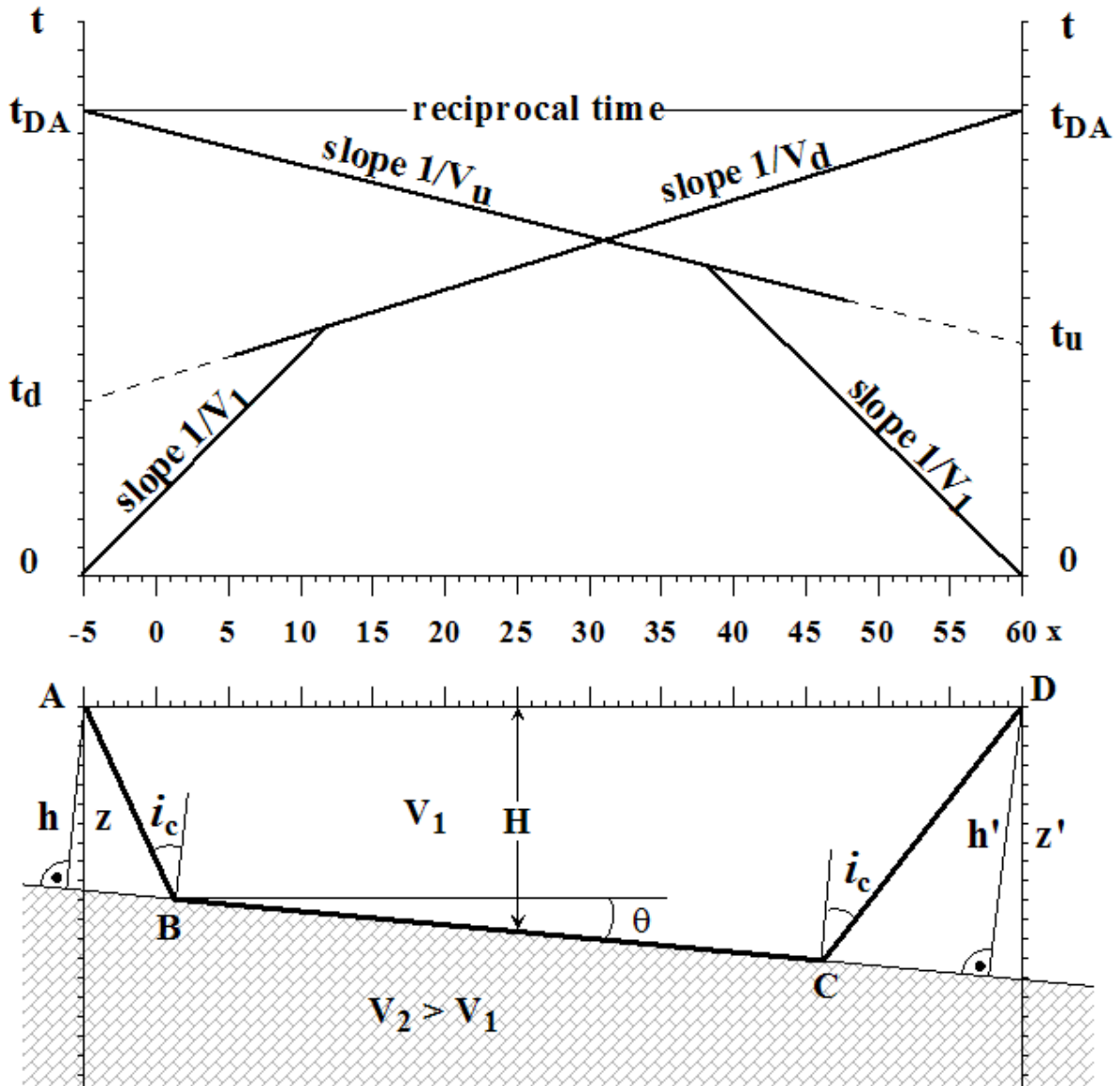


Figure 3.8. Example of refracted wave travel times for a dipping second layer.

The SH refraction survey for all referent test points in GTA was performed with two shot points from each side (4 in total) and was processed using eq.3.10 to 3.17.

3.3. Surface Wave Methods for Shear Wave Velocity estimation

These relatively new in-situ methods are widely used for determining shear wave velocity profiles. There are two surface-waves methods: the spectral analysis of surface waves (SASW) and the multi-channel analysis of surface waves (MASW).

The basis of the SASW method is the dispersive nature of Rayleigh waves when traveling through a layered medium. Rayleigh wave velocity is determined by the material properties (primarily shear wave velocity, but also compressional wave velocity and material density) of the subsurface to a depth of approximately 1 to 2 wavelengths. There are several options for interpreting dispersion curves, depending on the accuracy required in the shear wave profile.

The average shear wave velocity along the profile can be estimated using a simple empirical analysis. For greater accuracy, forward modeling of fundamental-mode Rayleigh wave dispersion as well as full stress wave propagation can be performed using specialized software.

The SASW/MASW methods have been widely used for shallow V_S characterization for different purposes (e.g., Nazarian et al., 1983; Nazarian and Stokoe, 1984; Stokoe and Nazarian; 1985; Brown et al., 2002).

The geophysical inversion methodology for determination of the shear wave velocity includes iterative adjustment of the dispersion curve for the velocity model along the profile. During this adjustment, errors may accumulate, increasing with depth. It is therefore essential to correlate the results of this method with results from other methods.

3.3.1. Spectral analysis of surface waves (SASW)

The technique was developed in the early 1980s by Nazarian on the basis of the Steady State Vibration Test (Richart et al., 1970). The SASW method uses two receivers to record seismic waves generated by an impact source (e.g. a sledge hammer), as shown in Figure 3.9. The tests have to be repeated with many different source and receiver spacing to cover different depths.

The idea of the SASW test is to measure the Rayleigh wave dispersion curve and to obtain shear wave velocity profile by inversion of the dispersion curve. Chen et al. (2004)

investigated the effects of source and receivers arrangement on the Rayleigh wave dispersion curve in SASW testing. The data collected during the SASW tests are processed to determine the dispersion curve and the coherence from cross-spectral phase.

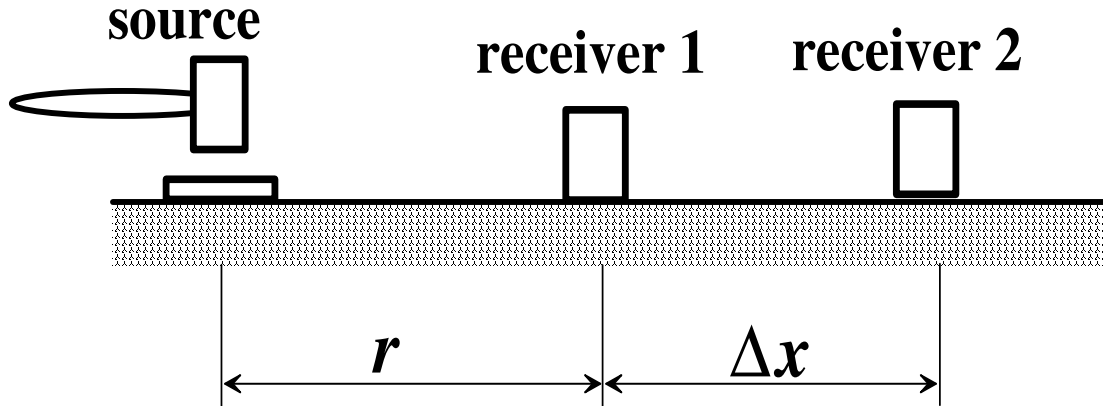


Figure 3.9. Arrangement of SASW test.

The wavelength λ_R and Rayleigh wave velocity V_R can be calculated as:

$$\lambda_R = \frac{2\pi \Delta x}{\Delta\phi} \quad (3.18)$$

$$V_R = \lambda_R f \quad (3.19)$$

where Δx and $\Delta\phi$ are, respectively, the spacing and phase angle difference between two receivers at frequency, f .

Ideal plane surface wave is difficult to generate, which causes a problem when choosing proper source to receiver distance. In order to establish correctly the phase angles and avoid aliasing in the space domain, the following criterion should be satisfied:

$$\Delta x < \lambda_{R_{\min}} / 2 \quad (3.20)$$

where $\lambda_{R_{\min}}$ is the shortest wavelength of interest.

Several studies have examined the arrangement of source and receivers scheme for the SASW technique. Based on experimental results, Heisey et al. (1982) suggested that for an arrangement of $r = \Delta x$ the acceptable wavelength can be expressed as:

$$\lambda_R \leq \Delta x \leq 2\lambda_R \quad (3.21)$$

Theoretical studies conducted by other researchers as Sanchez-Salinero et al. (1987) suggested that:

$$r = \Delta x \text{ and } \Delta x < 2\lambda_R. \quad (3.22)$$

More recently, Longzhu et al. (2004) found that the assumption for plane Rayleigh wave is only valid when the source and receiver arrangement meets certain criteria, which depends on Poisson's ratio and water saturation of soils.

Errors in V_R measurement will be less than 5% for any value of Poisson's ratio ν and source-to-near-receiver distance r if the spacing between receivers is calculated from:

$$\Delta x / \lambda_R \geq 2.6 \quad (3.23)$$

3.3.2. Multi-Channel Analysis of Surface Waves (MASW)

This method was developed at Kansas Geological Survey (Park et al., 1999a; 1999b). In the MASW method, the phase velocities are determined directly from multi-channel surface-wave records after applying an integral transformation of waveforms to the frequency-domain. The integration converts time-domain waveform data (time versus distance) into an image of phase velocity c versus frequency f .

The MASW method is superior to SASW because it allows visual distinction of the fundamental mode from other higher modes of Rayleigh wave and from body waves. The MASW can avoid spatial aliasing, which is a problem in SASW field arrangement. Xia et al. (1999) and Miller et al. (1999) applied the MASW method to continuous profiling shot records, and delineated 2-D S-wave velocity structures. Recently, Hayashi and Suzuki (2004) proposed common mid-point cross-correlation analysis (CMPCC) of multi-channel and multi-shot surface waves to calculate accurate phase-velocity curves, and to reconstruct two-dimensional velocity structures with high resolution. An example of this technique is shown in Figure 3.10.

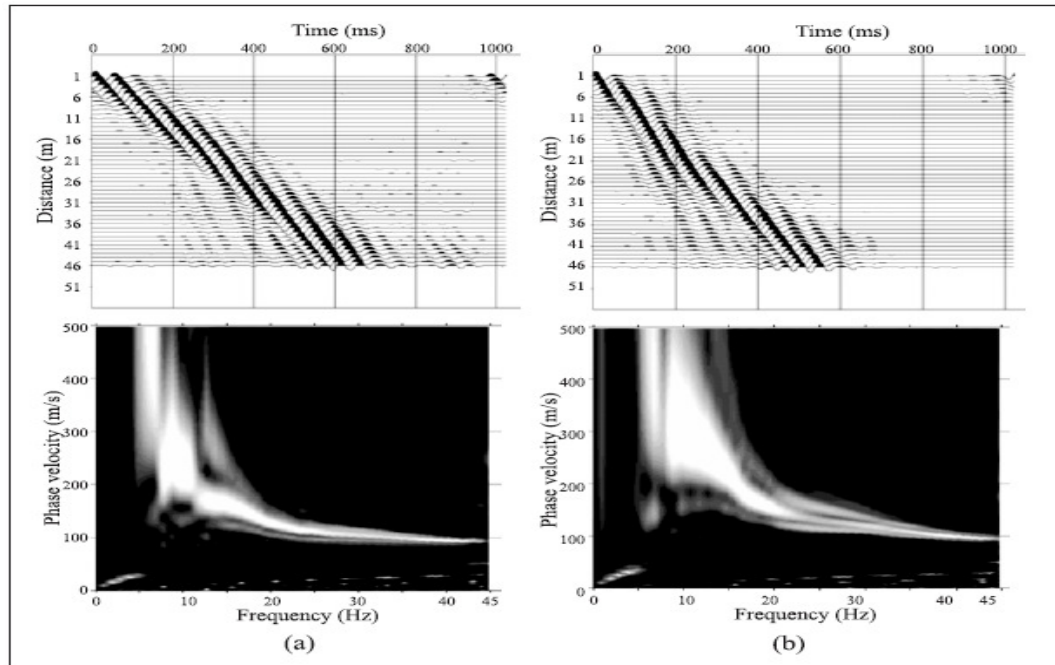


Figure 3.10. Example of MASW- CMPCC data and their interpretation
Time series (top) and their c - f images (bottom) obtained through MASW analysis.
The data correspond to two lateral distances: 50.8 m (a) and 70.8 m (b).
The velocity structure changes laterally (from Hayashi and Suzuki, 2004).

3.4. Application of SH velocity profiling, SASW and MASW in city conditions

The main limitation for applying SH velocity profiling, SASW and MASW techniques is that they required large area for deployment when a larger depth of investigation is needed. These methods can be used for seismic site response studies over open areas. SH profiling and MASW methods are less applicable in urban conditions.

SH refraction/reflection velocity profiling and MASW techniques are relatively inexpensive but time consuming. Their large scale utilization is justified for new building sites, before construction.

An example of successful implementation of SH refraction/reflection seismic profiling on 686 sites is demonstrated in a seismic microzonation in the Ottawa area (Motazedian, 2011).

The MASW method and SH velocity profiling are used in the first stage of our study to characterize the soil profiles. The results are compared with those from the HVSR.

Chapter 4

Equipment for Field Measurements

All field data for SH velocity profiling and MASW study was collected using a standard seismic station Geode. All waveforms for HVSR calculations were collected in field by a 3-component USB data acquisition system developed in UWO.

4.1. Seismic station GEODE, geophones, seismometers and cables.

The 24 channels stand-alone seismic module Geode is made by Geometrics. It is controlled from a remote personal computer running a Windows XP operating system via a network connection. The Geode for the field surveys in GTA is controlled using Multiple Geode Operating Software (MGOS) installed on the field laptop computer system.

Geode specification for the GTA geophysical surveys and building resonances tests:

Channels: 24 channels

A/D Conversion: 24 bit

Dynamic Range: 144 dB (system), 110 dB (instantaneous, measured)

Distortion: 0.0005% @ 2 ms, 1.75 to 208 Hz

Bandwidth: 1.75 Hz to 20 kHz

Common Mode Rejection: > 100dB at ≤ 100 Hz, 36 dB

Crosstalk: -125 dB at 23.5 Hz, 24 dB, 2 ms

Noise Floor: 0.20 μ V, RFI at 2 ms, 36 dB, 1.75 to 208 Hz

Stacking Accuracy: 1/32 of sample interval

Maximum Input Signal: 2.8V_{pp} at 0 dB

Input Impedance: 20 k Ω , 0.02 μ F

Preamplifier Gains: Software selectable between 24 and 36 dB

Anti-alias Filters: -3 dB at 83% of Nyquist frequency, down 90 dB.

Acquisition and Display Filters:

Low Cut: OUT.

Notch: OUT

High Cut: 32 Hz 48 dB/ octave

Sample Interval: 8 ms

Maximum Record Length: 16,384 samples per channel

Pre-trigger Data: OUT

Delay: 0

Data Transmission: Ethernet connection

Data Formats: SEG-2 standard

System Software: Multiple Geodes Operating Software (MGOS)

Data Storage: Stores data locally on the laptop hard drive

Operating System: Windows XP-SP3

Data Processing and Interpretation - Software: Includes refraction software and SASW/MASW SurfSeis© software developed at the Kansas Geological Survey

Geophones resonant frequencies:

Horizontal 17 Hz,

Vertical 4.5 Hz,

3-component seismometer L4-3D 1.0 Hz

Spread cable 1x24 twisted pairs

Cables for the L\$-3D 5x3 twisted pairs

4.1.1. Settings for SH refraction profiling in GTA:

Geode configuration:

Channels	12
Lines	1
Sample interval	8 ms
Analog filters	32 Hz/64 dB/oct
Preamplifier gain	All channels 24 dB
Record length	4.0 s

Geophones for SH profiling:

Horizontal geophones	12
Resonant frequency	17 Hz
Sensitivity	29 V/(m/s)
Damping Factor	0.65

Cable configuration for SH profiling

Channels	12
Spacing	5.0 m
Cable length	55 m

Shot point - horizontal impact

Impact source - I-beam and sledge hammer

Staking - ON	up to 24 stacks
Profile 1 -Distance to the first geophone	5 m
Profile 2 -Distance to the first geophone	30 m
Profile 3 -Distance from last first geophone ...	5 m
Profile 4 -Distance from last first geophone ...	30 m

4.1.2. Settings for MASW survey in GTA:

Geode configuration:

Channels	12
Lines	1
Sample interval	8 ms
Analog filters	32 Hz/64 dB/oct
Preamplifier gain	All channels 24 dB
Record length	4.0s

Geophones for MASW survey

Vertical geophones	12
Resonant frequency	4.5 Hz
Sensitivity	27 V/(m/s)
Damping Factor	0.70

Cable configuration for MASW survey

Channels	12
Spacing	1.25 - 1.25 - 2.5 - 5, 5 - ... - 5.0 m
Cable length	48.75 m

Shot point - vertical imp act

Impact source - aluminum plate and sledge hammer

Staking - ONup to 16 shots / MASW

Distance to the first geophone1.25 m

4.1.3. Settings for building resonances tests:

Geode configuration:

Channels	15
Lines	5
Sample interval	8 ms
Analog filters	32 Hz/64 dB/oct
Preamplifier gain	All channels 24 dB
Record length	131 s

Seismometers for the building resonances tests

3-component seismometers	5
Resonant frequency	1.0 Hz
Sensitivity	170 V/(m/s)
Damping Factor	0.70

Cable configuration for the building resonances tests

Cables for the 3-componet seismometers	5
Spacing	Based on the test scheme
Cable length	5x25 m

Seismic source - ambient vibration and wind loading

Staking - OFF.....one continuous record for each test

4.2. Portable three-component 1-40 Hz seismic station

A portable seismic station for measurement of ambient noise and building resonance is developed and assembled as part of this study.

This station has the following advantages compared to Geode: 10 times less power consumption, significantly cheaper, easy to deploy and tune-up, unlimited in time ASCII data files suitable to be processed without converting to decimal format and demultiplexing, visual control over the recorded waveforms etc.

The design was conformable to the recommendations of SESAME working group (SESAME H/V User Guidelines, 2005). The seismic station includes the following components:

1. Three-component seismometer Mark Product L4-3D with flat response between 1 and 40 Hz with velocity output.
2. Data acquisition system developed here, and connected to USB-9215 DAC made by National Instruments (Figure 4.1).

This three-component seismic station collects data on the computer hard disk using software working in Lab View environment (Bishop, 2007).

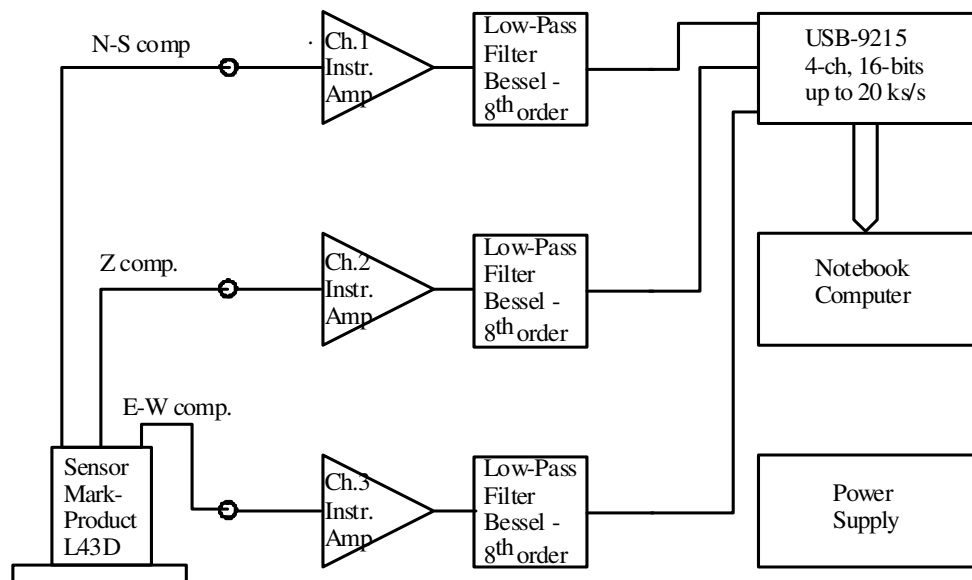


Figure 4.1. A simplified scheme of the equipment for HVSR field measurements.

Ch.1(2,3) Instr. Amp is a Differential instrumental amplifier

4.2.1. Electronic moduli

The differential instrumental amplifier shown on Figure 4.2a is made using AD8295 from Analog Devices (AD8295, 2009). The resistor R_G is used to control gain during channel calibration.

The 8th order low-pass filters for the 3-component seismic station consists of four second order Bessel filter sections connected in series with increasing quality factor Q . Each section is realized with Sallen-Key topology (Sallen and Key, 1955) shown on Figure 4.2b.

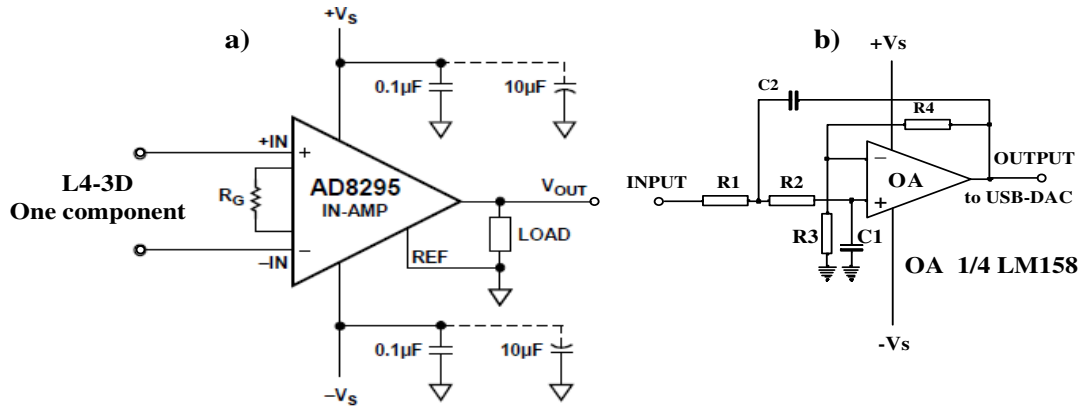


Figure 4.2. a) Instrumental differential amplifier R_G - gain control.

b) Schematic of Sallen-Key topology for a second order low-pass filter.

OA - operational amplifier - 1/4 LM 158.

The base equations for the Sallen-Key second order low-pass filter are (Williams and Taylor, 1988):

$$f_c = \frac{1}{2\pi\sqrt{R_1R_2C_1C_2}} \quad \text{and} \quad Q = \frac{\sqrt{R_1R_2C_1C_2}}{C_1(R_1 + R_2)} \quad \text{for} \quad K = 1 \quad (4.1)$$

$$R_2 = \frac{\frac{C_2}{Q} + \sqrt{\left(\frac{C_2}{Q}\right)^2 - 4C_1C_2}}{4\pi f_c C_1 C_2} \quad \text{and} \quad R_1 = \frac{1}{(2\pi f_c)^2 R_2 C_1 C_2} \quad \text{for} \quad C_1 > 4Q^2 C_2 \quad (4.2)$$

$$f_c = \frac{1}{2\pi\sqrt{R_1R_2C_1C_2}} \quad \text{and} \quad Q = \frac{\sqrt{R_1R_2C_1C_2}}{C_1R_1 + C_1R_2 + R_1C_2(1-K)} \quad \text{for} \quad K > 1 \quad (4.3)$$

After normalizing to R and C nominal values:

$$R_1 = mR, \quad R_2 = R, \quad C_1 = C, \quad C_2 = nC \quad \text{and} \quad f_c = \frac{1}{2\pi RC\sqrt{mn}} \quad (4.4)$$

$$R = \frac{1}{2\pi f_c C \sqrt{mn}} \text{ gives: } Q = \frac{\sqrt{mn}}{1+m+mn(1-K)} = \frac{\sqrt{mn}}{1+m(1+n(1-K))} \quad (4.5)$$

$$\text{Substituting } (1+n(1-K)) = E \text{ when } E = 0 \quad m = \frac{Q^2}{n}, \quad (4.6)$$

$$\text{when } E \neq 0 \text{ gives } m^2 E^2 + \left(2E - \frac{n}{Q^2}\right)m + 1 = 0 \quad (4.7)$$

$$\text{Substituting } \left(\frac{2}{E} - \frac{n}{E^2 Q^2}\right) = A \text{ gives: } m^2 + Am + \frac{1}{E^2} = 0 \quad (4.8)$$

$$\text{The Eq. (4.8) has two solutions: } m_{1,2} = \frac{-A \pm \sqrt{A^2 - \frac{4}{E^2}}}{2} \quad (4.9)$$

C and R can be found using Eq. (4.9) in eq. (4.3 to 4.5). For an 8th order Bessel filter the values for Q are calculated from the Bessel-Gauss polynomials. The corner frequency is the same for all four second order sections. An Excel worksheet shown on Figure 4.3 utilizes the above equations to calculate the real values for the passive components of four second order Sallen-Key low-pass filter sections. The resistors $R1$ and $R2$ shown on Figure 4.2b are substituted for $R11+R12$ and $R21+R22$ to ensure accuracy during adjustment.

Filter 1		Filter 2		Filter 3		Filter 4	
C1, nF	100	C1, nF	106	C1, nF	104	C1, nF	106
C2, nF	106	C2, nF	145	C2, nF	207	C2, nF	305
Q	0.5098	Q	0.60134	Q	0.89998	Q	2.5629
K	2	K	2	K	2	K	2
f,Hz	40	f,Hz	40	f,Hz	40	f,Hz	40
omega	251.3274	omega	251.3274	omega	251.3274	omega	251.3274
n=C2/C1	1.06	n=C2/C1	1.367925	n=C2/C1	1.990385	n=C2/C1	2.877358
E=1+n(1-K)	-0.06	E=1+n(1-K)	-0.36792	E=1+n(1-K)	-0.99038	E=1+n(1-K)	-1.87736
A=	-1166.26	A=	-33.3809	A=	-4.52474	A=	-1.18962
m=	0.238226	m=	0.222788	m=	0.237819	m=	0.330107
m1=	1166.027	m1=	33.15813	m1=	4.28692	m1=	0.85951
m2=	0.238226	m2=	0.222788	m2=	0.237819	m2=	0.330107
R1, kOhm	18.86	R1, kOhm	15.15	R1, kOhm	13.23	R1, kOhm	12.71
R2, kOhm	79.18	R2, kOhm	67.99	R2, kOhm	55.61	R2, kOhm	38.51
R11, kOhm	17.8	R11, kOhm	14.6	R11, kOhm	12.8	R11, kOhm	12.71
R21, kOhm	73.7	R21, kOhm	67.8	R21, kOhm	55.4	R21, kOhm	38.2
R12, kOhm	1.06	R12, kOhm	0.55	R12, kOhm	0.43	R12, kOhm	0
R22, kOhm	5.48	R22, kOhm	0.19	R22, kOhm	0.21	R22, kOhm	0.31

Figure 4.3. Excel worksheet for calculation of the 8th order low-pass filter.

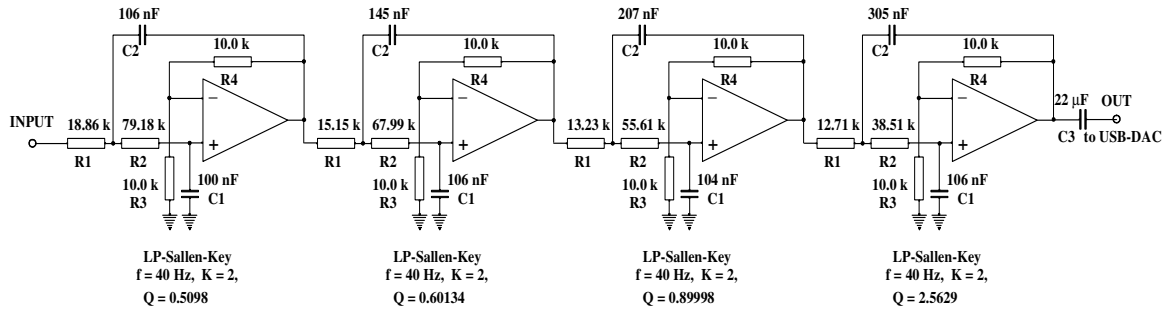


Figure 4.4. Schematic of the 8th order Bessel low-pass filter at 40 Hz.

The schematic of the 8th order Bessel low-pass filter is shown on the Figure 4.4. The resistors R1 and R2 are split in two in order to adjust the filter cut-off frequency and Q-factor to +/-1%.

4.2.2. Seismometer L4-3D - correction of the transfer function

The used seismometer (velocity sensor) type L4-3D has sensitivity V_R , natural frequency f_R , and damping factor D_R for each component, which are changed from the factory adjusted parameters due to deterioration of the magnetic induction and spring stiffness with aging. These parameters can't be restored and the complex transfer function of the real seismometer H_R has to be corrected mathematically to its original form. The original complex transfer function is the target of the transformation. The factory specification for sensitivity V_T , natural frequency f_T , and damping factor D_T are used for the calculations for each component.

The FFT of every recorded waveform has to be multiplied by a complex scaling function H_{SC} in the frequency domain. The transfer function of the seismometer (velocity sensor) L4-3D is for a single degree of freedom (SDOF) oscillator with an electromagnetic velocity transducer. The dimension of the transfer function is V / (m/s) because it is multiplied by the sensitivity V_R or V_T .

The modulus of the transfer function of the used seismometers can be calculated for each component as:

$$|H_R| = \frac{V_R (f / f_R)^2}{\sqrt{[1 - (f / f_R)^2]^2 + 4D_R^2 (f / f_R)^2}}, \quad (4.10)$$

and phase shift is:

$$\phi_R = \arctan\left(\frac{2D_R(f/f_R)}{1-(f/f_R)^2}\right) \quad (4.11)$$

where: V_R - sensitivity, f_R - natural frequency, and D_R - damping factor are results of calibration tests.

The modulus and phase shift of the targeted transfer function are:

$$|H_T| = \frac{V_T(f/f_T)^2}{\sqrt{[1-(f/f_T)^2]^2 + 4D_T^2(f/f_T)^2}}, \quad (4.12)$$

and phase shift is:

$$\phi_T = \arctan\left(\frac{2D_T(f/f_T)}{1-(f/f_T)^2}\right) \quad (4.13)$$

where: V_T - sensitivity, f_T - natural frequency, and D_T - damping factor are the original parameters for all components according to factory specification.

Modulus $|H_{SC}|$ of the complex scaling function and phase shift $\Delta\phi_{CORR}$ for recalculation of the amplitude spectrum from a recorded waveform, are:

$$|H_{SC}| = \frac{|H_T|}{|H_R|} = \frac{V_T}{V_R} \left(\frac{f_R}{f_T}\right)^2 \frac{\sqrt{[1-(f/f_R)^2]^2 + 4D_R^2(f/f_R)^2}}{\sqrt{[1-(f/f_T)^2]^2 + 4D_T^2(f/f_T)^2}}, \quad (4.14)$$

and

$$\Delta\phi_{CORR} = \phi_T - \phi_R \quad (4.15)$$

Only the eq. (4.14) is needed for correction of the spectra for HVSR because we use only the moduli of the amplitude spectra in these calculations.

Visualization and identification of the vibration modes and building resonances require correction of the recorded waveforms in the time domain. It was done using complex FFT from recorded waveform multiplied by complex scaling function H_{SC} :

$$H_{SC} = \text{Re } H_{SC} + \text{Im } H_{SC}, \quad (4.16)$$

where: $\text{Re } H_{SC} = |H_{SC}| \cos(\Delta\phi_{CORR})$ and $\text{Im } H_{SC} = |H_{SC}| \sin(\Delta\phi_{CORR})$ (4.17)

The corrected complex spectrum of the recorded waveform is converted back in time domain by Inverse FFT (IFFT). This procedure removes the phase shift between all components of all seismometers used for recording of the building vibrations. The corrected waveforms are in conformity with actual movement of the measured test points.

The normalized transfer function of the three-component long-period seismic station with corrected characteristic of a L4-3D seismometer is shown on Figure 4.5.

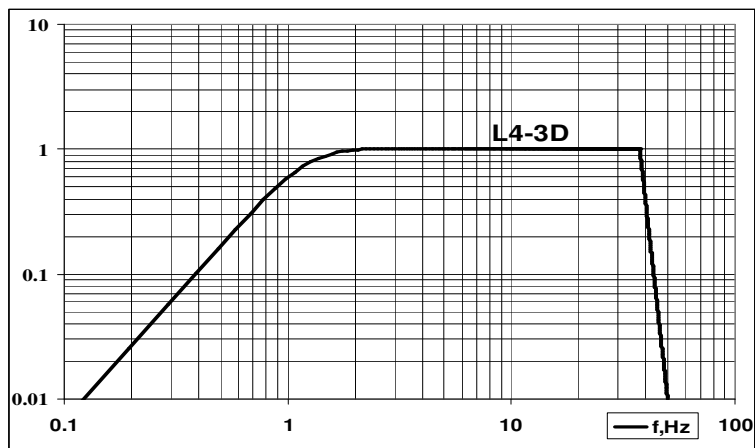


Figure 4.5. Normalized transfer function of L4-3D and the 8th order Bessel low-pass filter at 40 Hz.

Basic technical specification of the 3-component seismic station with L4-3D

designed and manufactured considering SESAME requirements.

Sensitivity	125.10 ³ V/(m/s)
Noise floor	5 nm/s p-p
Clipping level	80 microns/s
Damping	0.7 of critical
Frequency range -3 dB	1.0-40 Hz
Spurious free frequency range	0.1-180 Hz
DAC sample rate	100 sps
Sampling	simultaneously
Storage	on PS HD Excel files
Operating temperature Range	-10° to 60°C
Power supply	9-15V DC / 0.1 A

Chapter 5

Geophysical field investigations

5.1. Introduction

The microzonation study presented in this thesis covered a large part of the GTA area (approximately 2500 km²) as shown in Figure 5.1. The field investigation involved 187 test points distributed almost uniformly over the test area, with test points spaced at distances approximately 3 to 6 km (Figure 5.1). In order to establish a general characterization of the soil stratigraphy within the test area, 15 reference points were selected to conduct MASW, SH refraction profiling and HVSr testing.

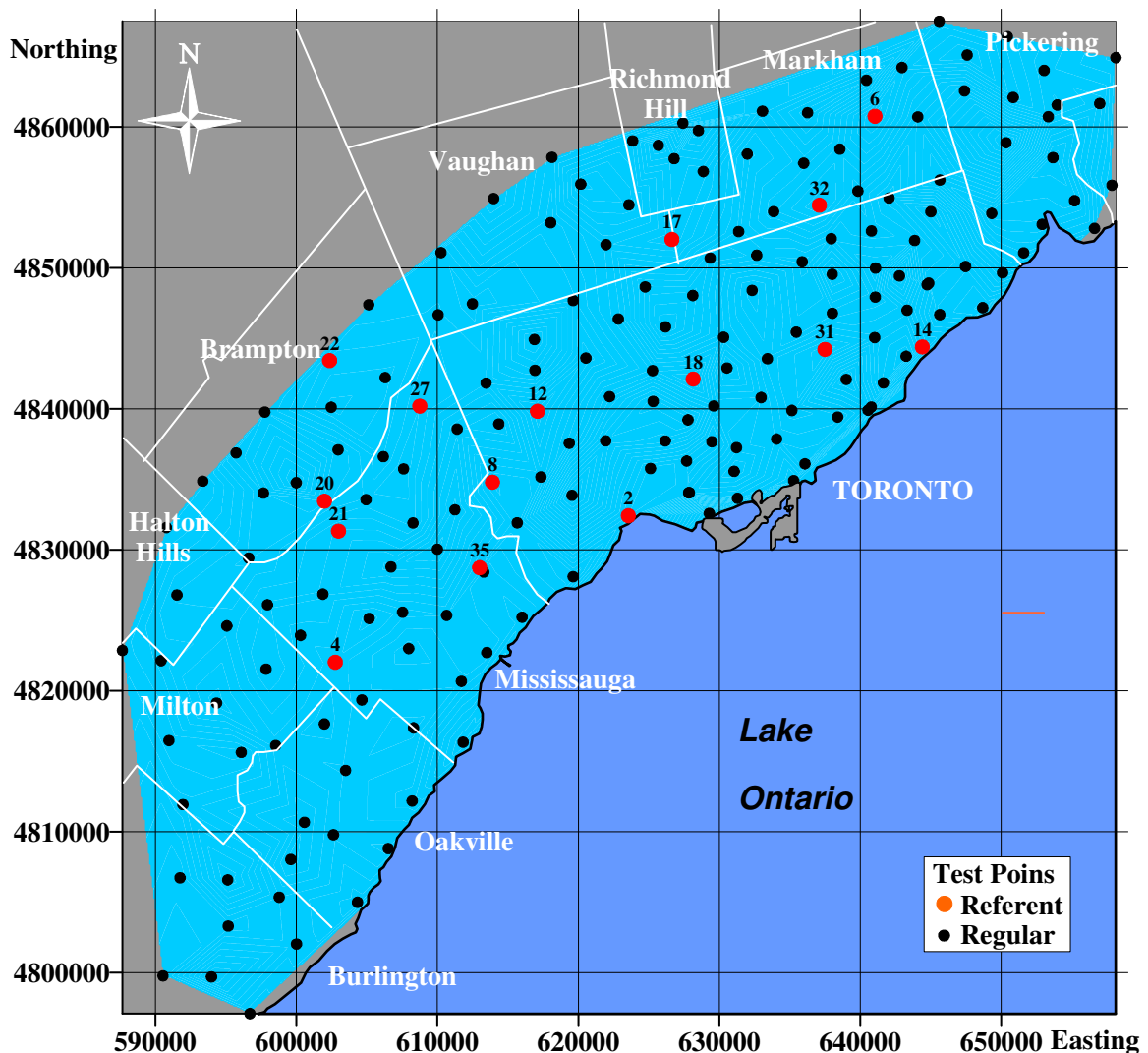


Figure 5.1. Test points over studied part of GTA.

The locations of these reference points were selected using the following criteria:

- The points should be located on supposedly undisturbed natural soil;
- The points to be on public terrains;
- The area surrounding the points should have sufficient free space for spreading of geophone lines for MASW and SH refraction survey;
- The soil layering has to be horizontal or with small inclination in order to obtain refracted SH wave at least from one seismic boundary.
- For sites that contain man-made fill, the test point should not be located over underground infrastructure;

All 187 test points were located as far as possible from local vibration sources (e.g. traffic and industrial vibrations);

Points were located far from high-voltage power lines, tall buildings, etc;

No measurements were taken during periods of strong winds.

5.2. Seismic SH refraction profiling.

5.2.1. Refraction survey data acquisition.

The geometry of SH refraction seismic profiling setup is shown in Figure 5.2. The distance between geophones was 5 m. Two shot points are located at each side of the geophone line at distances 5 and 30 m from the first and from the last geophone. All 12 channels are equipped with 17 Hz critically damped horizontal geophones.

The 24-channel stand-alone seismic module Geode with setting described in Ch.4.1.1 was used as data acquisition system. Data was recorded on a laptop computer running Windows XP with firmware from Geometrics and Multiple Geode Operating Software (MGOS) installed on the laptop computer. The active seismic source was 8 lb sledge hammer hitting horizontally on a steel I-beam with dimensions 1000x200x200 mm.

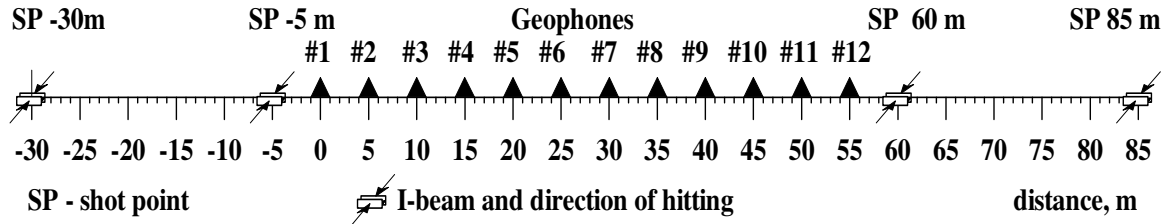


Figure 5.2. Geometry of the SH refraction seismic profiles.

5.2.2. Refraction surveys data processing

The collected data from the refraction survey in SEG2 format were converted into SEG-Y format, employing a computer program developed in MATLAB environment encoding Eqs. (3.4) to (3.7). The program reads the recorded data in SEG2 format converts the files in SEG-Y format and displays the seismograms (Figure 5.3). After manually picking the arrival times, the program calculates the wave velocity and thickness of each layer assuming all refractors are inclined no more than 15° from the horizontal surface. Only data for SH-waves are interpreted.

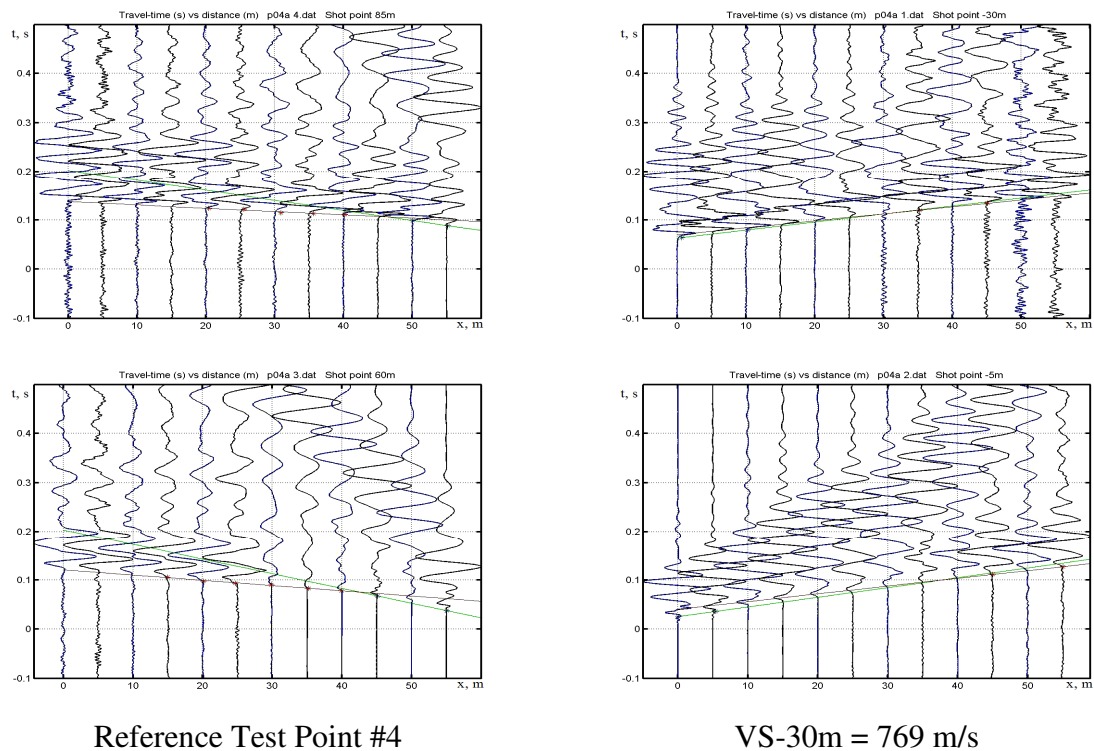


Figure 5.3. Example of seismic records and travel-time lines from all shot points for SH refraction seismic profiles.

The 15 SH refraction profiles at the reference points for all source-receiver configurations are given in the Appendix.

To compare the soil parameters at the measurement points with the soil classification (Table 1.2), the average Vs for the upper 30 m of a two layered soil profile is calculated:

$$V_{s30m} = 30 / [h_1 / V_{s1} + (30 - h_1) / V_{s2}], \quad (5.1)$$

where V_{s1} and V_{s2} are the shear wave velocities, h_1 is the depth to the intermediate boundary (this is not the bedrock-soil boundary).

These values are used to classify the sites at the reference points according to Table 1.2.

The results from the refraction profiles show more detailed information for shallower depths. The SH velocities in the first two layers and the depth to the boundary between them can be obtained with confidence. The accuracy is between 5 and 10 % of the expected depth based on standard deviation from several interpretations for each profile. However, there is no information about the depth to the lower boundaries due to the limited space for deployment of the refraction profile in urban areas. In some cases, serious concerns arose with regard to the presence of low-velocity (inverse) layers below the man-made fill. In these cases, the seismic waves can be trapped in the uppermost layer and interpretation of the refraction survey does not give real picture of the velocity in the ‘hidden’ layer, or the geometry of the soil profile.

5.3. MASW estimation of the velocity model for shallow soil profile

5.3.1. MASW field measurements

The arrangement of 12 geophones for MASW field test is chosen according Eqs. (3.20 to 3.22). The distances from the shot point to the first geophone and between geophones #1, #2 and #3 are 1.25m, between geophones #3 and #4 is 2.5m and all other distances are 5m, as can be noted from Figure 5.4.

After first 1-2 relatively weak impacts, the channels #1 to #3 were ‘frozen’ to avoid saturation during stacking of more intense impacts. Stacking is used to increase the signal-to-noise ratio in an urban environment because of high level of ambient vibrations.

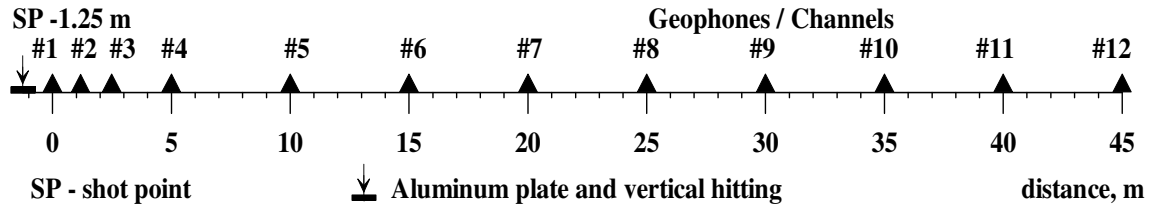


Figure 5.4. Geometry of the MASW field profiles.

The seismic records for MASW were collected using GEODE seismic module with settings described in Ch. 4.1.2. The active seismic source was 8 lb sledge hammer hitting vertically on an aluminum plate 20x20x3 cm.

5.3.2. MASW data processing

The recorded waveforms were processed using software SeisImager/SWTM from Geometrics.

SeisImager/SW is an easy-to-use, powerful program which allows analyzing multi-channel records of surface wave from an active seismic source. It includes functions to perform the following procedures:

- Import and display the recorded data.
- Control parameters for visualization.
- Make changes and corrections to the original data files.
- Calculate, edit and display the dispersion curves.
- Invert recorded waveforms for a one-dimensional shear wave velocity profile.
- Show the results in tabulated and graphical form.

SeisImager is the master program, which consists of three modules for surface wave and refraction data analysis. The individual modules are PickwinTM, PlotrefaTM, and WaveEqTM. Pickwin and WaveEq are used for surface wave data analysis and make up the program SeisImager/SW.

Change in phase velocity with frequency (dispersion), is the fundamental property utilized in surface wave methods (Ch.2.6.2). The shear wave velocity profile can be

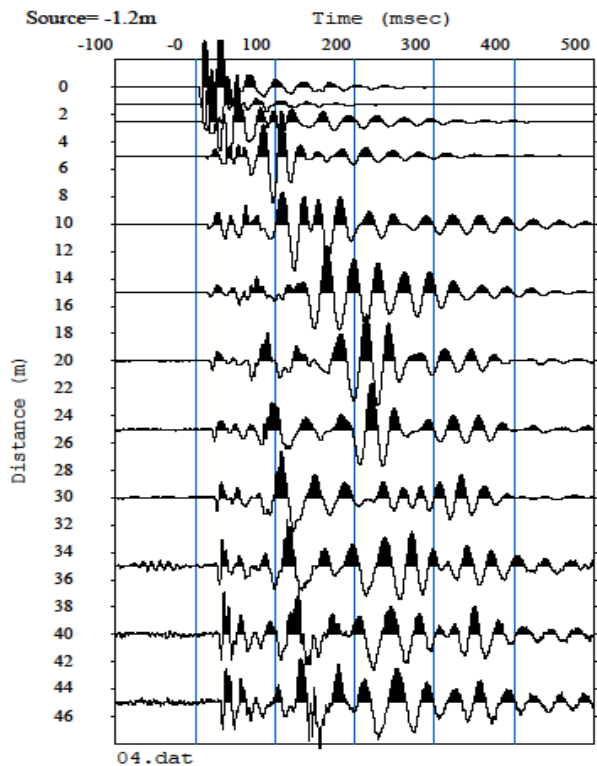
obtained by inverting the dispersive phase velocity of surface waves. Surface wave dispersion depends on velocity layering of the soil structure. There exist different types of surface waves but SeisImager/SW was designed to analyze the Rayleigh wave. The energy or amplitude at any frequency depends on the ratio of depth to wavelength. The lower frequency surface waves travel deeper and contain information about deeper velocity structure. An example for data processing using SeisImager/SW is presented in Figure 5.5a and Figure 5.5b. The MASW field records, dispersions and inversions for all reference test points are presented in the Appendix.

The SeisImager/SW follows the next processing flow:

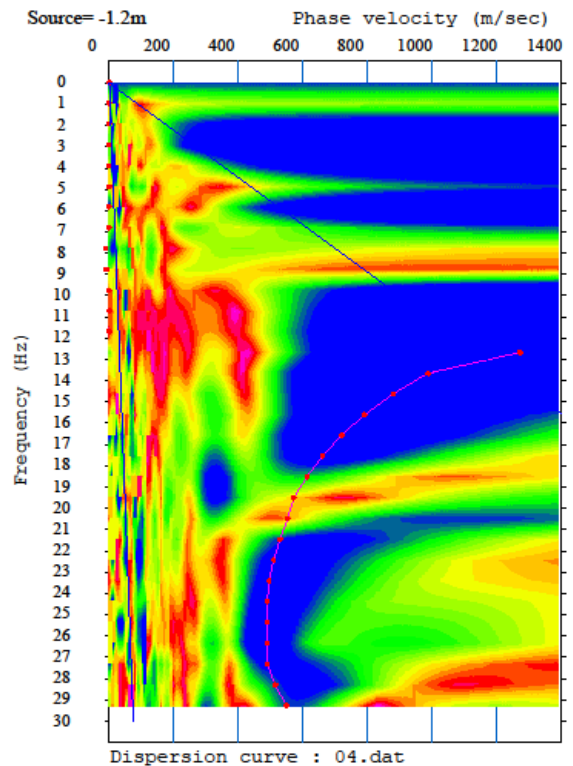
1. Input recorded seismic waveforms. After the file is open, the display settings can be modified to optimize the view on the computer screen. The geometry of MASW field setting can be imported from the file header saved at the time of acquisition or can be put in by hand. At this stage apparent velocity line can be drawn across the faster part of the surface wave package, which shows the maximum surface wave velocity used in the next steps.

2. Calculate the dispersion curve. At this step, SeisImager/SW shows a plot of phase velocity versus frequency. The default view is black shaded wiggle trace. The software automatically picks the mathematical maximum amplitude for each frequency, which defines the dispersion curve. The dispersion curve is more obvious in interpolated color contours. The view can be optimized at this step. Usually the picks need some manual adjustment. Additionally, the dispersion curve can be edited in the WaveEq module if needed. Usually, there are spurious picks on the low and high frequency ends of the curve, which can be removed.

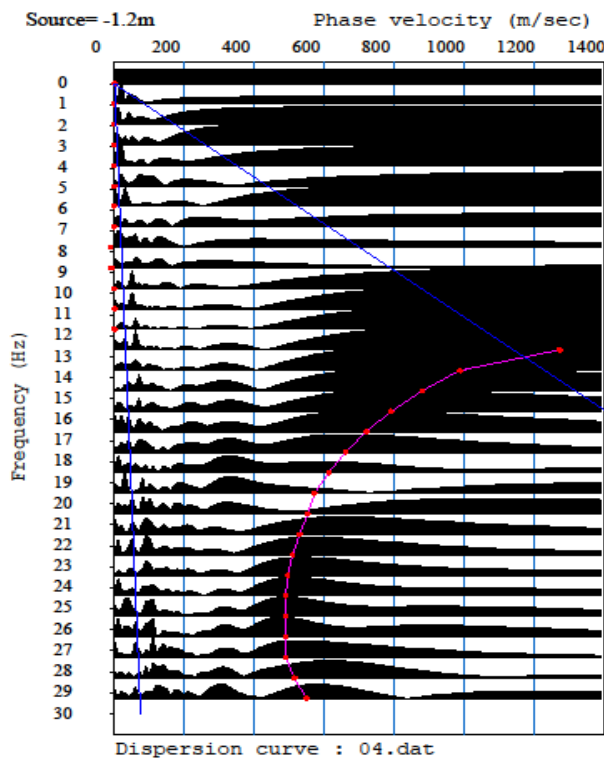
3. Create initial Vs model. The next step is to set-up the initial model of Vs with depth. The depth of penetration can be estimated as one-half the geophone spread. The software default is to calculate the initial model from the one-third-wavelength approximation. The default for the number of layers is 15. At this step the number of iterations for the inversion has to be set. The default number of iterations is 10.



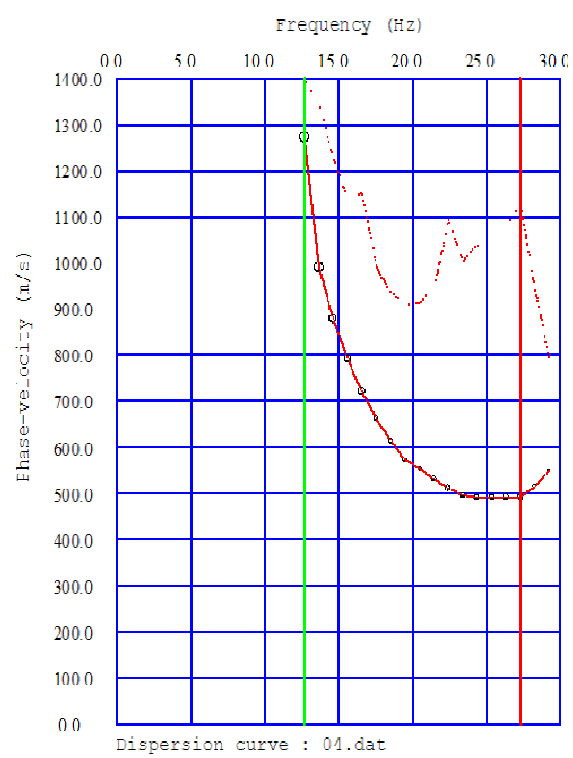
Test Point #4 MASW seismic waveforms



Surface Waves Dispersion - interpolated

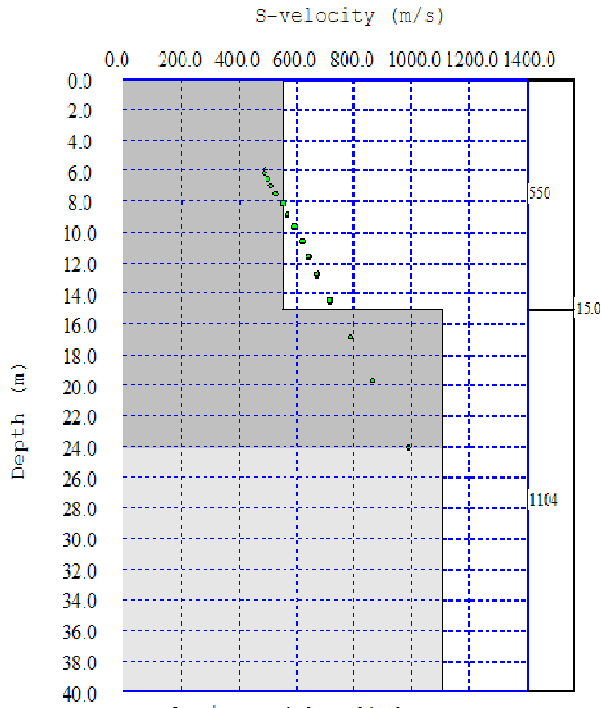


Surface Waves Dispersion



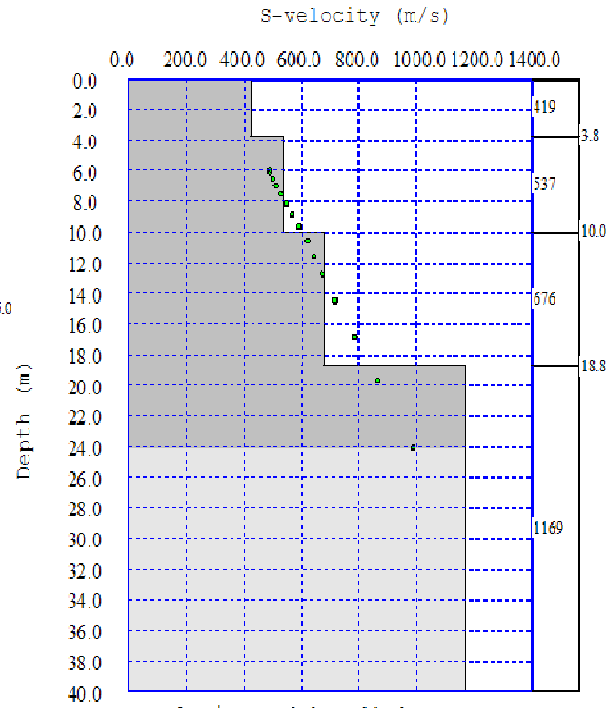
Phase velocity vs. frequency

Figure 5.5a. MASW field records at referent Test point #4 and dispersion curves.



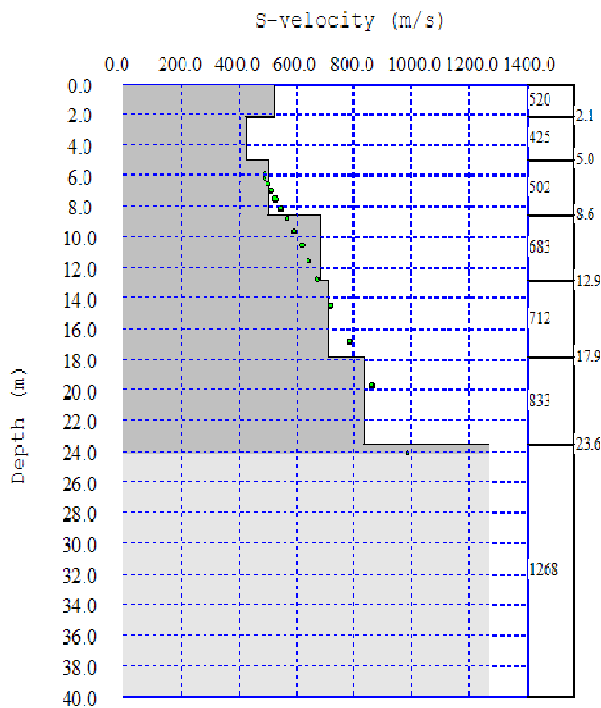
S-velocity model : 04.dat
Average Vs 30m = 734.7 m/s

Test point #4 2-layers inversion



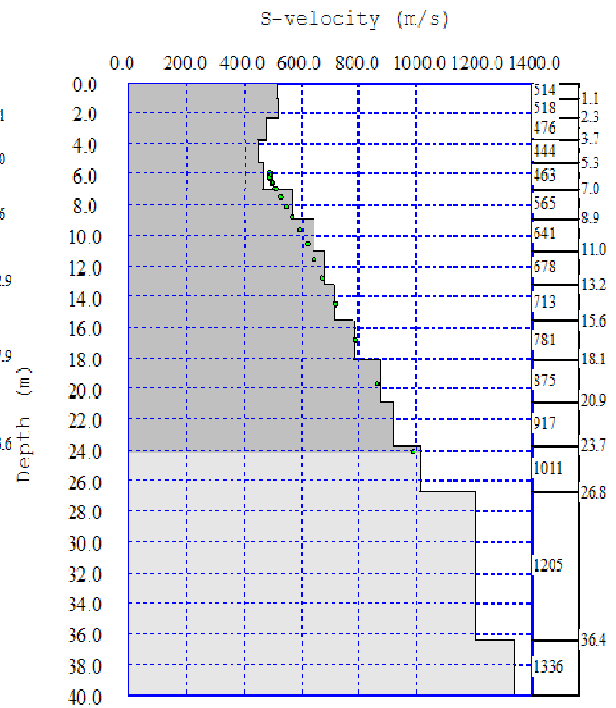
S-velocity model : 04.dat
Average Vs 30m = 695.8 m/s

Test point #4 4-layers inversion



S-velocity model : 04.dat
Average Vs 30m = 695.2 m/s

Test point #4 7-layers inversion



S-velocity model : 04.dat
Average Vs 30m = 696.7 m/s

Test point #4 15-layers inversion

Figure 5.5b. MASW inversion with different starting models for Test point #4.

4. Run inversion analysis to find a V_s model that best fits the dispersion curve obtained in step 2. The apparent velocity model (green points on Figure 5.5b) overlay the one-third-wavelength approximation, which is an indicator of the actual depth of penetration. The velocity model below the deepest green point should not be considered reliable. At this step the result can be saved in a file for further manipulation.

The processing of MASW field data using SeisImager/SW software described above seems to be straightforward in obtaining shear-wave velocity profile. Nevertheless, SeisImager/SW as well the other software which uses velocity inversion requires some preliminary knowledge about the soil structure and its physical and geotechnical properties. This is important for creating the initial velocity model at Step 3. There are parameters that have to be known before using this model in velocity inversion. The number of layers and their thicknesses as well as the water level table should be known in advance. On Figure 5.5b are shown some examples of inversions of the velocity soil profile for four different initial models with different number of layers: 2, 4, 7 and 15. It is obvious that there are significant differences in the results from these inversions. Similar differences can be observed when the depth to the water level table is varied.

To correctly employ SeisImager/SW software with MASW data, some preliminary information should be taken from existing borehole data, geophysical investigation, etc. If geophysical investigations include SH refraction/reflection seismic profiling, the MASW method can be applied only to verify the results from them. In terms of VS-30, MASW in this case can contribute to the result for the soil profile only by estimation of the accuracy of the interpretation of the seismic profiles.

Another problem which appears when comparing the inversion of the soil profiles at the reference points (see the Appendix) is the presence of a higher velocity soil layers in the upper part of the soil structure. This effect is common for multi-layered initial model. If such layers exist two questions arise:

1. How the seismic energy of the surface waves propagates below this layer without being trapped in it? There are some investigations, which demonstrate how the velocity profile below this layer could be unreliable (e.g. Parolai, 2006).

2. How the higher modes of Rayleigh waves propagate in such soil structure? The interpretation of the dispersion curve in this case requires additional information for sediments as well as significant skills to deal with inversion and establishment of reliable initial models of the soil structure.

The processing of the MASW data here was performed using SeisImager/SW with all changeable parameters by default except four different initial velocity models with different number of soil layers.

5.4. Comparison between VS-30 from SH refraction profiling and MASW survey.

The summarized VS-30 velocities from SH refraction profiling and from all calculated MASW models are in Table 5.1.

Results for VS-30 from SH profiling and MASW models **Table 5.1**

Point #	SH profile	MAWS 2 layers	MAWS 4 layers	MAWS 7 layers	MAWS 15 layers	MAWS AVERAGE	MAWS STDEV	MAWS AVE-STD	MAWS AVE+STD
18	262	327	296	295	293	302.8	16.2	286.5	319.0
27	341	339	363	363	361	356.5	11.7	344.8	368.2
14	420	560	502	484	485	507.8	35.8	472.0	543.5
17	463	380	366	362	363	367.8	8.3	359.4	376.1
20	550	438	423	415	409	421.3	12.6	408.7	433.8
31	582	560	577	583	578	574.5	10.0	564.5	584.5
12	600	634	588	595	593	602.5	21.2	581.3	623.7
21	647	554	580	597	583	578.5	17.9	560.6	596.4
32	683	678	528	537	520	565.8	75.2	490.6	640.9
6	728	544	550	544	541	544.8	3.8	541.0	548.5
4	769	734	695	696	697	705.5	19.0	686.5	724.5
35	804	458	505	508	503	493.5	23.8	469.7	517.3
22	946	624	820	768	765	744.3	84.0	660.2	828.3
8	966	808	806	803	797	803.5	4.8	798.7	808.3

The results from SH refraction profiling and MASW processing for each reference point are tabulated in the Appendix.

A comparison between VS-30 from SH refraction profiling and those from MASW inversion over four different initial models is presented on Figure 5.6. The MASW models give VS-30 which is consistent between them but their trend show significant deviations with increasing of the VS-30 value.

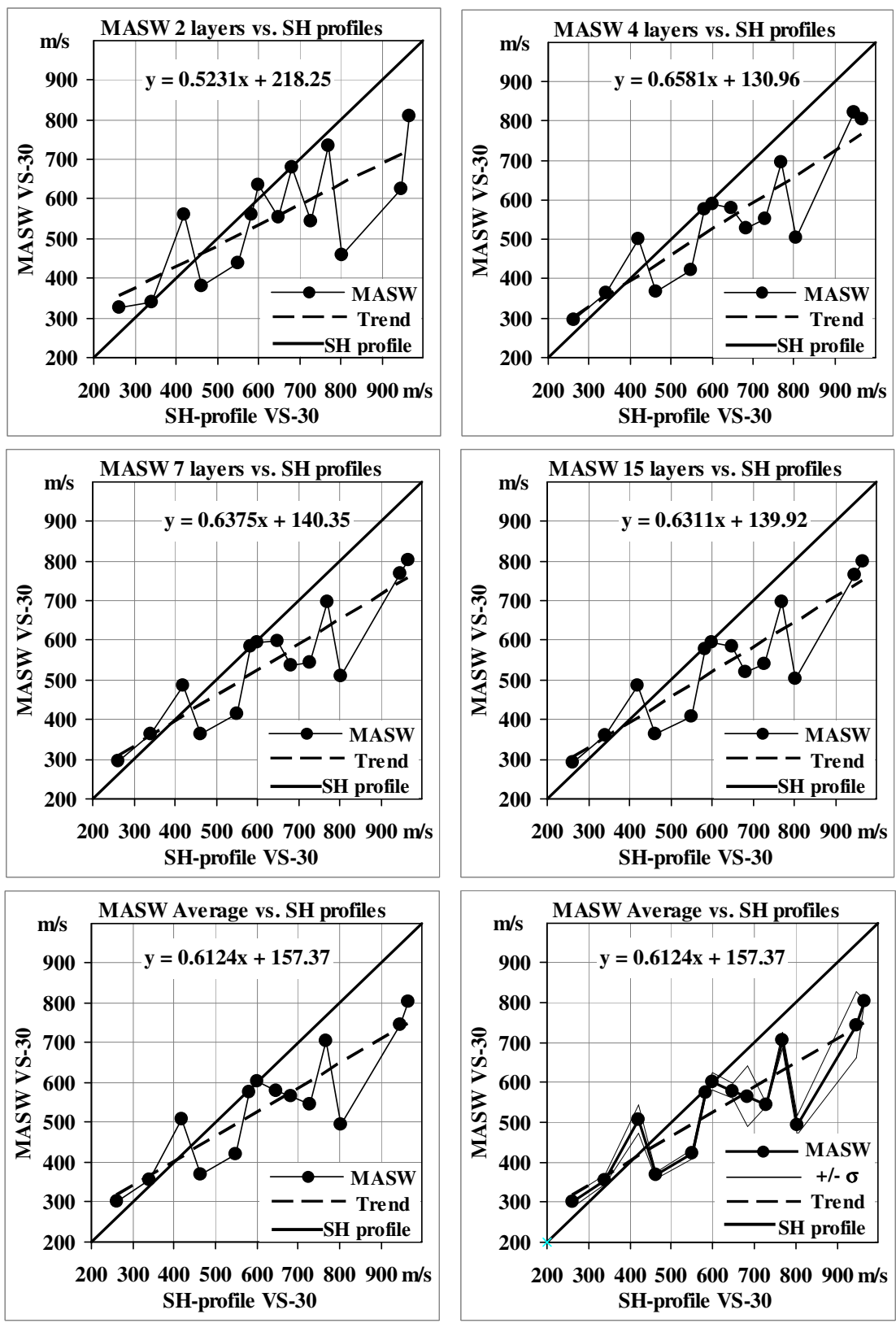


Figure 5.6. Comparison between VS-30 from SH profiling and from MASW inversions for four initial soil models.

The results for soil classification in Chapter 6 are presented using VS-30 from SH refraction profiling because the interpretation do not require preliminary knowledge for the soil parameters and layering as it is the case in MASW processing. Uncertainties in MASW inversion due to lack of preliminary information in city conditions make the results of inversion less reliable.

5.5. HVSR data acquisition and processing

HVSR data recording and processing were done in accordance with internationally accepted SESAME recommendations (SESAME H/V User Guidelines) to ensure correct comparison with the results from other investigations.

5.5.1. Field data acquisition

The equipment for HVSR field recording is described in Ch.4.2. The recording time was 650 seconds with sample rate 100 sps for each test point. A simplified scheme of the equipment for HVSR field measurements is shown on Figure 4.1. The 3-component seismometer L4-3D was installed on a concrete plate 300x300x50 in a shallow hole in the soil surface or on concrete slabs where available. This ensured a leveled, even and stable contact between the seismometer and soil surface. A plastic box was used to cover the seismometer against direct wind influence.

The test site were chosen far enough from the existing buildings and tall structures - at least at distance equal to the height of the closest building. This reduced the influence of the wind induced building vibrations. The data was recorded in ASCII format in EXCEL output file. At least two records separated in time were taken at each reference test point - before and after SH profiling and MASW test. Up to four records at the regular test points were taken to verify repeatability of the HVSR results.

5.5.2. HVSR data processing

The basic equations and the technique behind HVSR Method are described in Ch.3.1.1. The 3-component ambient seismic vibrations recorded at each test point were analyzed using a specially developed EXCEL workbook. The following notations are considered in this analysis: modulus is the sum of absolute values of all components for each time

increment (sample); L/H is Low and High level time series hysteretic thresholds; and Average is the mean value of the Modulus in a running 13-seconds time window. The analysis proceeds in the following sequence:

1. Import a copy of the 3-component field records into EXCEL worksheet.
2. Separate the waveforms into Low and High Level time series (Ch.3.1.3).
3. Divide the time series into 10.24 second time windows (automatically).
4. Put into corresponding cells the appropriate working parameters (Figure 5.6):
 - RMS or averaged vectors (Moduli) of the 3-component waveforms;
 - Time window for averaging of the RMS or Moduli (usually 13 seconds);
 - Manually or iteratively adjust the level for data separation;
 - Manually or iteratively adjust the hysteretic threshold levels (TL+, TL-);
 - The slope of triangle functions for smoothing of the FFT spectra.
5. Start the macros with incorporated VB program for HVSR calculation. The program calculates the individual FFT spectra of each component in 10.24 seconds time windows with 50% overlapping.

An example of the EXCEL INPUT worksheet loaded with necessary parameters and ASCII field data is shown on Figure 5.7.

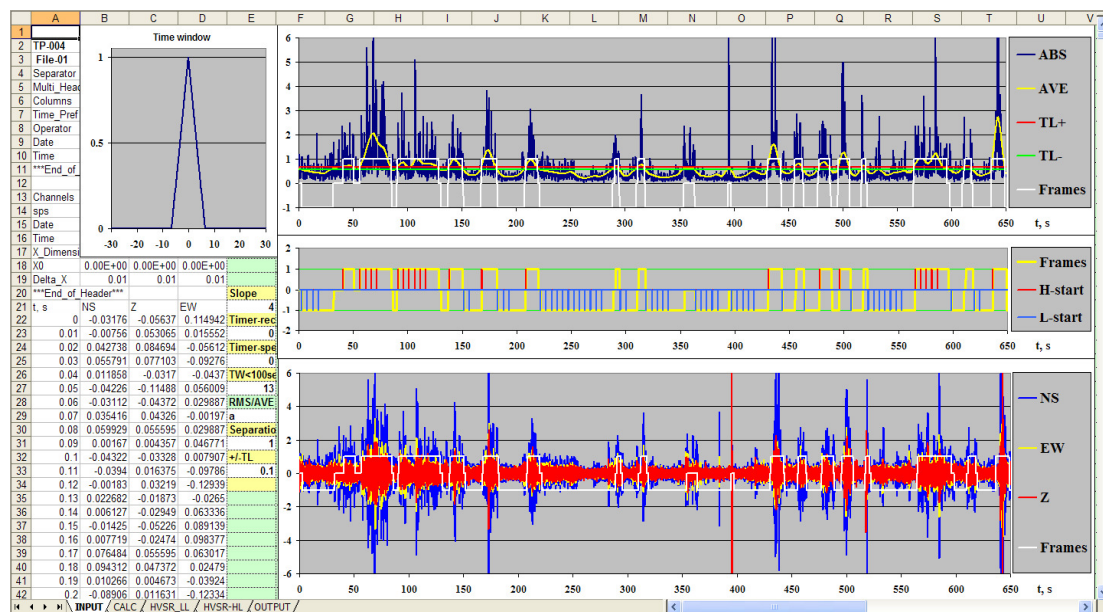


Figure 5.7. INPUT worksheet for HVSR calculations. TL+ and TL- hysteretic thresholds. Frames - the intervals with High (+1) and Low (-1) vibration levels.

The data from the consecutive overlapping time windows are processed automatically as follows:

1. Remove trend and offset from the working (current) 10.24 s time series. This reduces the amplitudes at zero and lowest frequencies calculated with FFT.

2. Apply a Hann window over the current rectangular time window (hanning the time series). The Hann window $W_{Hann}(n)$ can be expressed as a function of sample number in the time series:

$$W_{Hann}(n) = 0.5 \left[1 - \cos\left(\frac{2\pi n}{N-1}\right) \right] = \sin^2\left(\frac{\pi n}{N-1}\right), \quad (5.1)$$

where $n = 0$ to $N-1$ is the sample number and $N = 1024$ samples per window for HVSR.

The Hann window used here is shown on Figure 5.8a. The 3-component 10.24 seconds time series subjected to hanning over the original waveforms are on Figures 5.8b,c,d. The Hann window reduces the spectral “leakage”. The term leakage refers to the fact that some energy has “leaked” out of the original infinite spectrum into the working frequency range. The spectral “leakage” exists because of the sharp start and stop edges of the waveform, which is cut by the initially rectangular time window. Initially, the waveform has sharp edges which require high frequencies in order to have equal energy in both time and frequency domains (Parseval’s theorem). Because these high frequencies are above the Nyquist’s frequency, their energy is mirrored back below Nyquist’s frequency and produce some “spurious” or “phantom” parasitic resonances in the working frequency interval.

Applying a Hann window over time series containing exact 2^n number of samples removes the sharp edges and parasitic resonances. This causes a “sharpening” of the resonances connected to the soil structure and properties. This effect is illustrated on Figure 5.9. To mitigate the “losses of energy” at the edges of the Hann window, the individual series are overlapped 50% in time.

3. Calculate FFT over every corrected and Hann-windowed time series for each component.

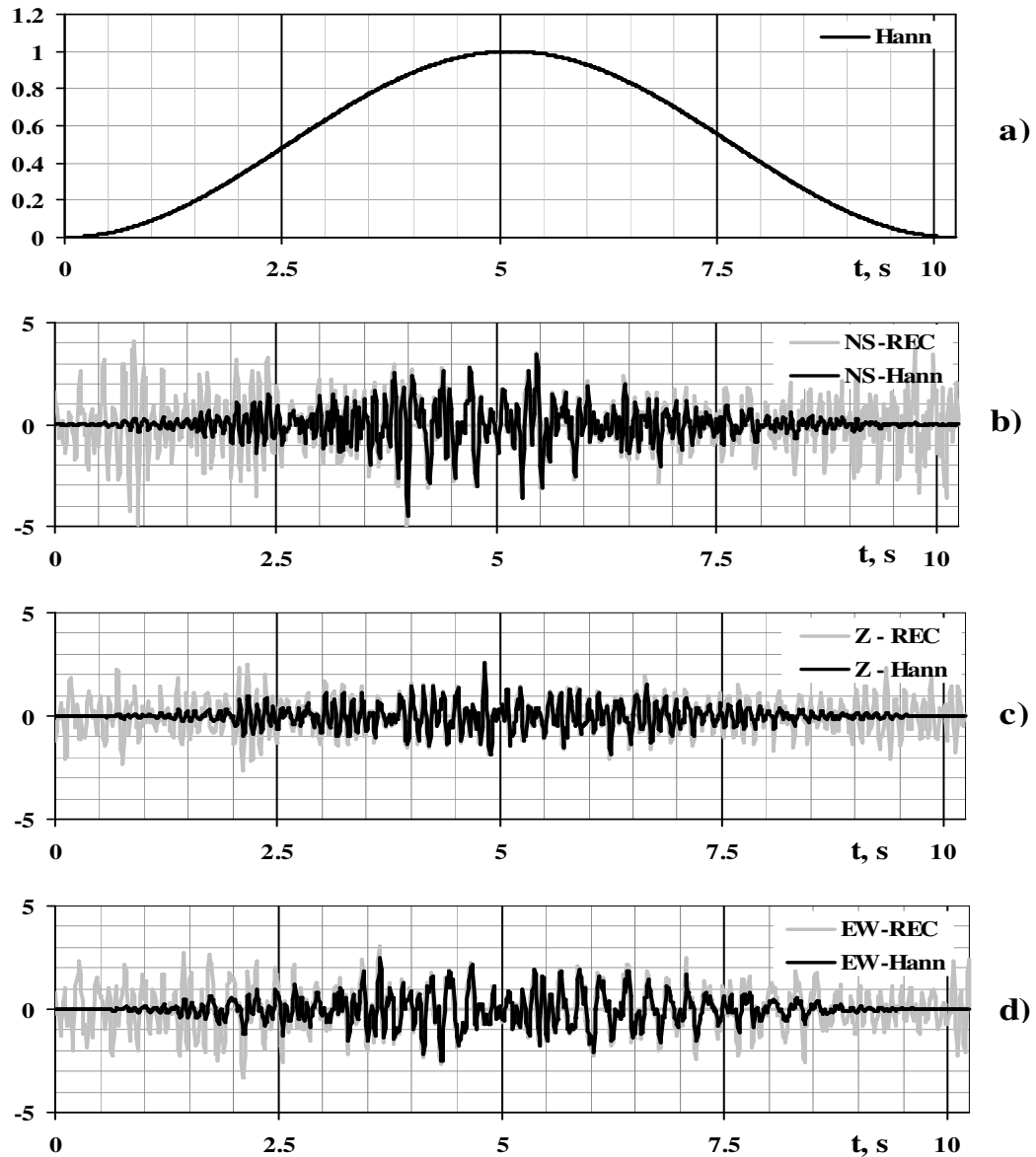


Figure 5.8. Hann window effect. a)The Hann window; b), c), d) - 3 components time series subjected to hanning (black lines) over the original waveforms (grey lines).

4. Apply appropriate corrections to the seismometer transfer function using equation (4.8) for each component and recalculate the current FFT spectrum with the ideal characteristic shown on Figure 4.5. This calculation uses the experimentally determined sensitivities, natural frequencies and damping factors for each component of the used L4-3D seismometers and calibrates the spectrum for the next calculations.

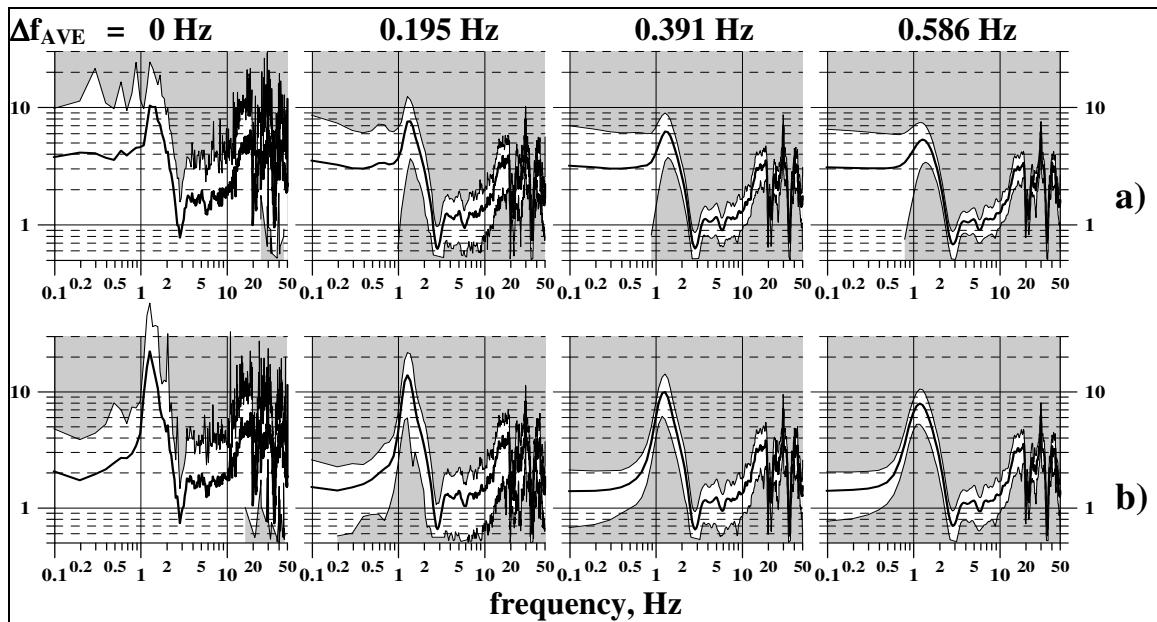


Figure 5.9. HVSR smoothed by triangle function with different width Δf_{AVE}
a) without applying of Hann window; b) using Hann window.

5. Apply averaging (smoothing) of the current FFT spectra with the triangle function which runs over all frequencies of the FFT spectrum of each component.

6. Calculate the current HVSR as a ratio between vector sum of the smoothed horizontal spectra and the smoothed vertical spectrum. This step produces the individual record of HVSR in the corresponding spreadsheet for Low or High Level HVSRs.

7. Repeat automatically steps 1 to 6 with all separated time windows for Low and High vibration levels.

8. Calculate the average HVSR and standard deviation for both Low and High Levels HVSR-s from all ensembles in the corresponding spreadsheets. This step produces two tables and two graphs containing average HVSRs and their dispersion from each 3-component waveforms separated for Low and High Level of ambient vibrations.

The resulting HVSR may have one or more maxima. The boundary between soil structure (overburden) and the bedrock is the deepest interface, and thus the maximum peak of the HVSR plot occurring at the lowest frequency is related to this boundary. More intense resonances could be noted on the HVSR pattern. They are dominant resonances from more contrast boundaries in the overburden and are not connected to the depth to

bedrock. Some typical HVSR patterns are shown on Figure 5.10, where the fundamental frequency is dominant in the HVSR plot (a,b and c) while Fig. 5.10d,e and f show the case when other resonances are dominant.

Figures 5.11 and 5.12 show examples of separation of waveforms and HVSR into low and high levels of ambient vibrations. On the other hand, Figures 5.13 and 5.14 manifest the advantage of separation of waveforms into time intervals with low and high level of ambient vibrations. For example, Figure 5.13 shows the resonance from the low level of ambient vibrations, including 25 ensembles with Low level and 47 ensembles with High level HVSR, which are averaged and the mean values are smoothed by a triangle function (0.25-0.5-1.0-0.5-0.25). Similarly, Figure 5.14 shows the fundamental resonance from the High level of ambient vibrations, including 60 ensembles with Low level and 20 ensembles with High level HVSR, which are averaged and the mean values are smoothed by a triangle function (0.25-0.5-1.0-0.5-0.25).

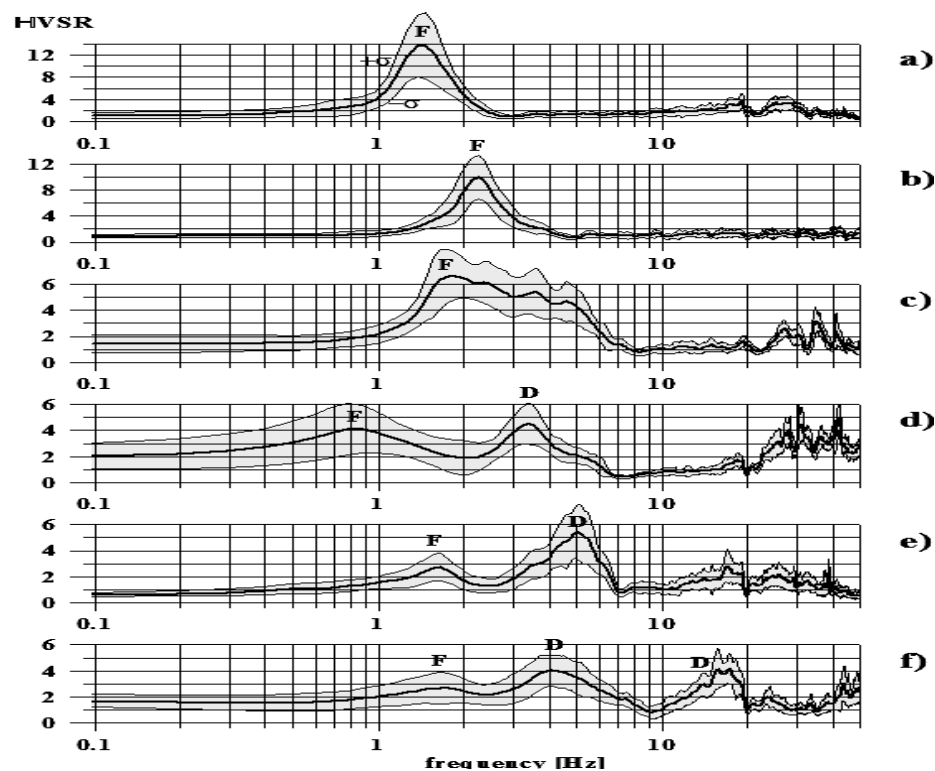


Figure 5.10. Examples of Fundamental (F) and Dominant (D) HVSR resonances:
a, b, c - fundamental resonances are dominant in HVSR;
d, e, f - fundamental resonance has smaller amplitude then the dominant ones.

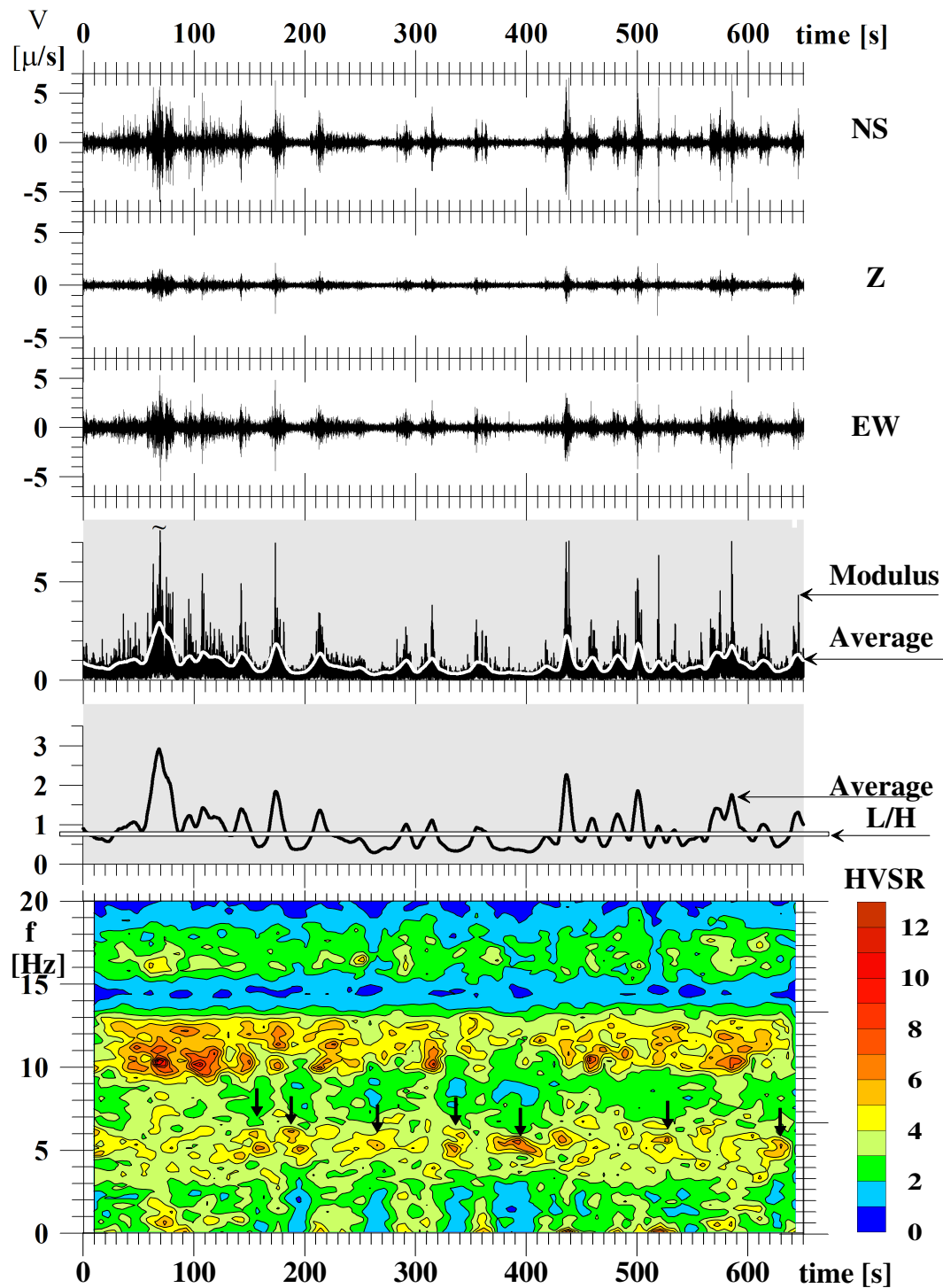


Figure 5.11. Separation of waveforms and HVSR into low and high level ambient vibrations. L/H - the hysteric thresholds. Average is mean value of Modulus in a running 13-seconds time window. The black arrows on f/t plot show maxima for low level HVSR.

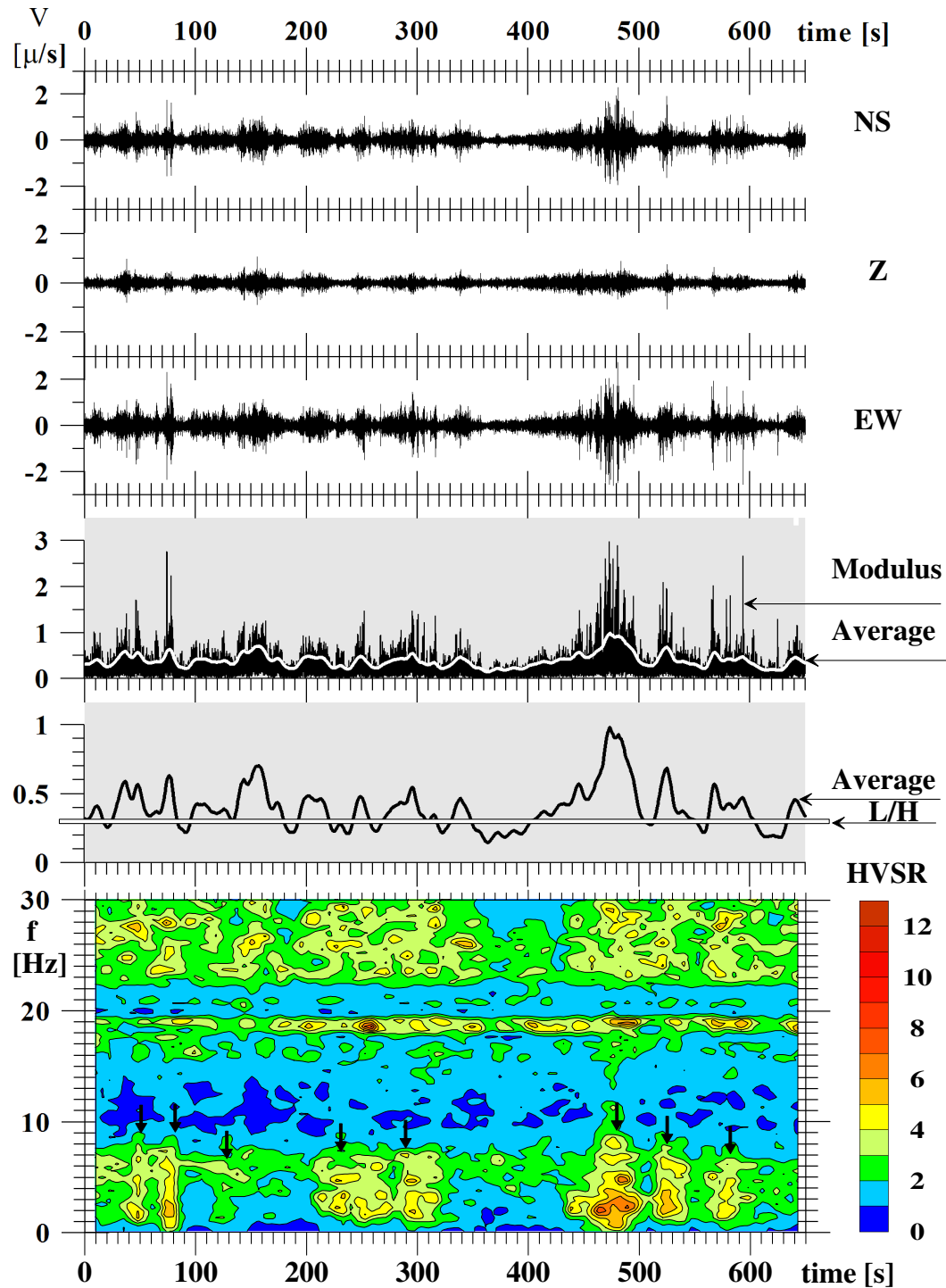


Figure 5.12. Separation of waveforms and HVSR into low and high level ambient vibrations. L/H - the hysteretic thresholds. Average is mean value of Modulus in a running 13-seconds time window. The black arrows on f/t plot show the maxima for the high level HVSR.

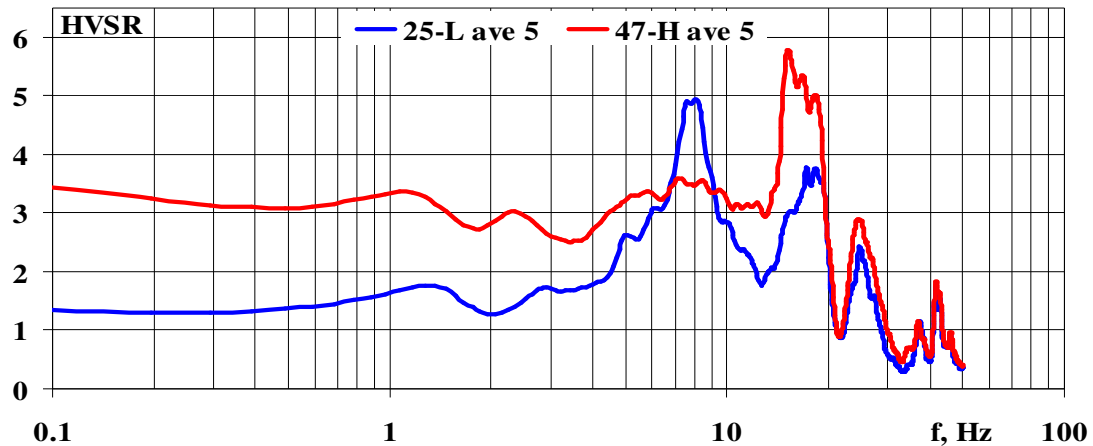


Figure 5.13. HVSR for low and high level of vibrations shown on Figure 5.11.

The resonance is from the Low level ambient vibrations.

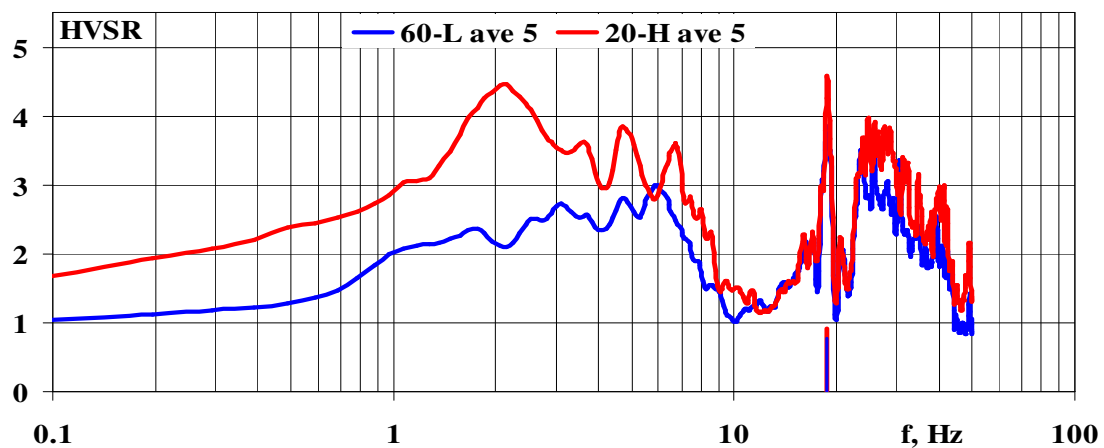


Figure 5.14. HVSR for low and high level of vibrations shown on Figure 5.12.

The fundamental resonance is from the High level ambient vibrations.

The fundamental resonances can be suppressed or hidden by intense Rayleigh waves from local sources when the boundary between overburden and bedrock has low seismic contrast. In this case, the fundamental resonance can be very weak or unstable. More field records are needed to identify credible solutions for all test points with different low and high HVSR resonances. An example for this case is shown in Figure 5.15. Similar graphs for all reference test points are presented in the Appendix.

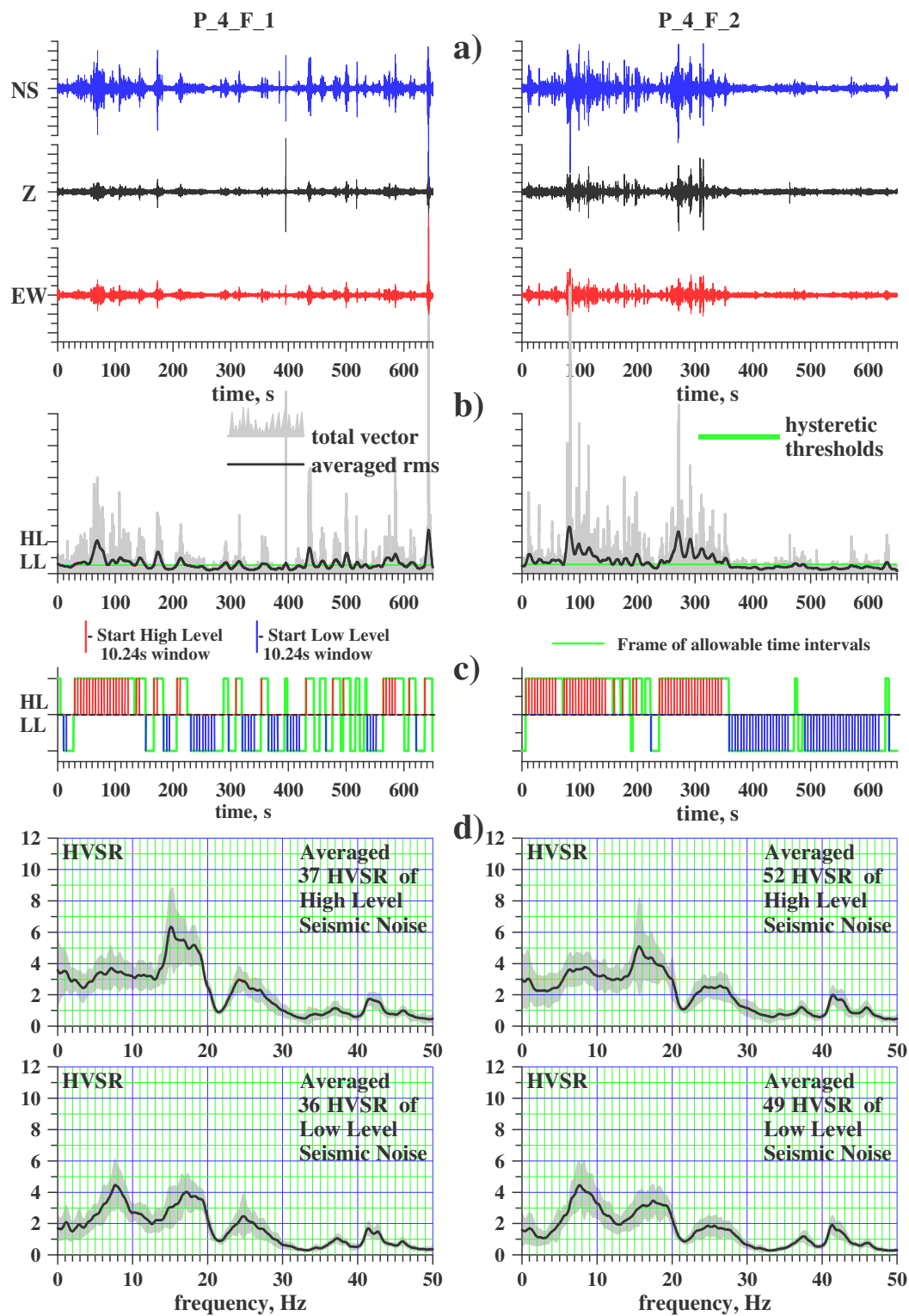


Figure 5.15. HVSR data processing of two field records for test point 4:
a) field records, b) separation of the signal for Low and High vibration levels,
c) start of the windows for the time series, d) HVSR for Low and High levels.

5.6. Comparing HVSR results with theoretical response functions using data from SH refraction profiling

The comparison between HVSR resonances and the theoretical site response using velocities and thicknesses obtained by SH profiling was performed using the Excel program described in Chapter 2.2. The spreadsheet is shown on Figure 5.16. The input parameters used in this spreadsheet are the average velocities in the first two layers and the depth of their interface, obtained from the refraction survey. The procedure involves adjusting iteratively the thickness of the second layer, and the mass density of the two layers until a good match is achieved between the theoretical site response and first resonance of observed HVSR.

The iterative procedure involves the following steps. The first two peaks in the theoretical response are adjusted to fit the observed HVSR peaks by changing the density of the second layer (assuming the shear wave velocity in this layer is known and constant). The fundamental frequency in HVSR is then fit by changing the thickness of the second layer. Once a reasonable match is achieved, the density of the second layer is re-adjusted. The damping values of the top two layers are adjusted after the lowest 2-5 natural frequencies of the theoretical site response fit reasonably the HVSR peaks. The damping factors are adjusted only to compensate for ‘smoothing’ the horizontal and vertical spectra before calculating HVSR. An estimation of the depth to bedrock is possible in case of good match of first four natural frequencies and HVSR. The damping factors established with this procedure are overestimated and should not be used in any further analysis.

Figure 5.17a-d shows the comparison results for four reference test points.

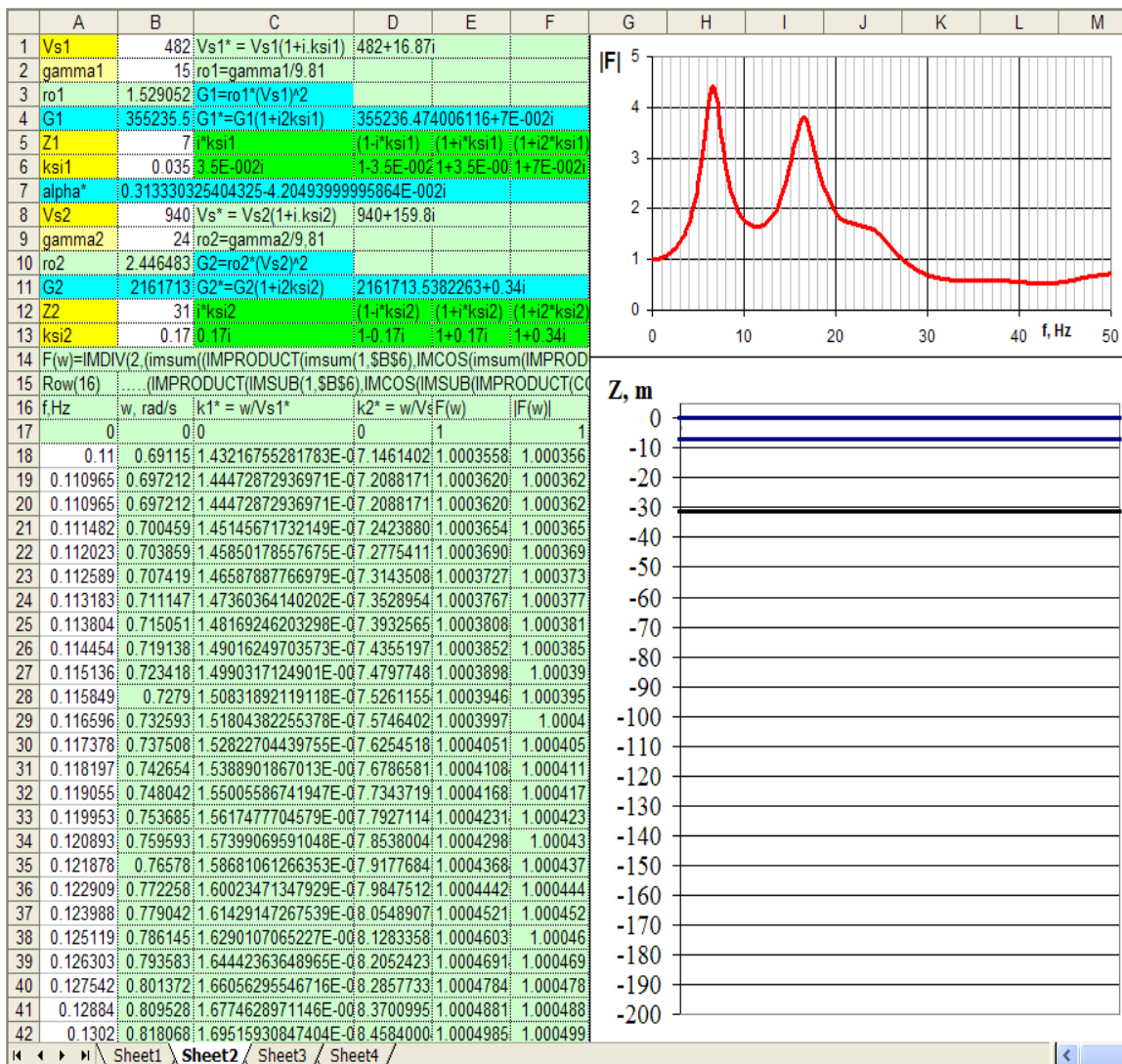


Figure 5.16. Spreadsheet for calculation of theoretical site response of two soil layers overlying bedrock using velocities and depth to the first boundary from SH refraction profiling.

Notations in the Figure 5.16:

Vs1, Vs2 - shear wave velocity in the first and second layer respectively;

gamma1, gamma2 - soil specific weight for the first and second layer;

ro1, ro2 - soil density in the first and second layer;

G1, G2 - shear moduli in both layers;

Z1, Z2 - depths between first two layers and from the surface to the bedrock boundaries;

ksi1, ksi2 - damping factors in corresponding soil layers.

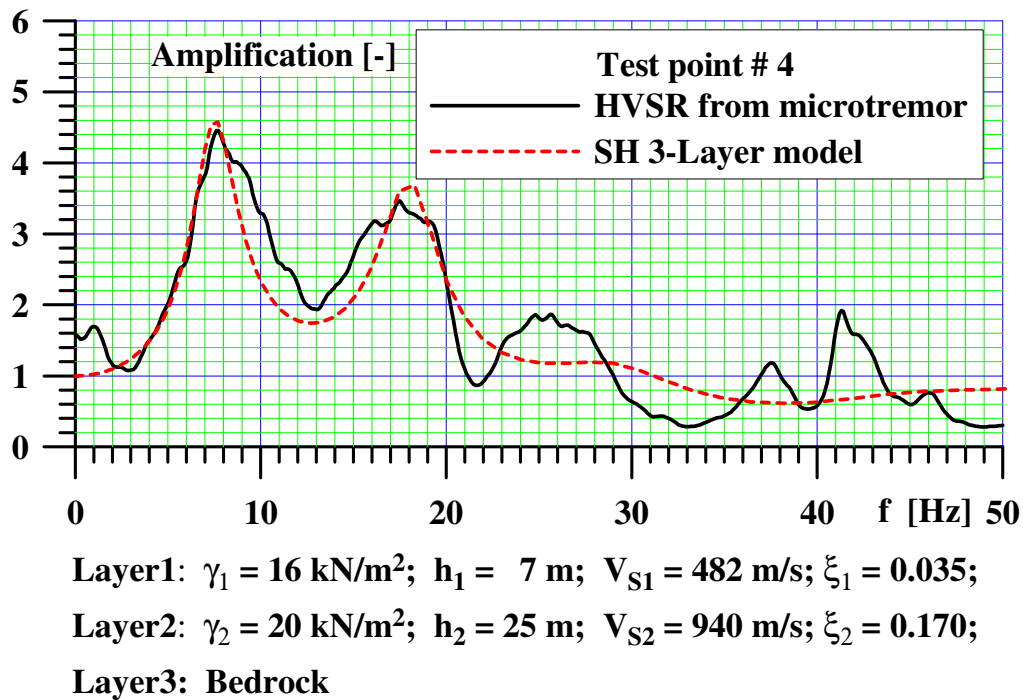


Figure 5.17a. Comparison between HVSR and calculated response for the referent test point #4.

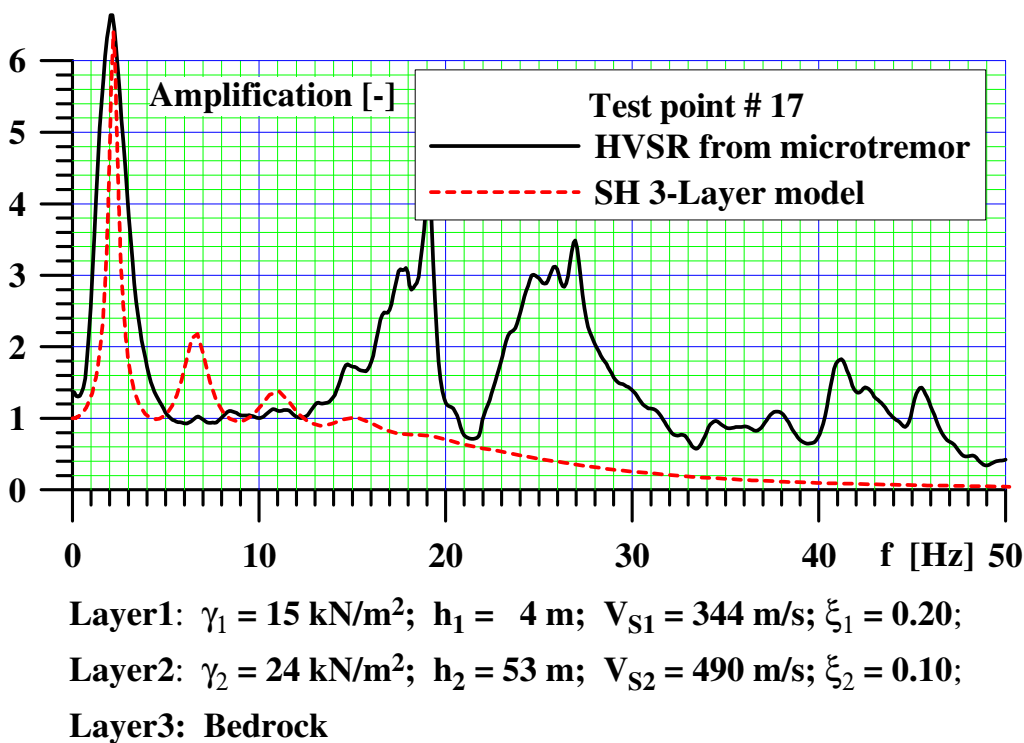


Figure 5.17b. Comparison between HVSR and calculated response for the referent test point #17.

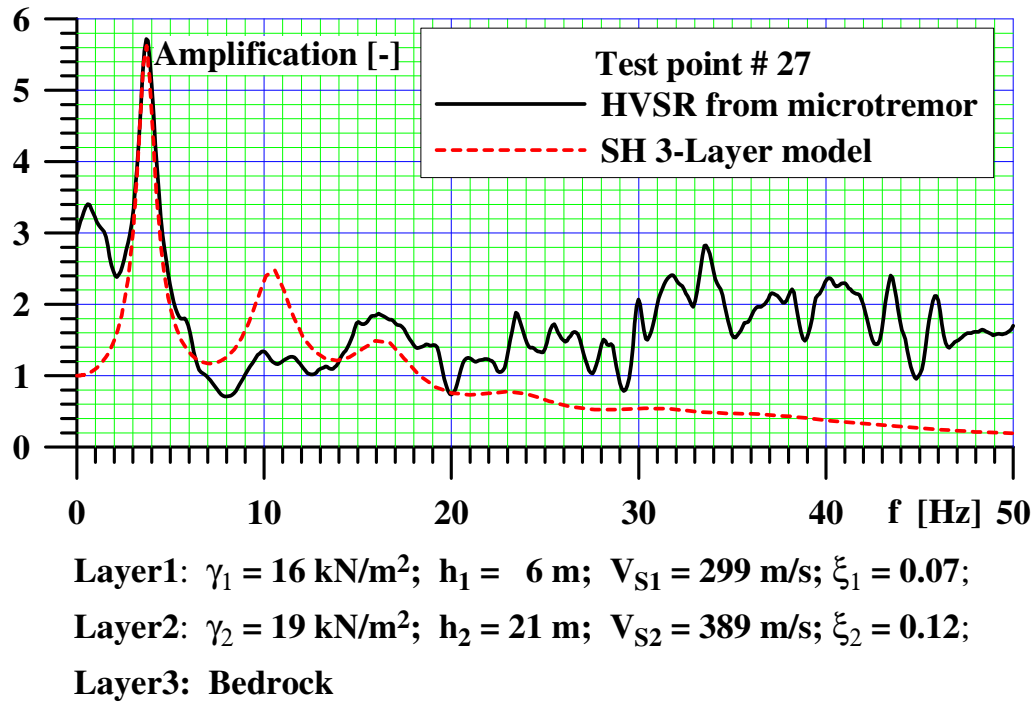


Figure 5.17c. Comparison between HVSR and calculated response for the referent test point #27.

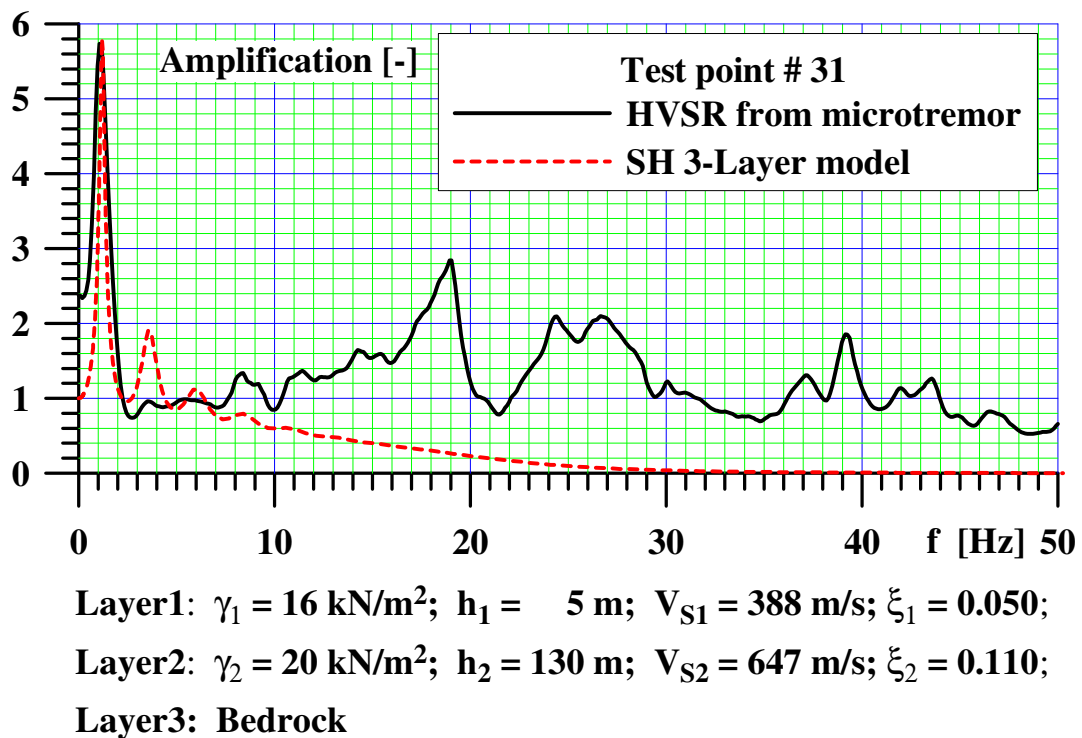


Figure 5.17d. Comparison between HVSR and calculated response for the referent test point #31.

The proposed iterative procedure using data from SH refraction profiling and HVSR allows assessment of depth to the boundary between bedrock and upper sedimentary layers. The elevation of this boundary is required when the NBCC 2005 provisions indicate site specific response analysis for to determine the amplification of ground input motion at the fundamental frequency.

On the other hand, the HVSR method provides information about the resonance frequencies. To estimate a reliable lowest resonant frequency, it is necessary to apply the procedure proposed in this study for separating the noise of close and distant sources. The obtained results confirmed the effectiveness and suitability of the proposed technique in determining the fundamental resonance frequency in the HVSR in urban areas even in the presence of intensive nearby traffic.

For cases where the presence of inverse (low-velocity) layers is a concern, additional methods for determining the boundaries between layers have to be applied. For example, the MASW method can be applied with some caution (SASW/MASW methods require initial model).

Chapter 6

Results from geophysical study for GTA microzonation

The main goals of the geophysical study for the GTA seismic microzonation were to evaluate soil classification at the test sites and to predict site response at these locations. The geophysical methods considered in this study utilized only weak seismic sources like ambient vibrations and sledge hammer impacts. The data were collected during daytime in summers of 2005 and 2006. No small or moderate earthquakes occurred at the time of field measurements in or around the GTA that could be used as stronger sources. The soil resonances which are an important part of the site response analysis were established using Nakamura's HVSR method.

6.1. Summary of the GTA Microzonation Results

The classification of surficial soil deposits according to the NBCC 2005 definition considering the V_s of the upper 30m of soil layers is a challenging task. Without coverage of the entire study area with seismic profiling or MASW estimated velocity profiles, the only available option would be to use the descriptions of surficial soil layers incorporated in the map: "Surficial Geology of the Greater Toronto and Oak Ridge's Moraine Area, Southern Ontario" published by GSC (Sharpe et al., 1997). This map has scattered and deficient information about soil layering and thicknesses. The lithological descriptions allow assigning a soil class to each soil type with some caution because of poorly specified soil properties. Figure 6.1 shows the correspondence between the expected classification and soil lithology for each unit specified in the map. The intermediate classes BC, CD and DE are added for convenience.

The test points at which the V_s soil profile is established by MASW and SH profiling are used as referent points. The other test points are characterized by the HVSR resonances. Additional geological information for each test point was retrieved from the surficial geology map. This information, however, describes only the upper soil layer.

In order to accommodate the soil classes from Figure 6.1 to the different soil units below each test point, the relation between HVSR fundamental and dominant resonances and the depth to the first contrast seismic boundary was used.

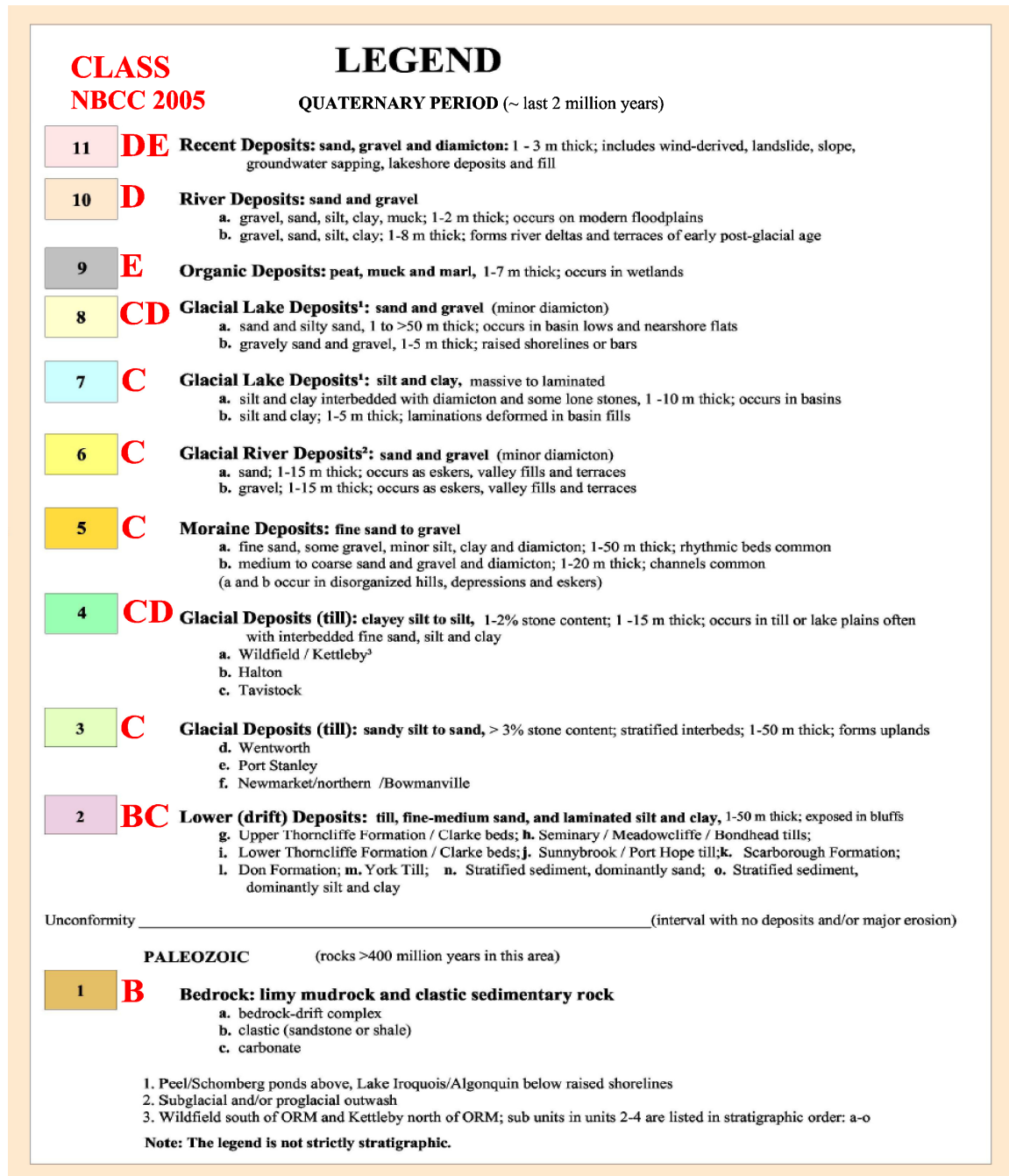


Figure 6.1. Classification of the soil deposits according to NBCC 2005 against the legend to the GSC map (Surficial Geology of the Greater Toronto and Oak Ridges Moraine Area, Southern Ontario); (Sharpe et al., 1997).

The following plausible suggestions were made:

- The dominant resonant frequency provides an estimate of the depth to first contrast seismic boundary given the surface wave velocity in the first soil layer $h = V_s/(4f)$.
- The amplification at the dominant resonant frequency from HVSR is related to the seismic contrast at the boundary between first and second soil layers.
- If the boundary between the first two layers is below 30 m, it would not affect the soil classification.
- The shear wave velocity in the first layer can be assumed between 160 and 600 m/s.
- If the dominant resonant frequency from HVSR is less than 1 Hz, the first boundary would be deeper than 30 m. The deeper soil layers could not change the average shear wave velocity to the top 30 m, which is suggested by NBCC 2005 for soil classification.
- If the dominant resonance is above 10 Hz, the thickness of the first soil layer could be between 4 and 40 m for the V_s from 160 to 600 m/s. The lithological information given in the surficial geology map provides an opportunity to separate the soil deposits into weaker and stronger units using the thickness of the first soil layer, which is less than 30m. In this case, the deeper soil layers would increase the average shear wave velocity estimated from the first layer. This effect allows soil classification for some test points to be improved relative to the preliminary determination from the surficial geology map.

All results from the geophysical field measurements and data processing are summarized in Table 6.1, where the notations areas follow:

F_1 - Fundamental soil resonant frequency, Hz; Amp-1 - HVSR amplification at F_1;

F_2 - Dominant resonant frequency if exists, Hz; Amp-2 - HVSR amplification at F_2;

VS1, VS2 - Shear wave velocities in the first and second soil layers, m/s;

VS-30m - averaged shear wave velocity in the upper 30m soil profile (NBCC 2005), m/s;

H1 - thickness of the first soil layer from V_s profiling, m;

CLASS - soil classification according to NBCC 2005 - classes and subclasses are estimated as it was described in the beginning of this chapter;

Class # - classes and subclasses converted to numerical scale from class B = 1 to E = 7;

Data Source: 1 - Seismic SH profiling, 2 - MASW velocity profile, 3 - classes are correlated using soil types on the surficial geology map from GSC and dominant resonant frequencies and amplifications from HVSR;

Type - RP - reference test point at which data from Vs profiles and MASW, surficial geology and dominant resonant frequency from HVSR are collected for the correlation between classes at the points which are tested with HVSR only and have surficial geology data.

Results from geophysical field investigations and soil classification. Table 6.1

Test Point #	POINT COORDINATES				HVSR test			SH profiling and MASW				CLASS 2005	Class #	Source Data Source	Type ID #	
	LAT degree	LONG degree	NORTHING m	EASTING m	F_1 Hz	Amp-1 -	F_2 Hz	Amp-2 -	VS1 m/s	VS2 m/s	VS-30 m/s					H1 m
1	43.838983	-79.036583	4855862.95	657841.6108	7.62	7	0	0					C =	3	3	1
2	43.634317	-79.4685	4832398.093	623539.0087	1.95	4	0	0	174.0	235.0	226.0	3.5	D =	5	1, 2	RP2
3	43.77255	-79.51355	4847684.711	619629.7343	1.37	3.4	0	0					C =	3	3	3
4	43.54395	-79.728083	4822008.26	602753.1028	7.91	2.7	0	0	482.0	940.0	769.0	7.0	BC =	2	1, 2	RP4
5	43.786117	-79.284867	4849547.362	638003.1902	1.17	4.2	0	0					C =	3	3	5
6	43.88615	-79.244317	4860726.112	641030.1047	1.07	2.2	0	0	474.0	869.0	728.0	7.0	BC =	2	1, 2	RP6
7	43.86425	-79.52995	4857845.884	618128.8809	0.98	4.2	0	0					BC =	2	3	7
8	43.657283	-79.58745	4834778.607	613900.3524	0.78	1.9	0	0	565.0	1266.0	966.0	7.5	B =	1	1, 2	RP8
9	43.66095	-79.842183	4834867.752	593354.2347	10.4	5.1	0	0					BC =	2	3	9
10	43.5535	-79.9147	4822855.204	587663.113	10.2	4.8	0	0					C =	3	3	10
11	43.418517	-79.7696	4808027.321	599604.9646	3.81	1.2	16.9	1.2					C =	3	3	11
12	43.702033	-79.546767	4839805.336	617093.7634	1.33	1.1	6.05	1.1	395.0	739.0	600.0	8.0	BC =	2	1, 2	RP12
13	43.654833	-79.322483	4834904.339	635271.6259	1.95	3.9	0	0					BC =	2	3	13
14	43.738267	-79.20695	4844365.73	644387.7158	1.66	5.9	0	0	289.0	474.0	420.0	6.0	C =	3	1, 2	RP14
15	43.776883	-79.355667	4848406.183	632326.7741	1.75	4.1	0	0					C =	3	3	15
16	43.879583	-79.4003	4859742.321	628514.3187	0.78	1.5	0	0					C =	3	3	16
17	43.810117	-79.425633	4851987.889	626626.025	2.15	4.1	0	0	344.0	490.0	463.0	4.0	C =	3	1, 2	RP17
18	43.720767	-79.409267	4842089.395	628132.9795	1.38	3.8	0	0	171.0	325.0	262.0	8.0	D =	5	1, 2	RP18
19	43.548667	-79.594833	4822705.418	613509.094	11.5	3.1	0	0					DE =	6	3	19
20	43.6469	-79.7354	4833433.003	601987.9407	0.87	1.9	0	0	347.0	684.0	550.0	7.5	C =	3	1, 2	RP20
21	43.6276	-79.723483	4831304.217	602981.9965	0.78	4.1	0	0	388.0	812.0	647.0	7.0	BC =	2	1, 2	RP21
22	43.73655	-79.729017	4843397.671	602350.126	10.2	3.7	0	0	574.0	1310.0	946.0	9.0	B =	1	1, 2	RP22
23	43.4547	-79.662483	4812179.337	608212.0189	10.7	4.3	0	0					DE =	6	3	23
24	43.495583	-79.874933	4816465.658	590962.2332	5.76	4.9	0	0					CD =	4	3	24
25	43.581417	-79.786767	4826098.524	597951.4876	9.47	4.1	0	0					C =	3	3	25
26	43.6402	-79.620767	4832836.133	611245.3554	11.7	6.2	0	0					C =	3	3	26
27	43.7066	-79.650233	4840171.641	608748.6918	3.8	2.5	0	0	269.0	369.0	341.0	6.5	D =	4	1, 2	RP27
28	43.8046	-79.629283	4851083.652	610256.4999	4.01	2.6	0	0					CD =	4	3	28
29	43.703517	-79.3915	4840201.16	629601.2997	1.23	6	0	0					C =	3	3	29
30	43.6949	-79.282667	4839420.016	638390.2196	1.17	5.3	0	0					CD =	4	3	30
31	43.738	-79.292767	4844190.089	637477.7036	1.07	3.6	0	0	388.0	647.0	582.0	5.0	BC =	2	1, 2	RP31
32	43.830117	-79.295	4854417.43	637087.1581	1.37	3.5	0	0	489.0	811.0	683.0	8.5	BC =	2	1, 2	RP32
33	43.822783	-79.143117	4853865.825	649317.4728	1.14	2.7	0	0					C =	3	3	33
34	43.682533	-79.48715	4837725.52	621936.9463	1.27	7.9	0	0					CD =	4	3	34
35	43.602817	-79.6	4828712.342	612990.3865	6.64	2.5	0	0	585.0	990.0	804.0	10.0	B =	2	1, 2	RP35
36	43.49145	-79.781433	4816113.083	598528.5349	0.78	2.8	0	0					CD =	4	3	36
37	43.568267	-79.82275	4824596.29	595067.0328	4.2	3.2	0	0					CD =	4	3	37
38	43.60435	-79.677783	4828779.73	606709.9531	5.07	5.7	0	0					C =	3	3	38
39	43.66685	-79.665317	4835737.206	607604.4324	12.8	2.1	0	0					BC =	2	3	39
40	43.575317	-79.6682	4825567.642	607535.0459	11.3	2.8	0	0					C =	3	3	40
41	43.668733	-79.41625	4836299.527	627680.8765	2.93	4.1	0	0					CD =	4	3	41
42	43.784133	-79.225683	4849427.383	642770.0482	1.46	2.8	0	0					C =	3	3	42
43	43.813217	-79.249467	4852616.883	640787.9181	1.46	6.1	0	0					C =	3	3	43

Table 6.1 (Cont.)

Test Point #	POINT COORDINATES				HVSR test				SH profiling and MASW				CLASS NBCC 2005	Class #	Source Data Source	Type ID #
	LAT degree	LONG degree	NORTHING m	EASTING m	F_1 Hz	Amp-1 -	F_2 Hz	Amp-2 -	VS1 m/s	VS2 m/s	VS-30 m/s	HI m				
44	43.7328	-79.22124	4843733.731	643250.0138	0.97	3.5	0	0					BC =	2	3	101
45	43.71609	-79.24178	4841842.53	641635.2055	1.17	4.4	0	0					BC =	2	3	102
46	43.69886	-79.25578	4839905.059	640547.6708	1.23	7.4	0	0					C =	3	3	103
47	43.70081	-79.25287	4840126.572	640777.5953	1.46	7.3	0	0					C =	3	3	104
48	43.66544	-79.31226	4836099.107	636072.0357	3.32	6.5	0	0					C =	3	3	105
49	43.64429	-79.37221	4833653.534	631284.6547	2.83	5.2	0	0					BC =	2	3	107
50	43.59618	-79.51793	4828090.14	619627.2688	1.86	1.6	25.9	4.1					C =	3	3	108
51	43.57088	-79.56339	4825215.823	616006.4456	1.66	4.2	39.1	3.4					DE =	6	3	109
52	43.39056	-79.71173	4804993.264	604337.7556	9.57	4.3	0	0					DE =	6	3	110
53	43.40607	-79.82516	4806580.089	595126.6436	0.6	1.7	7.2	6.1					C =	3	3	111
54	43.44212	-79.75723	4810663.484	600567.2721	0.68	1.6	0	0					BC =	2	3	112
55	43.4749	-79.72039	4814349.121	603492.528	0.68	3.1	0	0					C =	3	3	113
56	43.51974	-79.70514	4819348.099	604648.4523	0.78	3.3	0	0					C =	3	3	114
57	43.55207	-79.66338	4822992.059	607965.752	13.7	4.3	0	0					BC =	2	3	115
58	43.57282	-79.62958	4825341.021	610657.9877	0.69	3	1.46	3.1					B =	1	3	116
59	43.60015	-79.59637	4828421.085	613288.3626	0.78	3.8	8.01	4.5					DE =	6	3	117
60	43.63121	-79.56618	4831912.289	615665.4915	1.46	2.2	0	0					C =	3	3	118
61	43.64812	-79.51762	4833859.161	619549.3027	5.57	10.3	0	0					D =	5	3	119
62	43.454567	-79.86342	4811923.119	591955.2521	0.59	3.8	0	0					CD =	4	3	120
63	43.540317	-79.78885	4821531.483	597849.8161	8.3	4.5	0	0					CD =	4	3	121
64	43.6114	-79.80268	4829409.836	596618.7351	6.15	2.4	0	0					C =	3	3	122
65	43.65908	-79.75986	4834755.976	599995.0516	11.1	5.1	0	0					C =	3	3	123
66	43.70697	-79.72814	4840113.492	602471.162	9.77	4.7	0	0					C =	3	3	124
67	43.67488	-79.68293	4836606.348	606170.2714	8.79	3.5	0	0					C =	3	3	125
68	43.72533	-79.68018	4842213.016	606302.7655	9.86	4.2	0	0					CD =	4	3	126
69	43.7649	-79.63271	4846669.812	610053.6619	1.66	3.1	9.1	3					C =	3	3	127
70	43.69172	-79.61765	4838562.273	611401.4306	1.31	5.9	6.5	3.5					C =	3	3	129
71	43.58769	-79.73798	4826853.874	601879.8019	1.27	4.1	1.66	2.1					C =	3	3	130
72	43.56157	-79.75814	4823928.442	600295.6682	0.98	3.2	0	0					CD =	4	3	131
73	43.50476	-79.73837	4817643.16	601988.0615	0.68	2.2	0	0					C =	3	3	132
74	43.51911	-79.83271	4819125.565	594339.3562	0.78	1.7	0	0					CD =	4	3	133
75	43.77151	-79.60233	4847444.77	612486.59	0.78	2.2	0	0					C =	3	3	134
76	43.72082	-79.59153	4841829.645	613451.5131	7.13	3.5	0	0					CD =	4	3	135
77	43.7045	-79.78663	4839768.536	597762.723	1.37	2	12.7	8.2					C =	3	3	136
78	43.65281	-79.7889	4834025.03	597663.642	1.37	2	0	0					C =	3	3	137
79	43.67973	-79.72268	4837094.896	602957.6656	6.54	1.6	18.3	3.7					C =	3	3	138
80	43.48735	-79.81164	4815622.427	596092.597	2.05	5.2	13.4	7.2					CD =	4	3	139
81	43.5717	-79.69775	4825128.122	605155.3295	6.05	1.7	0	0					C =	3	3	140
82	43.61522	-79.63678	4830040.465	609999.329	9.18	6.7	0	0					C =	3	3	141
83	43.53057	-79.61756	4820664.779	611706.605	5.37	3.6	0	0					CD =	4	3	142
84	43.49167	-79.617	4816345.298	611823.6669	15.3	7.1	0	0					C =	3	3	143
85	43.50136	-79.66023	4817364.293	608310.9083	0.78	2.8	18.8	2.2					B =	1	3	144
86	43.42455	-79.68409	4808803.077	606516.771	0.68	2.3	0	0					CD =	4	3	145
87	43.3645	-79.7657	4802033.001	600009.4801	7.12	3.2	17.6	9.8					BC =	2	3	146
88	43.32048	-79.80734	4797095.226	596705.4146	0.49	2.1	0	0					BC =	2	3	147
89	43.34424	-79.84052	4799696.026	593978.3826	5.18	6.2	0	0					C =	3	3	148
90	43.63222	-79.65782	4831900.864	608271.0589	1.17	2.8	0	0					C =	3	3	149
91	43.64762	-79.6988	4833558.593	604938.4423	4.78	2.6	0	0					C =	3	3	150
92	43.69458	-79.58083	4838930.036	614363.2893	0.68	5.6	0.98	2					CD =	4	3	151
93	43.68145	-79.51922	4837558.588	619354.1978	0.78	4.2	8.6	6.2					D =	5	3	152
94	43.70722	-79.44473	4840530.594	625304.6452	1.27	8.8	23	3.1					C =	3	3	153
95	43.75464	-79.43268	4845815.555	626175.882	1.46	10.1	0	0					C =	3	3	154
96	43.73567	-79.50322	4843603.621	620535.1203	0.68	2.1	4.78	7.1					C =	3	3	155
97	43.67872	-79.81244	4836875.225	595724.1653	1.46	1.5	15.2	1.5					C =	3	3	156
98	43.63166	-79.87469	4831578.689	590777.2971	6.15	5.1	0	0					C =	3	3	157
99	43.58848	-79.86615	4826792.436	591531.6796	6.05	2.9	0	0					C =	3	3	158
100	43.54667	-79.88081	4822132.953	590410.7435	8.4	3.8	0	0					C =	3	3	159
101	43.4078	-79.86682	4806725.525	591750.8015	1.27	2.1	18.8	1.5					C =	3	3	160
102	43.43387	-79.7319	4809778.141	602630.9869	1.8	2.1	5.4	3.5					BC =	2	3	161
103	43.34534	-79.88294	4799771.298	590538.4877	0.78	1.7	29.7	3.5					C =	3	3	162
104	43.37657	-79.82529	4803303.751	595162.2684	0.58	2.2	11.7	2.2					C =	3	3	163
105	43.39453	-79.78024	4805350.721	598782.5906	0.58	2	16.2	3					C =	3	3	164

Table 6.1 (Cont.)

Test Point #	POINT COORDINATES				HVSr test				SH profiling and MASW				CLASS NBCC 2005	Class #	Source Data Source	Type ID #
	LAT degree	LONG degree	NORTHING m	EASTING m	F_1 Hz	Amp-1 -	F_2 Hz	Amp-2 -	VS1 m/s	VS2 m/s	VS-30 m/s	H1 m				
106	43.7589	-79.19086	4846685.511	645633.3515	1.56	9.2	0	0					DE =	6	3	201
107	43.7627	-79.15291	4847174.999	648678.9093	3.03	10.2	0	0					D =	5	3	202
108	43.78471	-79.13473	4849652.364	650087.2299	3.42	6.5	0	0					DE =	6	3	203
109	43.79717	-79.11578	4851070.787	651580.5425	4.69	4.5	0	0					CD =	4	3	204
110	43.81504	-79.09887	4853086.661	652895.3254	6.93	3.1	0	0					CD =	4	3	205
111	43.82969	-79.0698	4854767.932	655195.3014	1.27	2.2	0	0					CD =	4	3	206
112	43.81168	-79.05282	4852799.619	656607.6672	1.37	4.6	47.1	4.3					D =	5	3	207
113	43.85748	-79.08799	4857820.52	653661.3593	4.49	1.6	0	0					CD =	4	3	208
114	43.87064	-79.4359	4858694.302	625673.1073	2.3	2.3	7.81	4.3					C =	3	3	209
115	43.89132	-79.0456	4861658.734	656979.2534	5.47	4.7	0	0					C =	3	3	210
116	43.92035	-79.03041	4864912.032	658122.4536	4.69	6.7	0	0					C =	3	3	211
117	43.89101	-79.08316	4861553.616	653963.1516	3.22	5.6	0	0					E =	6	3	212
118	43.9133	-79.09404	4864009.11	653032.1137	2.15	5.3	0	0					DE =	6	3	213
119	43.8389	-79.2607	4855450.352	639824.5022	1.76	5.8	0	0					CD =	4	3	214
120	43.83407	-79.23336	4854960.491	642033.8881	1.46	7.8	0	0					C =	3	3	215
121	43.84481	-79.18814	4856232.007	645643.3891	2.44	4.3	17.2	9.1					C =	3	3	216
122	43.88367	-79.0913	4860723.238	653328.1603	4	5.1	0	0					C =	3	3	217
123	43.93541	-79.12583	4866406.416	650423.8708	1.27	4.2	0	0					C =	3	3	218
124	43.94619	-79.18569	4867496.398	645593.0303	1.66	3.8	0	0					C =	3	3	219
125	43.91719	-79.21948	4864216.358	642950.917	1.76	3.2	0	0					CD =	4	3	220
126	43.9014	-79.16472	4862558.845	647386.4123	1.46	6.9	0	0					C =	3	3	221
127	43.88543	-79.20646	4860711.459	644072.849	1.17	5.9	0	0					C =	3	3	222
128	43.867704	-79.129093	4858880.489	650332.3067	2.34	11.2	0	0					C =	3	3	223
129	43.824721	-79.196715	4853985.715	645002.7441	3.71	9.8	0	0					C =	3	3	224
130	43.806566	-79.211599	4851943.318	643849.4896	1.56	6.8	0	0					C =	3	3	225
131	43.789228	-79.16721	4850095.78	647462.6057	2.05	8.9	0	0					CD =	4	3	226
132	43.778196	-79.201412	4848810.133	644737.3641	2.15	7.1	0	0					C =	3	3	227
133	43.779131	-79.200011	4848916.43	644847.8502	2.25	8.4	0	0					BC =	2	3	228
134	43.762156	-79.219618	4846996.969	643310.5625	1.37	5.7	0	0					C =	3	3	229
135	43.745132	-79.248629	4845056.396	641015.2916	1.37	5.3	0	0					C =	3	3	230
136	43.770972	-79.247352	4847928.501	641057.3778	1.27	6.9	0	0					C =	3	3	231
137	43.789483	-79.246587	4849985.743	641075.4017	1.37	8.1	0	0					C =	3	3	232
138	43.772043	-79.693768	4847383.819	605126.529	5.12	2.6	0	0					BC =	2	3	233
139	43.838571	-79.582075	4854920.646	613989.1419	1.76	7.2	0	0					BC =	2	3	234
140	43.822479	-79.532118	4853203.439	618037.0145	0.88	3.7	0	0					C =	3	3	235
141	43.748057	-79.548274	4844914.821	616882.7963	2.25	7.3	0	0					CD =	4	3	236
142	43.728433	-79.548299	4842735.26	616918.9706	2.54	5.5	0	0					C =	3	3	237
143	43.660211	-79.54474	4835163.312	617338.5868	0.49	4.7	5	5.5					C =	3	3	238
144	43.634982	-79.397217	4832580.506	629287.7246	1.31	3.4	5.07	14					BC =	2	3	240
145	43.648479	-79.414433	4834052.851	627870.3499	12.6	6.1	0	0					BC =	2	3	241
146	43.64843	-79.415052	4834046.456	627820.5331	6.05	4.1	0	0					BC =	2	3	242
147	43.780393	-79.449827	4848649.835	624741.917	1.36	8.1	0	0					C =	3	3	243
148	43.774334	-79.408077	4848040.645	628114.5031	1.46	8.7	0	0					C =	3	3	244
149	43.732983	-79.343435	4843550.048	633408.6686	1.86	5.3	0	0					C =	3	3	245
150	43.749635	-79.317557	4845441.493	635455.1777	1.37	6.8	0	0					C =	3	3	246
151	43.761231	-79.285454	4846782.405	638013.1956	1.27	6.7	0	0					C =	3	3	247
152	43.747296	-79.381654	4845078.891	630299.6754	1.86	6.6	0	0					C =	3	3	248
153	43.727621	-79.379183	4842897.583	630541.3766	2.14	8.9	0	0					BC =	2	3	249
154	43.70834	-79.349667	4840803.07	632961.2799	1.76	6.5	0	0					BC =	2	3	250
155	43.699697	-79.322848	4839886.509	635141.4371	1.76	4.7	0	0					BC =	2	3	251
156	43.718795	-79.274412	4842087.712	639000.2089	1.27	9.2	0	0					C =	3	3	252
157	43.681659	-79.336801	4837860.488	634057.3007	1.95	5.9	0	0					DE =	6	3	253
158	43.676645	-79.372204	4837246.998	631214.6373	2.15	6.8	0	0					CD =	4	3	254
159	43.661538	-79.374704	4835565.21	631045.9855	3.61	8.1	0	0					CD =	4	3	255
160	43.680714	-79.393725	4837665.095	629471.082	2.34	4.1	0	0					CD =	4	3	256
161	43.695003	-79.41444	4839219.956	627771.0212	1.56	8.8	0	0					C =	3	3	257
162	43.681784	-79.434723	4837720.75	626164.2248	1.86	7.2	0	0					C =	3	3	258
163	43.664374	-79.44819	4835766.738	625114.9198	3.71	3.8	0	0					CD =	4	3	259
164	43.710758	-79.482993	4840866.414	622214.6554	1.95	5.9	0	0					C =	3	3	260
165	43.726858	-79.444727	4842711.676	625263.9607	1.17	5.1	0	0					C =	3	3	261

Table 6.1 (Cont.)

Test	POINT COORDINATES				HVSr test				SH profiling and MASW				CLASS	Class	Source	Type
Point #	LAT degree	LONG degree	NORTHING m	EASTING m	F_1 Hz	Amp-1 -	F_2 Hz	Amp-2 -	VS1 m/s	VS2 m/s	VS-30 m/s	H1 m	NBCC 2005	#	Data Source	ID #
166	43.760253	-79.474052	4846376.769	622833.7395	1.46	5.3	0	0					C =	3	3	262
167	43.807856	-79.483641	4851649.633	621965.0067	1.07	5.1	0	0					CD =	4	3	263
168	43.832995	-79.462914	4854472.481	623580.2787	1.17	6.9	0	0					C =	3	3	264
169	43.861903	-79.422176	4857744.869	626794.3448	1.27	3.7	0	0					CD =	4	3	265
170	43.798039	-79.392115	4850698.276	629347.966	1.95	7.9	0	0					C =	3	3	266
171	43.814565	-79.366599	4852573.949	631364.4198	1.66	7.1	0	0					C =	3	3	267
172	43.853369	-79.396693	4856836.427	628860.5694	1.46	4.3	0	0					CD =	4	3	268
173	43.863992	-79.357588	4858077.984	631980.1011	1.76	7.2	0	0					CD =	4	3	269
174	43.826929	-79.335399	4853997.184	633846.0426	1.37	5.1	0	0					C =	3	3	270
175	43.857432	-79.307964	4857429.814	635982.7219	3.13	5.7	0	0					CD =	4	3	271
176	43.86584	-79.27582	4858417.043	638546.571	2.05	4.8	0	0					CD =	4	3	272
177	43.80887	-79.28506	4852074.125	637935.2944	1.37	6.9	0	0					C =	3	3	273
178	43.794505	-79.311088	4850435.601	635874.357	1.46	7.7	0	0					C =	3	3	274
179	43.799283	-79.351041	4850901.458	632649.4928	1.37	7.4	0	0					C =	3	3	275
180	43.846747	-79.504952	4855937.912	620172.8181	0.98	7.7	0	0					BC =	2	3	276
181	43.873803	-79.45851	4859011.477	623849.8572	0.98	5.4	0	0					C =	3	3	277
182	43.88446	-79.4139	4860262.936	627411.3338	1.17	6.7	0	0					C =	3	3	278
183	43.891132	-79.343422	4861115.066	633058.0336	1.66	5.8	0	0					BC =	2	3	279
184	43.88959	-79.303689	4861008.557	636252.9823	1.76	7.9	0	0					C =	3	3	280
185	43.909579	-79.251136	4863316.705	640427.2518	1.76	7.5	0	0					C =	3	3	281
186	43.92423	-79.16168	4865099.965	647574.1043	0.98	1.9	0	0					C =	3	3	282
187	43.89647	-79.1219	4862088.578	650837.6704	1.66	3.7	0	0					C =	3	3	283

GIS files from Table 6.1 are converted into ESRI format. Location information for the data sets is stored in North American Datum 83 (NAD 83). This database can later facilitate incorporating the info into a HZAU-MH framework in order to evaluate the seismic hazard level of the GTA. In addition, it can be utilized, along with further analyses, to evaluate the liquefaction hazard and potential ground deformations, which can have a significant impact on the buried infrastructure in the GTA.

6.2. Maps using GIS and Surfer software

The maps produced from data in Table 6.1 in GIS and Surfer formats were converted to raster format with equal cell size 0.5x0.5 km, cropped to the investigated area and imported in the layers with NAD_1983_UTM_Zone_17N coordinate system with linear unit meter. The same coordinate system was used with Surfer software for triangulation and linear interpolation. The original maps established from this work are compared to the maps with sources indicated on the corresponding figure. All maps are spatially referenced by the same coordinates in UTM projection.

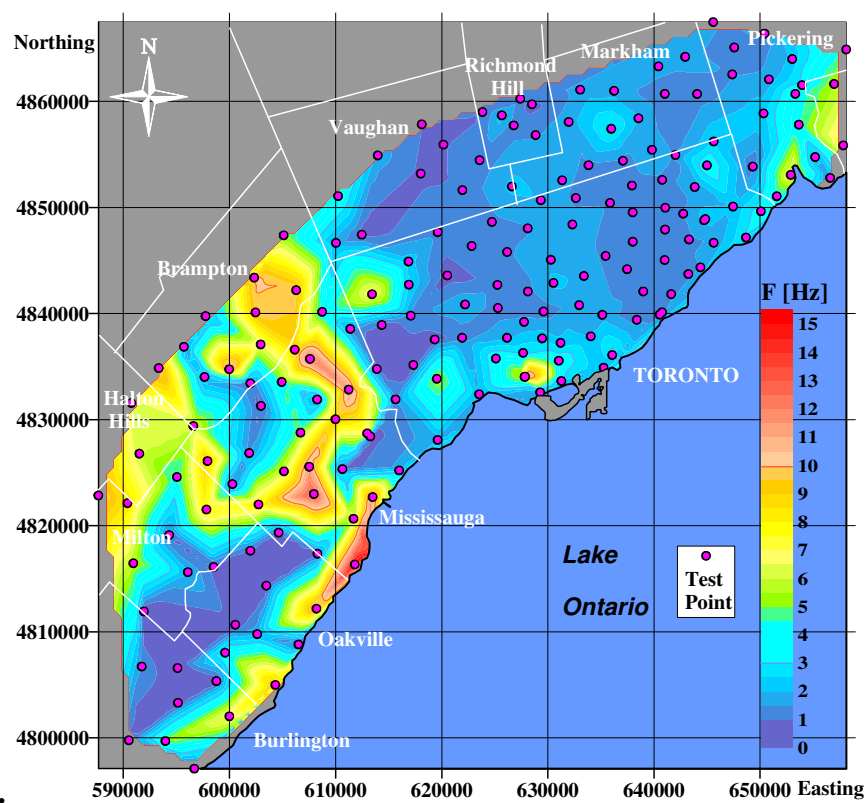


Figure 6.2. Fundamental soil resonant frequencies in GTA (this study).

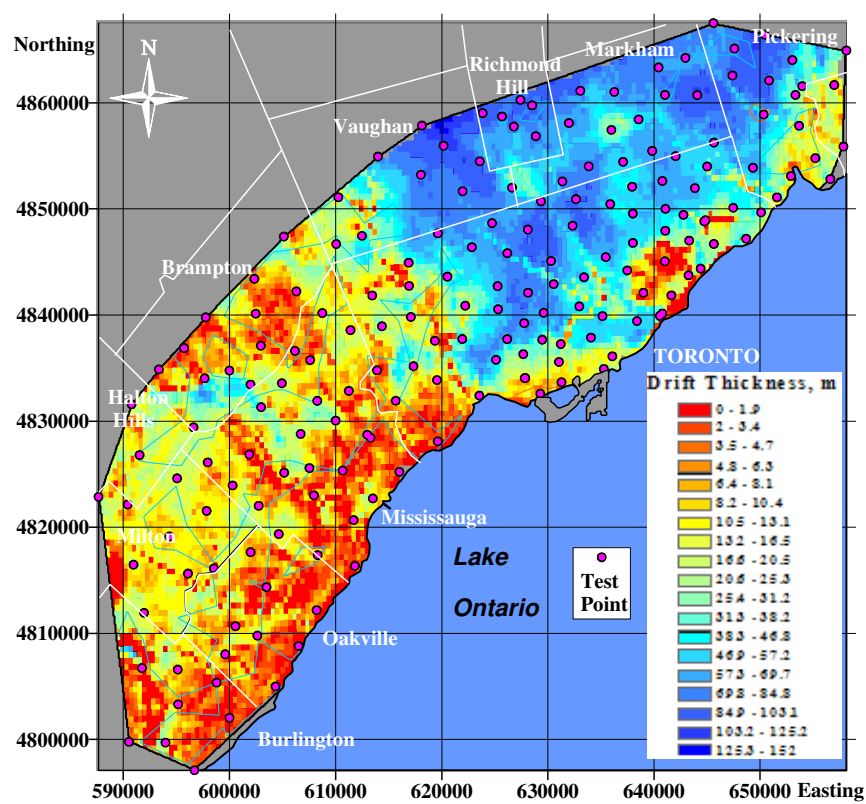


Figure 6.3. Drift Thickness in GTA (from Gao et al., 2006).

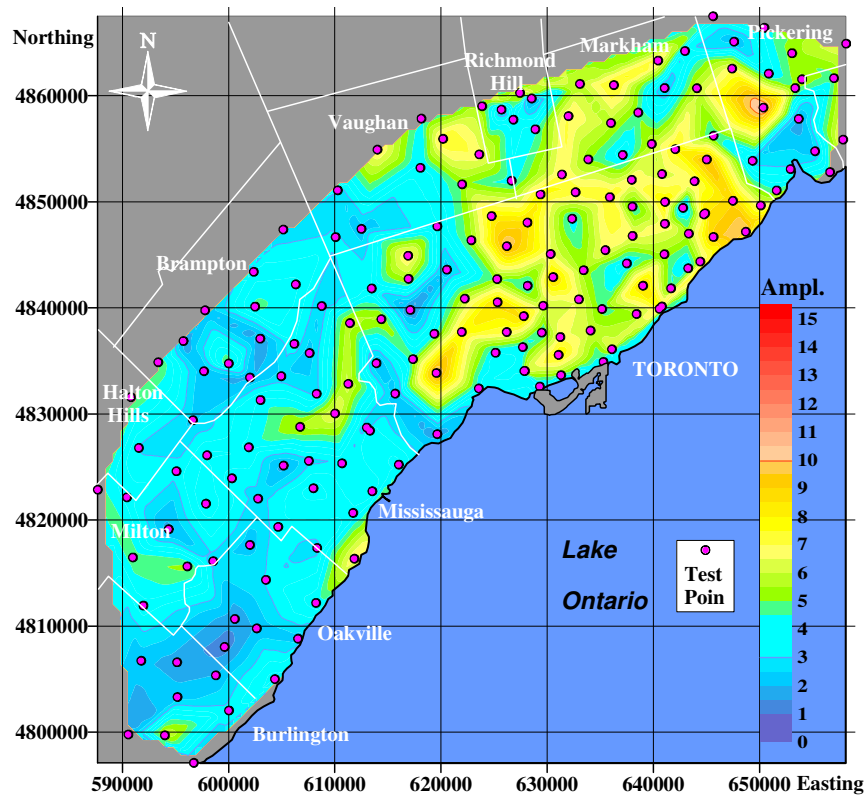


Figure 6.4. Relative amplification at the fundamental resonances (this study).

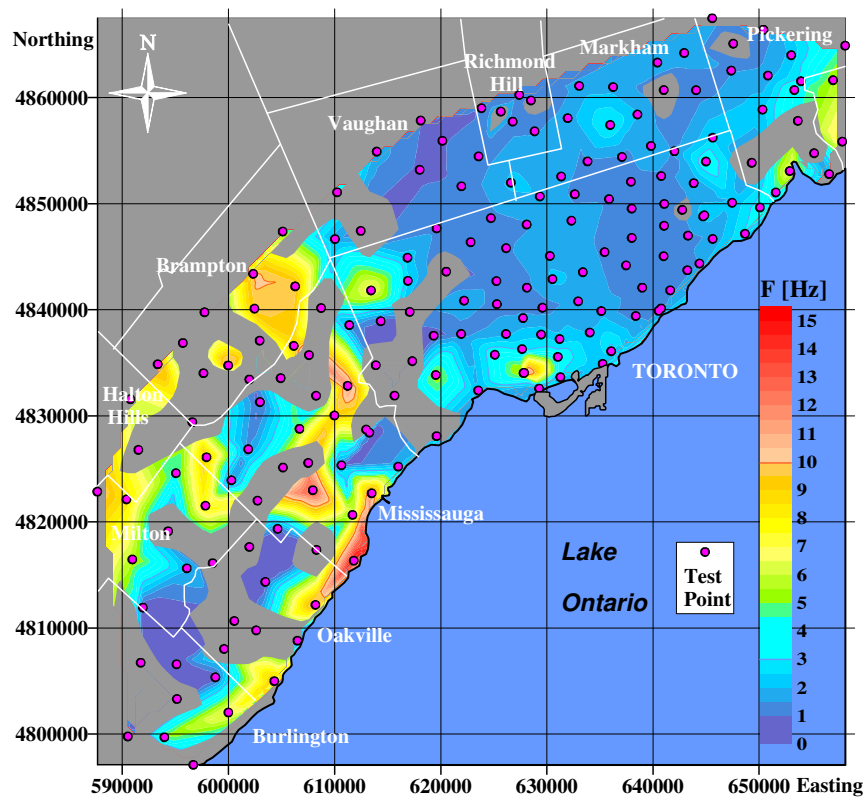


Figure 6.5. Fundamental resonances with relative amplification ≥ 3 (this study).

The map of the fundamental soil resonant frequencies over the study area (Figure 6.2) shows, in general, a correlation with the drift thickness (as it is known to the moment) (Figure 6.3). The HVSR maxima at the fundamental resonances are shown on Figure 6.4.

A deep negative geological structure was outlined for the first time at the bottom of shallow southwest drift thickness cover. This depression probably reflects a buried ravine or ancient river bed. In the same area, the map with excluded resonant frequencies if the amplification is less than 3 (Figure 6.5) shows an acceptable correlation between this deep structure and areas with low amplification. This correlation suggests that the structure has relatively steep rough borders and probably is filled with coarse material containing big boulders. The relatively small resonant amplitudes can be explained with irregular scatter of reflected seismic waves from this surface. This is a very important application of the map of the amplification at the fundamental resonant frequency obtained from HVSR.

Figure 6.6 presents an excerpt for the studied area from the map “Surficial Geology of the Greater Toronto and Oak Ridges Moraine Area, Southern Ontario” (Sharpe et al., 1997). The geological information from this map for the upper soil units was used in conjunction with data for dominant resonances from HVSR to construct acceptable soil structure bellow each test point. This allows assignment of the NBCC 2005 soil classification to the areas around test points.

While the distribution of the resonant frequencies can be mapped more or less confidently, the same can not be said for the soil classification map (Figure 6.7), which gives only a tendency of the spatial distribution of the classified soils. The soil classification according to NBCC 2005 relies on horizontally homogeneous soil layers without vertical disruptions. In city conditions however, there are numerous vertical disruptions due to filling of the negative relief forms, digging trenches and channels for underground facilities etc. This fact does not allow using any interpolation techniques correctly to produce a map of the spatial distribution of soil classes. Therefore, the soil class designation represents the soil layering in the close proximity to each test point, and that the soil classification should be extended around the test point very carefully. Such map was developed for the GTA, which is shown on Figure 6.8.

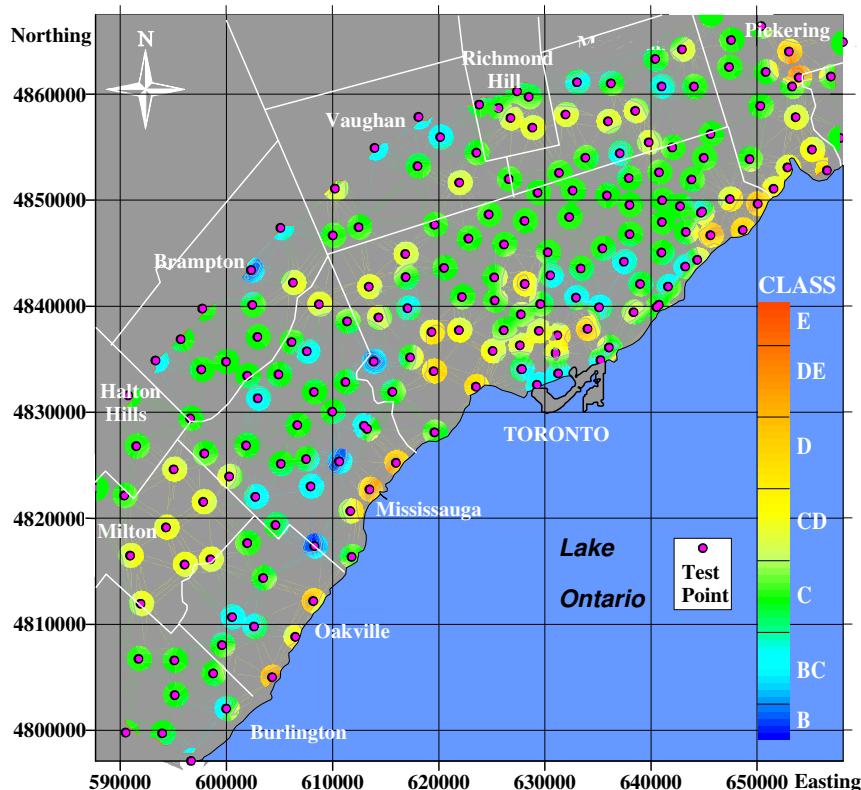


Figure 6.8. Applicable NBCC 2005 soil classes for GTA (this study).

The results of the preliminary seismic microzonation for the GTA reported herein are presented as maps of the fundamental soil resonances and site classification independently.

The seismic microzonation in Canada is based on five different soil categories defined in the NBCC 2005. The soil classification is specified in terms of the average shear wave velocity of the top 30 meters of soil profiles below the foundation (V_{s-30}). However, the NBCC 2010 introduced an important change for soil classes A and B. If an intervening soft-soil layer of thickness 3 m or more exists in the top 30 m, the classification should be specified in terms of the average shear wave velocity for this layer (Adams, 2010; Humar et al. 2010). This provision changes the idea of averaging the shear wave velocities over the whole depth of 30 m below the building foundation.

The approach in this study for classification of the soil structure beneath each test point using the information from the surficial geology map and dominant resonances from HVSR can not be applied according to the above provision without V_s profiles.

Chapter 7

Influence of Building Resonances on HVSR Results

7.1. Introduction

Building vibrations and resonances of structures under wind load and normal activities in and around a building can be influential factors, which may alter the results of HVSR measurements at the test points close to the building. For this reason, the actual building resonances have to be obtained experimentally and their effect on the HVSR should be estimated and compensated for (e.g. Lin et al., 2011).

The best scenario to trace out some potential changes in the HVSR due to the proximity of a building is to first get the HVSR at test points within and close to the construction site of a future building. After building completion, the HVSR has to be evaluated again at the same points. If differences are identified between the two sets, they can be explained by the impact of building vibrations and resonances caused by wind load and residential activities.

The determination of frequency resonances and mode shapes of the building is usually undertaken at the design phase. These parameters are critical to predict the vulnerability of buildings and to determine their vibration performance during a potential earthquake or severe wind loading. One approach to determine the building frequency resonances and mode shapes is to use the provisions of a building code. However, different building codes suggest usually different empirical correlations between building resonances and its structural geometry. Another approach to assess fundamental resonances is to use finite element analysis to model the structure using appropriately distributed mass and stiffness matrices incorporated in readily available software packages.

An experimental verification of the design parameters can be accomplished after the construction is completed, but before the building is populated. Mechanical, electro-magnetic or hydraulic actuators can be used for this purpose. However, these tests are expensive and thus they are not commonly used in the case of residential buildings. Wind

loading and/or some residential activities offer an alternative means as a no-cost vibration source that can be used to collect information about the building vibration behavior and mode shapes. The excitation of a building by ambient forces has a broad frequency range, and potentially is capable to reveal most of the vibration modes of a structure. The use of ambient excitation does not disturb building occupants and normal residential activities. The excitation by wind and ambient vibration has advantages over other test methods because it doesn't require heavy equipment such as mechanical, electro-magnetic or hydraulic actuators.

Morgan et al. (1987) analyzed published information for modal parameters of tall building structures in the USA, which were estimated experimentally using both ambient vibration and forced vibration tests. They concluded that modal parameters obtained by ambient excitation are as good as those obtained by external artificial excitation.

There are different approaches available in the literature for calculation of the resonant frequencies of a building using experimentally recorded waveforms. They generally utilize different methods for modal analysis of structures. The modal parameters established from these approaches are then used to describe the dynamic behavior of the building.

The modal parameters are:

- Modal frequencies or eigenfrequencies - are the eigenvalues of the natural building resonances;
- Modal damping - is characterized by different damping ratios for each modal frequency;
- Modal vectors - are the eigenvectors which give the mode shapes at modal frequencies;
- Modal scaling - includes geometry, masses, and elastic modules matrices.

7.2. Some techniques for modal identification using wind and ambient vibrations.

In order to evaluate the effect of building resonances on the Nakamura's HVSR results at some test points close to an existing building, it is necessary to identify the modal frequencies of the structure at which the damping ratios are sufficiently small to ensure

relatively sharp building resonances. The vibration amplitudes at these frequencies are usually significant and they could propagate through the soil structure, interfere with the microtremors in the ground, and might distort the resulting HVSR. On the other hand, modal vectors (mode shapes) allow the identification of the vibration mode. The different mode shapes representing the lateral and rocking vibration modes can be visualized using a simple animation algorithm implemented in Excel.

The techniques for modal identification using wind and ambient vibration as active sources are usually named Output Only or Responses Only techniques. Most of the methods based on these techniques assume that the structure is impacted by multiple input sources, which are randomly distributed such that they activate all possible building vibration modes. The modal identification techniques aim to construct a dynamic structural model from the measured data employing different algorithms, which assume that a transfer function can be approximated by cross power spectral density of the responses (e.g. Jacobsen, 2008). In the current application, there is no need to model the building and it is not necessary to find exact values for the damping or scaling factors of the building, which are usually used for modeling the structure.

7.2.1. Basic frequency domain decomposition versus other identification techniques for structural vibration modes

All Output Only techniques for modal identification rely on using a cross-correlation function of the random response of the structure under natural excitation. The input excitation is from randomly distributed sources in time and space and the response of the structure is supposed to be broadband process.

The technique for modal identification used in this study is based on the well-known classical frequency domain decomposition usually referred to as Basic Frequency Domain (BFD) decomposition or Peak Picking technique. The classical approach employs simple signal processing using Discrete Fourier Transform (DFT) or Fast Fourier transform (FFT) over multi-component synchronously registered time series. For well separated resonances, the vibration modes can be estimated directly from the peaks in amplitude or power spectral density matrices (Bendat and Piersol, 1986). This

technique is implemented herein using cross-correlation between the recorded three-component waveforms.

The main advantage of the classical approach is its user friendly processing compared to other approaches, such as: Ibrahim Time Domain (Ibrahim and Mikulcik, 1977); Stochastic Subspace Identification algorithm proposed by Van Overschee and De Moor (1996); and even compared to different modifications of the widely used Singular Value Decomposition (SVD) technique and other methods that employ decomposition of the spectral matrices from input data into eigenvalues and eigenvectors. Most approaches that are based on the SVD technique approximate the building vibration modes considering a set of single degree of freedom (SDOF) oscillators. The SVD technique is widely used for modal identification of civil structures subjected to ambient and harmonic excitations (e.g. Brincker et al. 2000, 2003, 2007; Andersen et al, 2008). This representation of the resonant frequencies is convenient for appreciative calculation of modal damping ratios.

It is a common practice to use waveforms or spectra from all components recorded simultaneously at all test points. However, this approach results in pre-determined consecutive enumeration of the mode shapes excluding the direction of the movement (i.e. orthogonal translations or rotations) and discrimination between bending and torsional vibration modes. Many test results are presented in such enumeration (e.g. Turek, 2006), which makes it difficult to assign published resonant frequencies to appropriate mode shapes, if it is not pointed out explicitly. It was difficult to compare such resonances with our test result. However, the goal in the current study was to identify real vibrations excited in the ground and propagated through the soil structure around the building, not to model the vibration modes of the building.

Recently, there have been some attempts to use HVSR inside the building in order to establish building resonances (e.g. Gallipoli et al., 2004; Mucciarelli et al., 2004). This approach has been examined here using recorded waveforms at different test points inside the building.

7.2.2. Mode shapes derived for a building approximation

In this study, the enumeration of the mode shapes is consistent with their physical interpretation. The mode shape number is equal to the number of “zeros” in the deflected geometrical shape. Repeatable numbers have been used for orthogonally disposed mode shapes to which suffix for each orthogonal orientation has been added. The enumeration for bending (deflection) modes is derived here using the classical Euler-Lagrange equation.

The mode shapes are defined for a column, which can roughly substitute a slender building as shown in Figure 7.1. This model presumes very stiff foundation and inflexible half space below the column or building structure. Thus, the rocking movement and soil-structure interaction (SSI) are excluded from the calculations.

The classic governing Euler-Lagrange differential equation for a cantilever beam is modified for free horizontal vibration of a column:

$$-EI \frac{\partial^4 X(z,t)}{\partial z^4} = \rho \frac{\partial^2 X(z,t)}{\partial t^2}, \quad (7.1)$$

where: E is the modulus of elasticity

I is the areal moment of inertia

ρ is the mass density (mass per length)

This equation neglects shear deformation and rotational inertia.

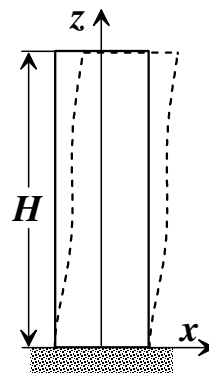


Figure 7.1 Simplified approximation of a tall building as a column

After separation of the dependent variable $X(z,t)$ as:

$$X(z,t) = X(z)T(t),$$

Let assume a constant c such that:

$$\left(\frac{-EI}{\rho}\right) \frac{\left(\frac{d^4}{dz^4} X(z)\right)}{X(z)} = \frac{\left(\frac{d^2}{dt^2} T(t)\right)}{T(t)} = -c^2. \quad (7.2)$$

As a result there are two independent equations:

- the equation of harmonic oscillator with resonant frequency c for the time variable:

$$\frac{d^2}{dt^2} T(t) + c^2 T(t) = 0, \quad (7.3)$$

- the equation for the spatial variable:

$$\frac{d^4}{dz^4} X(z) - c^2 \left(\frac{\rho}{EI}\right) X(z) = 0. \quad (7.4)$$

A possible solution of the equation (6.4) is:

$$X(z) = a_1 \sinh(\beta z) + a_2 \cosh(\beta z) + a_3 \sin(\beta z) + a_4 \cos(\beta z), \quad (7.5)$$

Where β is a constant, which includes all parameters in Equation (7.4).

The derivatives of Equation (7.2) in this case are:

$$\frac{d}{dz} X(z) = a_1 \beta \sinh(\beta z) + a_2 \beta \cosh(\beta z) + a_3 \beta \sin(\beta z) + a_4 \beta \cos(\beta z), \quad (7.6)$$

$$\frac{d^2}{dz^2} X(z) = a_1 \beta^2 \sinh(\beta z) + a_2 \beta^2 \cosh(\beta z) + a_3 \beta^2 \sin(\beta z) + a_4 \beta^2 \cos(\beta z), \quad (7.7)$$

$$\frac{d^3}{dz^3} X(z) = a_1 \beta^3 \sinh(\beta z) + a_2 \beta^3 \cosh(\beta z) + a_3 \beta^3 \sin(\beta z) + a_4 \beta^3 \cos(\beta z), \quad (7.8)$$

$$\frac{d^4}{dz^4} X(z) = a_1 \beta^4 \sinh(\beta z) + a_2 \beta^4 \cosh(\beta z) + a_3 \beta^4 \sin(\beta z) + a_4 \beta^4 \cos(\beta z). \quad (7.9)$$

After substitution of Eqs. (7.5) and (7.9) into Eq. (7.4), grouping and simplifying, we have:

$$\left[\beta^4 - c^2 \left(\frac{\rho}{EI} \right) \right] [a_1 \sinh(\beta z) + a_2 \cosh(\beta z) + a_3 \sin(\beta z) + a_4 \cos(\beta z)] = 0 \quad (7.10)$$

Equation (7.10) is satisfied if:

$$\beta^4 = c^2 \frac{\rho}{EI} \quad \text{or} \quad \beta = \sqrt[4]{c^2 \frac{\rho}{EI}}. \quad (7.11)$$

To find $a_{1,2,3,4}$ in Eq. (7.10), the following boundary conditions are satisfied:

1. Zero displacement and zero slope at the foundation level, i.e.:

$$X(0)=0, \quad \text{and} \quad \left. \frac{dX(z)}{dz} \right|_{z=0} = 0. \quad (7.12)$$

2. Zero bending moment and zero shear force at the top of the building, i.e.:

$$\left. \frac{dX^2(z)}{dz^2} \right|_{z=H} = 0, \quad \text{and} \quad \left. \frac{dX^3(z)}{dz^3} \right|_{z=H} = 0, \quad (7.13)$$

where H is the building height (Figure 7.1).

Applying these boundary conditions to Eqs. (7.6) to (7.9) yields:

$$a_4 = -a_2 \quad \text{and} \quad a_3 = -a_1. \quad (7.14)$$

Substituting Eqs. (6.14) and (6.13) into Eqs. (6.8) and (6.9), the following two equations are derived in terms of a_1 and a_2 :

$$a_1 [\sin(\beta H) + \sinh(\beta H)] + a_2 [\cos(\beta H) + \cosh(\beta H)] = 0, \quad (7.15)$$

$$a_1 [\cos(\beta H) + \cosh(\beta H)] + a_2 [-\sin(\beta H) + \sinh(\beta H)] = 0. \quad (7.16)$$

The trivial solution of the above system of equations is $a_1 = a_2 = 0$.

The nontrivial solution can be found when the determinant of the system is set to zero, i.e:

$$[-\sin^2(\beta H) + \sinh^2(\beta H)] - [\cos(\beta H) + \cosh(\beta H)]^2 = 0, \quad (7.17)$$

which yields:

$$\cos(\beta H) \cosh(\beta H) + 1 = 0. \quad (7.18)$$

A graphical presentation is used to find the roots of Eq. (7.18). To see zero-crossing points clearly, amplitudes are compressed in Figure 7.2 employing the function:

$$\tanh[\cos(\beta H)\cosh(\beta H)+1]=0. \quad (7.19)$$

To find the first three roots, a polynomial approximation is applied in the vicinity of each zero-crossing of Eq. (7.19). On the other hand, Eq. (7.18) has multiple roots indexed by integer subscripts, which can be rewritten as:

$$\cos(\beta_i H)\cosh(\beta_i H)+1=0, \quad i = 1, 2, 3, \dots \quad (7.20)$$

These indexes are used as mode numbers in Table 7.1. The first three roots $\beta_i H$ of Eq. (6.18) are listed in the second column of Table 7.1.

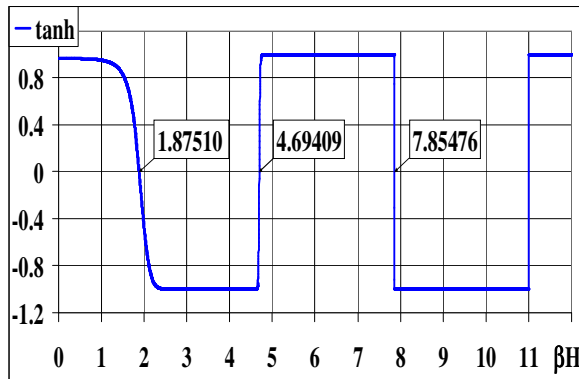


Figure 7.2. Plot of Equation (7.19).

Table 7.1.

MODE (<i>i</i>)	$\beta_i H$	a_{1i}
1	1.87510	-0.73410
2	4.69409	-1.01847
3	7.85476	-0.99922

Vibration modes - coefficients.

Assuming multiple roots of Eq. (7.18), Eq. (7.15) can be rewritten as:

$$a_{1i}[\sin(\beta_i H)+\sinh(\beta_i H)]+a_{2i}[\cos(\beta_i H)+\cosh(\beta_i H)]=0. \quad (7.21)$$

To find a_{1i} , let $a_{2i}=1$ for all i . From Eq. (7.21) for a_{1i} , we have:

$$a_{1i} = \frac{-[\cos(\beta_i H)+\cosh(\beta_i H)]}{[\sin(\beta_i H)+\sinh(\beta_i H)]}. \quad (7.22)$$

The values of a_{1i} for the first three roots $\beta_i H$ are listed in the third column of Table 7.1.

Knowing a_{1i} and substituting Eq. (7.14) into Eq. (7.5), the normalized eigenvectors for the first three modes are obtained as:

$$X_1(z) = A_1 \{[\cosh(\beta_1 z) - \cos(\beta_1 z)] - 0.73410[\sinh(\beta_1 z) - \sin(\beta_1 z)]\}, \quad (7.23)$$

$$X_2(z) = A_2 \{[\cosh(\beta_2 z) - \cos(\beta_2 z)] - 1.01847[\sinh(\beta_2 z) - \sin(\beta_2 z)]\}, \quad (7.24)$$

$$X_3(z) = A_3 \{[\cosh(\beta_3 z) - \cos(\beta_3 z)] - 0.99922[\sinh(\beta_3 z) - \sin(\beta_3 z)]\}. \quad (7.25)$$

The normalization parameters for Eqs. (7.23), (7.24), and (7.25) are:

$$A_i = [X_{i \max}(z)]^{-1} = [X_i(H)]^{-1}. \quad (7.26)$$

The normalized eigenvectors give the first three mode shapes shown in Figure 7.3.

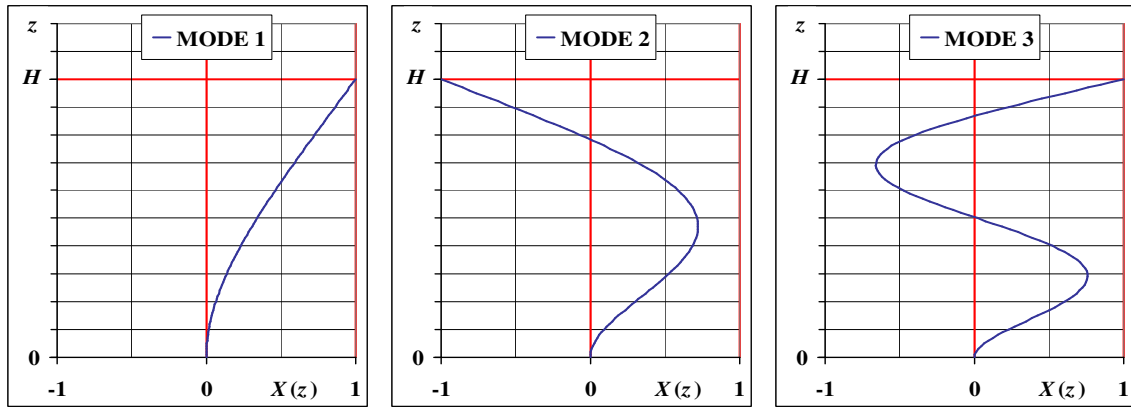


Figure 7.3. Plots of first three mode shapes from normalized eigenvectors.

Torsional vibration modes can be illustrated by parity of reasoning. If Eq. (7.1) is rewritten for angular rotation:

$$-GJ \frac{\partial^4 \phi(z,t)}{\partial z^4} = \rho \frac{\partial^2 \phi(z,t)}{\partial t^2} \quad (7.27)$$

where: G is the shear modulus,

ρ is the mass density,

J is the polar moment of inertia.

After some transformation similar to those applied to the bending modes, the eigenvectors for torsional mode shapes can be obtained. The first torsional mode shape is shown in Figure 7.4. Solving the above equations and their graphical plots indicated how translational (bending) and torsional mode shapes are enumerated.

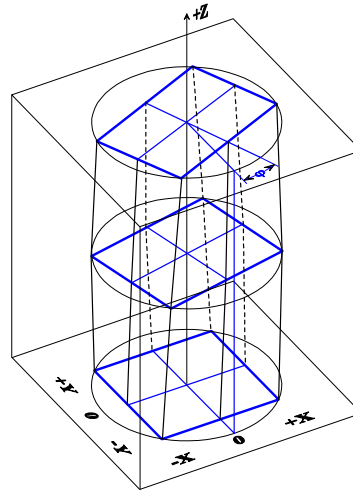


Figure 7.4. Torsional mode-1.

The above approximation of the building structure considering a uniform column is useful for visualizing the eigenvectors, but it does not allow even approximately calculating the eigenvalues (resonant frequencies). This is because converting the structure's mass and stiffness matrices into equivalent homogeneous distributed mass and uniform elasticity is almost impossible.

7.3. Case Study of Interaction between Building Vibration and Soil Resonances obtained by HVSR Technique

A thirteen stories building located in London, Ontario was chosen as a case study to demonstrate the effects of interaction between building vibration and soil resonances obtained using the HVSR technique. To demonstrate these effects, two sets of field HVSR measurements are conducted; one is conducted before the construction started and another is conducted after completion of the structure.

7.3.1. Short description of the studied building

The building considered in the case study is a thirteen story structure with reinforced concrete (RC) frame, reinforced concrete slabs, and reinforced concrete shear walls. Figure 7.5 shows the building after completion. The building foundation is constructed as a combined footing with rectangular concrete slab supported by cast-in-place individual concrete pad footings underneath each column. The flexibility of the structure is reduced by the shear walls.



Figure 7.5. Photo of the case study building after completion.

Two stair cases and an elevator shaft additionally increase the stiffness of the entire structure. All floor slabs are constructed as two parts connected through a thermal expansion joint which is perpendicular to the longitudinal axis. The shear walls, stair cases, elevator shaft and the thermal expansion joint were visible at the level of the underground garage, as schematically depicted in Figure 7.6.

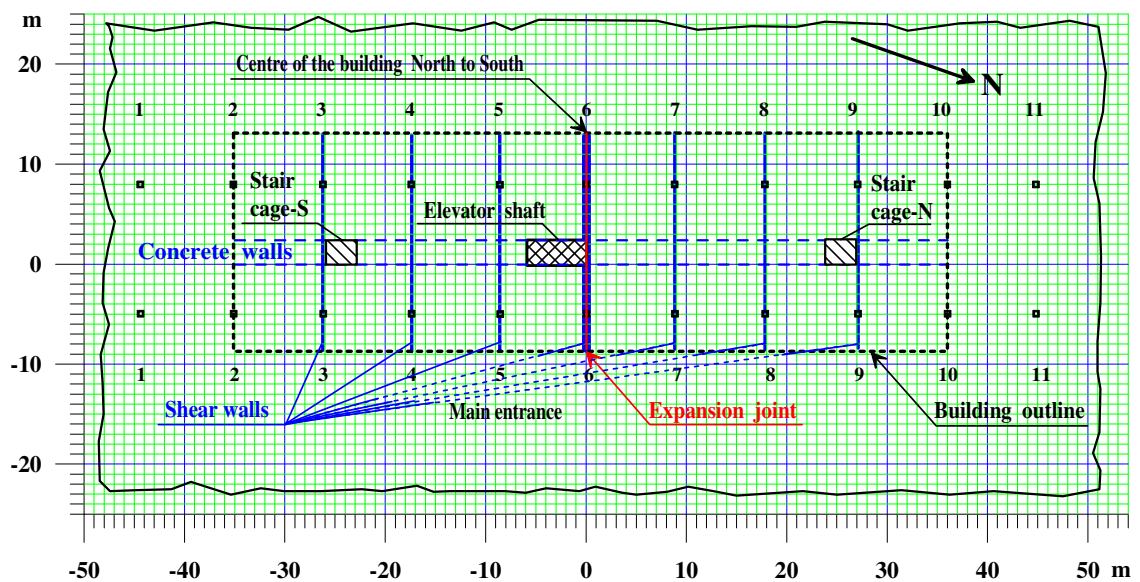


Figure 7.6. Sketch of shear resistant elements at the building base.

7.3.2. Test points locations

Figure 7.7 shows the location of measurement points around the building and at the level of building base and underground parking garage.

There were some limitations on the choice of test points locations imposed by the surrounding property. This is why the distribution of these points is not ideal.

All test points marked as SideWalk X were situated above the concrete slabs of the East sidewalk along the Richmond St. The seismometer L4-3D was installed consecutively at predetermined locations of the test points directly on these slabs.

The test points marked as Ditch-Xx and test point P-1 lie on the soil surface. The seismometer was placed consecutively on a 300mm x 300mm concrete plate in shallow holes 300mm deep.

The measurements at test points outside the building: SideWalk-D, -C, -B, -A, -0, -1, -2, -3, -4, Ditch-1, -2, -3, -4, test point P1 (closest to the building) and at the test points inside the building, BASE CENTER, BASE-N, NORTH and SOUTH were used for determination of the HVSR changes due to influence of building vibrations.

The test points inside the building footprint marked as BASE-CENTER, BASE-N, NORTH and SOUTH were measured after removing 1-1.5m of soil, then soil compaction and pouring the foundation but before the erection of the building.

The data acquisition system described in Chapter 4.2 was used to record 3-component readings of seismic microtremors for the HVSR calculation.

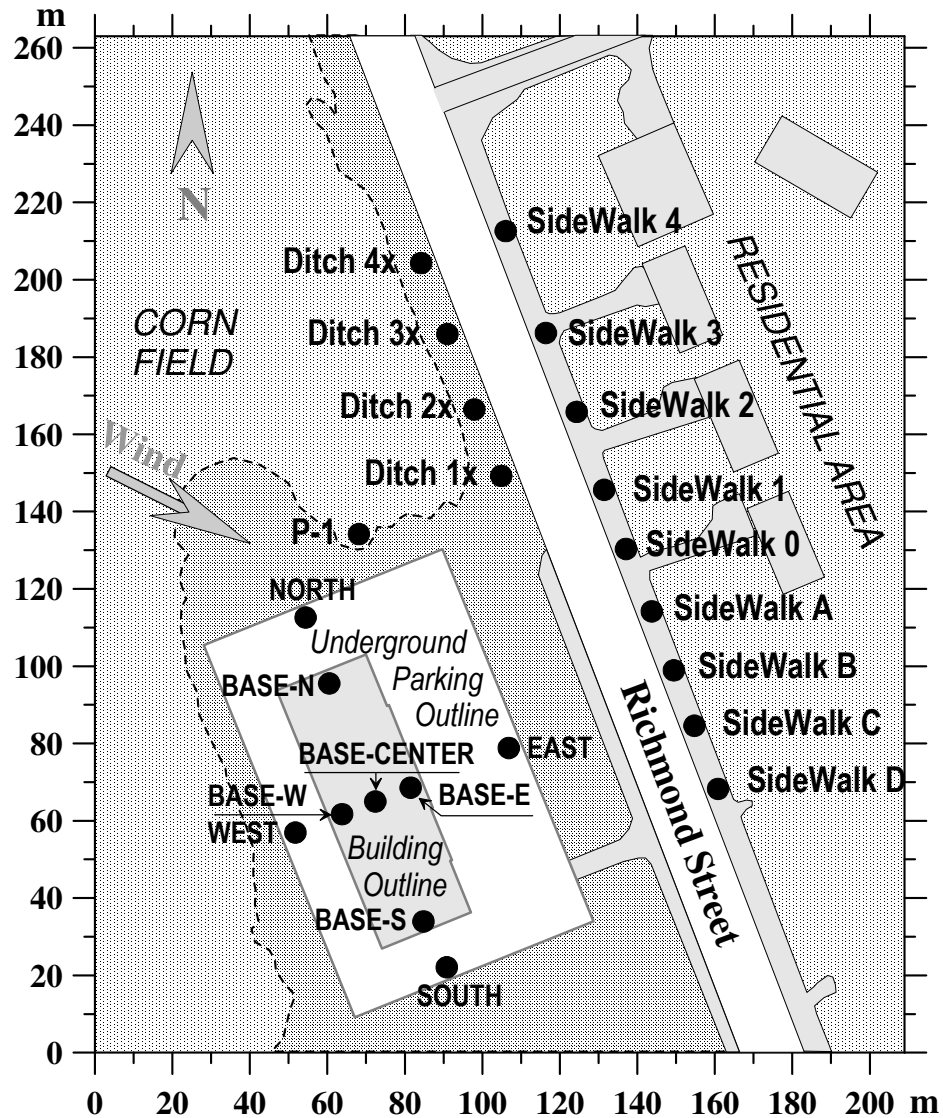


Figure 7.7. Measurement locations around the building and at ground level.

The vibration measurements were taken again at all test points after the building was completed and partially (~60%) populated, including test points on Figure 7.7 marked as BASE-S,-E,-W, EAST and WEST, at which no measurements were taken before construction.

The locations of all test points inside the building are shown in Figure 7.8 over a wireframe sketch of the structure and underground garage. The measurements at these points were used for determination of the building resonances at different vibration modes.

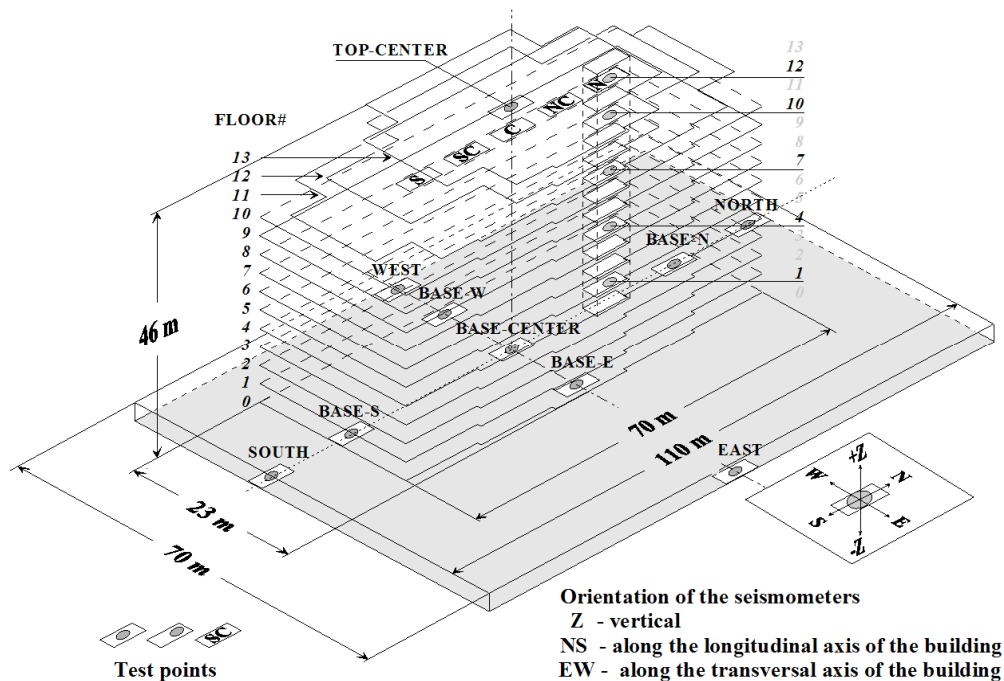


Figure 7.8. Wireframe sketch of the building, parking-garage and the test points.

Limited access was available to the construction site at the beginning of construction. After the building was completed and populated, another set of measurements was taken at the TOP-CENTER test point on the 13th floor. Additional test points were later considered along the staircase at the building north side and along the corridor on the 12th floor, as well as in the basement and underground garage.

7.3.3. Building resonant frequencies at dominant vibration mode from three-component waveforms recorded at TOP-CENTER

The test point TOP-CENTER (Figure 7.9) was selected at the geometrical center of the building's 13th floor in order to evaluate the vertical response without any contribution from rocking, and the maximum horizontal response without the influence of the torsional vibration. The waveforms were recorded at a sampling rate of 100sps and frequency bandwidth of 0.1 – 44 Hz using an L4-3D seismometer oriented with NS component parallel to longitudinal axis. The record length was 650 seconds.

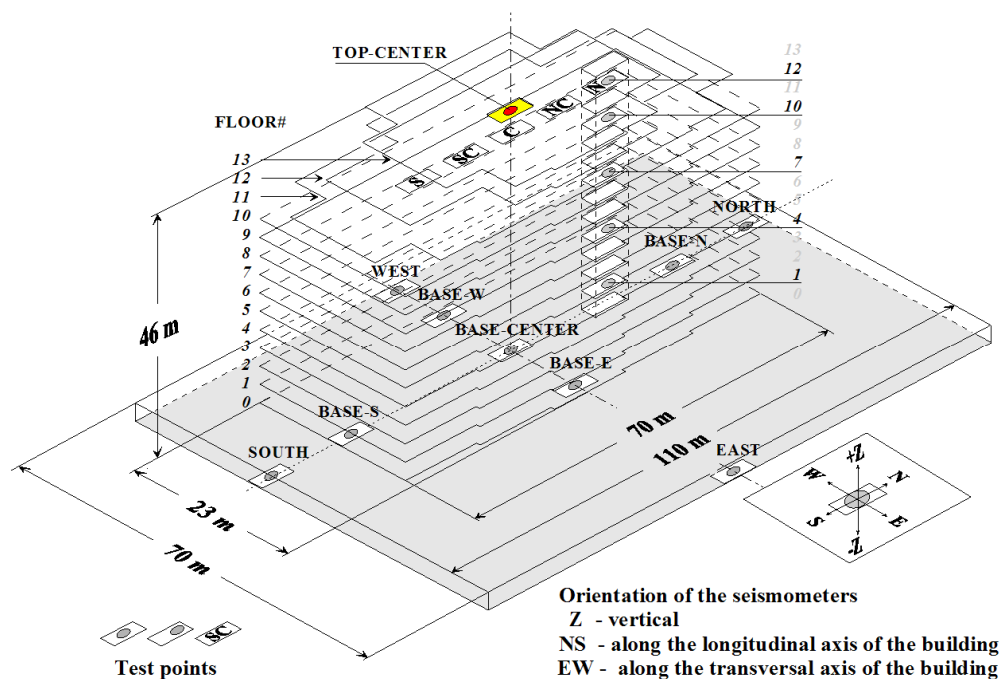


Figure 7.9. TOP-CENTER test point on the 13-th floor of the building.

After calculating the FFT for 32768 samples, all spectra were smoothed by triangle averaging function over ± 0.03 Hz. An example of the spectrum for test point TOP-CENTER is shown in Figure 7.1 in log/linear and log/log scales. The expected resonant frequencies according to the equation proposed by ASCE/SEI 7-05 are shown by colored strips in Figure 7.10.

Two significant resonances can be noted on the spectra of the horizontal components: one in NS direction at 2.16 Hz and one along the EW direction at 2.37 Hz. The dominant vibration modes at the center of 13th floor are presented on Figures 7.10 to 7.12.

The spectra shown in Figures 7.11 and 7.12 display a rotating resultant horizontal response calculated from the recorded waveforms of the two orthogonal horizontal components.

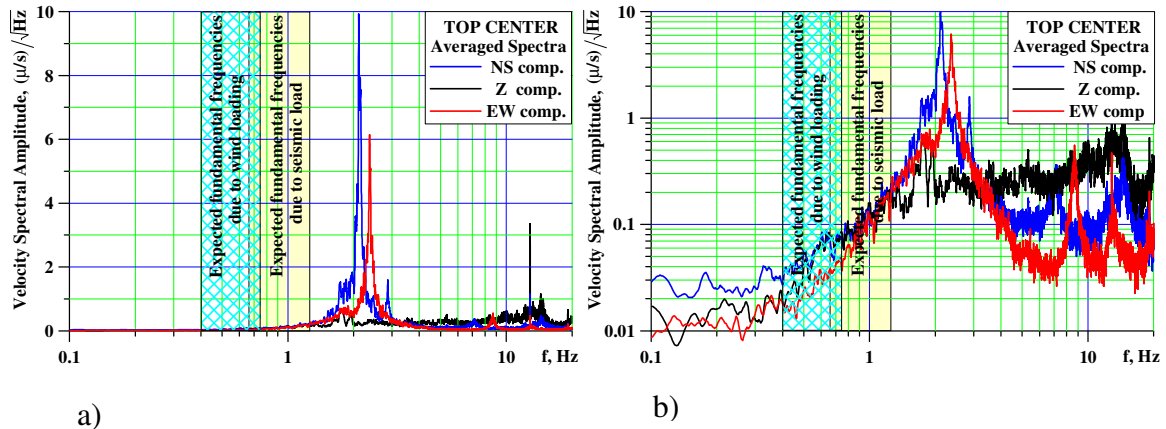


Figure 7.10. Averaged velocity spectra at the building TOP-CENTER test point, a) linear scale; b) logarithmic scale.

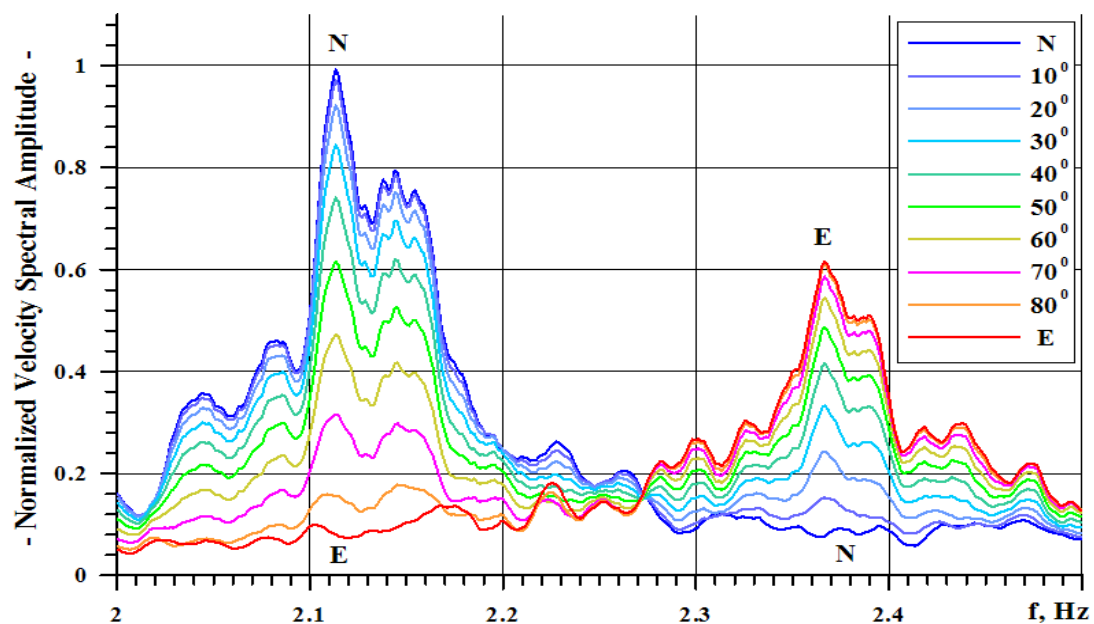


Figure 7.11. Normalized velocity spectra at dominant vibration mode at TOP-CENTER test point. Axis is rotated by 10° increments from North to East.

Figure 7.12 presents the distribution of the dominant vibration mode at the TOP-CENTER test point in polar coordinates. For the rectangular structure under consideration, this represents a symmetrical distribution of the resonant responses in different azimuths. In a case of more complex asymmetrical building, this method for

presenting the response could help identify the direction of the main resonance or orientation and interaction between dominant vibration modes.

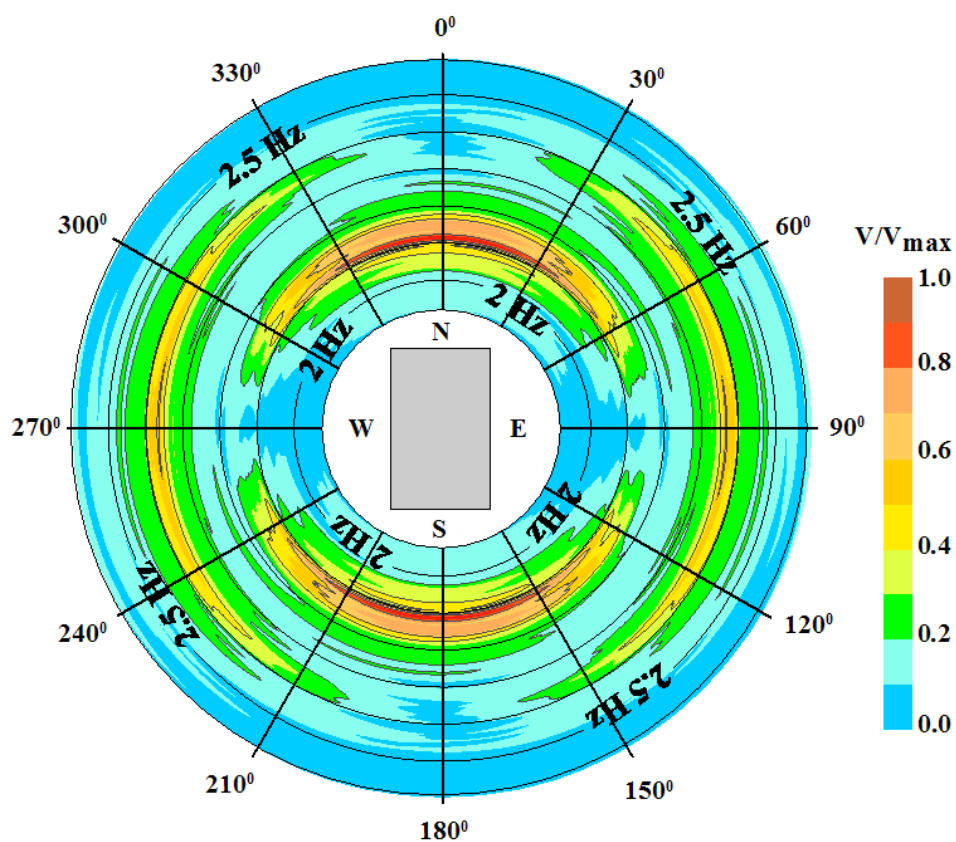


Figure 7.12. Changes of spectra in different azimuths - normalized velocity spectra at the dominant vibration mode at TOP-CENTER test point.

7.3.4. Separation of building vibration modes considering three-component waveforms recorded simultaneously at test points along northern staircase

The dominant resonant frequencies established at the TOP-CENTER test point were more than three times higher than resonant frequencies calculated using the empirical provisions from the existing building codes. To identify the vibration modes corresponding to these resonances, simultaneously recorded waveforms at five test points along the northern staircase were used. The locations of the test points are shown on Figure 7.13.

The filtered signals are used in an EXCEL animation to visualize the vertical profiles of the first two vibration modes. The results for 20 consecutive positions of the vertical profiles for the first and second vibration modes are shown in Figure 7.15.

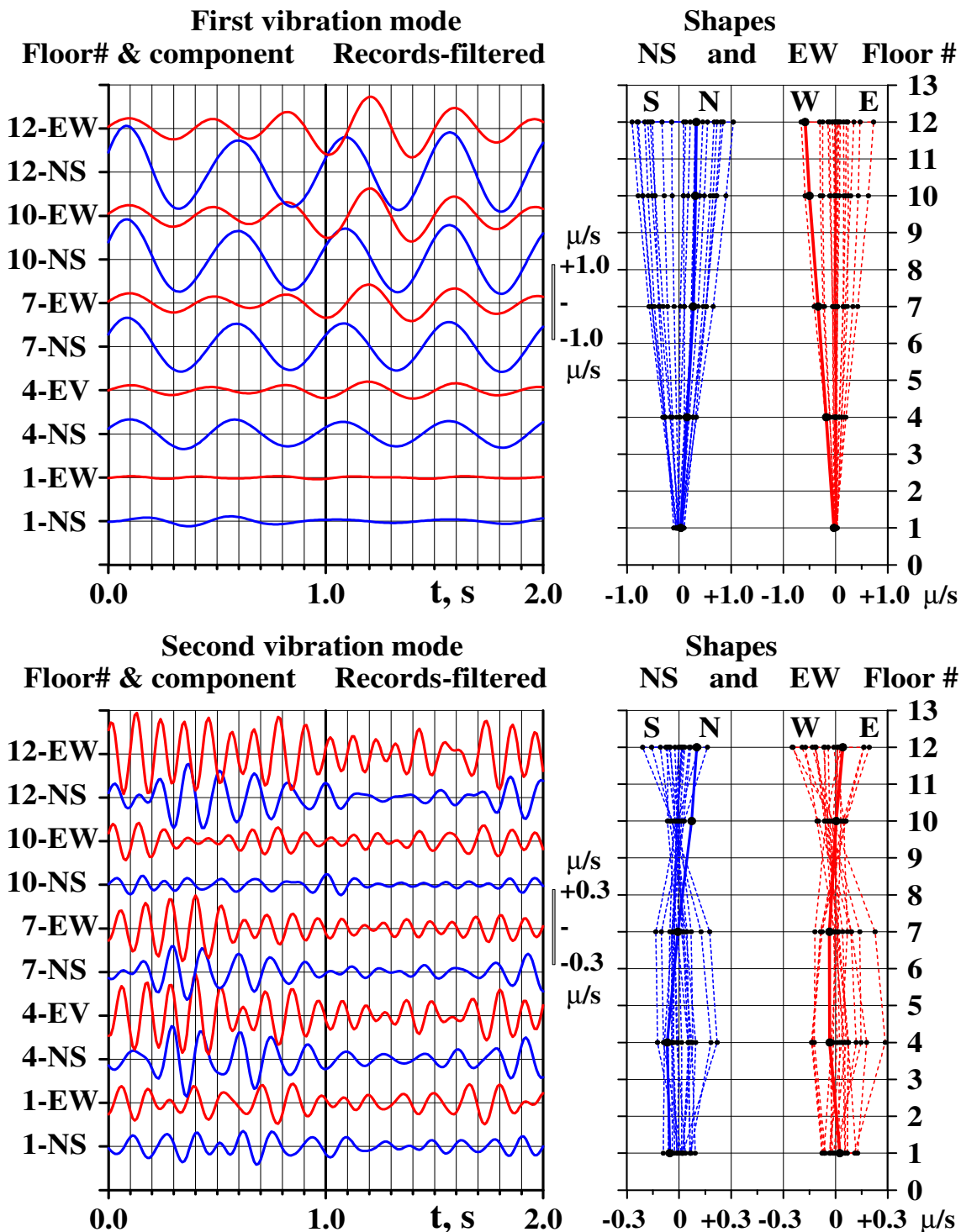


Figure 7.15. First and second mode shapes - each with 20 positions in time.

7.3.5. Separation of torsional vibration modes from considering two-component waveforms recorded simultaneously at test points along the corridor on 12th floor

The locations of the 5 measurement points considered in the analysis to identify the torsional vibration mode are shown on Figure 7.16.

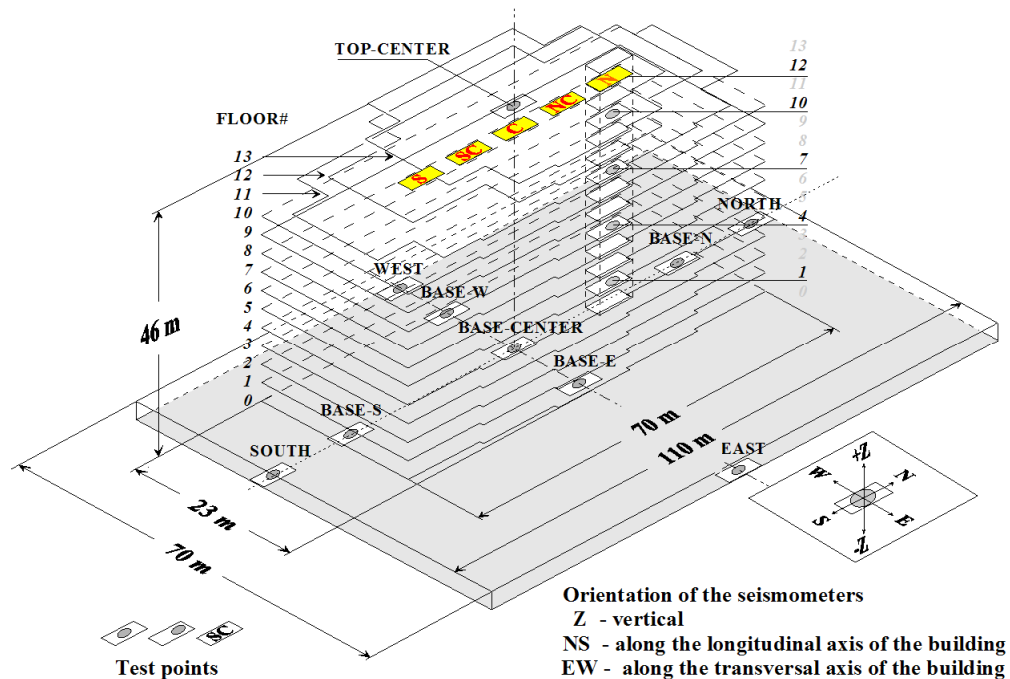
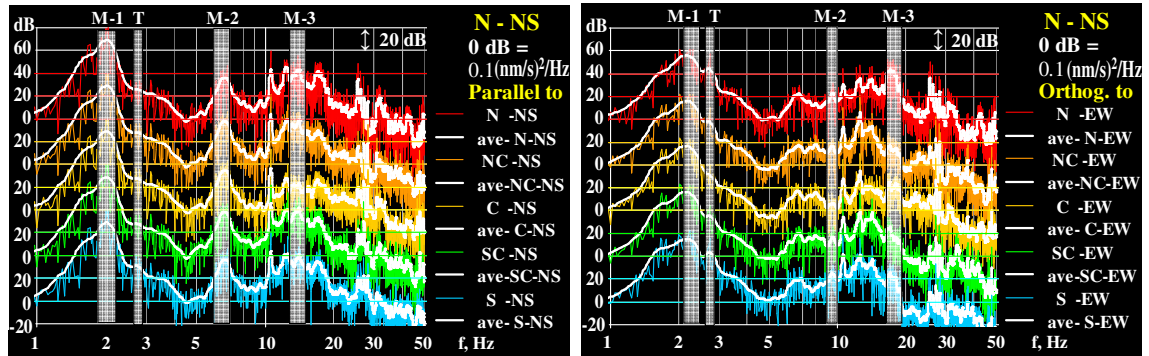
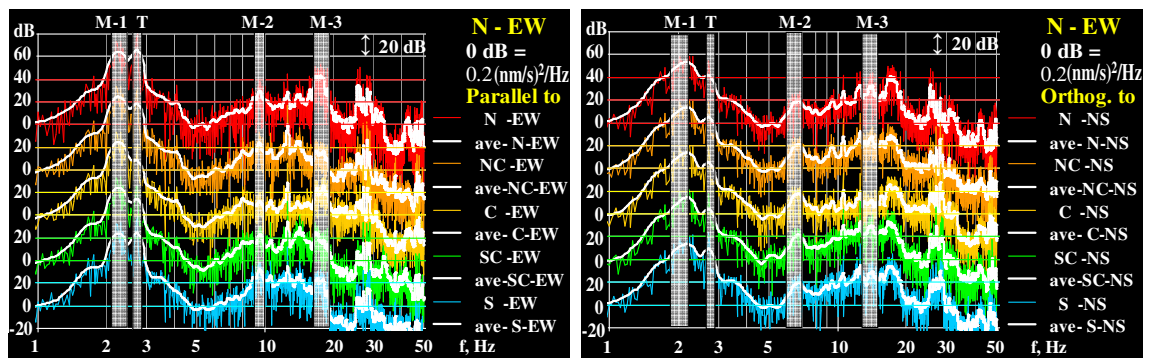


Figure 7.16. Locations of the test points on the twelfth floor.

The separation of the torsional vibration mode from the first, second and third vibration modes requires a more precise filtering technique. Using BFD decomposition, it is possible to identify building resonances using direct cross-correlation between waveforms recorded simultaneously at the test points. Building resonances can also be estimated in the frequency domain because the cross-spectrum of any two waveforms is the forward Fourier Transform of the cross-correlation function between them. The cross-spectrum is, in general, complex and can be calculated from the individual Fourier spectra of each pair of recorded waveforms. The cross-spectra were calculated as a complex product of the spectrum of one waveform and the complex conjugate of the spectrum of the other waveform. Some examples of cross-spectra are shown in Figure 7.17.



a) N-NS parallel to all NS components, b) N-NS orthogonal to all EW components



c) N-EW parallel to all EW components, d) N-EW orthogonal to all NS components

Figure 7.17. Cross-spectra between parallel and orthogonal components.

a) and c) - cross-spectrum between parallel pairs of horizontal components;

b) and d) - cross-spectrum between orthogonal pairs of horizontal components.

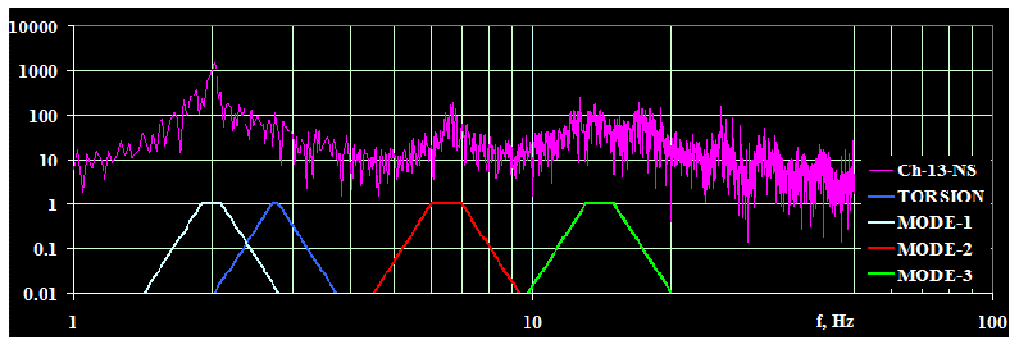
Points M-1, M-2, M-3 and T on Figure 7.17 mark the positions of the bandpass filters for the first three translational and the torsional vibration modes, respectively. The line legends in Figure 7.17 denote the location of measurement and the orientation of the cross-spectra component. For example: N-NS denotes NS component recorded at the North side of the building.

The cross-spectra between pairs with same orientation provide clear solution for the expected resonances for all modes. The cross-spectra between pairs with orthogonal orientation, used in some techniques for spectral decomposition, do not contribute to the solution. It may be concluded that the orientation of measurements along the primary axes of the building is an important condition, which can simplify data processing.

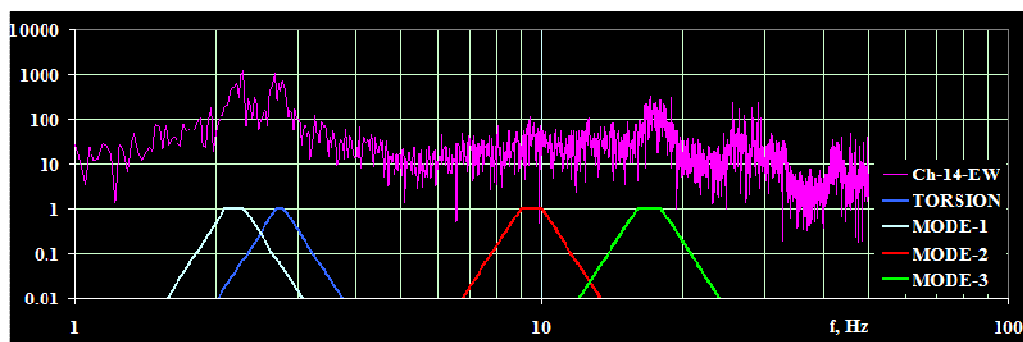
The local maxima from cross-spectra obtained from all parallel components are used to define two sets of band-pass filters for both orthogonal primary axes of the structure. These sets, along with their parameters and visualization, are shown on Figure 7.18. The higher order of the filters ensures better separation of the vibration modes.

MODE	T	M1	M2	M3	T	M1	M2	M3
COMP.	NS	NS	NS	NS	EW	EW	EW	EW
f_HP, Hz	2.7	1.9	6	13	2.7	21	9	16
f_LP, Hz	2.8	2.1	7	15	2.8	23	10	18
ORDER	16	16	16	16	16	16	16	16

a)



b)



c)

Figure 7.18. The filter sets for the torsional and first three vibration modes for both primary axes of the structure, a) Data of band pass filters f_{HP} and f_{LP} (high-pass and low-pass); b) Band-pass filters for NS direction over Ch#13 (FFT on the NS-component); c) Band-pass filters for EW direction over Ch#14 (FFT on the EW-component)

An automatic procedure was used to separate each frequency band for each recorded waveform. The filtered waveforms were used in an EXCEL animation of the movement of the 12th floor. Figure 7.19 presents examples of vibrations along different modes.

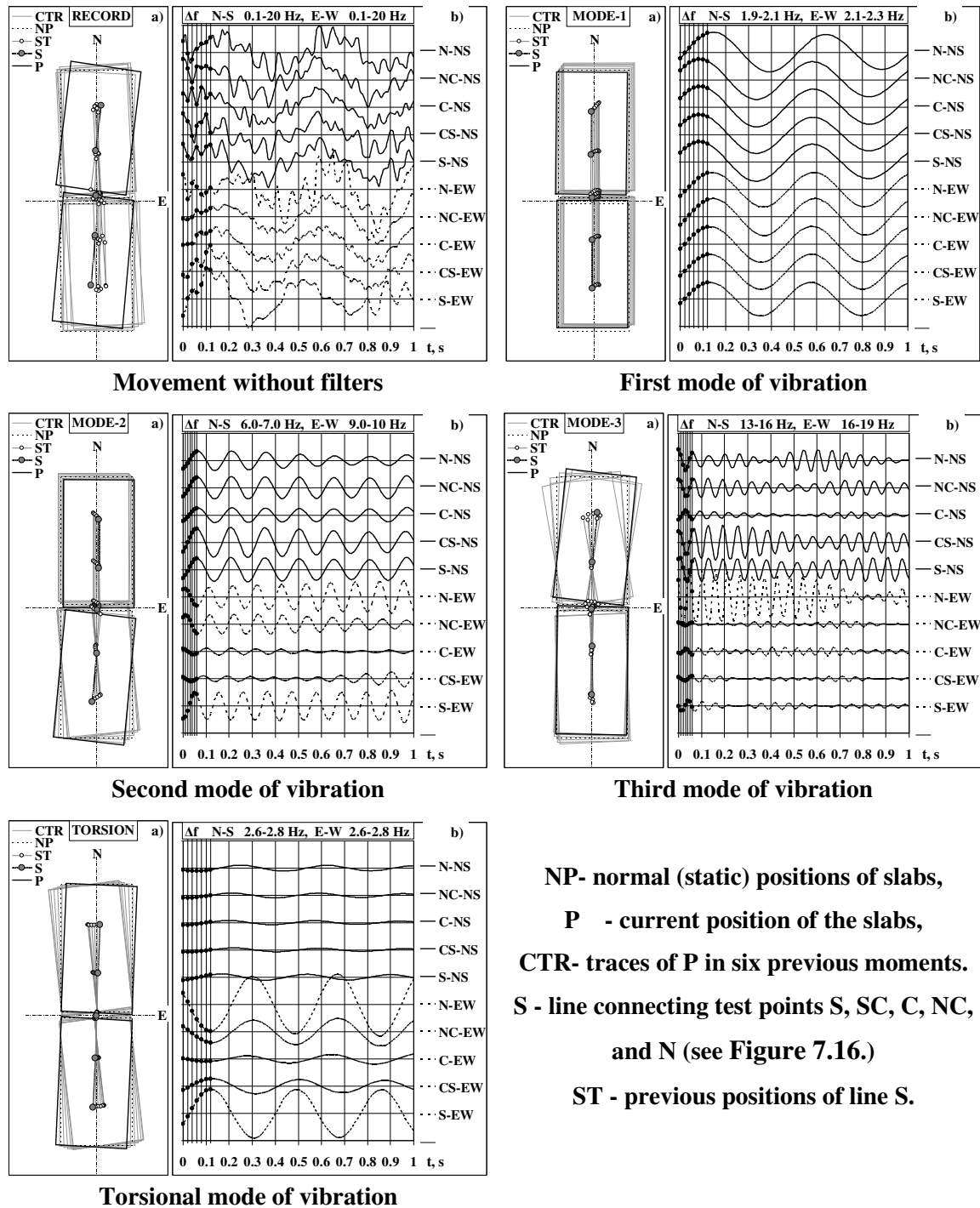


Figure 7.19. Screen-shots of animated movements at points on 12th floor for unfiltered and filtered horizontal waveforms.

7.4. Application of the Horizontal to Vertical Spectral Ratio (HVSR) for Determination of Building Resonances

Recently, there have been some reports on successful use of Nakamura's HVSR technique for determination of the resonant frequencies of buildings (e.g. Irie and Nakamura, 2000; Chavez-García and Cardenas-Soto, 2002; Volant et al., 2002, Gallipoli et al., 2004). In spite of some doubts about its applicability, the HVSR procedure offers a convenient method to evaluate building resonances, and its validity should be verified.

The three-component waveforms collected at 6 different points at two levels of the building are used for this verification. The test points are: TOP-CENTER, BASE-CENTER, BASE-N, BASE-S, BASE-E, and BASE-W. Their positions are shown on Figure 7.20. The measurements at these points were not taken simultaneously, because there is no such requirement for the Nakamura's HVSR technique.

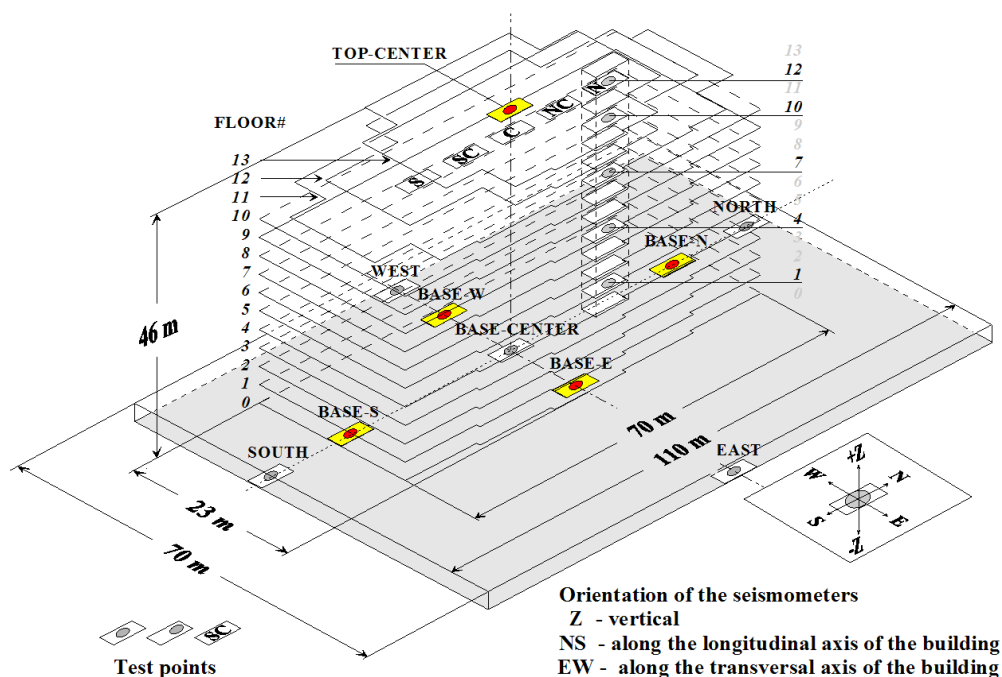


Figure 7.20. Test points used for comparison between building first vibration modes obtained directly from spectra and from HVSR are marked in yellow.

The measurements taken at points at the ground level around the perimeter (edges) of the building were used in the analysis because these points would experience significant vertical movement associated with the building rocking vibration mode.

Thus, the HVSR at these points will be affected by the large vertical movement. In addition, the horizontal component of movement would be associated with the rocking behavior and would have the same resonant frequency as the vertical component. This assumption can be applied to any point which is not aligned vertically with the center of gravity (CG) of a symmetrical structure. If the building is asymmetrical, the HVSR at any point will be distorted by the vertical component of the movement, which would be unpredictable at the time of measurements.

The waveforms were recorded using the three-component seismometer L4-3D at a sampling rate of 100 sps. The spectra were calculated using FFT over records with 32768 samples. This 3-component record was 5 times longer than normally used for HVSR determination in field conditions in order to have better resolution in the frequency domain and more detailed spectral and HVSR presentations of the resonant frequencies at first vibration mode.

The comparison between the original spectra of horizontal and vertical movements and the HVSR from the same waveforms is shown on Figure 7.21. The spectra on the left panes were smoothed by running time window with triangle averaging function on 201 samples (+/- 0.0061 Hz) in linear frequency scale. The HVSR on the right panes are calculated directly from the smoothed spectra. The well distinguished resonant peaks are obvious on both horizontal and vertical spectra for all test points. The HVSR alters the resonances because of the peaks in the vertical spectra.

The horizontal spectra from all test points have two resonances, one along the (NS) axis and one along the (EW) axis. On the other hand, the HVSR plots display both resonances only at the TOP-CENTER point with significantly distorted ratio between them. At the ground level, the HVSR does not display one or both resonances at the first vibration mode due to the significant values of the vertical spectral component around building resonant frequencies due to rocking around the hinge point.

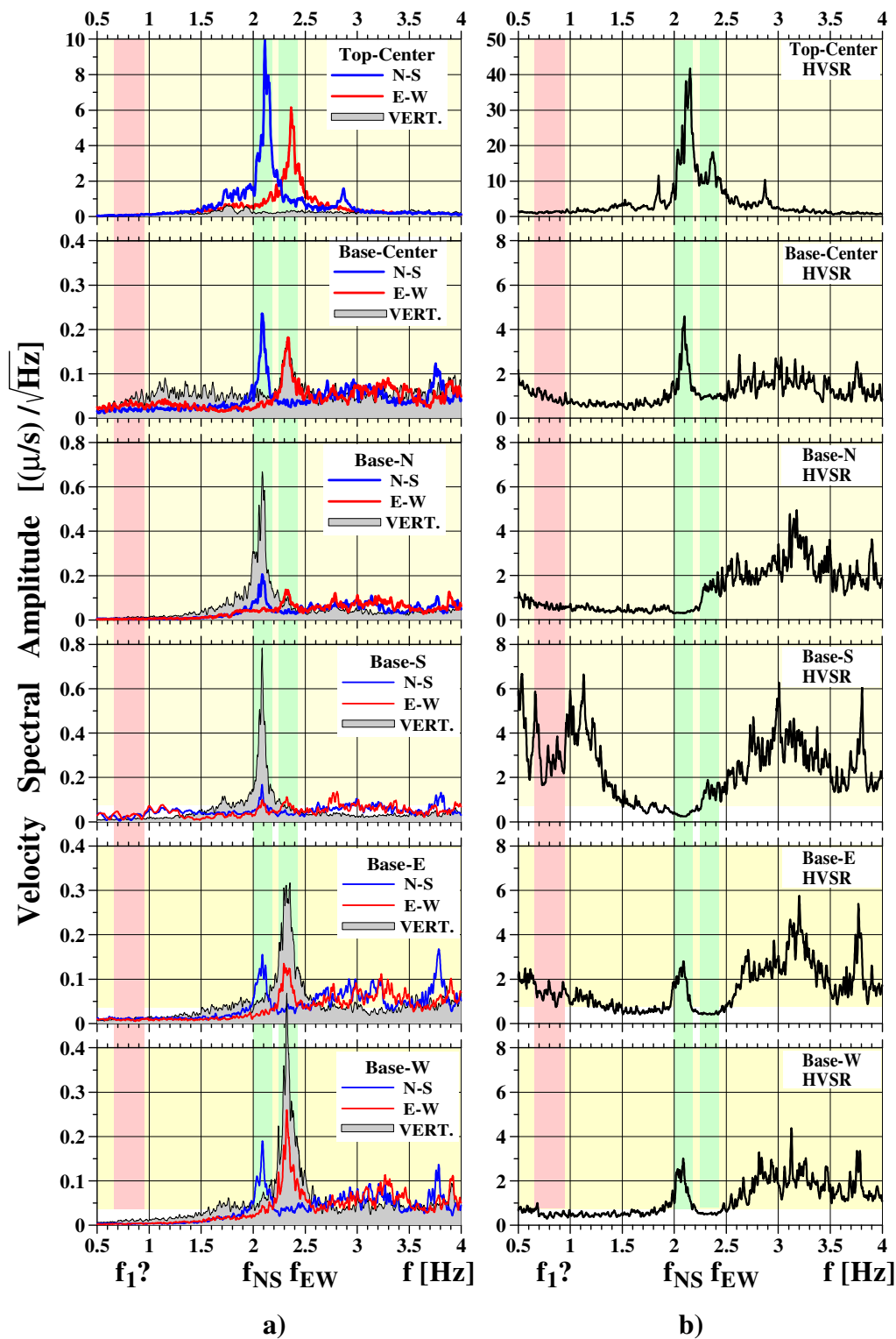


Figure 7.21. Comparison between, a) original spectra from horizontal (N-S and E-W) and vertical (VERT.) movements, and b) HVSR from same waveforms.

$f_1?$ = dominant resonant frequencies calculated from ASCE, f_{NS} and f_{EW} = observed frequency of first vibration mode along (NS) and (EW) building axes.

Determining soil resonances using HVSR assumes different attenuation/amplification of seismic wave amplitudes when propagating in geological strata. Applying HVSR for determination of building resonance has no such physical explanation.

The only plausible justification for using this ratio is to normalize the resonant amplitudes of the horizontal spectra by the values from the vertical spectra and to impose common non-dimensional scale for different buildings in different conditions. Depending on the location of the measurement point, it is possible to miss some or all the horizontal resonances when the HVSR is used for their identification.

The comparison shown in Figure 7.21 is a practical justification for using HVSR inside a building. However, it does not offer any theoretical basis for employing the HVSR technique in order to identify the dominant resonances of the structure.

The HVSR technique should not be used for distinguishing the vibration modes or for establishing potential rocking vibrations. Therefore, it is preferable to either use the resonances from horizontal spectra directly or to employ methods based on spectral decomposition to separate the different vibration modes.

7.5. Influence of Building Vibrations on HVSR Results for Estimation of Soil Resonances

In this section, the effect of building resonances on the HVSR results from measurements taken around the building and the extent of zone of influence of building vibrations.

The first vibration mode produces significant vibrations that propagate in the soil surrounding buildings. The building vertical vibration includes translational component as well as a significant rocking component, which can be noted on Figure 7.15. The movement at the lowest level infers a hinge point of rotation (rocking).

The existence of resonance on the vertical spectra at a frequency equal to that of the first vibration mode at the top centre of the building (see Figure 7.10) can be attributed to the building rocking around a hinge point, which is not exactly below the center of gravity or geometrical center of the building.

7.5.1. Identifying rotation center (hinge point) from collected data set

The waveforms recorded at the edges of building base were used to identify a potential rotation center. One seismometer was installed consecutively at points: BASE-N, BASE-S, BASE-E and BASE-W which are marked in yellow on Figure 7.22.

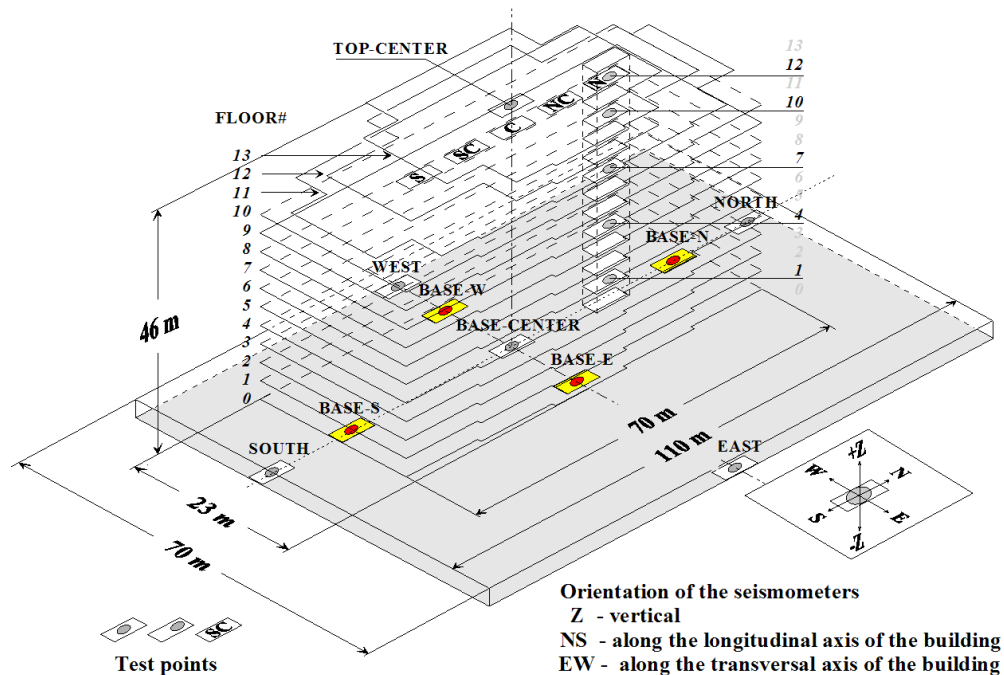


Figure 7.22. Test points (marked in yellow) used to identify a potential hinge point.

All three-component waveforms recorded at the test points shown on Figure 7.22 are filtered in the frequency band from 1.8 to 2.5 Hz at 24 dB/octave for the first vibration mode at which the maximum movement was expected. The records are collected asynchronously. This limits the analysis to proceeding point by point. The filtered records were used to visualize the movement trajectory onto horizontal and two vertical planes. The filtered signal from every record is animated using VB program in an EXCEL worksheet. The records are decimated from 100 sps to 50 sps in order to accelerate the animation. This facilitated selecting suitable time windows for the presentation of polarization and space movement. Usually, these windows coincide with the wind gusts.

A snap-shot of the EXCEL animation for test point BASE-N is shown in Figure 7.23. Figure 7.23a shows the waveforms between 0 and 6 seconds that are used to trace the

movement on the movement polarograms presented in Figure 7.23b for one horizontal and two vertical planes. Figure 7.23c shows filtered waveform decimated to 50 sps and the moving time window, which is extended on Figure 7.23a.

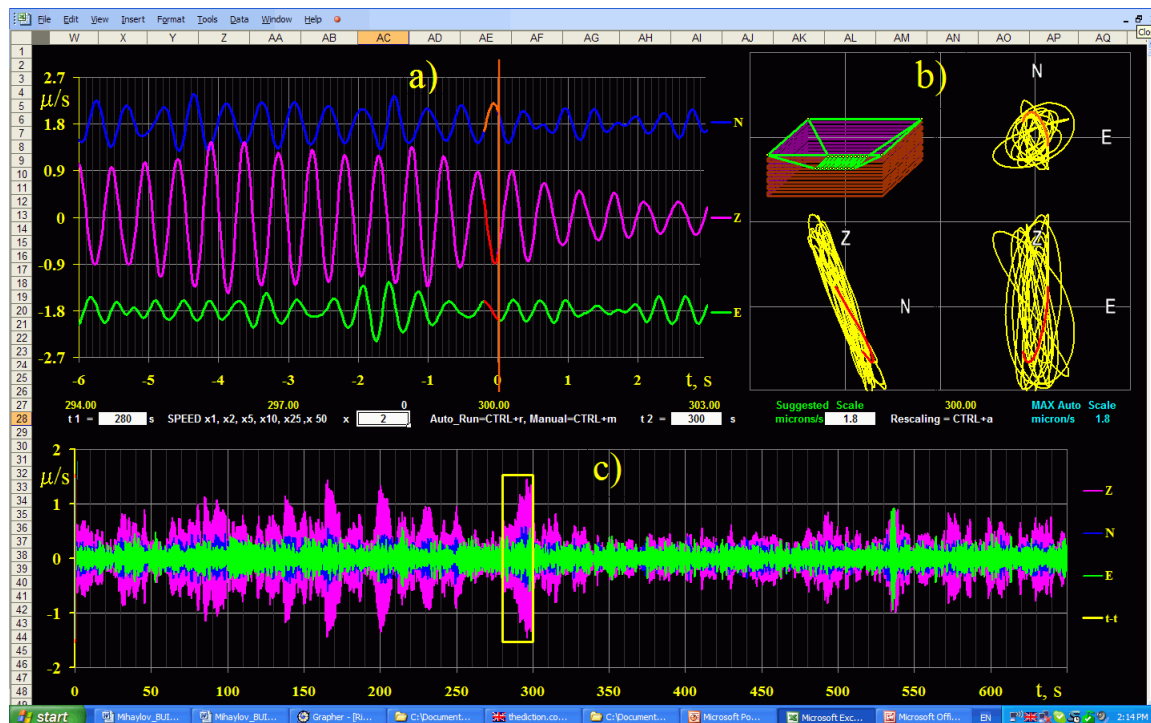


Figure 7.23. Snap-shot of EXCEL animation for test point BASE-N. Polarization of vibrations and movement trajectory.

- a) Extended time window which is marked with yellow rectangle on pane (c);
- b) Polarograms and animated trajectory of test point in different projections;
- c) Filtered waveform and running time window used for pane (a).

Polarizations on Figure 7.23b are traced using the waveform shown in Figure 7.23a as past time series (to the left from the vertical red line). All three selected waveforms were normalized to 90% of maximum movement in order to facilitate reading the trajectories. Figure 7.24 shows the projected movement trajectories on the vertical planes overlaid by main directions of the polarization for the test points which are selected on Figure 7.22. The polarization diagrams display tilting in the vertical planes parallel to the corresponding building axes and almost only vertical movement in the vertical planes perpendicular to these axes.

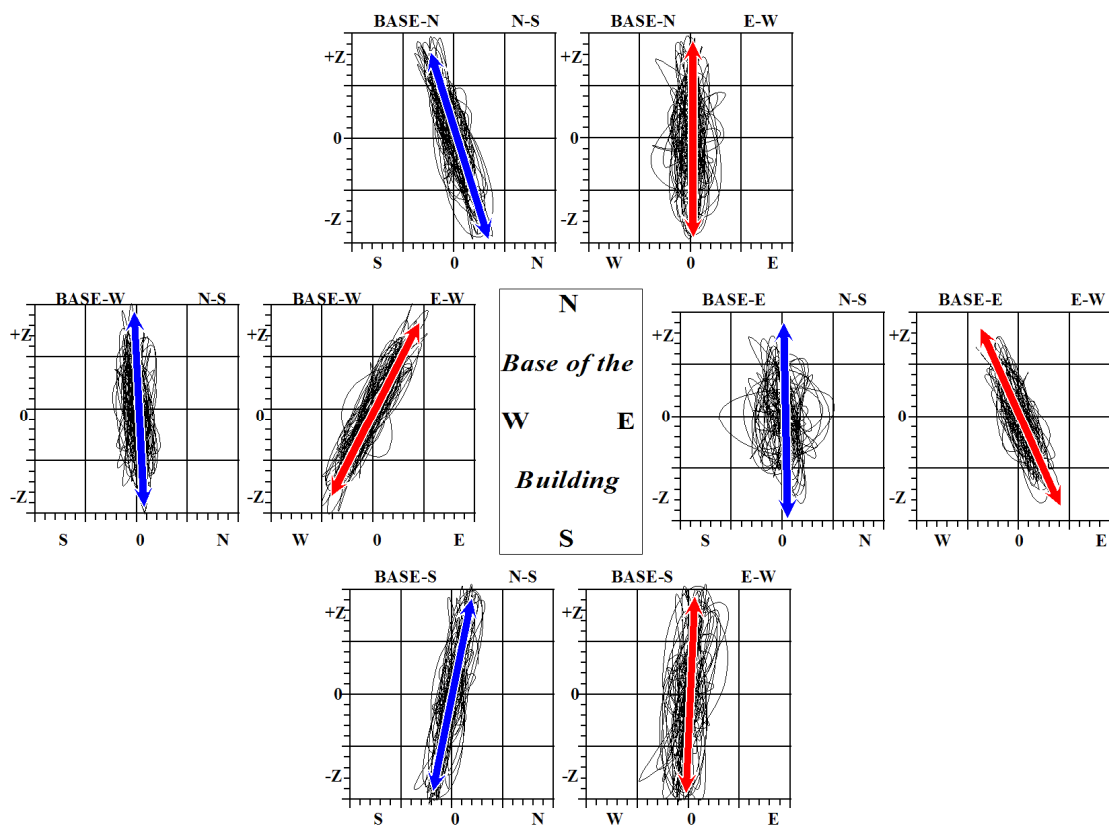


Figure 7.24. Trajectories of vibration in two vertical projections at basement edges. Horizontal components are marked as N-S and E-W; major axes of polarization are marked with arrows over the trajectory projections.

The main movement directions from all four base points were used to define the movement of the building basement and location of the hinge point shown in Figure 7.25. Figure 7.25a illustrates the movement (tilting) of the building basement, while Figure 7.25b depicts a simple geometrical approach used to identify the location of the hinge point. In this case, it is obvious that the hinge point is located aside of the vertical projection of the centre of gravity.

The rotation centre can be identified in Figure 7.25 as an intercept of the perpendiculars to the main movement directions or to the major axes of polarization ellipses.

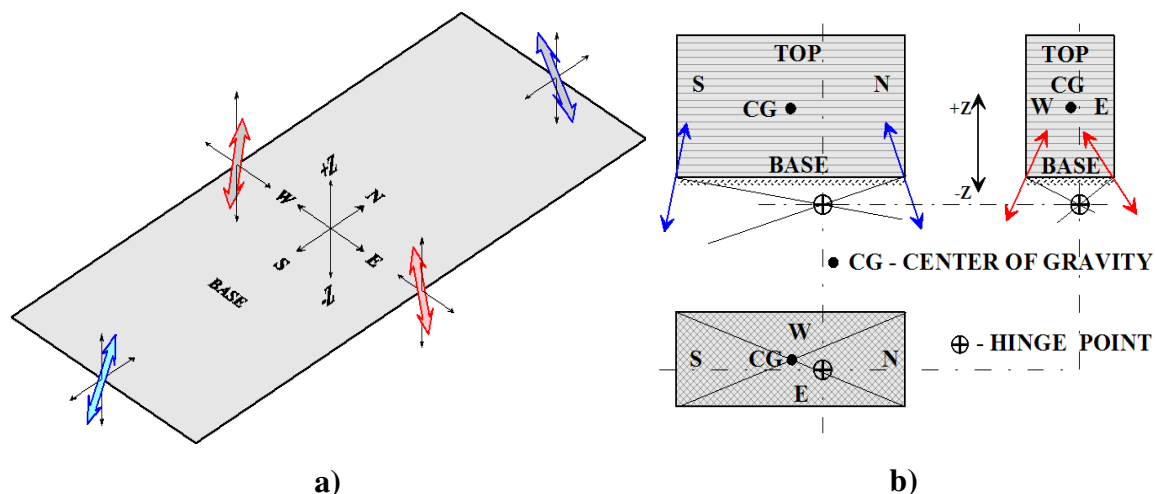


Figure 7.25. Tilting (rocking) of building basement and rotation center point established from main movement directions.

a) Movement directions of basement edges from major axes of polarograms from Figure 7.24;

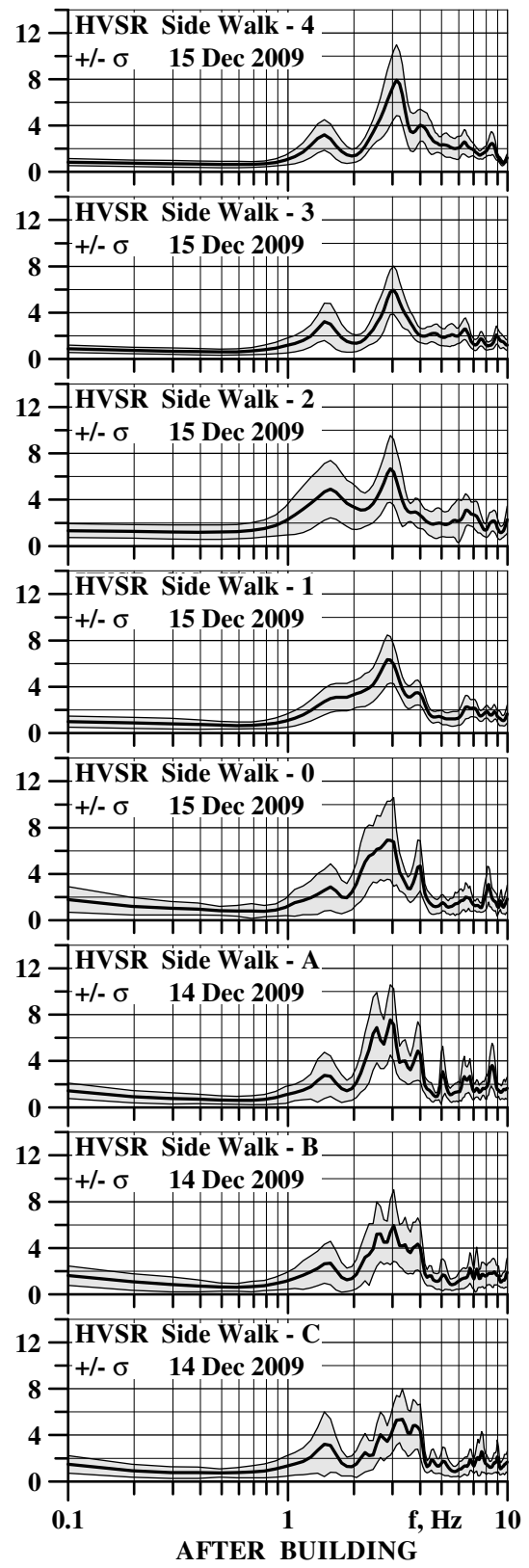
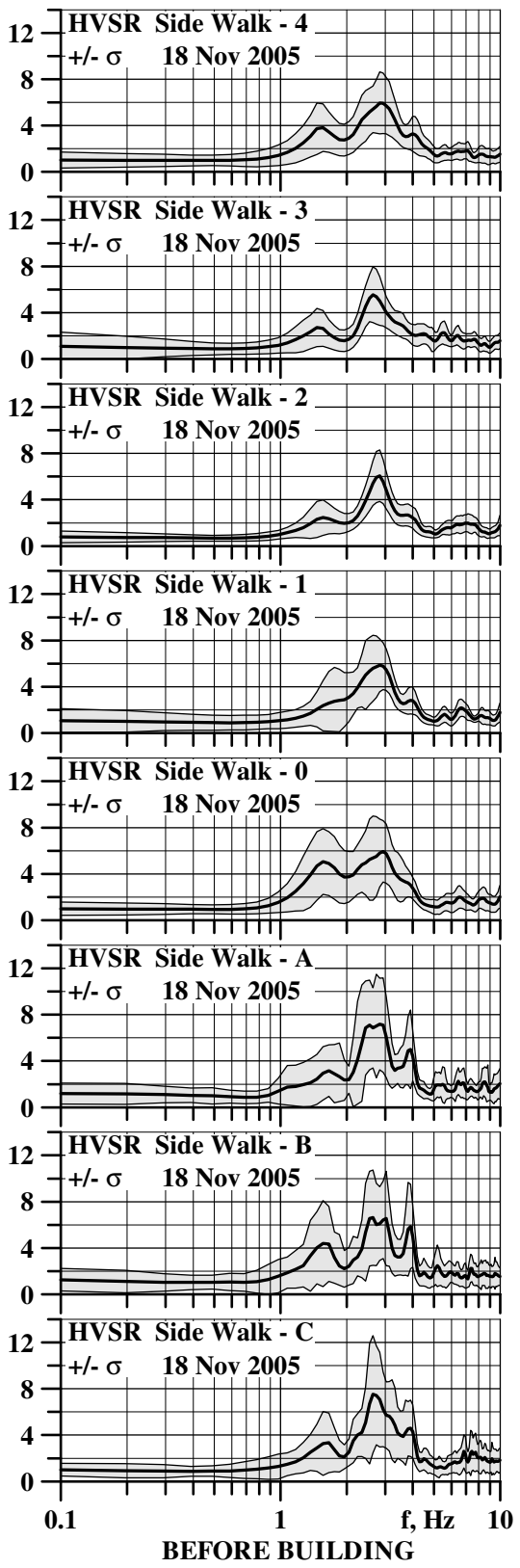
b) Center of rotation identified from main directions in plan view and vertical projections.

This possible rotation center may be attributed to a volume of denser sediments or rocks in the soil structure below the building, which has larger stiffness than the surrounding sediments. Finding the hinge point is important for evaluation of the building vibration and should be considered to predict the dynamic behavior of the structure during an earthquake.

7.5.2. Comparison of HVSR results before and after completion of building.

The vibration measurements were taken at the test points around and inside the building shown on Figure 7.7 once in 2005-2007 before building construction and in 2009-2010 after completion. All measurements were taken at similar wind speed 10-15 km/h gusting up to 25-35 km/h. The measurements along the sidewalk were taken at night time between 10 p.m. and 4 a.m. to avoid the influence of traffic noise from Richmond St. The measurements on the opposite building side were taken in the morning.

The comparison between the HVSR before and after construction is shown in Figure 7.26. In general, both resonant frequencies (at approximately 1.6 Hz and 3.0 Hz) are visible, but with some variation in the HVSR amplitudes.



(Continues on the next page.)

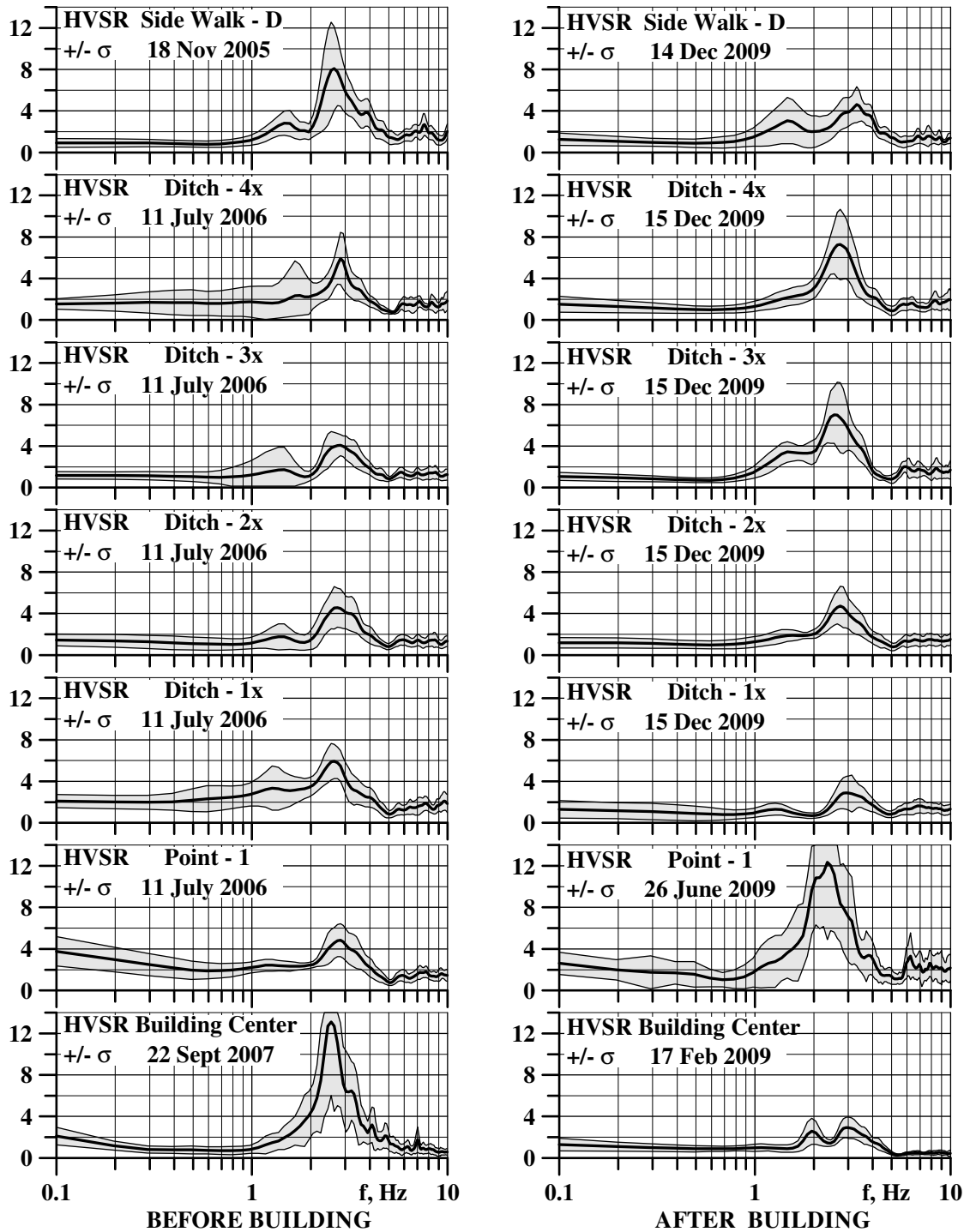


Figure 7.26. Comparison between HVSR before and after building completion.

The locations of test points around the building are shown in Figure 7.7

The differences between HVSR amplitudes before and after the completion of the building were significant for the Building CENTER, edge of underground parking and for point P-1 (Figures 7.26). These differences diminish with the distance from the building and they are almost negligible at distances larger than 50 – 70 m.

These effects are described in general because it is difficult to take into account the changes in the soil profile under each test point, the irregularities in the topography and the irregular changes in the wind speed. In cases of stronger wind gusting above 25–35 km/h, the affected area is expected to be larger.

7.5.3. Seismic wave excitation from building vibrations and wave propagation through soil below and around building foundation.

To better understand and explain the observed large differences between measurements at the building ground level and at the closest test point P-1 outside the building, a simple sketch is shown on Figure 7.27.

Typically, it is assumed that HVSR corresponds to the spectral ratio between shear and compressional waves, which produce horizontal and vertical movements. In this case, recorded horizontal and vertical movements were not necessarily only shear and compressional waves. The vertical movement is possibly due to the first vibration mode (building rocking around a hinge point).

The polarogram for point BASE-N shows the most intense vertical dynamic load obtained from the filtered waveform within frequency range 1-4 Hz. It clearly demonstrates that the vertical component of movement was larger than the horizontal component. These movements can be considered as a source of seismic waves, which propagate with attenuation shown over their ray paths. The idealized ray paths to points NORTH and P-1 and attenuation are also shown on Figure 7.27.

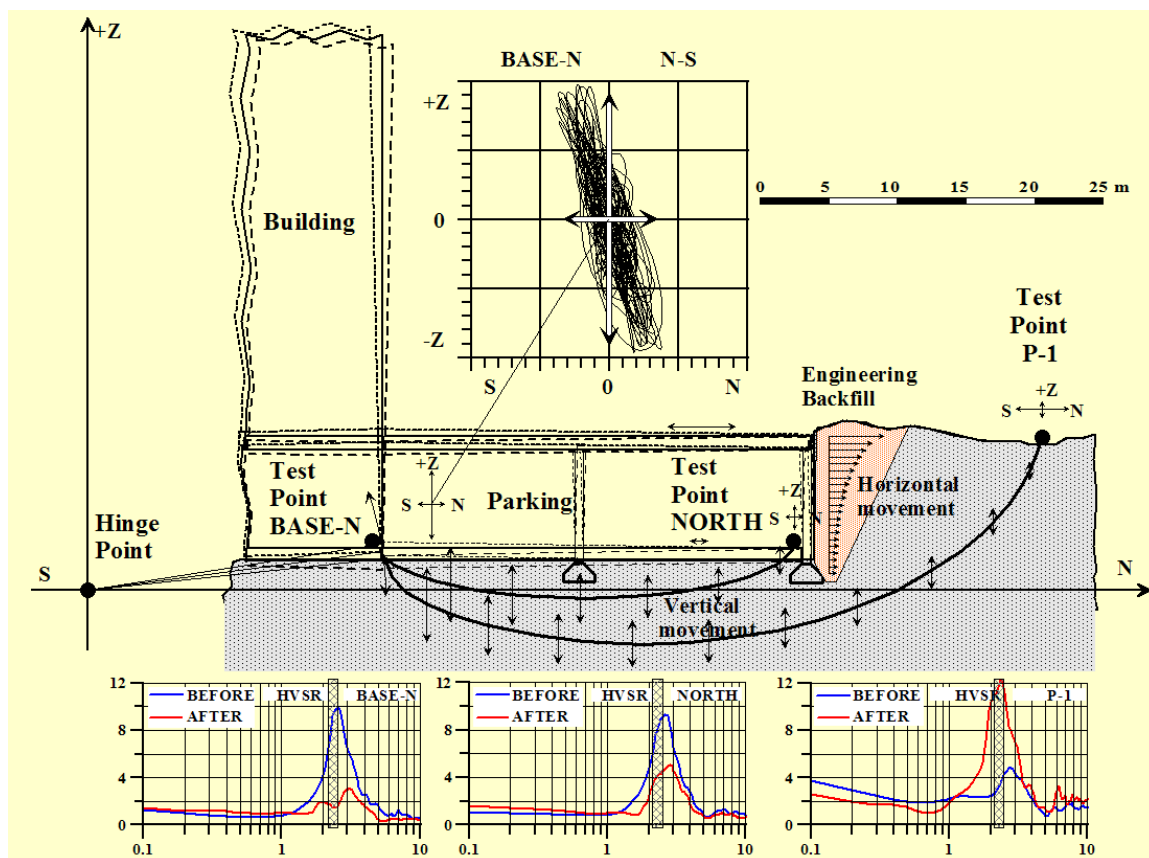


Figure 7.27. Sketch of propagation of seismic waves due to building rocking around hinge point S. Polarogram for point BASE-N and HVSR for points BASE-N, NORTH and P-1; attenuation of waves vertical components over their ray paths.

The movement due to the horizontal rocking component follows different path. The building rocking pushes the parking walls/concrete slab, which compresses the outer wall toward the engineering backfill. The wall top points transfer larger horizontal motion, which is transmitted into the soil structure and attenuates fast with the distance and depth (a simplified loading diagram is shown in Figure 7.27). This mechanism of generation, propagation and attenuation of seismic waves would give similar horizontal movement at Base-N (the building edge) and NORTH (edge of parking slab). The large horizontal movement just outside of the parking at point P-1 gives a strong but false HVSR maximum, which is not related to the soil parameters. The above analysis can explain the differences and scattering of the HVSR maxima after completion of building relative to those before construction found over same data set (Oskirko, 2010).

7.5.4. Influence of first vibration mode of building on the HVSR results

The first building resonances varied between 2.0 and 2.4 Hz, which is close to the HVSR resonance at the field points (between 2.5 and 3.2 Hz). It should be noted that the HVSR measurements at the base center (on top of the concrete foundation) were taken before the building was erected but after the foundation was completed. The foundation construction involved removing of 1-1.5 m of soil. The comparisons provided in the previous section show that it is useful to establish experimentally the resonant frequencies of the closest building to the HVSR measurement point in order to avoid misinterpretation of HVSR results for the soil profile. If it is not possible to verify the influence of building resonances on the calculated HVSR results, their value would be questionable.

The HVSR technique presumes a horizontal movement produced by propagation of horizontally polarized SH shear waves. The building vibrations generate mainly compressional P-waves and Rayleigh waves. In case of a soil resonance close to the fundamental building period, the building vibrations could cause suppressing or splitting of the HVSR soil resonance: for example Side walk-D on Figure 7.26.

The HVSR resonances are obtained after smoothing of the individual spectra using triangle or rectangular windows in the frequency domain following by averaging of all HVSR ensembles. These procedures lead to widen of the resulting HVSR resonances in cases with not very contrast boundaries between overburden and bedrock. On other hand the buildings dominant resonances are usually very sharp and they are calculated without so much averaging and smoothing. These resonances are narrow relatively to those obtained from HVSR. That's why parts of HVSR resonances remains after suppressing by the sharp building resonance.

At distances approximately 50 – 70 m (comparable to the building largest dimension), both the horizontal and vertical movements created by the building vibrations attenuate and do not affect the HVSR ratio.

All field measurements were taken when the wind speed was 20-25 km/h gusting to 30-35 km/h. If the wind speed is higher, the affected area should be bigger. That's why the field HVSR records in GTA was collected when the wind speed was less than 20 km/h.

Chapter 8

Building Resonances Estimated by Empirical Correlations and from Field Measurements

8.1. Introduction.

The results from seismic microzonation have to be used in conjunction with responses of the buildings and other structures during earthquake shaking. It is important to study the real building resonances and potential nonlinear effects before, during, and after an earthquake. The vibration measurements which have been taken on an RC building (Figure 7.5) are used to establish the changes of resonant frequencies due to wind loading and with time. The records were collected after completion of the construction and about two and a half years later. The first resonant frequencies of the building established from the measurements of the building vibration due to wind loading were significantly higher than it is supposed to be according to the empirical formulae in existing building codes and design guidelines. In the following an explanation for this discrepancy is given.

8.2. Building resonant frequencies estimated using empirical correlations and finite element modeling

The resonant frequency at the dominant vibration mode of a building can be estimated using empirical formulas that relate the fundamental period to the type of the construction and building dimensions. One of the widely accepted formulae is the simple relation:

$$T[\text{sec}] = \frac{\text{Number of storeys}}{10} \quad (8.1)$$

Similarly, the NBCC 2005 and many design guidelines (e.g. International Handbook of Earthquake Engineering, 1994) estimate the fundamental period of a framed structure as:

$$T[\text{sec}] = 0.09 \frac{H}{\sqrt{D}} \quad (8.2)$$

where H is the height of the building and D is the width of a braced frame or span between columns. In our case $H = 46$ m and $D = 7.5$ m (Figures 7.5 and 7.8.)

For buildings with shear walls, the NBCC 2005 provides the following equation:

$$T[\text{sec}] = 0.05(h_n)^{3/4} \quad (8.3)$$

where $h_n = H = 46$ m is the height of the building.

A Finite Element Model (FEM) of the building was developed (by Dr. Alper Turan and Dr. Richard Oskirko, former graduates of UWO) considering the as-built geometry of the structure and commonly accepted parameters for concrete and reinforcement of this type of buildings. The first resonant frequencies calculated from the FEM were in the range 0.6-0.8 Hz. The fundamental frequencies obtained using the above empirical equations (Eqs. 8.1, 8.2, and 8.3) and from FEM calculations as well as that established from the building vibration measurements are summarized in the Table 8.1.

Table 8.1. Building first resonance obtained from empirical correlations, FEM and field measurements.

Basis	$T[\text{sec}]$	f [Hz]
$T[\text{sec}] = (\text{Number of storeys})/10$ (eq.8.1)	1.30	0.77
$T[\text{sec}] = 0.09 H / \sqrt{D}$ (eq.8.2)	1.51	0.65
$T[\text{sec}] = 0.05(h_n)^{3/4}$ (eq.8.3)	0.88	1.14
$T[\text{sec}]$ from FEM average	1.40	0.71
From field measurements	0.47	2.12

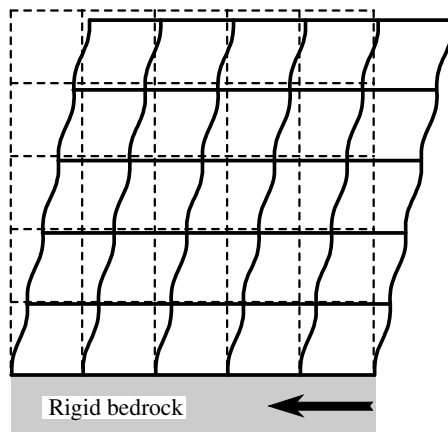
8.3. Building with RC Frame Construction Under Dynamic Loading

The examined RC framed construction includes RC frame, floor slabs and shear resisting elements - shear walls, stair and elevator cages. The RC frames consist of beams and columns, which provide resistance to the gravity by the axial strength of the columns and to the lateral loads through the flexural rigidity of the beams and columns. The joints should have sufficient strength to enable redistribution of the dynamic load to the adjoining flexural members.

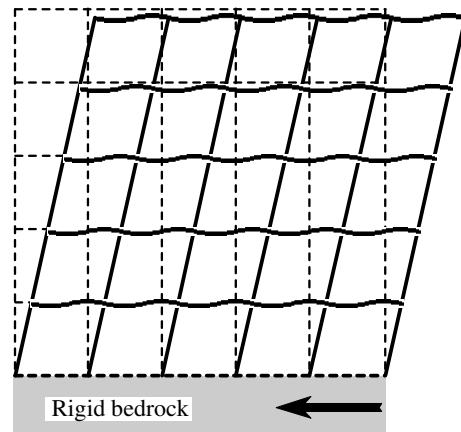
Figure 8.1 shows several types of RC frame constructions subjected to seismic loading. The direction of the seismic movement at a moment of time is indicated by arrows on the figure. The description of the different RC frame constructions is as follows:

a) - The weak column-strong beams design, which is not recommended by the current building codes but many existing buildings still have this construction (Figure 8.1a). This configuration can lead to “soft” first floor due to removing of some shear walls at the ground level in order to have bigger open spaces. This type of construction is prone to loss of stability and could collapse even during moderate earthquakes due to plastic hinges formed in the columns.

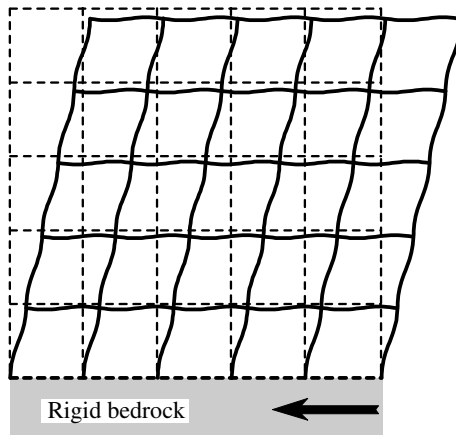
b) - The strong column-weak beam design (Figure 8.1b) is recommended by most current building codes. In this case, it is expected that plastic hinges would develop at the end of the beams. This construction usually needs additional shear resistant elements.



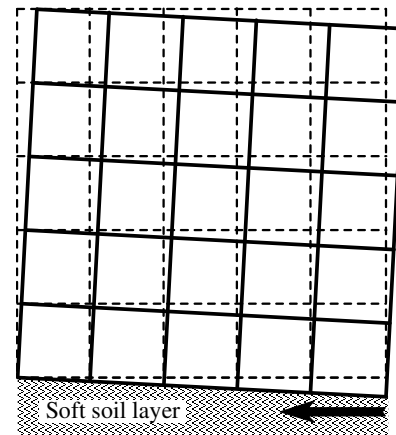
a) strong beam and slab - weak column



b) strong column - weak beam



c) uniformly distributed strain energy



d) relatively rigid structure over soft soil

Figure 8.1. Deformation of RC frame buildings with different stiffness of the columns and beams. The joints are assumed undeformed. The arrows show the seismic movement.

c) - A building may experience plastic deformations at ends of the beams and columns (Figure 8.1c). It is difficult to ensure strong column-weak beam design in case of cast in place beam-slab elements. This can be compensated by adding infill or concrete shear walls or other bracing members.

d) - A relatively rigid RC frame with shear walls on weak soil layers can react to an earthquake by tilting (rocking) without sizable deformation of the structure (Figure 8.1d).

The building considered in the study belongs to type (d) – RC frame with cast in place floor slabs and concrete shear walls from the basement level to the last floor of the building. The construction should be considered as a rigid structure on relatively soft soil layers. The building exhibited rocking as first vibration mode with hinge point shown in Figure 7.25.

8.4. RC structure under dynamic lateral load.

Several studies have been focused on experimental dynamic testing of different concrete specimens and RC structural elements (e.g. Celebi and Penzien, 1973; Otani, 1980). Many theoretical models were developed to describe the behavior of concrete elements under dynamic loading. Most of these models are based on modifications of the classic viscoelastic Maxwell model or on the viscoelastic-plastic-model proposed by Sercombe et al. (2000) (e.g. Pedersen et al., 2008; Ile and Reynouard, 2000). The response of RC elements and structures under dynamic load has been investigated extensively using numerical models (e.g. Filippou and Issa, 1988; D'Ambrisi and Filippou, 2000; Haselton, 2006). In addition, there are many studies on the assessment of the damage after strong earthquakes using models and data from cyclic load tests (e.g. Lee and Fenves, 1998; Repapis et al., 2006).

Over the last 50 years, numerous papers examined the nonlinear effects and stiffness degradation of RC elements and structures subjected to cyclic loading or affected by earthquakes.

The stiffness reduction is considered here in order to explain the observed difference between resonant frequencies obtained from direct measurements and these suggested by the building codes or calculated by numerical modeling (Table 8.1).

The concrete is assumed as brittle composite subjected to gradual degradation under weak lateral forces usually produced by gusting winds. The dynamic loads from an earthquake are significantly larger and cause abrupt changes of elastic properties and integrity of RC members and structures. The following main properties of the structural members and concrete should be taken into account:

- A concrete member consists of aggregates, rebar and additives bonded by hardened cement paste (binder). The total strength of the member is due to cohesive internal forces in the binder, and adhesion to the other components in the composite. Equal cohesive and adhesive forces are assumed to be distributed evenly before dynamic loading.
- Concrete is a brittle material with high compressive strength and little tensile strength. After pouring, the properly hardened and cured cement paste exhibits drying shrinkage. This process causes loss of volume in the binder and develops tensile stresses directed inward at any point of the binder and has the same direction with chemical cohesive forces, which keep the particles bonded. The shrinkage apparently increases the cohesive force and adhesion between the binder and other components. The concrete paste without restraints contracts evenly, virtually without cracking.
- All concrete members of an RC frame are subject to some restraints caused by the rebar, aggregates or by the adjacent members. These restraints change the distribution of the tensile stress in the real concrete structure during the shrinkage. Concrete cracks when the induced tensile stress in the critically overloaded directions overcomes the tensile capacity of the binder or aggregates. Usually, these small cracks are accounted for during the design of the concrete members.
- Concrete members are subjected to very slow gradually vanishing internal tensile stress. This rheological process is usually expressed as viscoelastic creep.
- The gravitational load is assumed to be large enough to keep the RC members under compression during the dynamic loading. This ensures that the concrete will not experience excessive tension due to bending resulted from applied lateral dynamic force. The loading diagram according to these conditions for a segment of a RC column close to its upper end and below the beam-column joint is illustrated in Figure 8.2 for a cross-section experiencing maximum curvature due to bending.

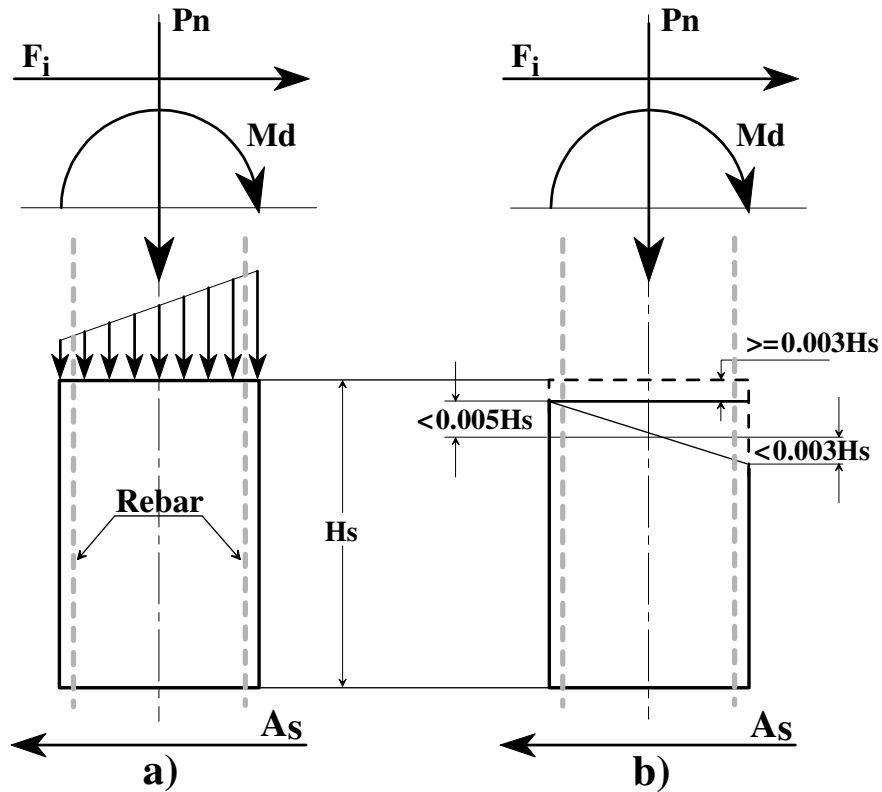


Figure 8.2. Segment of a RC column under static and dynamic loads.

H_s - unloaded height.; a) Forces and stress distribution: seismic movement, F_i - dynamic inertial force, P_n - gravitational load, M_d - dynamic bending moment; b) Deformation diagram: static deformation $\geq 0.003H_s$, maximum rebar extension $< 0.005H_s$, maximum compression $< 0.003H_s$.

- The segment shown in Figure 8.2 has reinforcement only along the direction of static load. Transverse reinforcement is not considered here to simplify the model (i.e. ignoring redistribution and concentration of stresses and potential forming of zones of additionally pre-stressed concrete which surrounds this type of reinforcement).

The static and dynamic loads of this segment are shown on Figure 8.2a. The corresponding deformation is shown on Figure 8.2b. The gravitational load P_n is supposed to cause evenly distributed compressional stress over the entire cross-section. The deformation under this static stress is assumed to be more than $0.003H_s$. This prevents the development of resultant any tensile strains during cyclic loading. The seismic horizontal ground movement is A_s . It causes an inertial dynamic force F_i at the joint above the segment, which produces bending moment M_d .

8.5. Change of resonant frequencies of the studied building 2.5 years after construction.

Redistribution of tensile stresses and consecutive cracking of the overstressed parts of the concrete are not limited by the intensity of the lateral dynamic loading. The processes which lead to degradation of concrete can arise during weak vibration produced by gusting winds. The loading scheme on Figure 8.2 is applicable in this case too. Figure 8.3 shows velocity spectra for the top floor of the studied building obtained from waveforms recorded in a 2.5 years interval. In spite of difference of outside temperature during both tests, the temperature of the structure and inside the building was almost the same.

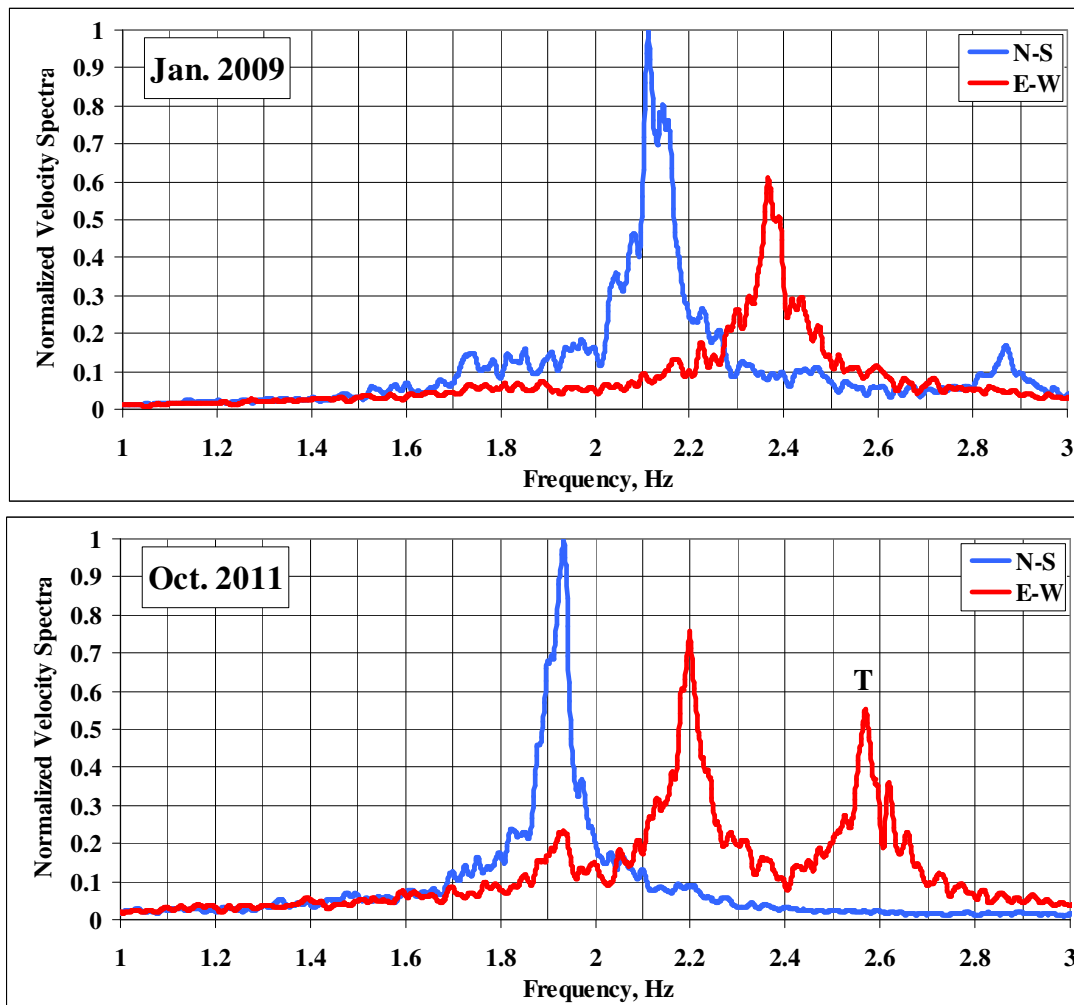


Figure 8.3. Velocity spectra from the waveforms recorded in 2009 and 2011 at the top floor of the building smoothed with triangle window ± 0.01 Hz

T - marks the torsional vibration mode recorded in 2011.

The torsional mode marked with **T** on the E-W spectrum on Figure 8.3 is recorded in 2011 only, because the measurement was taken at the North end of the building. At that time, the top center point of the building was occupied and inaccessible. The torsional resonance appears also on the N-S spectrum from 2009 because the test point was slightly aside in West direction from the CG vertical projection.

Table 8.2. Changes of the building first and torsional resonances (Hz) with years.

MODE Year	First N-S	First EW	Torsional
2009	2.12	2.36	2.88
2011	1.93	2.20	2.57
Change	-9 %	-7 %	-10 %

To apply the experimental results to the studied building in a case of strong earthquake, two scaled transfer functions are calculated considering the proposed from building codes empirical relation and measured building vibrations. Two reference points (**RP-1** and **RP-2**) are shown on Figure 8.4 in order to illustrate possible changes in resonant frequencies and the dynamic properties of the building due to gusting wind loading and expected shaking from moderate or strong earthquake.

The first reference point (**RP-1**) involves the response of the new building to small lateral load due to gusting wind. In this case, the response function is found by approximation of the smoothed FFT spectra of the horizontal movement at the top level of the building recorded in 2009. For this reference point, a resonant period of 0.47 s and damping ratio of 1% are measured from the best SDOF approximation of the smoothed spectra.

The second reference point (**RP-2**) is from calculating of the building first resonant frequency employing the empirical correlations considering the building dimensions. It is supposed that after intense earthquake shaking the resonant frequencies will reach the values predicted by the building codes.

At the beginning of a strong earthquake shaking, the building will respond with higher resonant frequencies corresponding to the undamaged structure.

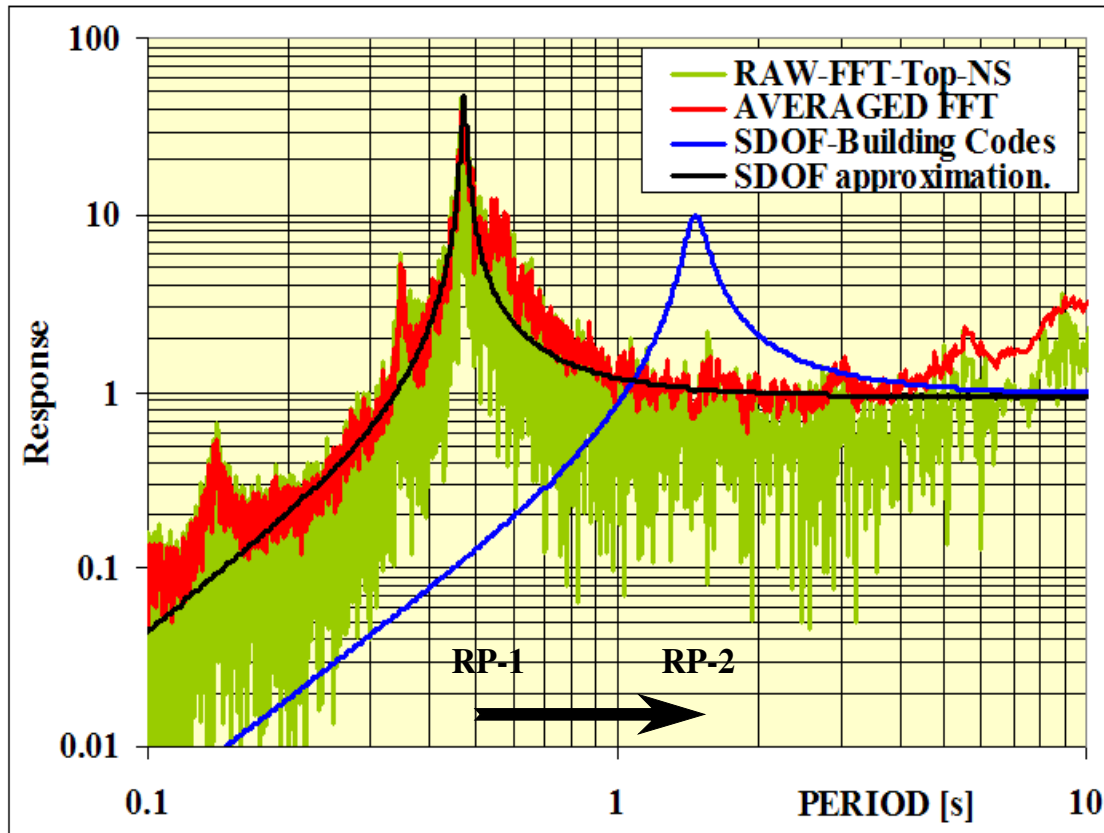


Figure 8.4. Reference SDOFs over transfer function calculated from NS unfiltered velocity waveform recorded at the Top-Center test point of the building and calculated from equations in the building codes.

The designations on Figure 8.4 are:

- RAW-FFT-Top-NS FFT is the FFT amplitude spectra over 32k samples,
- AVERAGED FFT is the smoothed spectra in the frequency domain with a running triangle window ± 0.014 Hz.
- SDOF-Building Codes is calculated from the empirical relations for a 13 story RC building (resonant period of 1.5 s with suggested damping ratio 5 %).
- SDOF approximation is calculated over AVERAGED FFT for the first building vibration mode with measured resonant period of 0.48 s and 1 % damping ratio.

It is important to verify independently the SDOF parameters obtained from the approximation of the smoothed transfer function. This was done using NS component of the recorded vibration velocity at the Top-Center test point. A fourth order Bessel-Gauss filter was applied between 1 and 10 Hz. Relatively short time intervals of the waveform after wind gusts were extracted for analysis, which are shown on Figure 8.5.

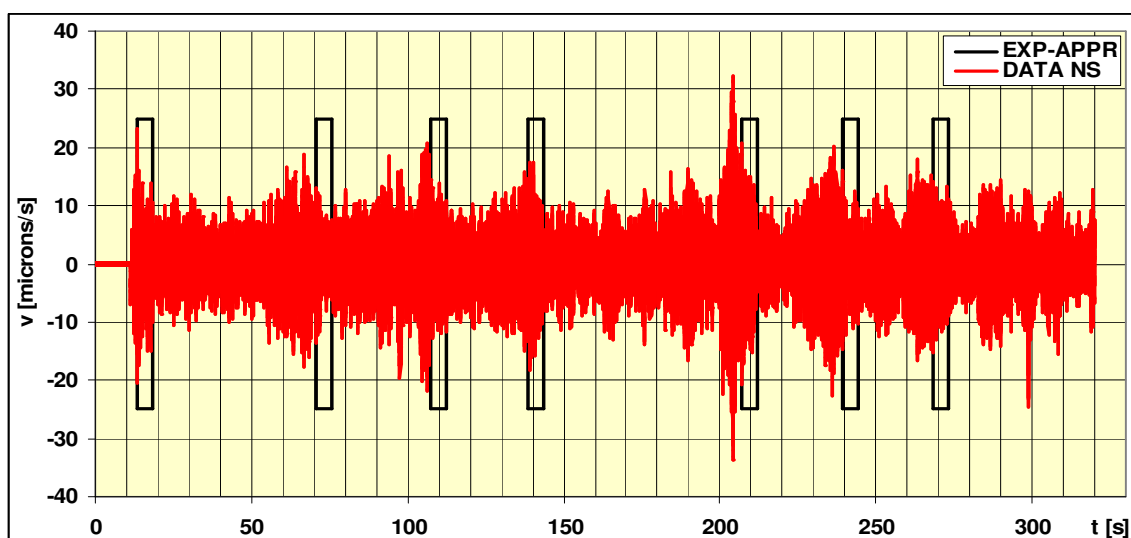


Figure 8.5. Velocity waveform at the top of building and time windows after wind gusts used for approximating the free oscillations with damped sinusoid. DATA NS - velocity waveform NS component; EXP-APPR - time windows.

The waveform during the first several seconds after each gust contains almost free oscillations of the top of the building in the chosen NS direction. After that, the waveform is affected by the closely spaced resonances for the first orthogonal (EW) and torsional vibration modes which can be seen on Figure 8.6.

The resonant frequency and damping factor for the first mode were found by approximation of the recorded waveform with an exponentially attenuating sinusoid:

$$x = X_0 e^{-D\omega_0 t} \cos(\omega_D t), \quad (8.4)$$

where: $\omega_0 = 2\pi/T_0$ and $\omega_D = \omega_0 \sqrt{1-D^2}$,

X_0 is a scaling coefficient; D is the damping factor;

ω_0 and ω_D are undamped and damped frequencies (rad/s);

T_0 is the undamped period at the first vibration mode.

The approximation with a faded sinusoid and its envelope are shown on Figure 8.6.

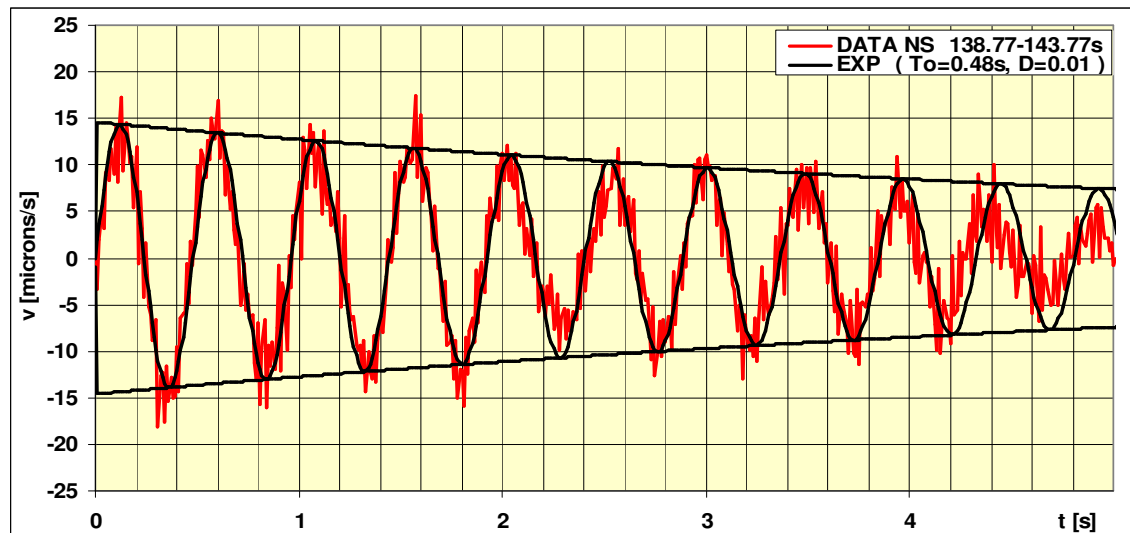


Figure 8.6. Approximation of the free oscillations at the first vibration mode in NS direction for the TOP-CENTER test point.

(DATA NS 138.77-143.77s - used time window; EXP - the approximation).

The phase shift between the originally recorded waveform and the approximation with the attenuated sinusoid after fourth second can be explained by the interference between NS, EW first vibration mode and torsional resonant vibrations. The results from this approach give the same values for the resonant period of 0.48 s and damping factor of 1% as those obtained from the spectral decomposition (Figure 8.5).

8.6. Relation between resonant frequencies and damping ratios obtained from direct measurement and from empirical calculation

When a building is subjected to high excitation level, its stiffness degrades and consequently its resonant period and damping ratio increase. The decreasing of the resonant frequencies of the structure is proportional to the square root of the inverse value of the stiffness reduction. This assumption is based on the classical steady-state test results (e.g. Jennings and Kuroiwa, 1968). It is also confirmed by observations of damping in buildings under low-amplitude and strong motions vibrations before, during and after 1989 Loma Prieta earthquake (Celebi, 1996).

The resonant frequency and damping ratio obtained from direct measurements depend on the current condition of the tested structure, which is a result of its dynamic loading history. A new building, which is still unaffected by significant but nondestructive lateral dynamic load, will have a sharp short period resonance with low damping. These two parameters will slowly increase due to cracking which is provoked by weak ambient vibrations. During a moderate local earthquake, the structure will react to the ground shaking with considerable amplification at high frequency body waves, which arrive first. This increased dynamic load causes damages of the structure, absorbing the vibration energy. This process increases the building resonant period and damping ratio. The low frequency surface waves, which arrive after the body waves, shake the already damaged structure close to the newly created resonance and additionally increase the damaged volumes.

If the building survives this moderate earthquake, its resonant period and damping ratio will have increased permanently. The formed zones with plastic deformation and reduced stiffness will behave as frictional energy absorbers increasing the resonant period and global damping ratio and reducing the resonant amplification.

The basis for the empirical response functions used currently in building codes is the experimental data, which is usually collected from some buildings in seismic active zones. The older buildings in those zones most probably had been subjected to some moderate or strong earthquakes after which they were already damaged and had relatively longer resonant periods and larger damping ratios. As a result, at the time of in-situ tests and measurements the obtained response functions have longer resonant period and higher damping. The relations between the resonant frequency and some dimensions of the structures used in the building codes tend to be consistent with the resonances obtained from some buildings in seismic active zones. The widely used value of 5% for the initial damping of the RC structures can be explained with an adoption of the results from buildings already affected by strong motion.

This empirical approach can be justified if the dynamic behavior of some benchmark buildings with different construction is monitored starting from the free field response function, after completion of the structure, during the life time of the building, before,

during and after moderate and strong earthquakes, strong wind etc. Such a program for monitoring of benchmark building was proposed by ASCE Task Group on Structural Health Monitoring in 2000 (Johnson et al., 2001). This long-term monitoring would allow structural engineers to use real structural responses in standard data analysis and modeling techniques in order to predict the response of the structure. After an earthquake, the collected data from instrumented buildings can be complemented by inspection and documentation of the damages that the building has experienced.

8.7. Implementation of stiffness reduction and increase of resonant period and damping ratio of a building during strong earthquake

Investigating damages after Mw 8.8 Chile Earthquake on February 27, 2010, Kovacs noted (Kovacs, 2010): “Most of the larger buildings in Chile performed well. The Earthquake Engineering Research Institute reports (EERI -June 2010) that 50 multi-storey reinforced concrete buildings were severely damaged and will need to be demolished, while four buildings collapsed. Any poor performance of newer structures appears to be the result of oversights in the design process, perhaps failing to anticipate the effects of soft soil deposits, or due to construction deficiencies”. The (EERI Special Earthquake Report – June 2010) specifies that “majority of damage was concentrated in newer buildings”.

To check out how the initial stiffness and resonant parameters will affect the survivability and damage of a 13-story building and its structural elements, the 3-component record of acceleration waveforms in Vina Del Mar, Chile (Figure 8.7) is used. From Figure 8.7, the maximum horizontal acceleration is 0.32 g in EW and 0.22 g in NS directions. Visually the periods of acceleration records are less than 1 second for the part with maximum intensity and less than that for the body wave part before it.

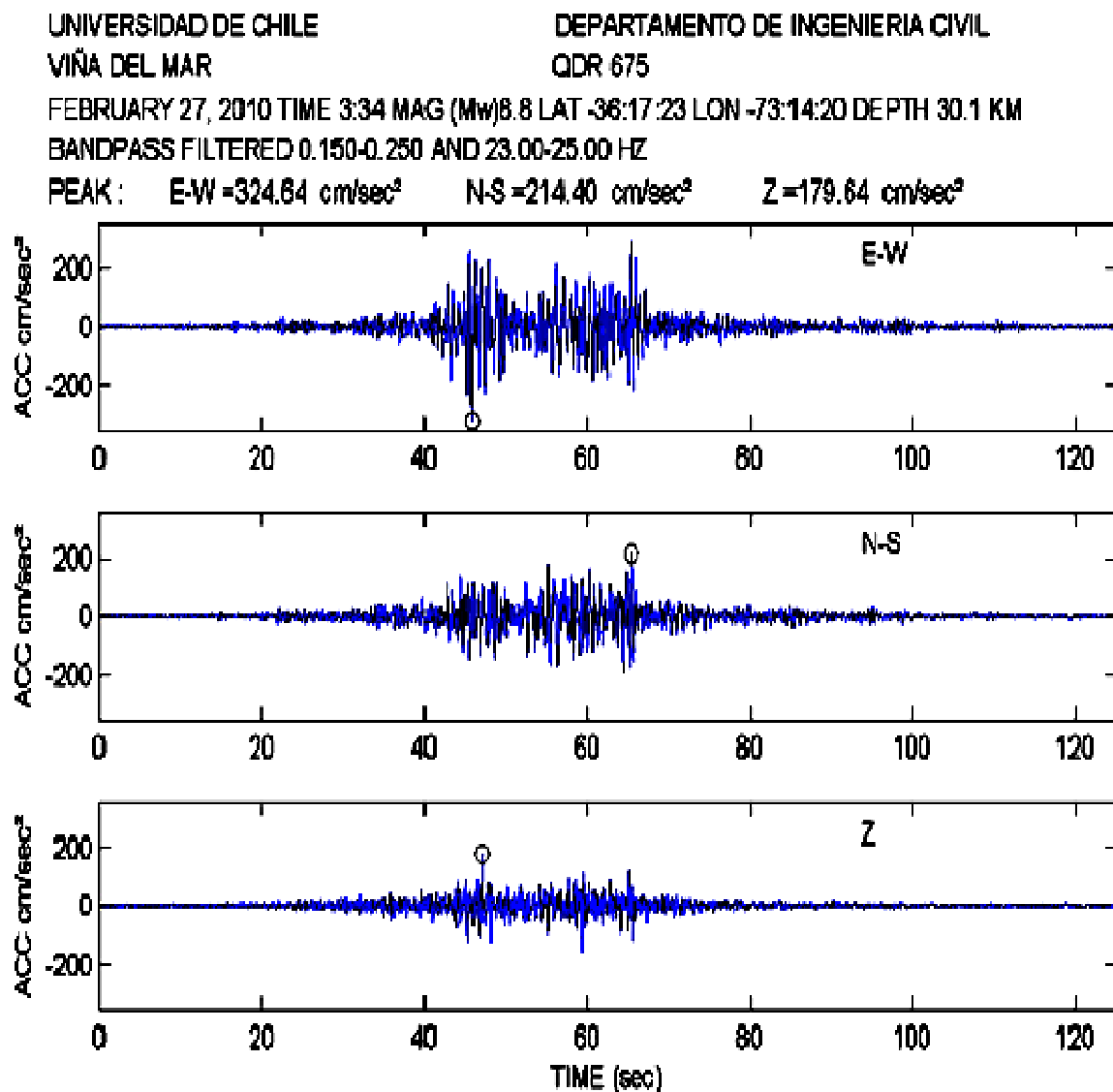


Figure 8.7. Acceleration waveforms, Vina Del Mar, Chile Mw=8.8 February 27, 2010 (source: Boroschek et al., 2010).

The earthquake response spectra for the same place considering for five damping factors: 0, 2, 5, 10 and 20% are shown in the Figure 8.8 (Boroschek et al., 2010). The regions containing the measured building resonant period considered in the current study and that calculated using standard empirical relations are shown with red and green strips on the same figure. An arrow points the expected increase of the resonant period of our study building during an event similar to the Chilean earthquake.

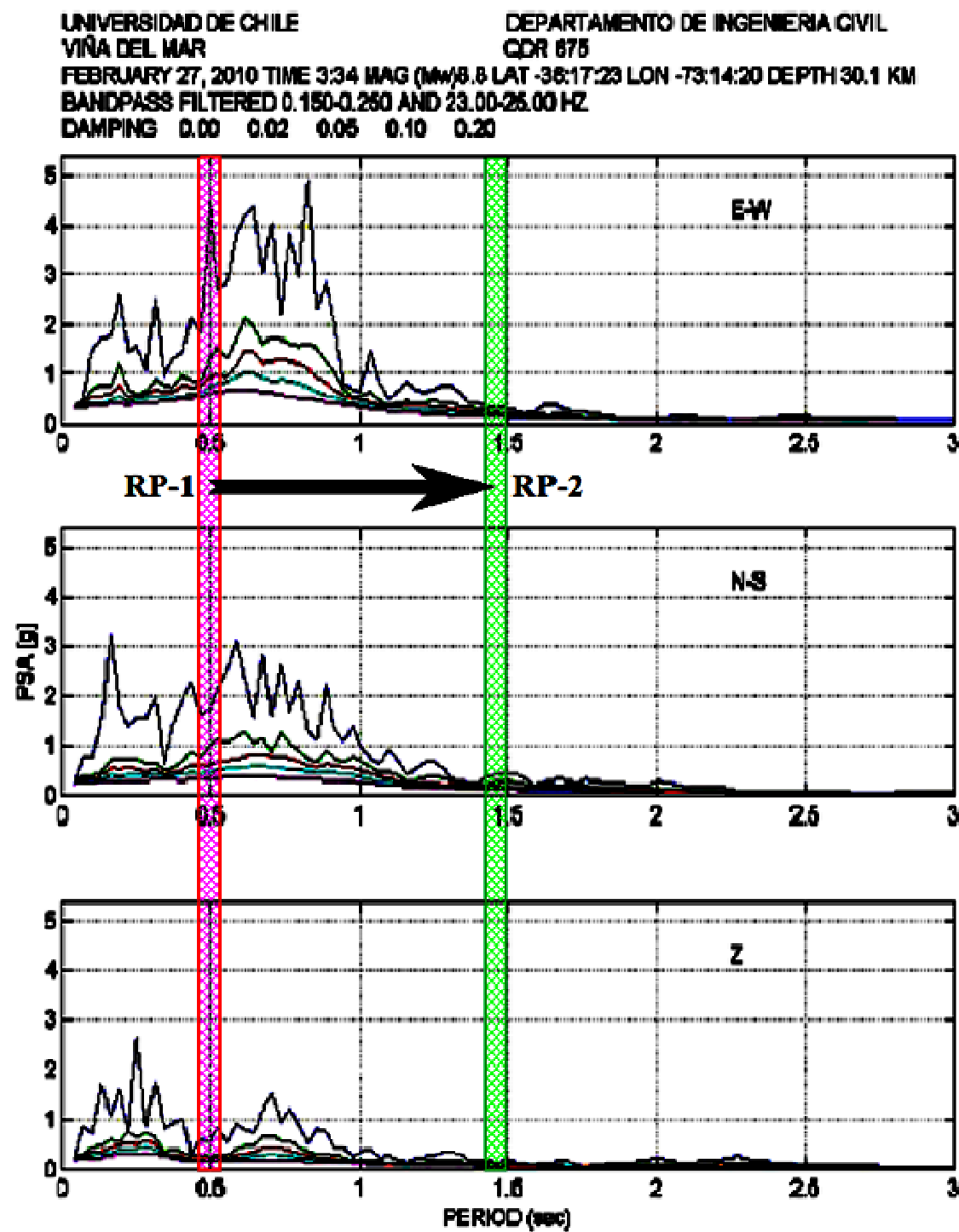


Figure 8.8. Earthquake response spectra for Vina Del Mar, Chile Mw=8.8 February 27, 2010 (source: Boroschek et al, 2010) overlaid by the intervals with the experimentally (red) and empirically (green) obtained resonant periods for our test 13-stories building. RP-1 and RP-2 are the reference points shown in Figure 8.4.

The earthquake response spectra for 5% damping is presented in Figure 8.9. The amplification factor, α , for different soil classes in the Chilean code is shown in Figure 8.10.

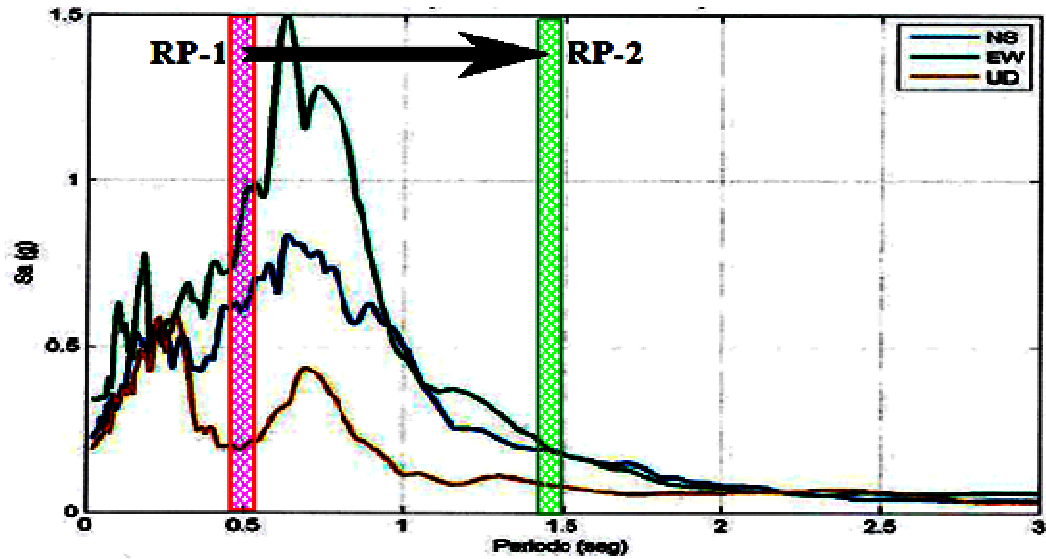


Figure 8.9. Earthquake response spectra with 5% damping for Vina Del Mar, Chile Mw=8.8 February 27, 2010 (from Boroschek et al, 2010). RP-1 and RP-2 - reference points.

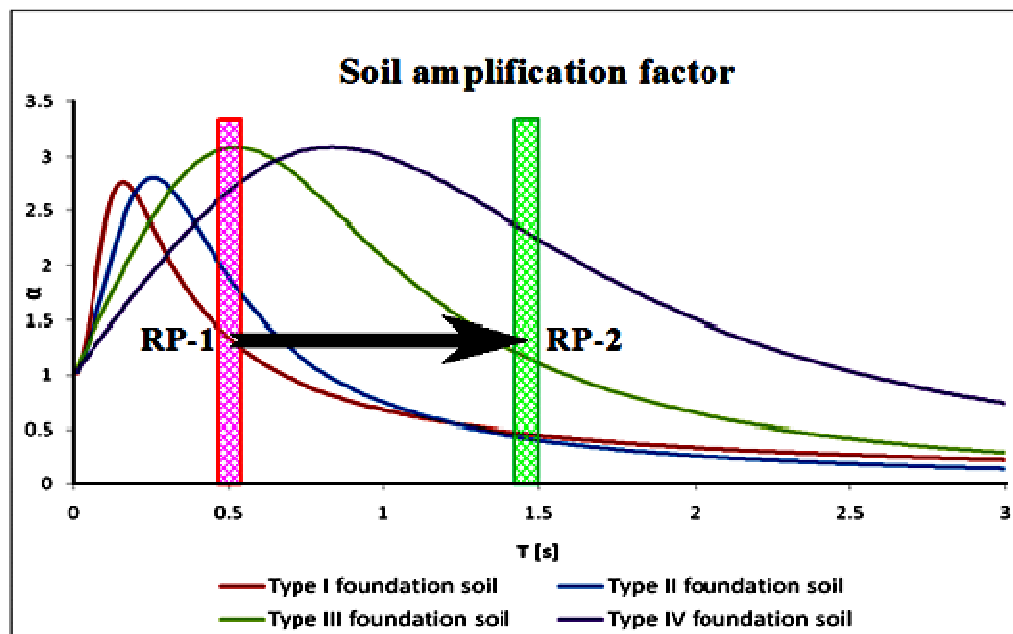


Figure 8.10. Amplification factor, α , for four soil classes in the Chilean code (modified from Ene and Craifaleanu, 2010). RP-1 and RP-2 - reference points.

The actual and empirically calculated resonant periods fall in intervals characterized by different dynamic loading conditions (see Figures 8.8, 8.9 and 8.10). By inspection, it is obvious that the initial resonant period falls in the middle of earthquake response spectra and in the interval with significant soil amplifications.

The earthquake response spectrum was most probably calculated from the acceleration spectra and includes actual soil amplification for this site.

The total response of the RC structure during the Chile earthquake can be assumed as a product of earthquake response spectra (Figure 8.9) multiplied by the response function of the building (Figure 8.4 - SDOF approximation). The total amplification for actual resonant frequency most probably will be significantly higher than for the case of period and damping calculated from empirical correlation.

This large amplification at actual resonant period can occur under some conditions:

- The waveform of the acceleration contains relatively small vibrations with frequencies close to the resonant frequency of a new building.
- The existence of stable (long enough) vibration at the resonant frequency, which is long enough for a gradual increase of the response of the building. The duration of this transient process is inversely proportional to the actual damping ratio.
- The induced stresses due to the seismic load should be less than the yielding point of the RC members during the increase of the response. This condition will prevent rapid decrease of the stiffness, and the resonant period at the beginning of shaking would be close to its initial value.
- Soil-structure interaction during the building resonance does not change the initial soil dynamic properties which assume absence of liquefaction due to overloading.

There are three possible outcomes if the above conditions are not fulfilled:

- The duration of small vibrations with the resonant frequency is short. The resonant amplification will be less than its maximum value. The building will retain, or change slightly, its initial dynamic parameters. This is the case for small earthquakes and ambient vibration.

- The vibrations with resonant frequency are prolonged and large enough to cause cyclic loading of the building (or its structural elements) close to the yielding point. This will result in a decrease of the building stiffness and an increase of the resonant period and damping ratio. This case is related to moderate earthquakes or strong gusting winds. Plastic hinges and other zones of deformation in the structural elements of the building are formed during the dissipating of vibration energy. The changes of resonant period and damping ratio are permanent even after stress relaxation. Probably this is the main reason for the longer resonant period and larger damping ratio of the older buildings, which are repeatedly subjected to relatively higher level of dynamic loads.

- In case of very strong vibration close to the initial resonant period of new buildings, some structural elements lose strength during the first cycles of deformation. This process leads to formation of temporary zones with negative stiffness. The resonant period and damping ratio increase extremely. These elements will be totally destroyed during the next cycles. Despite this destruction, the building can have for a while the resonant period and damping close to its initial values because the damaged elements usually are unevenly distributed. After that the resonant period of the building will be shifted to a longer value and the damping ratio will increase. The other structural elements that remain almost intact during the first cycles of deformation will collapse during the next cycles because of their overloading and due to the increasing of the periods of the body or surface waves which can lead to a subsequent resonant amplification after the building resonances are shifted.

The last scenario probably can contribute to the explanation why the new buildings suffered more severe damages or collapse during the Chilean earthquake while the older structures did survive.

Chapter 9.

Summary and Conclusions

Chapter 1. Seismic microzonation and site specific geophysical and geological studies will have significance for engineering design for many years to come. Five different soil categories are defined in the NBCC 2005 based on the average shear wave velocity of the top 30 meters of soil profiles below the foundation (VS-30). The GTA is situated over complex subsurface geology, including different soil types and soil structures, altered by human activities. As a result, the original near-surface soil structure is disrupted by underground artificial structures and facilities, landfills, artificially filled ravines and other negative topographic forms, etc. This renders the seismic microzonation very complicated. In addition, there would be seismic noise produced by (the) city traffic, human activities, etc. This noise limits the depth resolution of seismic methods. Another limitation for microzonation in a city is the densely distributed residential and commercial buildings, etc. with their underground infrastructures and constricted free spaces for deployment of the geophysical equipment.

Chapter 2. The important parameters for seismic site assessment include soil resonances, which can be determined using the HVSR method or by theoretical modeling using soil shear wave velocity for soil deposits above the bedrock and the density of soil layers. These soil resonances can not be estimated from VS-30 data solely. The data from seismic investigations is collected using vibration sources with small intensity, ambient vibrations, sledge hammer, etc. The site response calculated from these sources does not include changes of elastic moduli and geotechnical properties at significant strain, when the soil structure is subjected to strong shaking during an earthquake. The PGV values at points of interest can be used to estimate the changes of soil properties in case of a strong earthquake. The PGV values are recorded sparsely. The macroseismic Intensity estimated using the MM scale can be found for many places where PGV is not measured. The relationship between PGV and I_{MM} can be used to estimate the shear strain for the soil layers close to the surface. Changes of soil resonances including resonant frequency and damping ratio can be evaluated from the estimated shear strain. This procedure is proposed in a simplified manner.

Chapter 3. The geophysical methods used for seismic microzonation give satisfactory results if the conditions and limitations for their application are satisfied. The geophysical methods suitable for city conditions have their own requirements and limitations and can not be applied everywhere. In urban areas, the HVSR yields better resolution for the fundamental soil resonances if the recorded waveforms are separated into two data sets according to the intensity of ambient vibrations. A procedure and software for its implementation are proposed.

The MASW method can give an adequate V_s soil profile if the initial model for inversion of the dispersion curve is based on preliminary information for soil layering. SH refracted wave profiling gives a stable VS-30 value. Both MASW and SH profiling work well if the soil profile has relatively thick layers and positive velocity gradient with depth. If a thin interlaying soil layer or low velocity layer is sandwiched between two high velocity layers, the interpretation should be considered after gathering additional geological information. There is a recent proposal for classes A and B: “if a 3-m thick intervening soft-soil layer exists in the top 30 m, the classification should be done using the average shear-velocity for this layer” (Adams, 2010). If this layer and its velocity have to be discovered using seismic methods, preliminary geological information related to the soil layering should be available. Seismic tomography or very dense reflection survey could give acceptable interpretation.

Chapter 4. The geophysical equipment for HVSR, SH profiling and MASW including seismic stations, seismometers, geophones and other necessary hardware have to be adequate for the dynamic and frequency ranges of the expected seismic wave of interest. All SH profiles and MASW field measurements were carried out using Geode 24-channel standard seismic station with pre-installed firmware and commercially available software for MASW calculations. Waveforms for the HVSR method and for identification of building vibration modes were recorded with the 3-component portable seismic station designed for this purpose. This station was designed using a simplified Excel spreadsheet for calculations and adjustments of the 8th order low pass Bessel filters for all channels.

Chapter 5. Data acquisition and processing were consistent with the requirements for seismic microzonation and with conditions and limitations of urban area. The HVSR for

each test point was calculated using separation of the waveform into time intervals with low and high ambient vibration. SH refracted profiles for the reference test points were processed using Matlab to obtain the VS-30 for each one. The Rayleigh wave dispersion curve and inversion for MASW were processed using software SeisImager/SWTM from Geometrics.

Chapter 6. The maps produced from HVSR, MASW and SH profiles data were cropped to the boundary of the investigated area and imported in (a) GIS layers with coordinate system NAD_1983_UTM_Zone_17N. The maps obtained in this work are compared to the known geological maps of drift-thickness, surficial geology and bedrock topography. All maps are spatially referenced by the same coordinates in UTM Projection. An unknown depression of the bedrock surface is outlined.

Chapter 7. The building resonances and their influence over the HVSR results are obtained from vibration measurements. Separation of torsional vibration modes from translational vibration modes of building was conducted using the resonant frequencies from two-component or three-component waveforms recorded simultaneously or consecutively at test points in and around the building. The concept of using HVSR inside a building in order to identify its resonances is rejected based on the analysis of the vibration measurements.

Chapter 8. The experimental data show increasing of the resonant period at the dominant vibration modes with time due to wind loading. The building resonances during intense seismic loading could be estimated starting from high frequency dominant vibration modes of a new building and taking into consideration the nonlinear behavior of RC members and structure and stiffness degradation. The experiment shows a gradual degradation of stiffness during consecutive wind cycles in a 2.5 years period. The results can be extended over an RC structure similar to the studied benchmark building in a case of earthquake shaking. This can be implemented in case of the Chile earthquake in 2010 (Mw 8.8) to explain the phenomenon why the new RC buildings were damaged while the older ones were intact.

9.1. Summary of the results and discussion

Site classification based on the first 30 m of soil profile (after NEHRP 1994) was adopted in many national building codes. The result is generation of many VS-30 maps for urban areas around the world. From Figure 6.8 and its appended comments, it is obvious that it would be expensive to cover the entire GTA with enough dense grid of test points to produce a detailed VS-30 map, outlining the disturbances in the upper soil layers. This raises questions about the necessity and the reasonable limit of a potential densification of the geophysical test points.

In addition, the VS-30 averaged values and interpolated maps are not directly connected to the site response because:

- They are not directly related to the fundamental or dominant frequency of the site.
- They are not connected to the slope effects or edge effects of sedimentary basin.
- They do not reflect focusing of the energy due to topography of the earth surface as well as due to topography of the deeper geological structure.
- They are very sensitive to the position of the measurement point in the city conditions because of the horizontal delineation of the soil structure caused by deep trenches, underground structures, etc. This is the reason to have different site classes at closely situated measurement points.
- Assuming that site classification is based mainly on the shear-wave velocity, VS-30 maps do not include the depth to the water level table and consequently potential soil liquefaction.

Most of the VS-30 maps, including this work (e.g. map shown in Figures 6.7), are based on relatively sparse measurement points with subsequent interpolation. The interpolation of soil classes between distant test points is not correct and can be used only to illustrate in general the distribution of soil classes. It is inappropriate to use the interpolated classes for sites between measurement points. There is a possibility of using these classes in the vicinity of the measurement points with caution as shown on Figure 6.8. In some cases interpolated VS-30 maps (similar to this on Figure 6.7) are used as an addition for re-

calculating of Uniform Hazard Spectra. This is unacceptable for the reasons mentioned above.

VS-30 data can be used for static or pseudo-dynamic calculations for relatively small volumes below building foundations, which include expected soil disturbances from soil-structure interaction. It can not be used for calculation of soil response function, because it is not connected with the depth to the boundary between soil and bedrock. For example, Adams (2007) used data from some distant moderate earthquakes and found amplification factors around 20 times larger than those calculated from VS-30 values. In another example, for Eastern Canada (Benjumea et al., 2008) a clear resonance on a site with soft clay layers over hard rock is observed which does not correspond to the VS-30 map of Ottawa. The conclusion in Benjumea et al. (2008) is: "Using 30 m criteria may not provide an adequate description of the site effects in this environment."

On the other hand, VS-30 is convenient for soil classification because the average V_s can be obtained with simple seismic refraction technique using geophone spreads between 70 and 100 m. This geophone spread can be accommodated for city conditions. Another suitable geophysical technique is MASW. It gives satisfactory V_s profile and VS-30 values with the same spread of geophones and proper initial model for the inversion.

The determination of resonances in the soil response function is carried out mainly using the HVSR (Nakamura's method). Despite its unclear geophysical background, this method gives acceptable results for the resonant frequencies. The amplitudes of these resonances can not be used as absolute values of soil amplification (see Chapter 2).

The fundamental resonances and the relative amplifications obtained by the HVSR method can be mapped using interpolation because they presumably are produced by almost vertically propagated refracted/reflected seismic waves which are less affected by lateral disturbances close to the upper surface of the soil structure. The mapped fundamental frequencies (Figure 6.2) in comparison with drift-thickness map (depth to bedrock) (Figure 6.3) and relative amplifications (Figure 6.4) show an unnoticed until now depression in the bedrock surface in the southwestern part of GTA.

There are some limitations for using the HVSR to find the site response besides the unknown exact value of the amplification:

- The HVSR fundamental resonances from ambient noise can be suppressed by the vibrations of nearby traffic due to high intense vertical movement from elliptically polarized Rayleigh wave. In other case, if the ambient vibrations have very low intensity, the reflected/refracted seismic waves from a deep soil-bedrock boundary would have amplitudes below the noise level of the equipment. In this case, the HVSR calculated over low-intensity vibration could not exhibit the resonant amplification. If a distant high-intensity source (train, traffic) exists, the resonant frequency can be determined using HVSR. The problem is to separate the HVSRs from low- and high-intensity vibrations. A solution to this problem is developed in Chapter 2. The separation allows determination of soil resonances from suitable sources with low or high vibration levels.

- Using the HVSR with ambient noise as a seismic source does not allow identification of the resonances at relatively low frequency, which should exist because of deep layering in the earth's crust. The main reason for this is the low energy of the seismic excitation from the ambient noise and the longer path of propagation for SH wave in sedimentary layers with high attenuation. This problem can be solved using the HVSR from recorded small and moderate local earthquakes.

- The site response obtained by HVSR can be approximated with theoretical displacement spectra for 2-3 layered soil structure (Chapter 4). The correlation between theoretical and observed spectra is acceptable for the resonant frequencies calculated from an adequate soil-structure model. The amplitudes of these resonances and the damping factors from the model can not be used even as a first approximation for design purposes.

- Using the HVSR in city conditions requires estimating the influence of building resonances on the HVSR results. In Chapter 7, it was shown that the building resonance at the first vibration mode induced by gusting winds up to 35 km/h can affect the soil resonances obtained by the HVSR method at distances comparable to the building dimensions. This influence affects the HVSR resonances by splitting or suppressing them if the building resonance at first vibration mode and soil fundamental resonance have almost the same frequencies. The effect is due to the rocking component of the building

vibrations at first vibration mode which produces mainly vertically polarized compressional and Rayleigh waves.

Seismic microzonation for areas with low seismicity like the GTA usually is carried out using seismic sources with low energy: ambient noise, impact with sledge hammers, etc. However, in zones with high seismic activity the results should be adapted for significantly more intense impacts during moderate and strong earthquakes. For this purpose, changes in dynamic behavior of the soil structure and building should be taken into account (Chapter 2 and Chapter 8).

9.2. Conclusions

The main conclusions from this work are:

1. The map of soil classification for the GTA established in this thesis provides a general idea about distribution of the soil classes over the whole area. There is no essential reason for uniform densification of the geophysical test points over the whole GTA. Some additional test points can be situated in the SW part of the GTA for a more precise delineation of the newly found depression. A very detailed VS-30 survey can be carried out in close vicinity of a future building site if this is necessary.

2. Geophysical investigation for Vs profiles is suitable for the areas of future building activities. More than one geophysical profile should be used if it is necessary to establish potential heterogeneity in the upper soil layers.

3. MASW can be used only for correlative estimation of the Vs vertical profile using inversion of phase velocity dispersion curve of Rayleigh waves in cases when additional information is available e.g. depth to water level table, layering of the soil structure, Poisson's ratio, etc.

4. Shear-wave seismic refraction profiling and MASW methods for estimation of VS-30 should be used with caution in built-up areas in the city. Applying these methods along the streets or in stadiums, parks, etc. or over other sites not-allocated for building is acceptable if the results are used as references.

5. VS-30 from the seismic profiles altogether with HVSR data can be used in conjunction with well known geology of shallow sediments for classification according to NBCC 2005 of other points which have only HVSR data.

6. The fundamental resonant frequencies obtained by HVSR method can be interpolated to produce a map which outlines the relief of soil-bedrock boundary. The actual depth can not be evaluated from HVSR resonances and VS-30 values. Additional seismic reflection/refraction techniques or seismic tomography have to be applied to obtain the depth and topography of soil-bedrock boundary.

7. The HVSR soil responses as well as building resonances are usually determined with low excitation sources (ambient vibration, moderate winds, etc.). During moderate or strong earthquakes, the soil layers and the building construction are subjected to significantly stronger dynamic forces. In this case, both the soil and building resonances undergo changes to the lower fundamental resonant frequency and higher damping factor.

8. The dynamic change in building resonances during a strong earthquake should be considered in their seismic design. Strong ground shaking in the epicentral zone of an earthquake disturbs soil stability, soil-structure interaction, and building integrity. New RC buildings have higher resonant frequencies and are vulnerable to the shaking from a strong shallow earthquake. If an earthquake causes significant deformation in the soil structure and in the building, both of them absorb part of the seismic energy by plastic deformations. Soil rheologically recovers after the earthquake to its initial condition gradually releasing the excess water pressure and rebound of its original cohesion. Before the next strong earthquake, the soil properties will be close to their original conditions. On the other hand, the structure of a building after absorbing energy by plastic deformation would have lower resonant frequencies (longer fundamental period) and higher damping than their original values. This effect should be accounted for estimation of resonant behavior and integrity of the buildings.

9.3. Recommendations for future research

The present seismic microzonation of GTA is based on techniques (methods) and equipment for assessment of the site response using mainly seismic sources with low intensity, ambient vibrations, wind load, etc. For areas with low to moderate seismicity like GTA it requires long periods of time to register moderate earthquake that can be used for the microzonation.

- Recording the ambient vibrations and local and regional earthquakes is important to be done at a significant number of test points on the sites for future constructions and in the existing buildings. It will be necessary to develop relatively cheap 3-component autonomous seismograph (based on the prototype used in this research) which will be capable to collect continuous data and to communicate with a central computer using existing communication technologies.

- Nakamura's HVSR method will continue to be used for long time regardless of its questionable theoretical background and some problems with the interpretation of the spectral ratio. An adequate geophysical model should be created to overcome these problems.

- Changes of the building resonances impacted by an earthquake as well as during the lifetime of buildings should be established experimentally based on long-term data sets and should be used in the design process. This will also help to predict the response of buildings and the potential damages during strong shaking.

- The discovered depression in the bedrock-soil boundary under southwestern part of GTA should be verified using more test points and transversal deep seismic profiling. It is possible that this subsidence can cause focusing of seismic energy at some points on the ground surface during a relatively strong earthquake.

- Investigations related to the seismic microzonation are being conducted and will continue to be conducted in the near future all over the world. Significant improvement of the methodology for prediction of the intensity of ground shaking can be reached in the next few years. The application of these methods will be extremely difficult without

an adequate database, which includes vibration records, earthquake catalogs, geological maps, etc.

- The future GTA development includes high-rise buildings (commercial or residential), situated on reclaimed land from Lake Ontario, old ravines filled with different materials, old garbage sites, etc. All new constructions and building sites have to be investigated in advance to ensure the appropriate application of the building guides, codes, design methods, etc.

References

- AD8295 (2009). Data Sheet Precision Instrumentation Amplifier with Signal Processing Amplifiers, Rev A, 06/2009, Analog Devices, Inc.
- Adams, J., and Halchuk, S. (2003). Fourth generation seismic hazard maps of Canada: values for over 650 Canadian localities intended for the 2005 national building code of Canada, *Geological Survey of Canada, Open File 5813*, 2008, 32 p.
- Adams J., and Halchuk, S. (2004). A review of NBCC 2005 Seismic Hazard Results for Canada – the interface to the ground and prognosis for urban risk mitigation, *Proceedings of the 57th Canadian Geotechnical Conference*, Québec city, Canada, October 25-27, 2004.
- Adams, J., and Halchuk, S. (2007). A Review of NBCC 2005 seismic hazard results for Canada – the interface to the ground and prognosis for urban risk mitigation, OttawaGeo2007.
- Andersen, P., Brincker, R., Ventura, C., and Cantieni, R. (2008). Modal estimation of civil structures subject to ambient and harmonic excitation, *Conference Proceedings : IMAC-XXVI: A Conference & Exposition on Structural Dynamics*, Society for Experimental Mechanics, 2008.
- Applegate, D. (2004). Stepping up to the plate, *Seismological Research Letters*, 75 (3), 335-337.
- Applied Technology Council (2005). *Improvement of nonlinear static seismic analysis procedures*, FEMA 440, 392 p.
- Applied Technology Council. (2009). *Effect of Strength and Stiffness Degradation on Seismic Response*, FEMA P440A, 312 p.
- Atkinson, G., and SanLinn I. Kaka (2007). Relationships between Felt Intensity and Instrumental Ground Motion in the Central United States and California. *Bull. Seism. Soc. Am.*, **97**, 497-510.
- Atkinson, G., and Sonley, E. (2000). Empirical relationships between Modified Mercalli Intensity and response spectra. *Bull. Seism. Soc. Am.*, **90**, 537-544.

- Baker, C., Lahti, L., and Roumbanis, D. (1998). Urban geology of Toronto and surrounding area, *Urban Geology of Canadian Cities*, Edited by P.F. Karrow and O.L. White, Geological Association of Canada, GAC Special Paper, 42, 323-352.
- Bendat, J., and Piersol, A. (2000). *Random data: analysis and measurement procedures*, John Wiley & Sons, Inc., New York, NY, USA.
- Ben-Zion, Y. & Sammis, C.G. (2003). Characterization of fault zones, *Pure appl. Geophys.*, 160, 677–715.
- Ben-Zion, Y., and Shi, Z. (2005). Dynamic rupture on a material interface with spontaneous generation of plastic strain in the bulk, *Earth and Planetary Science Letters*, 236, 486–496.
- Beresnev, I.A., and Wen, K.L. (1996). Review nonlinear soil response-a reality? *Bulletin of the Seismological Society of America*, 86, 1964–1978.
- Bishop, R. H. (2007). *LabVIEW 8*, Prentice Hall.
- Boore, D. M. and G. M. Atkinson (2008). Ground-Motion Prediction Equations for the Average Horizontal Component of PGA, PGV, and 5%-Damped PSA at Spectral Periods between 0.01 s and 10.0s, *Earthquake Spectra*, 24 (1), 99–138.
- Borcherdt, R.D. (1970). Effects of local geology on ground motion near San Francisco bay, *Bulletin of the Seismological Society of America*, 60 (1), 29-61.
- Boroschek, R., P. Soto, L. Leon, D. Comte (2010). *Central-South Chile Earthquake February 27, 2010, 4th Preliminary Report.*, Univ. Of Chile, April 5 (Spanish).
- Bour, M., Fouissac, D., Dominique, P., and Martin, C. (1998). On the use of ambient noise recordings in seismic microzonation, *Soil Dyn. Earthq. Eng.*, 17, 465-474.
- Brincker, R., Zhang, L., and Andersen, P. (2000). Modal identification from ambient responses using frequency domain decomposition, *Proceedings of the 18th International Modal Analysis Conference (IMAC)*, San Antonio, Texas, USA, February 7-10, 2000, 625-655.
- Brincker, R., Ventura, C., and Andersen, P. (2003). Why output-only modal testing is a desirable tool for a wide range of practical applications, *Proceedings of the 18th*

- International Modal Analysis Conference (IMAC)*, A Conference on Structural Dynamics, February 3-6, 2003, The Hyatt Orlando, Kissimmee, Florida, 265-272.
- Brincker, R., Andersen, P., and Jacobsen, N. (2007). Automated frequency domain decomposition for operational modal analysis, *Proceedings of the 18th International Modal Analysis Conference (IMAC – XXIV)*, A Conference & Exposition on Structural Dynamics, Society for Experimental Mechanics, 2007.
- Brown, L., Boore, D., and Stokoe, K. (2002). Comparison of shear-wave slowness profiles at 10 strong-motion sites from noninvasive SASW measurements and measurements made in boreholes, *Bulletin of the Seismological Society of America*, 92 (8), 3116-3133.
- Celebi, M., Penzien, J., and (US), N.S.F. (1973). *Experimental investigation into the seismic behavior of critical regions of reinforced concrete components as influenced by moment and shear*, Report N°. UCB/EERC-73/04, Earthquake Engineering Research Center, University of California, Berkeley, California.
- Celebi, M. (1996). Comparison of damping in buildings under low-amplitude and strong motions, *Journal of wind engineering and industrial aerodynamics*, 59(2-3), 309-323.
- Chen, L., Zhu, J., Yan, X., and Song, C. (2004). On arrangement of source and receivers in SASW testing, *Soil Dynamics and Earthquake Engineering*, 24 (5), 389-396.
- Chouinard, L., Rosset P., De La Puente, A., Madriz, R., Mitchell, D., Adams, J. (2004). Seismic Hazard Analysis for Montreal, *Proceedings of the 13th World Conference on Earthquake Engineering*, Vancouver, B.C., Canada August 1-6, 2004, Paper No. 7010 on CD-ROM.
- Chavez-Garcia, F., and Cardenas -Soto, M. (2002). The contribution of the built environment to the free-field ground motion in Mexico city, *Soil Dynamics and Earthquake Engineering*, 22 (9-12), 773-780.
- Cramer, C. (2003). Site-specific seismic-hazard analysis that is completely probabilistic. *Bulletin of the Seismological Society of America*, 93 (4), 1841-1846.

- Cramer, C. H., J. S. Gomberg, E. S. Schweig, B. A. Waldron, and K. Tucker (2004). *The Memphis, Shelby County, Tennessee, Seismic Hazard Maps*, USGS Open-File Report 04-1294, 40 p.
- Davis, P.M., J.L. Rubinstein, K.H. Liu, S.S. Gao, and L. Knopoff (2000). Northridge earthquake damage caused by geologic focusing of seismic waves, *Science*, 289 (5485), 1746-1750.
- D' Ambrisi, A. and F.C. Filippou (2000). A shear model for RC structures under cyclic lateral loads, *Proceedings of the 12th World Conference on Earthquake Engineering*, Auckland, New Zealand, 2000.
- Dineva, S., Eaton, D., and Mereu , R. (2004). Seismicity of the southern great lakes: revised earthquake hypocenters and possible tectonic controls, *Bulletin of the Seismological Society of America*, 94 (5), 1902-1918.
- Dineva, S., Eaton, D., Ma, S., and Mereu, R. (2007). The October 2005 Georgian Bay (Canada) earthquake sequence: Mafic dykes and their role in the mechanical heterogeneity of Precambrian crust, *Bull. Seism. Soc. Am.*, 97 (2), 457-473.
- Duval, L., A.-M., P.-Y., Bard, J.-P. Meneroud, S. Vidal (1994). Usefulness of microtremor measurements for site effect studies, *Proceedings of the 10th European Conference on Earthquake Engineering*, Vienna, Austria, Balkema, Duma Ed., Rotterdam, I, 521-528.
- Duval, L., A.-M., J.-P. Meneroud, S. Vidal & A. Singer (1998). Relation between curves obtained from microtremor and site effects observed after Caracas 1967 earthquake, *Proceedings of the 11th European Conference on Earthquake Engineering*, Balkema, Rotterdam, p. 9.
- EERI (2010). *The Mw 8.8 Chile Earthquake of February 27, 2010*, EERI Special Earthquake Report, 20 p.
- Ene, D., and Craifaleanu , I. (2010). Seismicity and design codes in Chile: characteristic features and a comparison with some of the provisions of the Romanian seismic design code, *Constructii*, 10 (2), 69-78.

- Enomoto, T., Kurijama, T., Abeki, T., Iwatate, T., Navarro, T. and Nagumo, M. (2000). Study on microtremor characteristics based on simultaneous measurements between basement and surface using borehole, *Proceedings of the 12th World Conference on Earthquake Engineering*, Auckland/New Zealand, 2000.
- Eyles, N. (2004). *Toronto rocks: the geological legacy of the Toronto region*, Fitzhenry & Whiteside, Markham, Canada, 48p.
- Field, E.H., S.E. Hough & K.H. Jacob (1990). Using microtremors to assess potential earthquake site response: A case study in Flushing Meadows, New York City, *Bulletin of the Seismological Society of America*, 80 (6), 1456-1480.
- Field, E., and Jacob, K. (1995). A comparison and test of various site-response estimation techniques, including three that are not reference-site dependent, *Bulletin of the Seismological Society of America*, 85 (4), 1127-1143.
- Field, E.H., Johnson, P.A., Beresnev, I.A., and Zeng, Y. (1997). Nonlinear ground-motion amplification by sediments during the 1994 Northridge earthquake, *Nature*, 390, 599–602.
- Filippou, F.C. and Issa, A. (1988). *Nonlinear analysis of reinforced concrete frames under cyclic load reversals*, Report No. UCB/EERC 88-12, Earthquake Engineering Research Center, University of California, Berkley, CA.
- Finn, W.D.L., and Wightman, A. (2003). Ground motion amplification factors for the proposed 2005 edition of the National Building Code of Canada, *Canadian Journal of Civil Engineering*, 30, 272-278.
- Finzi, Y., Hearn, E.H., Ben-Zion, Y. & Lyakhovsky V. (2009). Structural properties and deformation patterns of evolving strike-slip faults: numerical simulations incorporating damage rheology, *Pure appl. Geophys*, 166, 1537-1573.
- Gallipoli, M., Mucciarelli, M., Castro, R., Monachesi, G., and Contri, P. (2004). Structure, soil-structure response and effects of damage based on observations of horizontal-to-vertical spectral ratios of microtremors, *Soil Dynamics and Earthquake Engineering*, 24 (6), 487-495.

- Gao, S., H. Liu, P.M. Davis, and L. Knopoff (1996). Localized amplification of seismic waves and correlation with damage due to the Northridge earthquake; evidence for focusing in Santa Monica [Monograph]: The Northridge, California earthquake of January 17, 1994, *Bulletin of the Seismological Society of America*, 86 (1, Part B Suppl.), 209-230.
- Geomatrix Consultants Inc. (1997). Final Report, Part 2: *Seismic hazard results and sensitivity, seismic hazard in southern Ontario*, July 1997.
- Hartzell, S., E. Cranswick, A.D. Frankel, D.L. Carver, and M.E. Meremonte (1997). Variability of site response in the Los Angeles urban area, *Bulletin of the Seismological Society of America*, 87 (6), 1377-1400.
- Hartzell, S., L. F. Bonilla, and Robert A. Williams (2004). Prediction of Nonlinear Soil Effects, *Bulletin of the Seismological Society of America*, 94, 1609-1629.
- Hayashi, K. and Suzuki, H. (2004). CMP cross-correlation analysis of multi-channel surface wave data, *Exploration Geophysics*, 35, 7-13.
- Haselton, C. (2006). *Assessing seismic collapse safety of modern reinforced concrete moment frame buildings*, Stanford University, PHD thesis.
- Heisey, J.S., Stokoe, K.H., II, Hudson, W.R., Meyer, A.H. (1982). Determination of in situ shear wave velocities from Spectral Analysis of Surface Waves, *Research Report 256-2*, Center for Transportation Research, Univ. of Texas at Austin, 277p
- Humar, J., Adams, J., Tremblay, R., Rogers, C., and Halchuk, S. (2010). Proposals for the seismic design provisions of the 2010 National Building Code of Canada, *Proceedings of 10th Canadian and 9th US National Conference on Earthquake Engineering*, Toronto July 25-39, 2010, Canada, Paper No. 1387.
- Hunter, J.A., and Motazedian, D. (2006). Shear Wave Velocity Measurements for Soft Soil Earthquake Response Evaluation in the Eastern Ottawa Region, Ontario, Canada, In: *SAGEEP conference bulletin*.
- Hunter, J. A., H. Crow, G. R. Brooks, M. Pyne, M. Lamontagne, A. Pugin, S. E. Pullan, T. Cartwright, M. Douma, R. A. Burns, R. L. Good, D. Motazedian, K. Kaheshi-Banab, R. Caron, M. Kolaj, I. Folahan, L. Dixon, K. Dion, A. Duxbury, A.

- Landriault, V. Ter-Emmanuil, A. Jones, G. Plastow, and D. Muir, D. (2010). *Seismic site classification and site period mapping in the Ottawa area using geophysical methods*, Geological Survey of Canada, Open File Report 6273.
- Ibrahim, S., and Mikulcik , E. (1977). A method for the direct identification of vibration parameters from the free response, *Shock and Vibration Bulletin*, 47 (4), 183-198.
- Ile, N., and Reynouard , J. (2000). Nonlinear analysis of reinforced concrete shear wall under earthquake loading, *Journal of earthquake engineering*, 4 (2), 183-213.
- Irie, Y., and Nakamura, K. (2000). Dynamic characteristics of a R/C building of five stories based on microtremor measurements and earthquake observations, *Proceedings of 12th World Conf. Earthquake Engineering*, 500-508.
- Jacobsen, N., Andersen , P., and Brincker, R. (2008). Applications of frequency domain curve-fitting in EFDD technique. *Proceedings IMAC-XXVI conference, A Conference & Exposition on Structural Dynamics*, Society for Experimental Mechanics, 2008.
- Jennings, P., and Kuroiwa, J. (1968). Vibration and soil-structure interaction tests of a nine-story reinforced concrete building, *Bulletin of the Seismological Society of America*, 58 (3), 891-916.
- Johnson, E., Lam , H., Katafygiotis , L., and Beck, J. (2000). A benchmark problem for structural health monitoring and damage detection, *Structural control for civil and infrastructure engineering: Proceedings of the 3rd International Workshop on Structural Control*, Paris, France 6-8 July, 2000, 317.
- Kaka, S., and Atkinson, G. (2004). Relationships between Instrumental Ground-Motion Parameters and Modified Mercalli Intensity in Eastern North America, *Bulletin of the Seismological Society of America*, 94 (5), 1728–1736.
- Karabulut, H. & Bouchon, M. (2007). Spatial variability and non-linearity of strong ground motion near a fault, *Geophys. J. Int.*, 170, 262–274.
- Kausel, E., and D. Assimaki (2002). Seismic simulation of inelastic soils via frequency-dependent moduli and damping, *Journal of Engineering Mechanics*, 128, 34–45.

- Kim, W.-Y., Dineva, S., Ma S., and Eaton, D. (2006) The 4th August 2004, Lake Ontario, Earthquake, *Seism. Res. Letters*, 77 (1), 65-73.
- Kovacs, P. (2010). Reducing the risk of earthquake damage in Canada: lessons from Haiti and Chile, *ICLR Research Paper Series*, 49, 37 p.
- Kramer, S. (1996). *Geotechnical earthquake engineering*, Prentice Hall, Upper Saddle River, New Jersey, 653 p.
- Kokusho, T. (2004). Nonlinear site response and strain-dependent soil properties, *Current Science*, 87 (10), 1363-1369.
- Kudo, K. (1996). Practical estimates of site response; state-of-art report, *Proceedings of the Fifth International Conference on Seismic Zonation*, III, 1878-1907.
- Kudo, K., T. Kanno, H. Okada, A. O. Ozel, L. M. Erdik, T. Sasatani, S. Higashi, M. Takahashi & K. Yoshida (2002). Site-specific issues for strong ground motions during the Kocaeli, Turkey, earthquake of 17 August 1999, as inferred from array observations of microtremors and aftershocks, *Bulletin of the Seismological Society of America*, 92 (1), 448-465.
- Lachet, C., and P.Y. Bard (1994). Numerical and theoretical investigations on the possibilities and limitations of Nakamura's technique, *Journal of Physics of the Earth*, 42, 377-397.
- Lachet, C., Hatzfeld, C., P.-Y. Bard, N. Theodulis, C. Papaioannou, and A. Savvaidis (1996). Site effects and microzonation in the city of Thessaloniki (Greece): comparison of different approaches, *Bulletin of the Seismological Society of America*, 86, 1692-1703.
- Lang, D.H., J. Schwarz, and C. Ende (2002). The reliability of site response estimation techniques, *Proceedings of the 12th European Conference on Earthquake Engineering, London/UK, 2002*.
- Langston, C., Chiu, S., Lawrence, Z., Bodin, P., and Horton, S. (2009). Array observations of microseismic noise and the nature of H/V in the Mississippi Embayment, *Bulletin of the Seismological Society of America*, 99 (5), 2893 - 2911.

- Lee, J. and Fenves, G. L. (1998). Plastic-damage model for cyclic loading of concrete structures, *Journal of Engineering Mechanics Division*, ASCE, 124, 892-900.
- Lermo, J., Francisco, S. and Chavez-Garcia, J. (1992), Site Effect Evaluation using microtremors: a review(abstract), *EOS*, 73, 352.
- Lermo, J., and F.J. Chavez-Garcia (1993). Site effect evaluation using spectral ratios with only one station, *Bulletin of the Seismological Society of America*, 83 (5), 1574-1594.
- Lermo, J., and F.J. Chavez-Garcia (1994). Are microtremors useful in site response evaluation? *Bulletin of the Seismological Society of America*, 84 (5), 1350-1364.
- Lin, L., J., Adams, J., Paquette, R., Glazer, and D., Duchesne (2011). Dynamic Characteristics of Three Major Towers on Parliament Hill, Ottawa, from Recorded Vibrations during the Val-des-Bois, Quebec, Earthquake of June 23, 2010, *CSCE 2011 General Conference*, Ottawa, Ontario, June 14-17, 2011.
- Longzhu C. , Jinying Z., Xishui Y., Chunyu S. (2004). On arrangement of source and receivers in SASW testing, *Soil Dynamics and Earthquake Engineering*, 24, 389–396.
- Marano, G., and Greco , R. (2006). Damage and ductility demand spectra assessment of hysteretic degrading systems subject to stochastic seismic loads, *Journal of earthquake engineering*, 10 (5), 615-640.
- McQuest Marine Services Ltd. (1995). *The geological survey of Lake Ontario in 1993*, Report prepared for the Atomic Energy Control Board, Ottawa, Canada, March, AECB Project No.2.243.3.
- Mereu, R.F., Asmis, H.W., Dunn, B., Brunet, J. Eaton, D., Dineva S. and Yapp, A. (2002). The seismicity of Western Lake Ontario Area: Results from the Southern Ontario Seismic Network (SOSN), 1992-2001, *Seismological Research Letters*, 73 (4), 534-551.
- Miller, R., Xia, J., Park, C., and Ivanov, J. (1999). Multichannel analysis of surface waves to map bedrock, *The Leading Edge*, 18, 1392-1396.

- Mohajer, A., N. Eyles, and C. Rogojina (1992). Neotectonic faulting in metropolitan Toronto: implications for earthquake hazard assessment in the Lake Ontario region, *Geology*, 20, 1002–1006.
- Molnar, S., Cassidy, J.F. and Dosso, S.E. (2004). Site response studies in Victoria, B.C., analysis of Mw 6.8 Nisqually earthquake recordings and shake modeling, *Proceedings of the 13th World Conference on Earthquake Engineering*, Vancouver, Canada, 1-6 August 2004, Paper No. 2121 on CD-ROM.
- Molnar, S., Cassidy, J., Monahan, P., Onur, T., Ventura, C., and Rosenberger, A. (2007). Earthquake site response studies using microtremor measurements in southwestern British Columbia, *Proceedings of the 9th Canadian Conference on Earthquake Engineering*, Ottawa, Ontario, Canada, 26-29 June 2007, 410-419.
- Morgan, B.J., S.C. Larson & R.G. Oesterle (1987). Field Measured Dynamic Characteristics of Buildings, *Proceedings of the Sessions of Structures Congress 87*, Ed. D.R. Sherman, 1987.
- Motazedian, D., Hunter, J., Pugin, A., and Crow, H. (2011). Development of a Vs30 (NEHRP) map for the city of Ottawa, Ontario, Canada, *Canadian Geotechnical Journal*, 48 (3), 458-472.
- Mucciarelli, M., Masi, A., Gallipoli, M., Harabaglia, P., Vona, M., Ponzio, F., and Dolce, M. (2004). Analysis of RC building dynamic response and soil-building resonance based on data recorded during a damaging earthquake (Molise, Italy, 2002), *Bulletin of the Seismological Society of America*, 94 (5), p. 1943-1953.
- Murphy, C., and Eaton, D. (2005). Empirical site response for POLARIS stations in southern Ontario, Canada, *Seismological Research Letters*, 76 (1), 99-109.
- Nakamura, Y. (1989). A method for dynamic characteristics estimation of subsurface using microtremor on the ground surface, *Railway Technical Research Institute, Quarterly Reports*, 30 (1), 25-33.
- Nakamura, Y. (2000). Clear identification of fundamental idea of Nakamura's technique and its applications, *Proceedings of the 12th World Conference on Earthquake Engineering*, Auckland/New Zealand, 2000.

- Nastev, M., Lin, L., Naumoski, N. (2007). Characteristics of seismic motions recorded on bedrock in the Quebec City region, *60th Canadian Geotechnical Conference & 8th joint CGS/IAH-CNC Groundwater Conference*, Ottawa, 8 p.
- Nazarian, S., Stokoe, K.H., and Hudson, W.R. (1983). Use of spectral analysis of surface waves method for determination of moduli and thickness of pavement system, *Transport. Res. Record*, 930, 38–45.
- Nazarian, S., Stokoe, K.H. (1984), In-situ shear wave velocities from spectral analysis of surface waves, *Proceedings, 8th World Conference on Earthquake Engineering Vol.3, Soil stability, soil structure interaction and foundations*, , San Francisco
- NBCC 2005. *National Building Code of Canada 2005*, Document NRCC 47666, National Research Council of Canada, Ottawa, Ontario.
- NBCC 2010. *National Building Code of Canada 2010*, Document IRC-10NBC, National Research Council of Canada, Ottawa, Ontario.
- National Earthquake Hazard Reduction Program (NEHRP, 1997 and 1994):
www.nehrp.gov
- Nogoshi, I., and Igarashi, T.(1971). On the amplitude characteristics of microtremor (Part 2), *Journal of Seism. Soc.of Japan*, 24, 24-60 (in Japanese with English abstract).
- Ontario Geological Survey (1991). *Bedrock geology of Ontario*, southern sheet (map M2544).
- Oskirko, R. (2010). Assessment of topography seismic site effects, PhD thesis, School of Graduate and Postdoctoral Studies, University of Western Ontario, 273 p.
- Otani, S. (1980). Nonlinear dynamic analysis of reinforced concrete building structures, *Canadian Journal of Civil Engineering*, 7 (2), 333-344.
- Ozel, O., E. Cranswick, M. Meremonte, M. Erdik, and E. Safak (2002). Site effects in Avcilar, west of Istanbul, Turkey, from strong- and weak-motion data, *Bulletin of the Seismological Society of America*, 92 (1), 499-508.
- Palermo, D., and Vecchio, F. (2002). *Behavior and analysis of reinforced concrete walls subjected to reversed cyclic loading*, Rep. No. ISBN 0-7727-7553-02, Publication

- No. 2002-01, Department of Civil Engineering, University of Toronto, Toronto, Canada, 2002, 351 pp.
- Palermo, D., and Vecchio, F. (2003). Compression field modeling of reinforced concrete subjected to reversed loading: formulation, *ACI Structural Journal*, 100 (5), 616-625.
- Park, C.B., Miller, R.D., and Xia, J., (1999a). Multimodal analysis of high frequency surface waves, *Proceedings of the symposium on the application of geophysics to engineering and environmental problems '99*, 115–121.
- Park, C.B., Miller, R.D., and Xia, J. (1999b). Multichannel analysis of surface waves, *Geophysics*, 64, 800–808.
- Parolai, S., S.M. Richwalski, C. Milkereit, and D. Fah (2006). S-wave Velocity Profiles for Earthquake Engineering Purposes for the Cologne Area (Germany), *Bulletin of Earthquake Engineering*, 4, 65–94.
- Pavlenko, O.V., and Irikura, K. (2003). Estimation of nonlinear time-dependent soil behavior in strong ground motion based on vertical array data, *Pure appl. Geophys.*, 160, 2365–2379.
- Paz, M. (1994). *International handbook of earthquake engineering: codes, programs, and examples*, Chapman and Hall, London, New York, 543 p.
- Pedersen, R., Simone, A., and Sluys, L. (2008). An analysis of dynamic fracture in concrete with a continuum visco-elastic visco-plastic damage model, *Engineering fracture mechanics*, 75 (13), 3782-3805.
- Peng, Z. and Ben-Zion, Y. (2006). Temporal changes of shallow seismic velocity around the Karadere-Düzce branch of the North Anatolian Fault and strong ground motion, *Pure appl. Geophys.*, 163, 567–600.
- Repapis, C., Zeris, C., and Vintzileou, E. (2006). Evaluation of the seismic performance of existing rc buildings: II A case study for regular and irregular buildings, *Journal of earthquake engineering*, 10 (3), 429-452.

- Reynolds, J. (1997). *An introduction to applied and environmental geophysics*, John Wiley and Sons Ltd, Chichester, 796 pp.
- Richart, F.E., Jr., Hall, Jr., J.R., and Woods, R.D. (1970). *Vibrations of Soils and Foundations*, Englewood Cliffs, N J, Prentice Hall, 448 p.
- Sallen, R. P.; E. L. Key (1955). A practical method of designing RC active filters, *IRE Transactions on Circuit Theory*, 2 (1), 74–85.
- Sanchez-Salinerio I, Rosset J.M., Shao K.Y., Stokoe II K.H., Rix G.J. (1987). Analytical evaluation of variables affecting surface wave testing of pavements, *Transp. Res. Rec.*, 1136, 86–95.
- Sercombe, J., Hellmich, C., Ulm, F., and Mang , H. (2000). Modeling of early-age creep of shotcrete. i: model and model parameters, *Journal of engineering mechanics (ASCE)*, 126 (3) , 284-291.
- SESAME H/V User Guidelines, (HV user guidelines), Guidelines for the implementation of the H/V spectral ratio technique on ambient vibrations - measurements, processing and interpretations, SESAME European research project, deliverable D23.12, 2005.
- ShakeMap: <http://www.cisn.org/shakemap/sc/shake/about.html#intmapshttp>.
- Stokoe K.H., II, and Nazarian, S. (1985). Use of Rayleigh waves in liquefaction studies, In: *Measurement and use of shear wave velocity for evaluating dynamic soil properties*, ed. R.D. Woods, A.S.C.E., New York, 1-17.
- Studer, J. & A. Ziegler (1986). *Bodendynamik*, Springer Verlag, Berlin - Heidelberg - New York.
- Trifunac, M. D., and A. G. Brady (1975). On the correlation of seismic intensity scales with the peaks of recorded ground motion, *Bulletin of the Seismological Society of America* , 65 (1), 139-162.
- Tsuboi, S., Satio, M., and Ishihara, Y. (2001). Verification of horizontal-to-vertical spectral-ratio technique for estimation of site response using borehole seismographs, *Bulletin of the Seismological Society of America*, 91 (3), 499-510.

- Turek, M., K. Thibert, C.E. Ventura, and S. Kuan (2006). Ambient Vibration Testing of Three Unreinforced Brick Masonry Buildings in Vancouver, Canada, *Proceedings of the Conference: 2006 IMAC-XXIV: Conference & Exposition on Structural Dynamics*, 7p.
- Van Overschee P., De Moor B., (1996). *Subspace Identification for Linear Systems: Theory, Implementation, Applications*, Kluwer Academic Publishers, 254 p.
- Vecchio, F.J. (1999). Toward cyclic load modeling of reinforced concrete, *ACI Struct. J.*, 96 (2), 193-202.
- Ventura, C. E., Onur, T., and X.-S. Hao, K. (2004). Site Period Estimations in the Fraser River Delta Using Microtremor Measurements – Experimental and Analytical Studies, *Proceedings of the 13th World Conference on Earthquake Engineering, Vancouver, B.C., Canada, August 1-6, 2004*, Paper No. 1075 on CD-ROM.
- Volant, P.H., Orbovic, N and Dunand, F. (2002). Seismic evaluation of existing nuclear facility using ambient vibration test to characterize dynamic behaviour of the structure and microtremor measurements to characterise the soil: a case study, *Soil Dyn. Earthquake Eng*, 22 (9-12), 1159-1167.
- Wald, D. J., V. Quitoriano, T. H. Heaton, H. Kanamori (1999a). Relationship between Peak Ground Acceleration, Peak Ground Velocity, and Modified Mercalli Intensity for Earthquakes in California, *Earthquake Spectra*, Vol. 15, No. 3, 557-564.
- Wald, D., V. Quitoriano, T. Heaton, H. Kanamori, C. Scrivner, and C. Worden (1999b). TriNet ShakeMaps: Rapid generation of peak ground motion and intensity maps for earthquakes in southern California, *Earthquake Spectra*, 15, 537–555.
- Williams, A.B., and F. J. Taylor (1988). *Electronic filter design handbook*, McGraw-Hill, 816 p.
- Xia, J., Miller, R.D., and Park, C.B. (1999). Configuration of near surface shear wave velocity by inverting surface wave, *Proceedings of the symposium on the application of geophysics to engineering and environmental problems '99*, 95–104.

APENDIX

TABLE OF CONTENTS

	page
Notations on the figures	182
Results for Referent Test Point #2.	183
Vs30m	183
SH Refraction Profiles	183
MASW	184
HVSr	186
Results for Referent Test Point #4.	187
Vs30m	187
SH Refraction Profiles	187
MASW	188
HVSr	190
Results for Referent Test Point #6.	191
Vs30m	191
SH Refraction Profiles	191
MASW	192
HVSr	194
Results for Referent Test Point #8.	195
Vs30m	195
SH Refraction Profiles	195
MASW	196
HVSr	198
Results for Referent Test Point #12.	199
Vs30m	199
SH Refraction Profiles	199
MASW	200
HVSr	202
Results for Referent Test Point #14.	203
Vs30m	203
SH Refraction Profiles	203
MASW	204
HVSr	206
Results for Referent Test Point #17.	207
Vs30m	207
SH Refraction Profiles	207
MASW	208
HVSr	210

Results for Referent Test Point #18.	211
Vs30m	211
SH Refraction Profiles	211
MASW	212
HVSR	214
Results for Referent Test Point #20.	215
Vs30m	215
SH Refraction Profiles	215
MASW	216
HVSR	218
Results for Referent Test Point #21.	219
Vs30m	219
SH Refraction Profiles	219
MASW	220
HVSR	222
Results for Referent Test Point #22.	223
Vs30m	223
SH Refraction Profiles	223
MASW	224
HVSR	226
Results for Referent Test Point #27.	227
Vs30m	227
SH Refraction Profiles	227
MASW	228
HVSR	230
Results for Referent Test Point #31.	231
Vs30m	231
SH Refraction Profiles	231
MASW	232
HVSR	234
Results for Referent Test Point #32.	235
Vs30m	235
SH Refraction Profiles	235
MASW	236
HVSR	238
Results for Referent Test Point #35.	239
Vs30m	239
SH Refraction Profiles	239
MASW	240
HVSR	242

Notations on the figures

Results for Vs30m:

SH-refraction	Vs30m from seismic profiling
2-layer MASW	- model for inversion with SeisImager/SW TM from Geometrics
4-layer MASW	“
7-layer MASW	“
15-layer MASW	“

SH Refraction Profiles- Referent Test Point #XX:

x, m- distances from first geophone to the others
 pXX.X.dat - the original seismic record in SEG-2 format

MASW - Referent Test Point #XX:

Distance, m - distances from first geophone to the others
 Source = -1.25 m from first geophone
 XX.dat - the original seismic record in SEG-2 format
 dark grey - reliable segment of the velocity profile

HVSR- Referent Test Point #XX:

P_xx_F_yy - the original ASCII file of recorded waveforms

total vector = $\sqrt{V_{NS}^2 + V_Z^2 + V_{EW}^2}$, where V_i are the recorded velocity of vibration

averaged rms - averaged total vector in a 13 seconds running triangle window

hysteretic threshold - two levels threshold for the separation of the waveform into

Low (LL) and High Level (HL) seismic noise.

Two records for HVSR were made in the referent points.

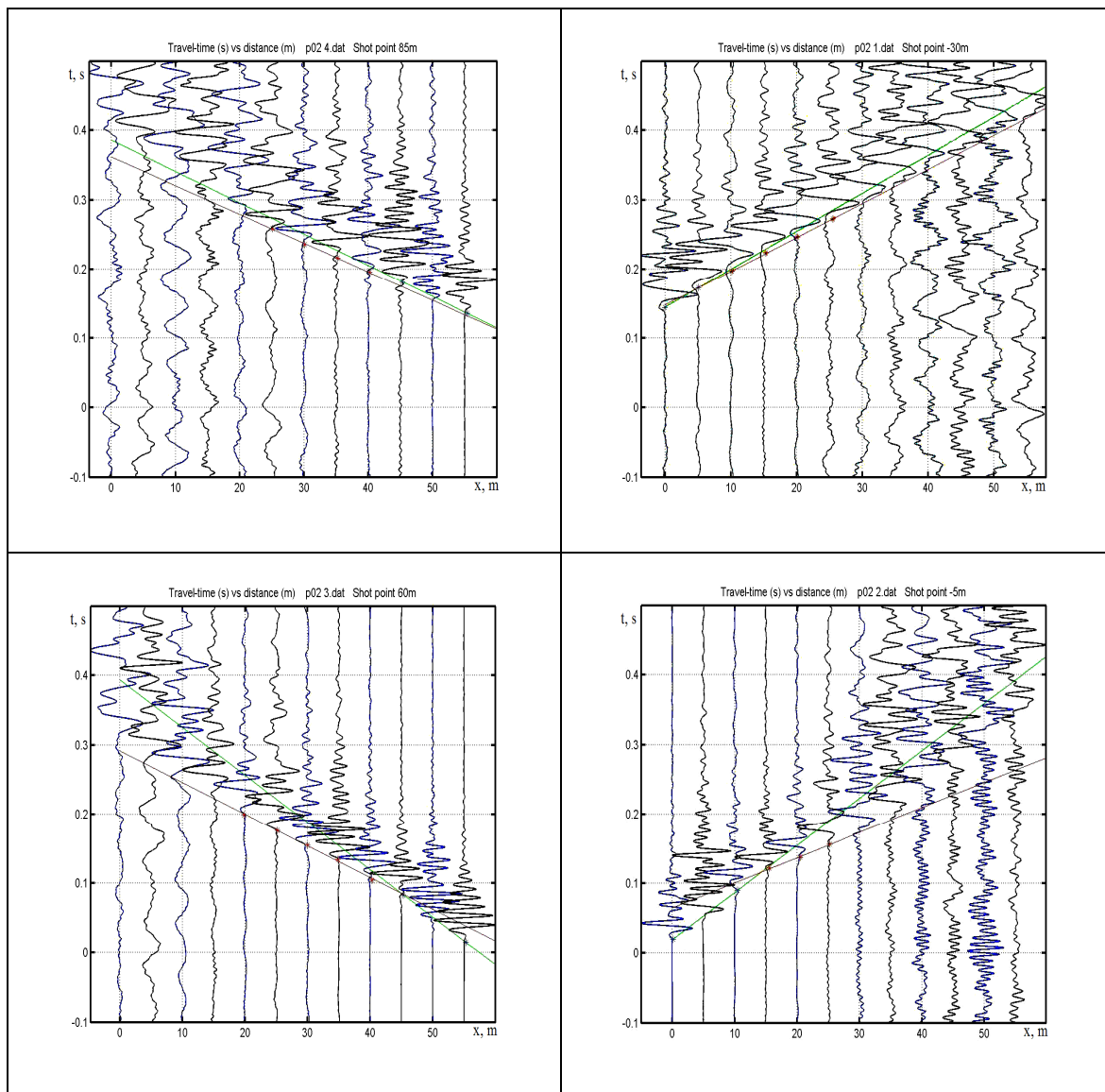
- a) - original 3-component waveforms, b) and c) - processing for waveforms separation,
- d) - HVSR from Low and High Levels of ambient seismic vibrations.

Result for Referent Test Point #2

Results for Vs30

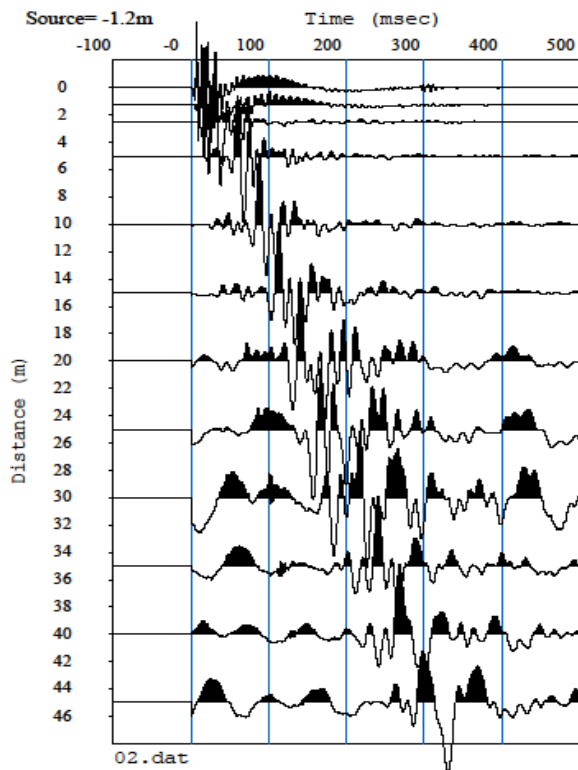
Vs30	SH-refraction	2-layer MASW	4-layer MASW	7-layer MASW	15-layer MASW
[m/s]	226	259	273	268	258

SH Refraction Profiles - Referent Test Point #2

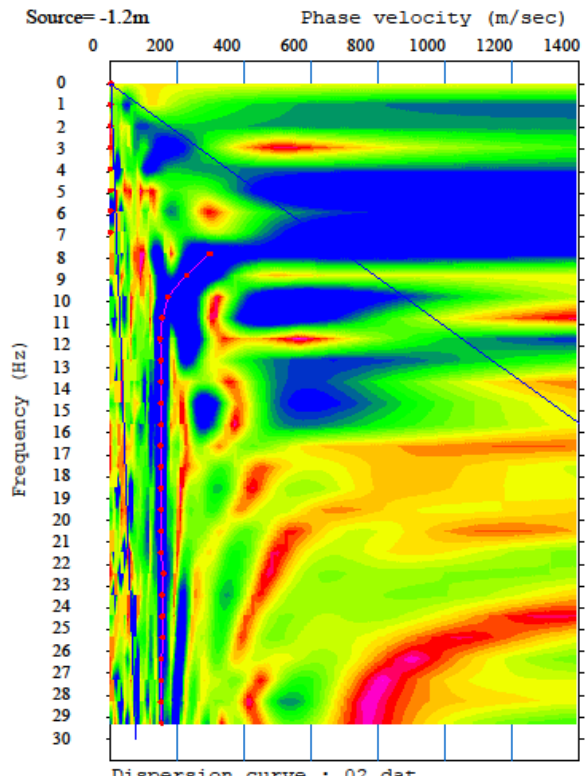


Vs30m = 226 m/s

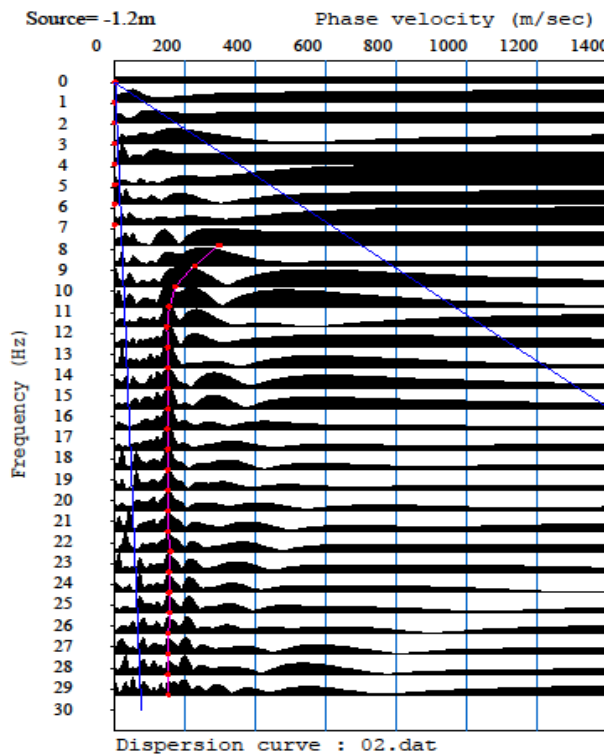
MASW - Referent Test Point #2



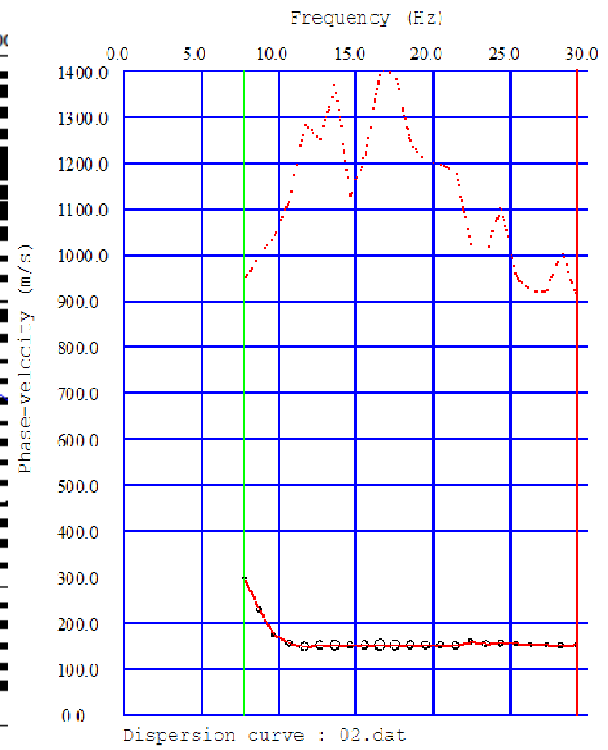
Test Point #2 MASW seismic waveforms



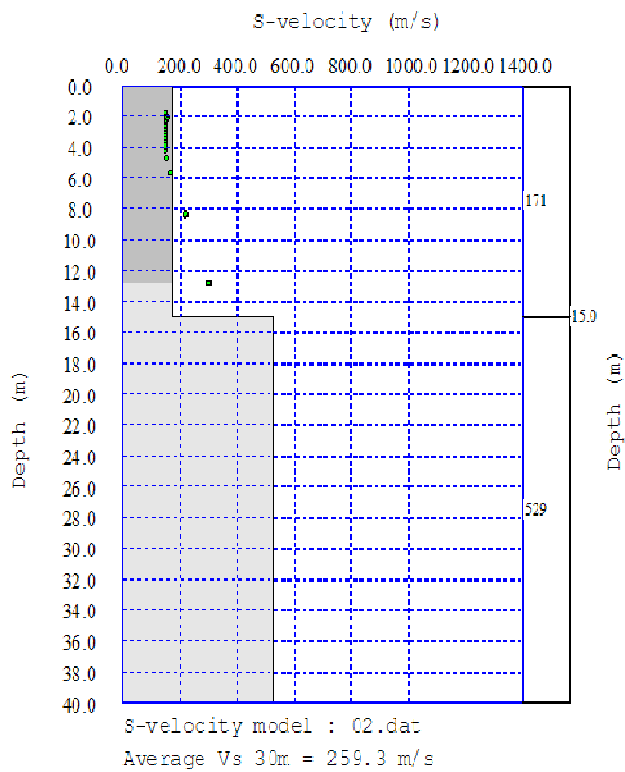
Surface Waves Dispersion - interpolated



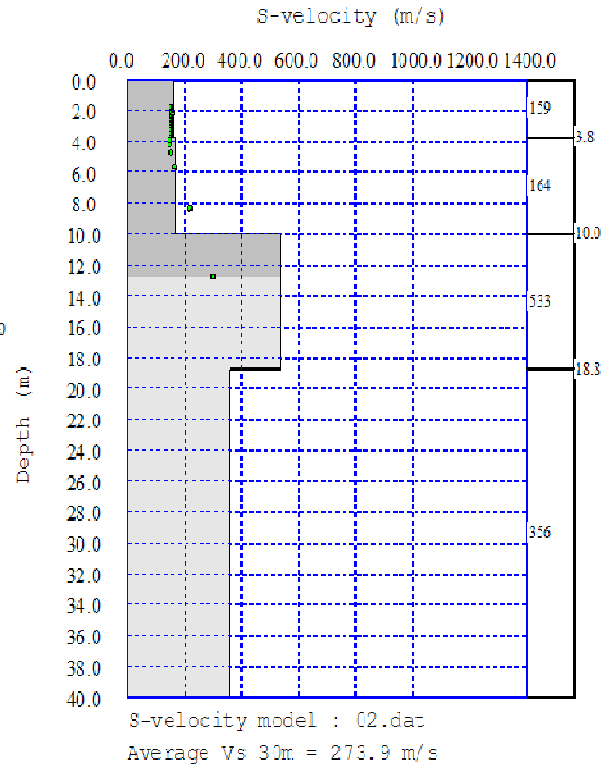
Surface Waves Dispersion



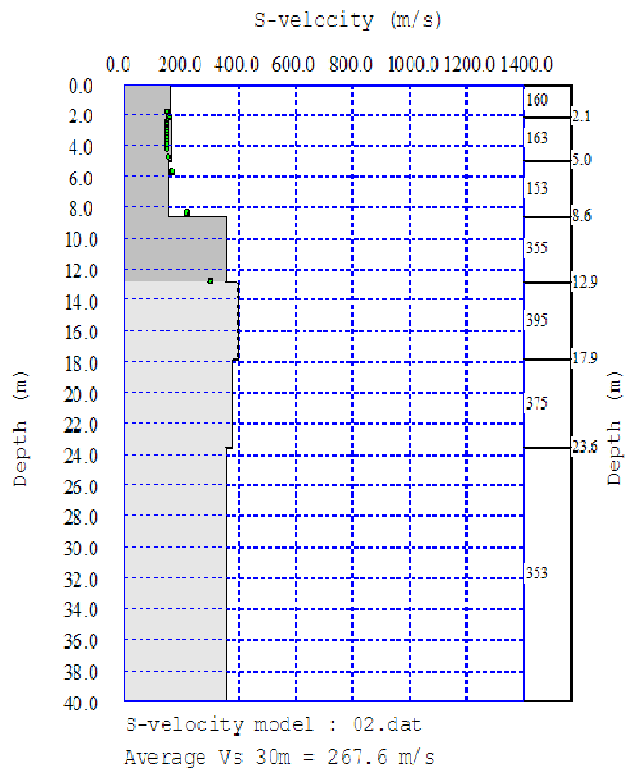
Phase velocity vs. frequency



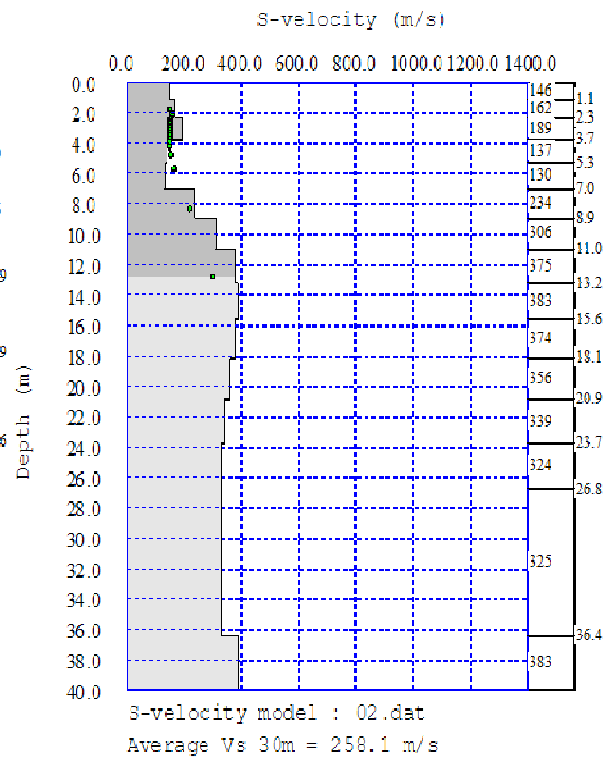
Test point #2 2-layers inversion



Test point #2 4-layers inversion

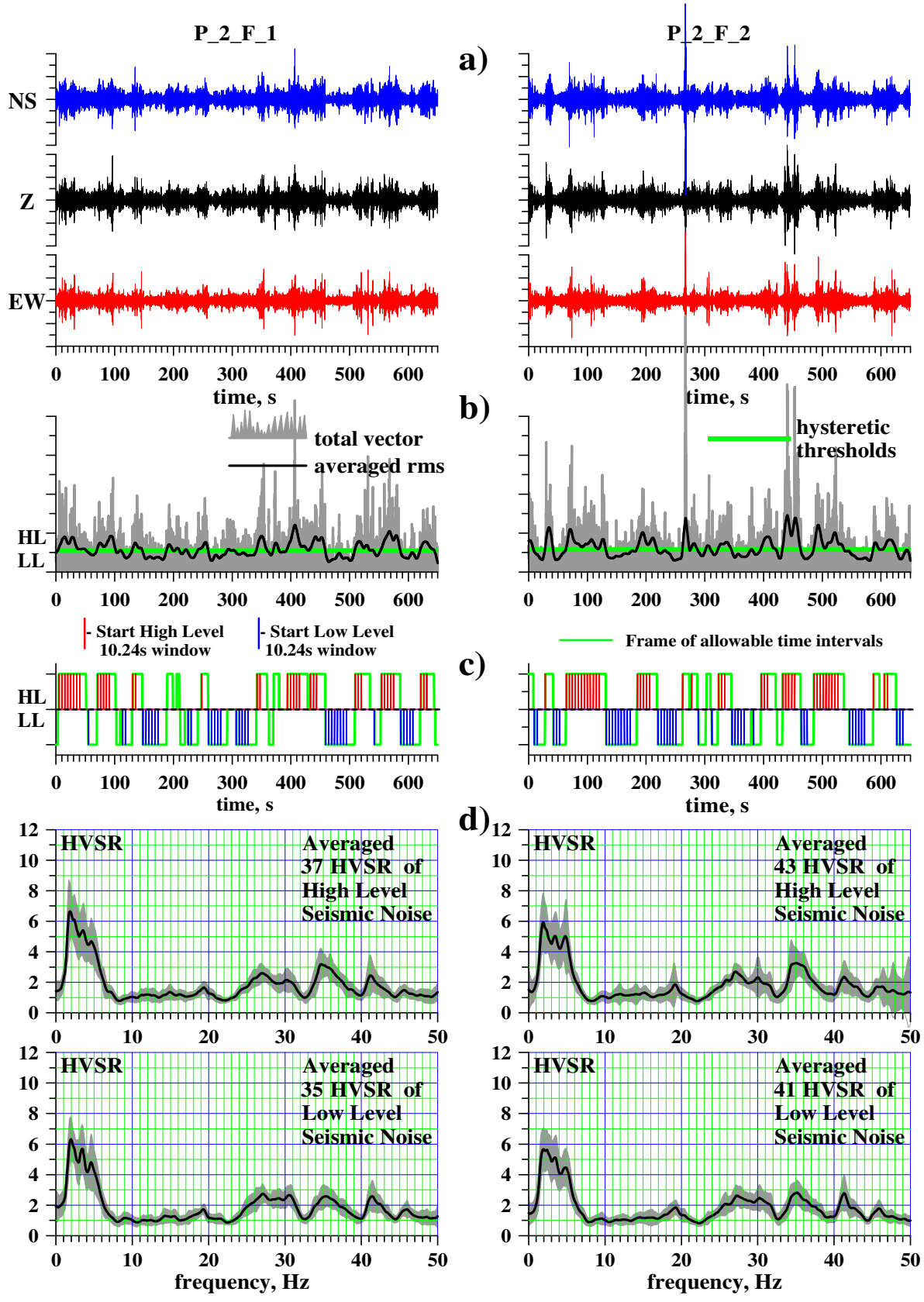


Test point #2 7-layers inversion



Test point #2 15-layers inversion

HVSR - Referent Test Point #2

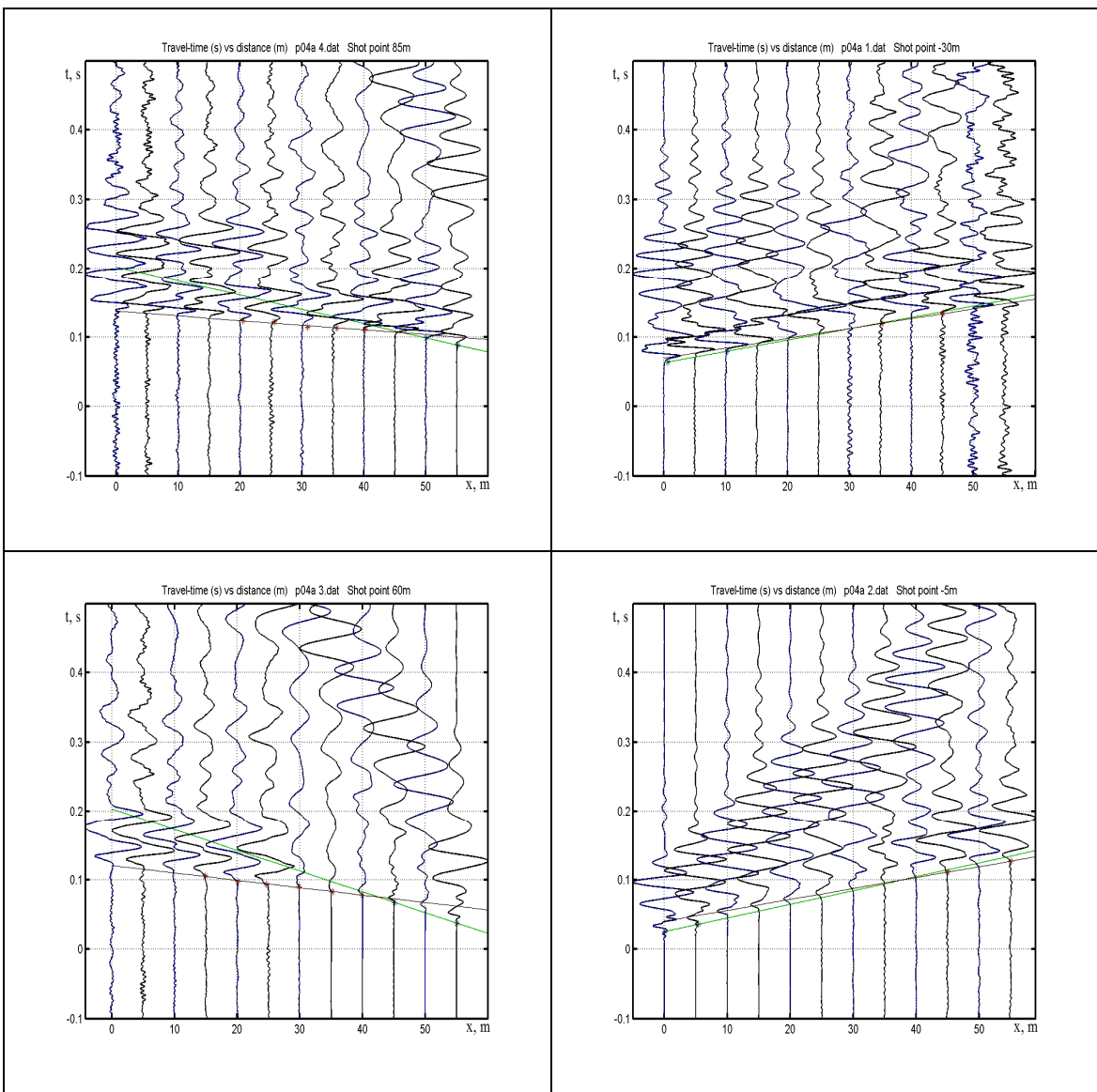


Results for Referent Test Point #4

Results for Vs30

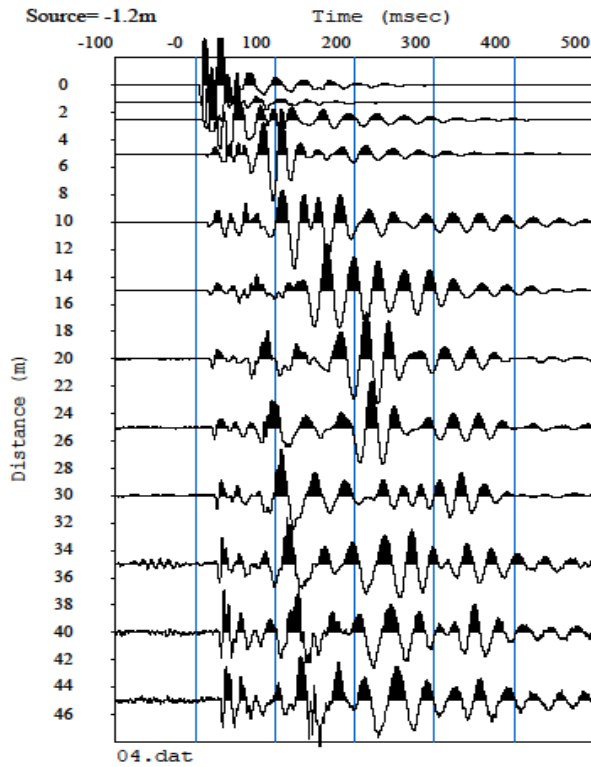
Vs30	SH-refraction	2-layer MASW	4-layer MASW	7-layer MASW	15-layer MASW
[m/s]	769	734	696	695	697

SH Refraction Profiles - Referent Test Point #4

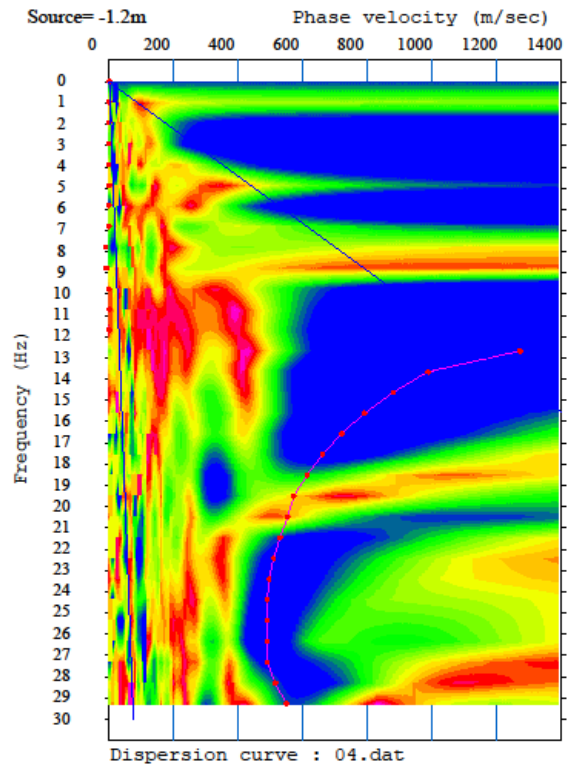


Vs30m = 769 m/s

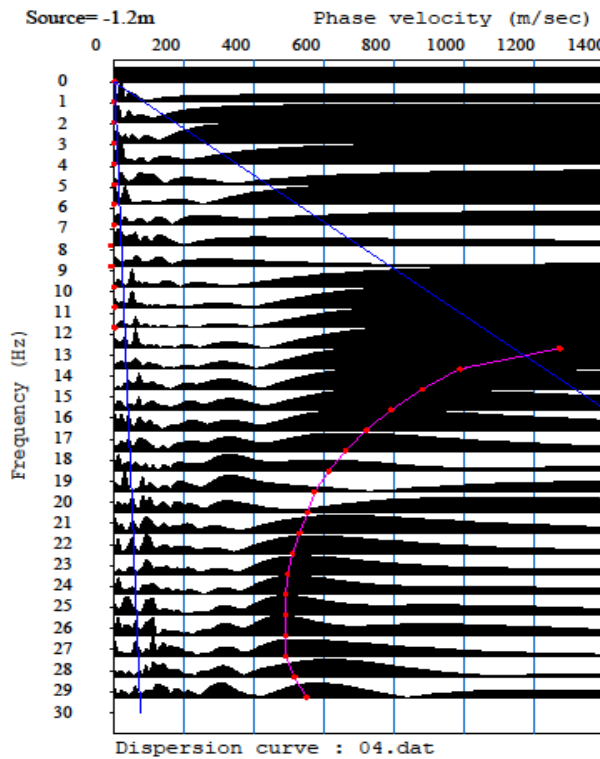
MASW - Referent Test Point #4



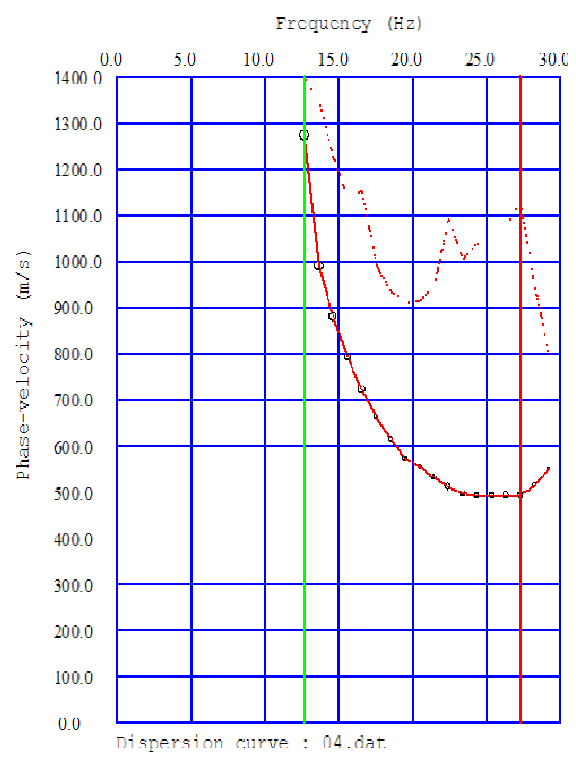
Test Point #4 MASW seismic waveforms



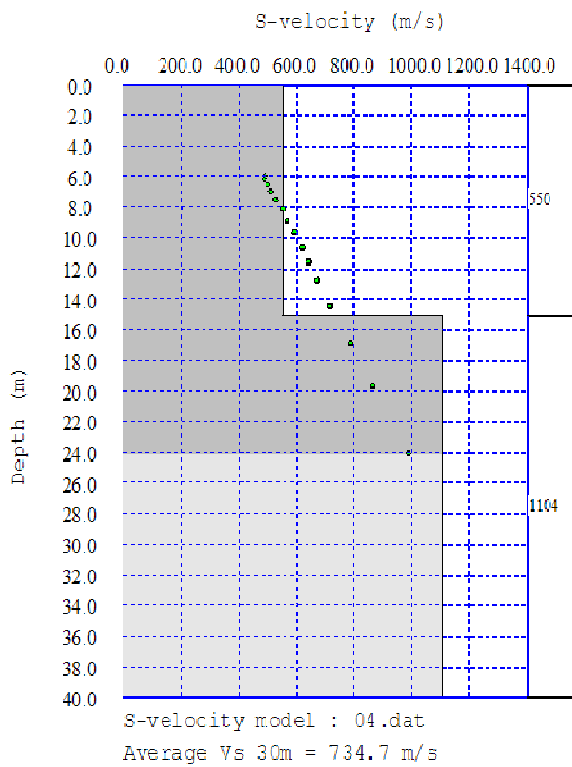
Surface Waves Dispersion - interpolated



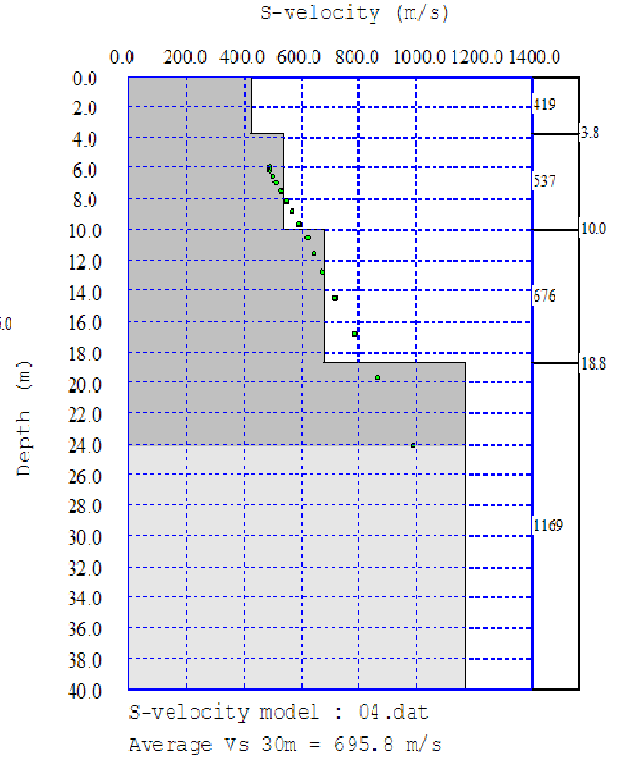
Surface Waves Dispersion



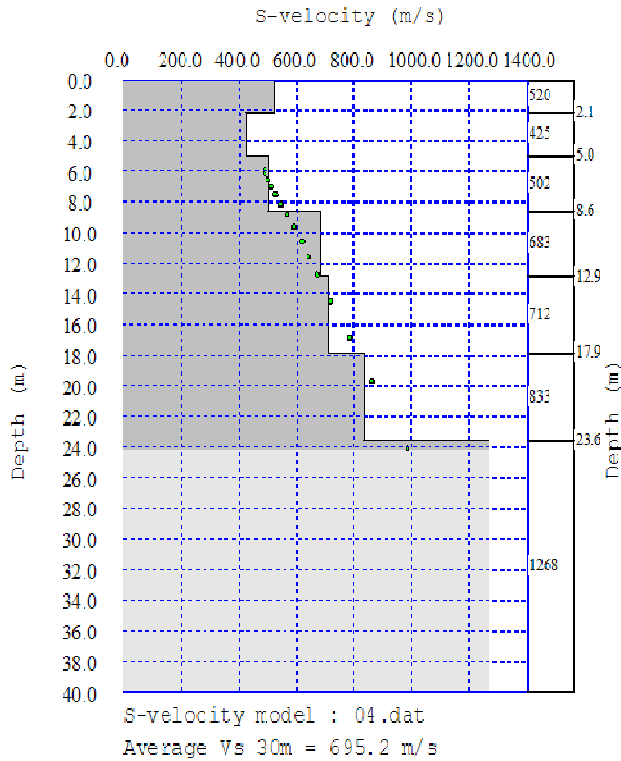
Phase velocity vs. frequency



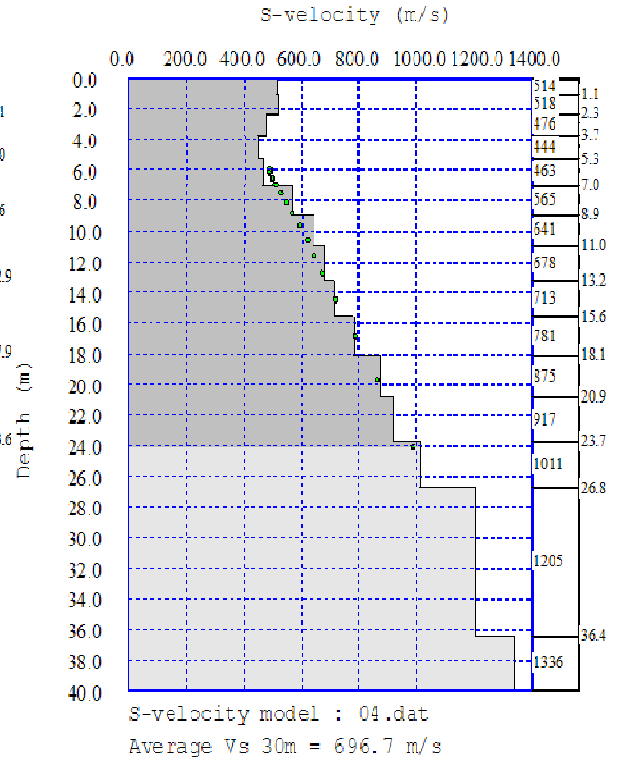
Test point #4 2-layers inversion



Test point #4 4-layers inversion

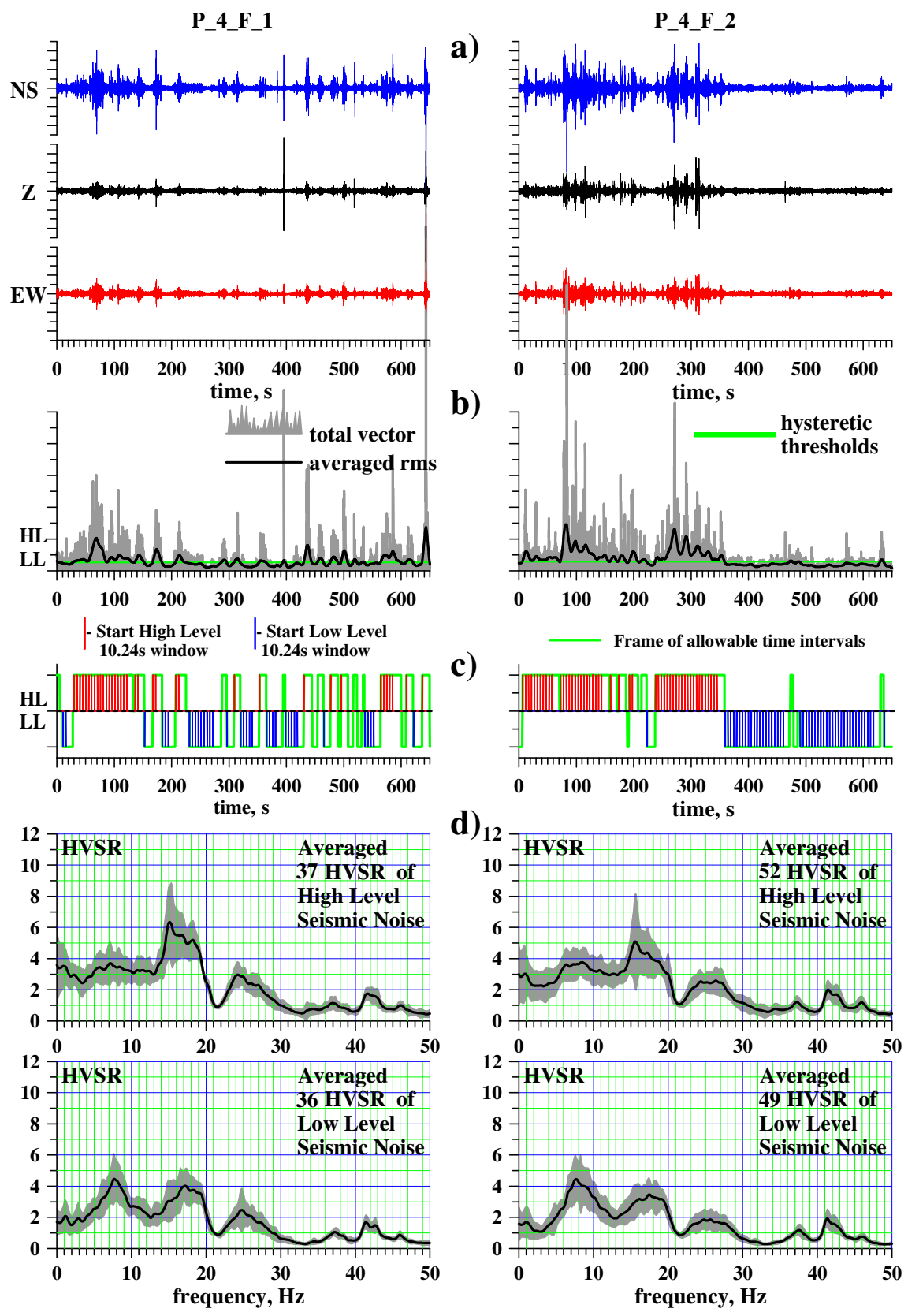


Test point #4 7-layers inversion



Test point #4 15-layers inversion

HVSR - Referent Test Point #4

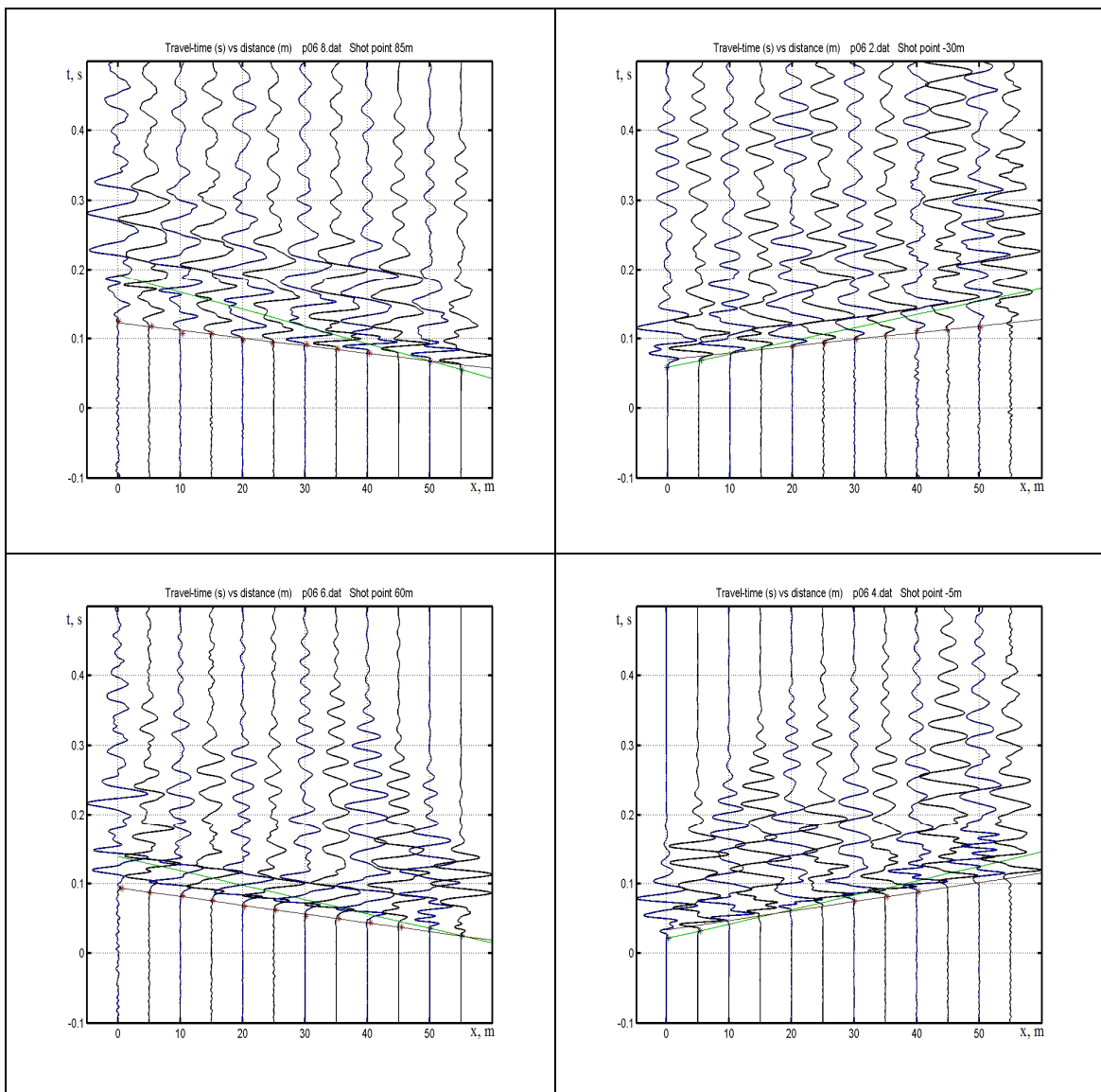


Results for Referent Test Point #6

Results for Vs30

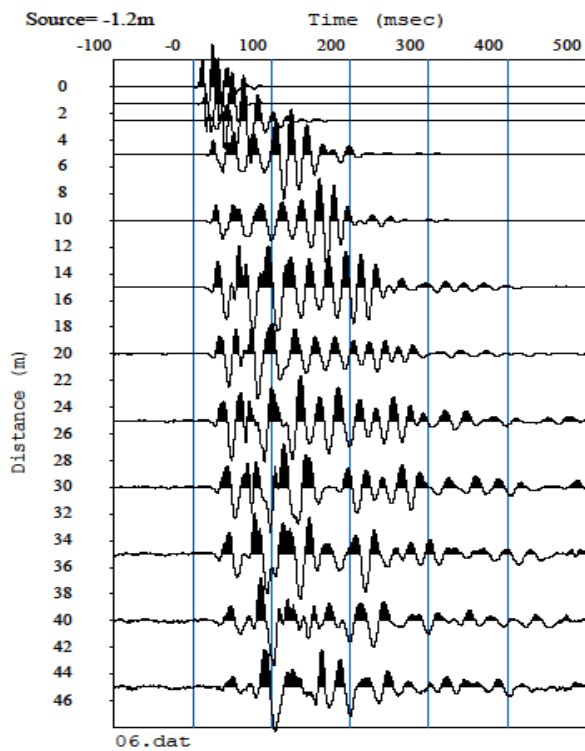
Vs30	SH-refraction	2-layer MASW	4-layer MASW	7-layer MASW	15-layer MASW
[m/s]	728	544	550	544	541

SH Refraction Profiles - Referent Test Point #6

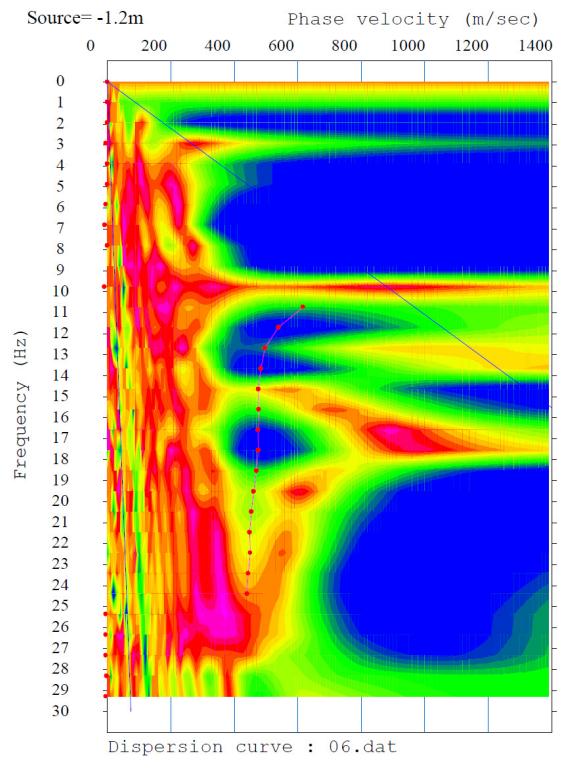


Vs30m = 728 m/s

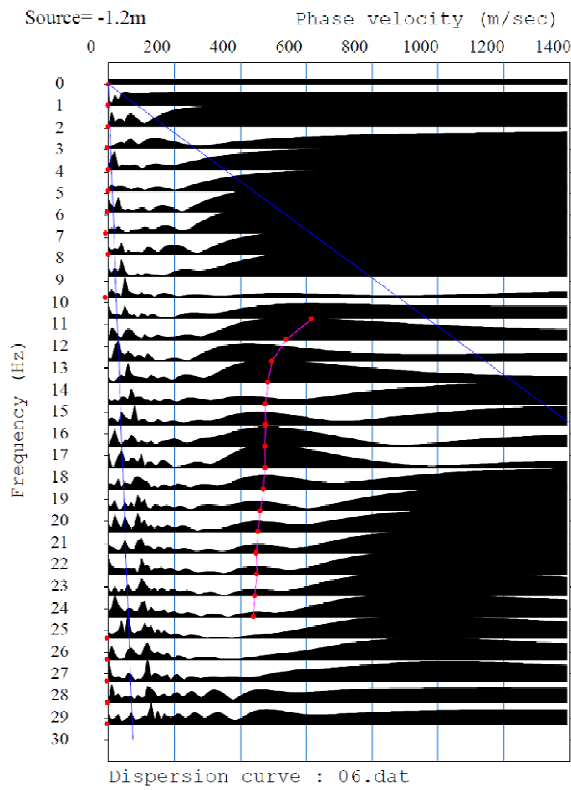
MASW - Referent Test Point #6



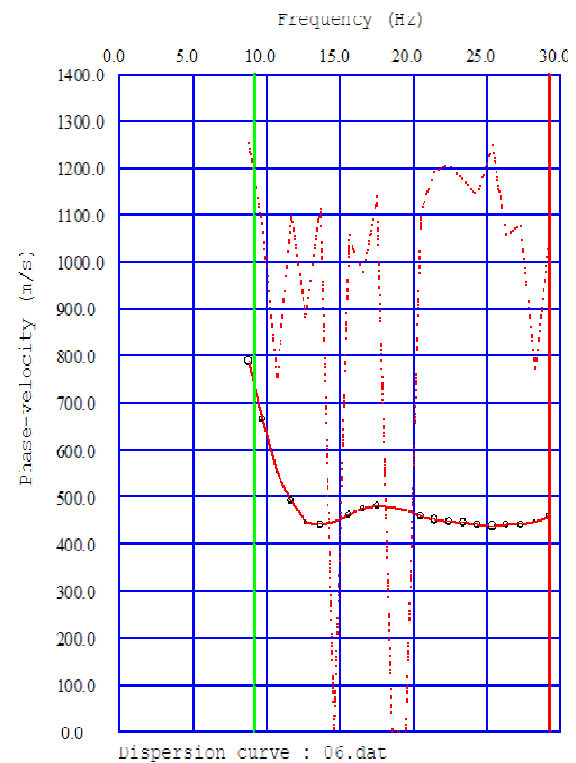
Test Point #6 MASW seismic waveforms



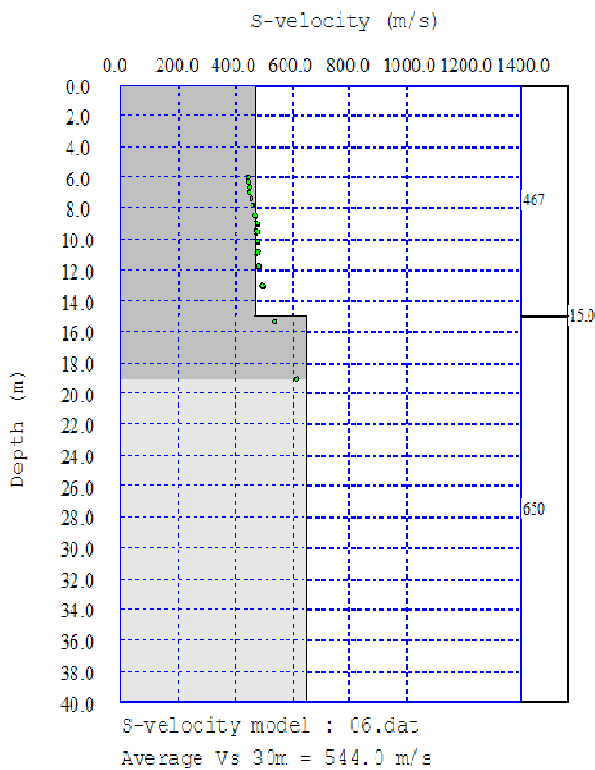
Surface Waves Dispersion - interpolated



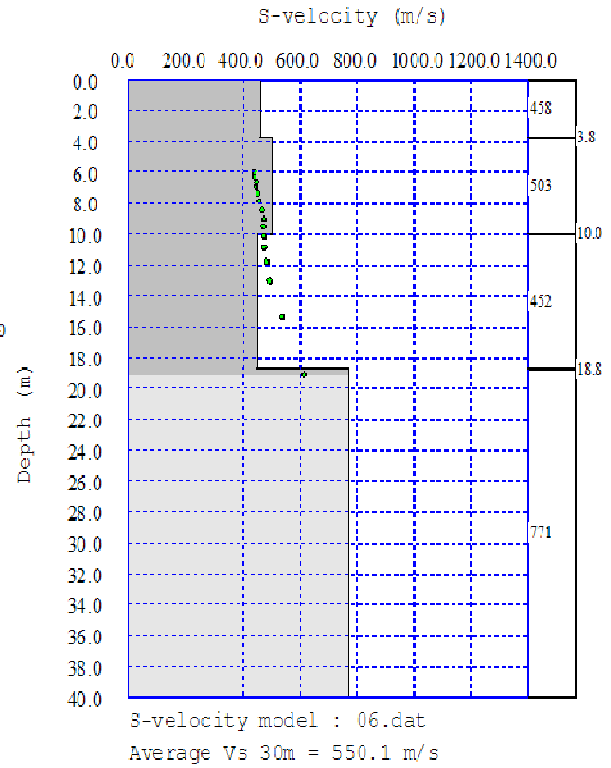
Surface Waves Dispersion



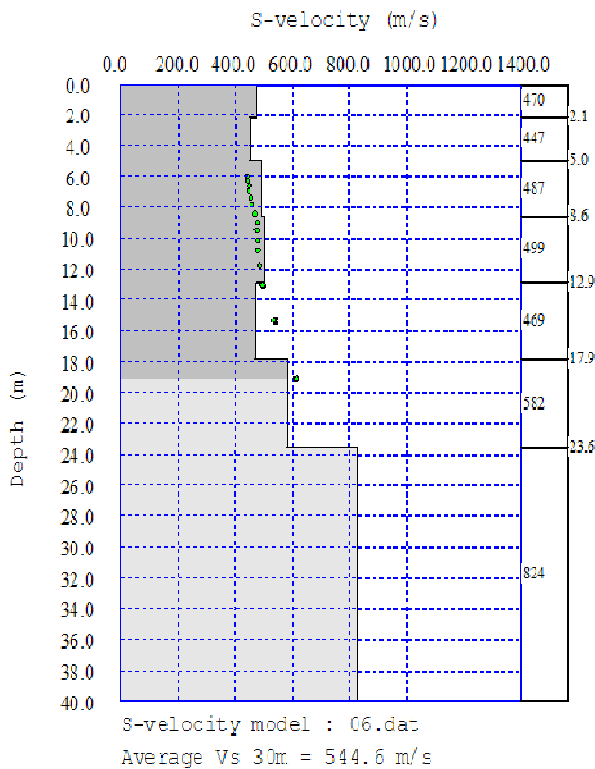
Phase velocity vs. frequency



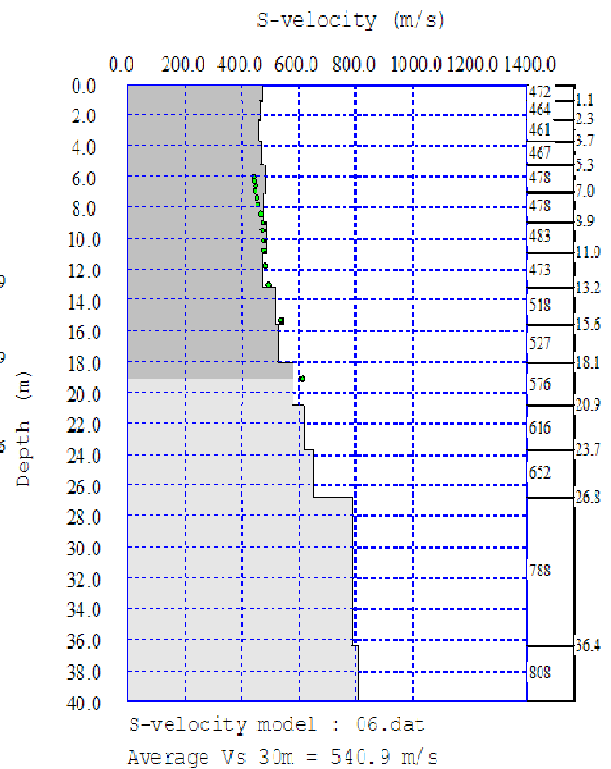
Test point #6 2-layers inversion



Test point #6 4-layers inversion

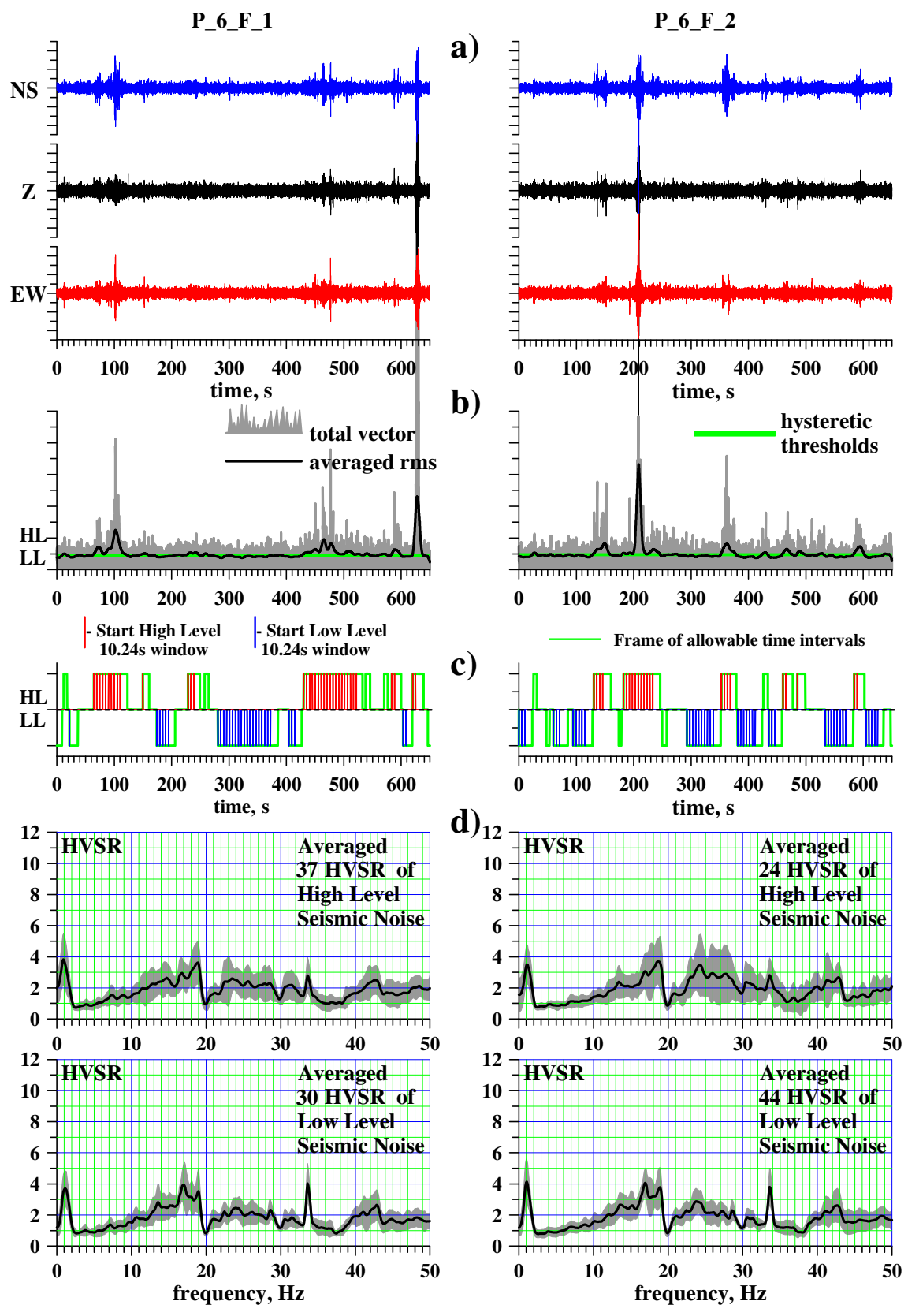


Test point #6 7-layers inversion



Test point #6 15-layers inversion

HVSR - Referent Test Point #6

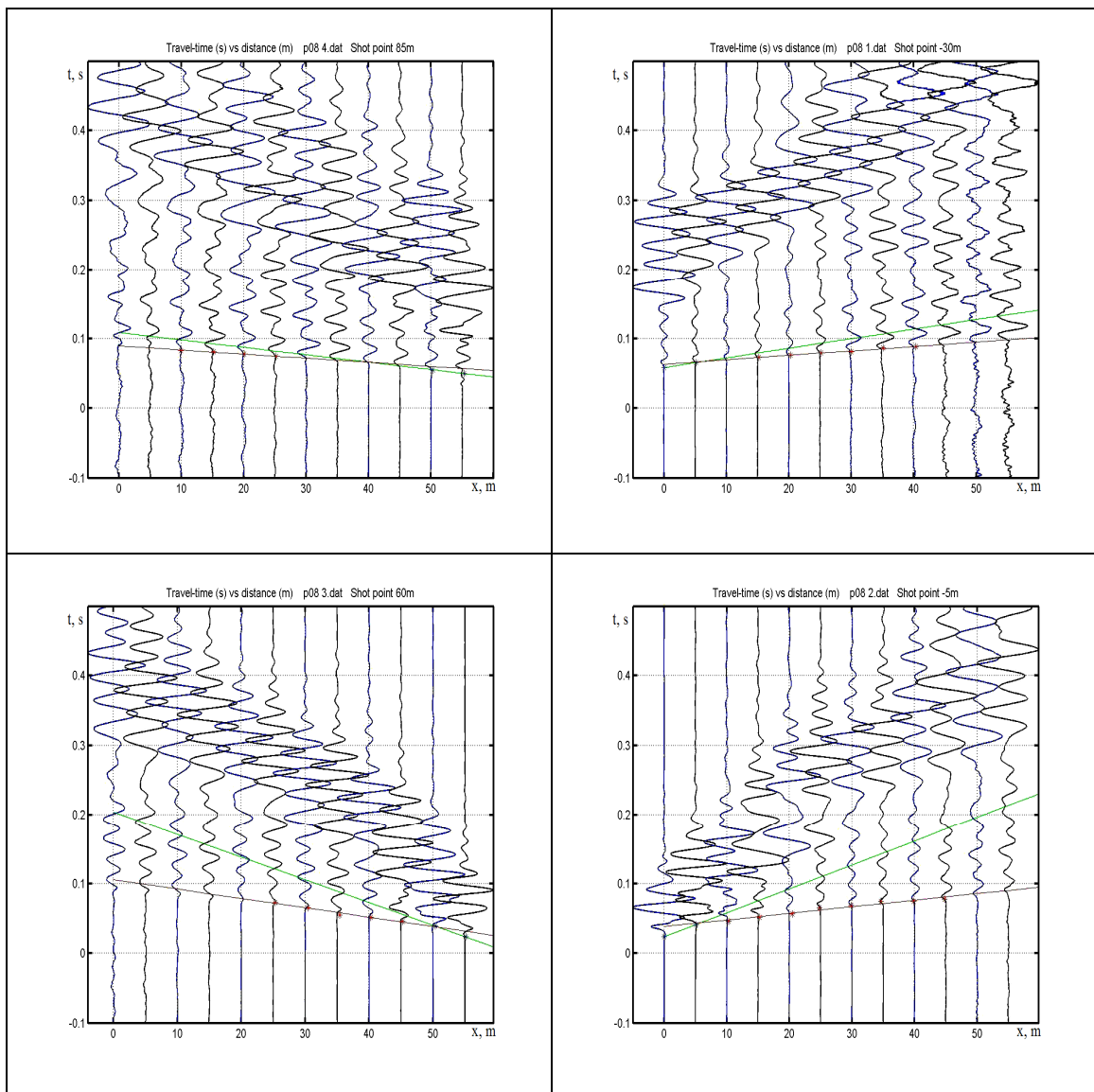


Results for Referent Test Point #8

Results for Vs30

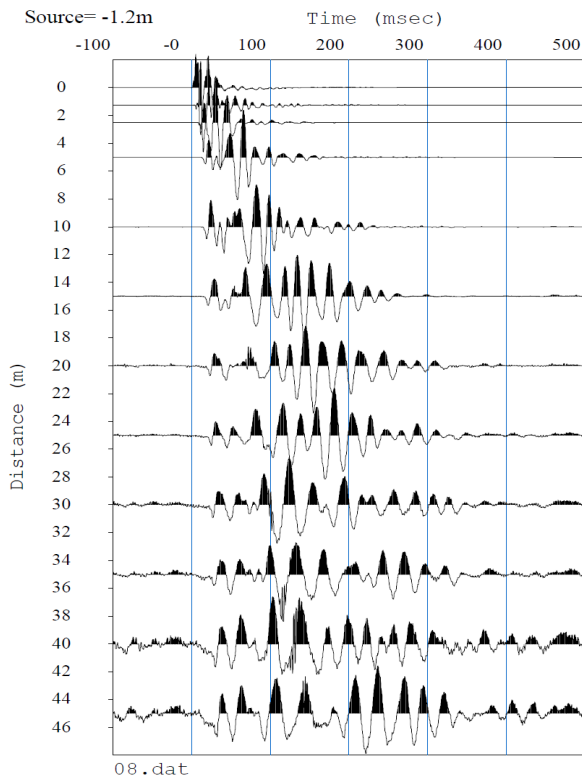
Vs30	SH-refraction	2-layer MASW	4-layer MASW	7-layer MASW	15-layer MASW
[m/s]	226	259	273	268	258

SH Refraction Profiles - Referent Test Point #8

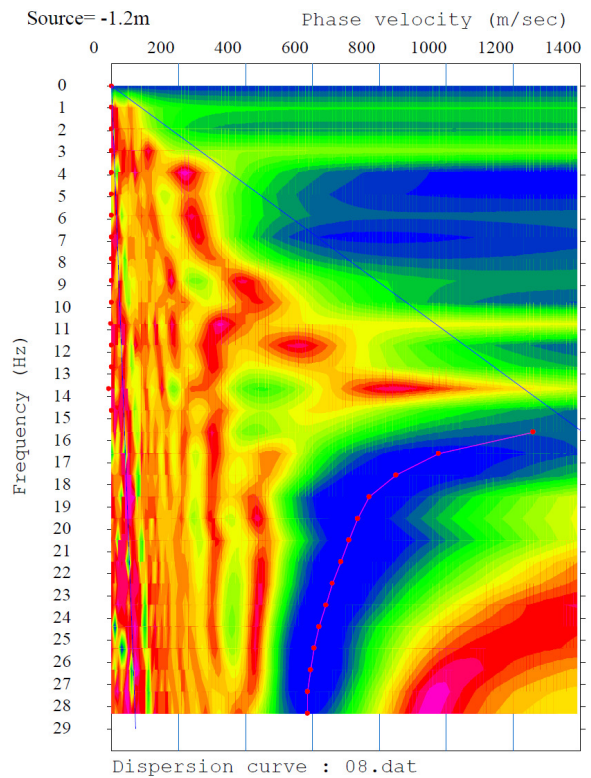


Vs30m = 966 m/s

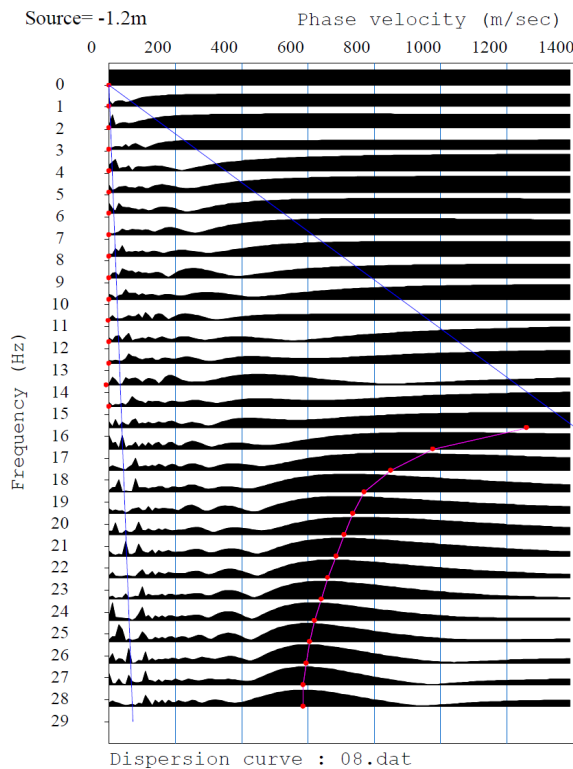
MASW - Referent Test Point #8



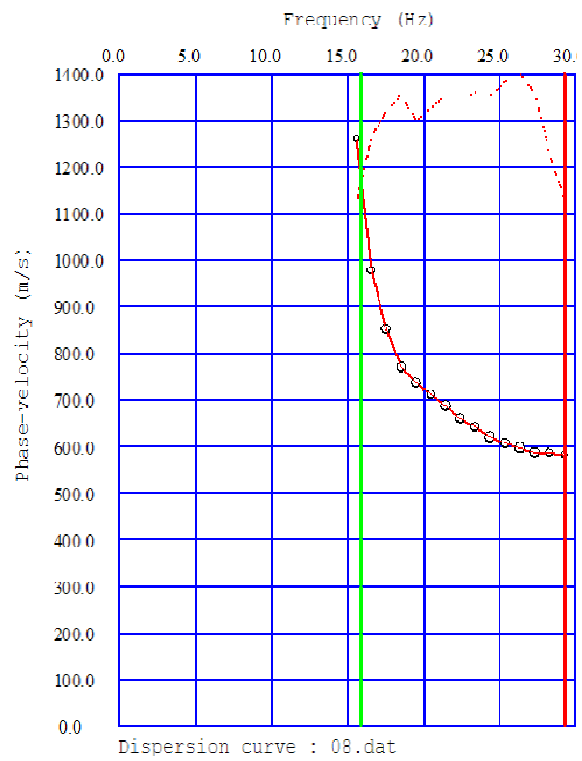
Test Point #8 MASW seismic waveforms



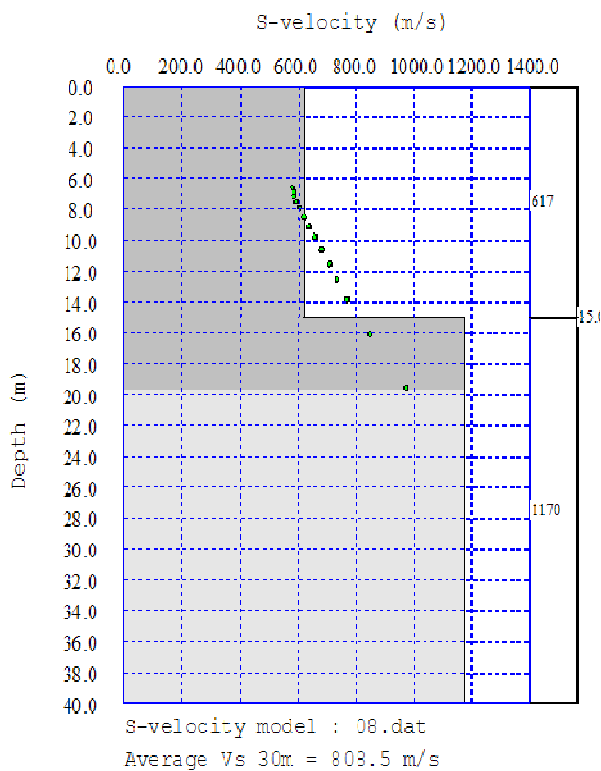
Surface Waves Dispersion - interpolated



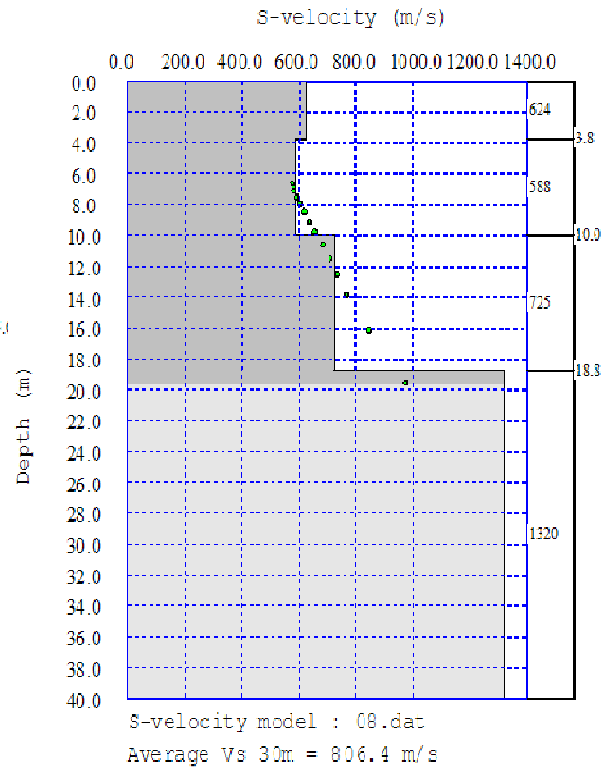
Surface Waves Dispersion



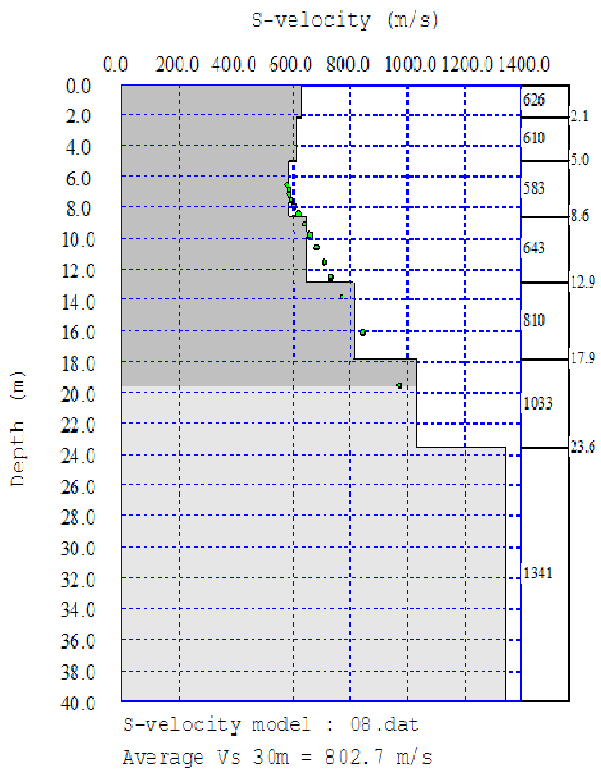
Phase velocity vs. frequency



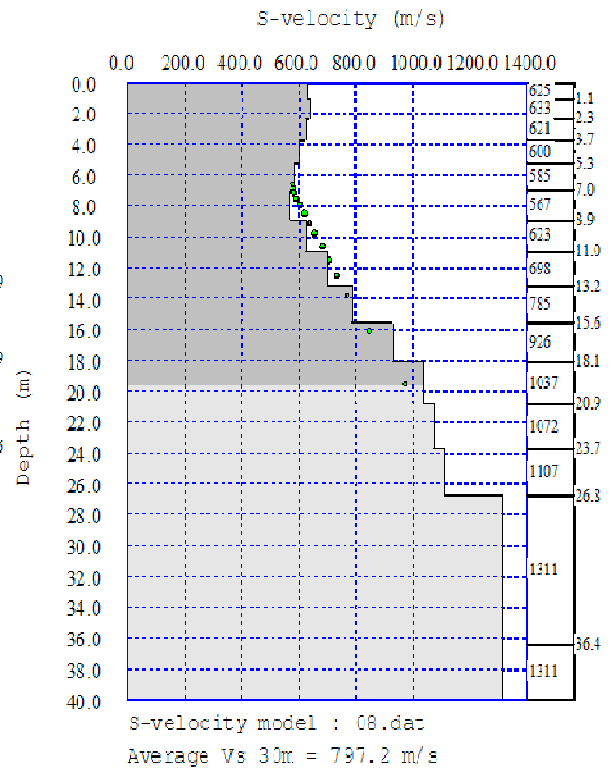
Test point #8 2-layers inversion



Test point #8 4-layers inversion

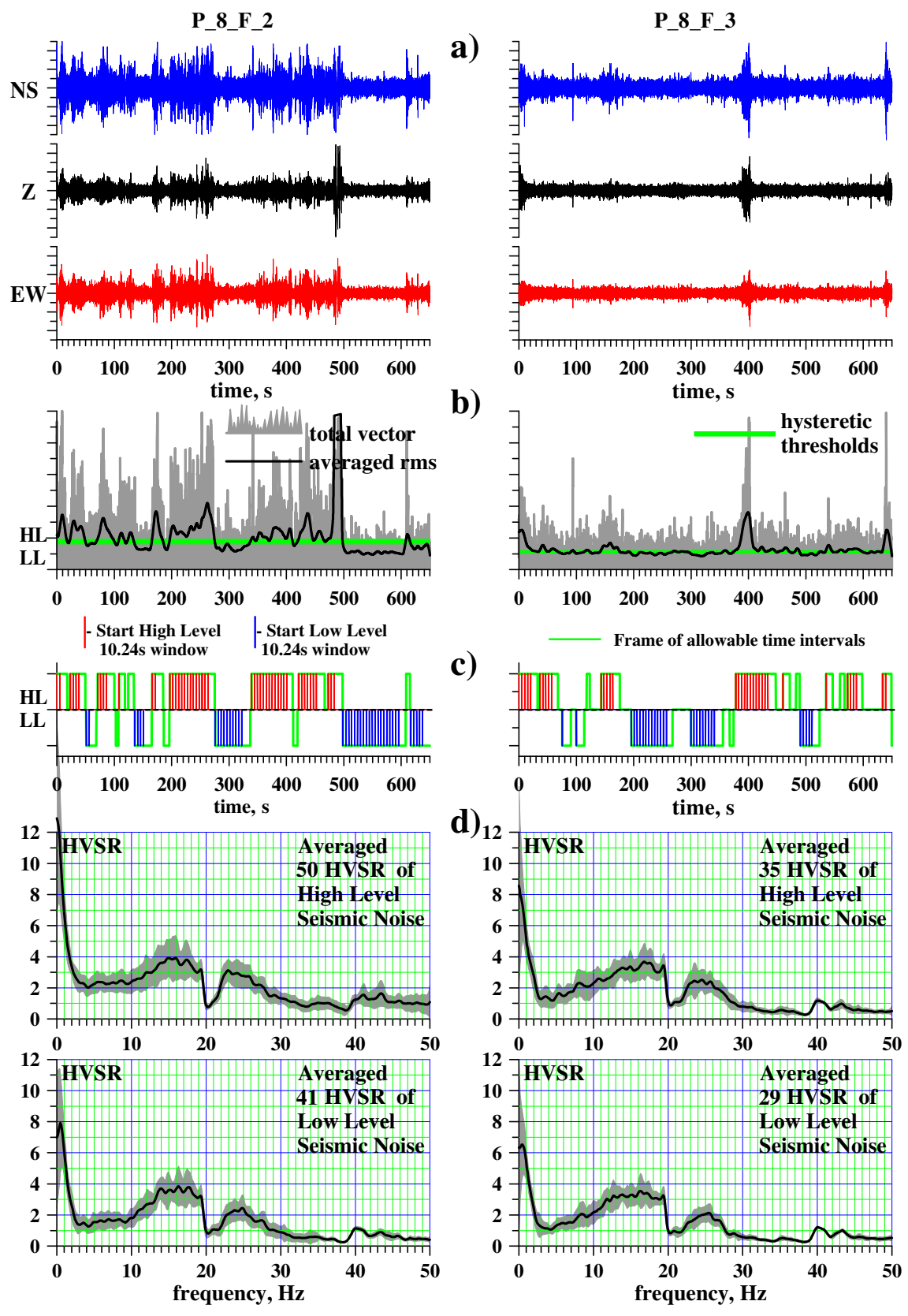


Test point #8 7-layers inversion



Test point #8 15-layers inversion

HVSR - Referent Test Point #8

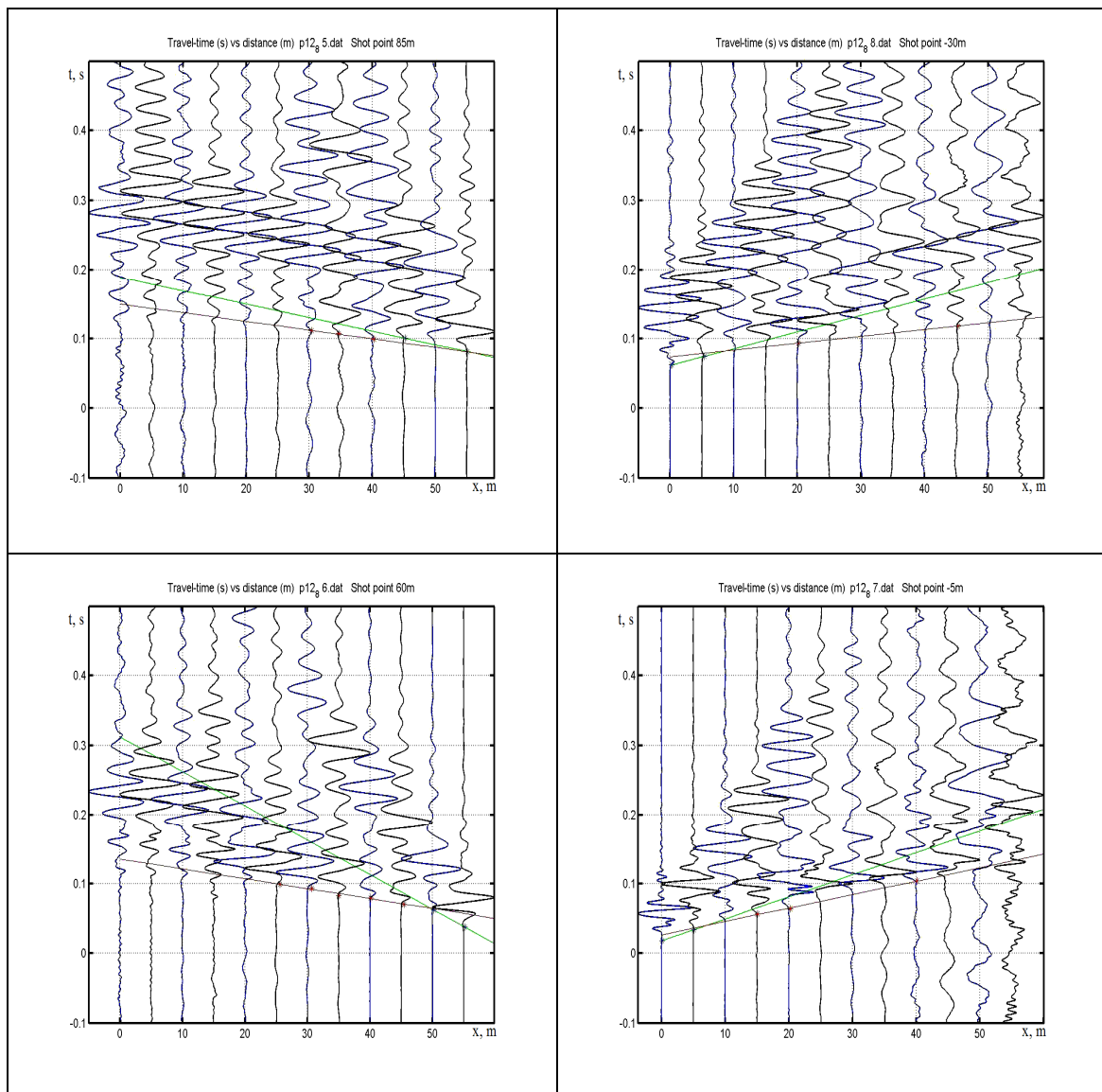


Results for Referent Test Point #12

Results for Vs30

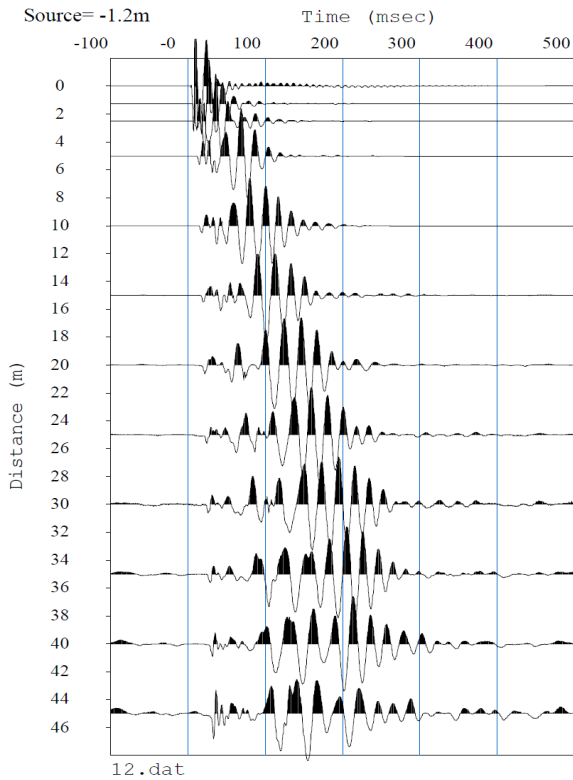
Vs30	SH-refraction	2-layer MASW	4-layer MASW	7-layer MASW	15-layer MASW
[m/s]	600	634	588	595	593

SH Refraction Profiles - Referent Test Point #12

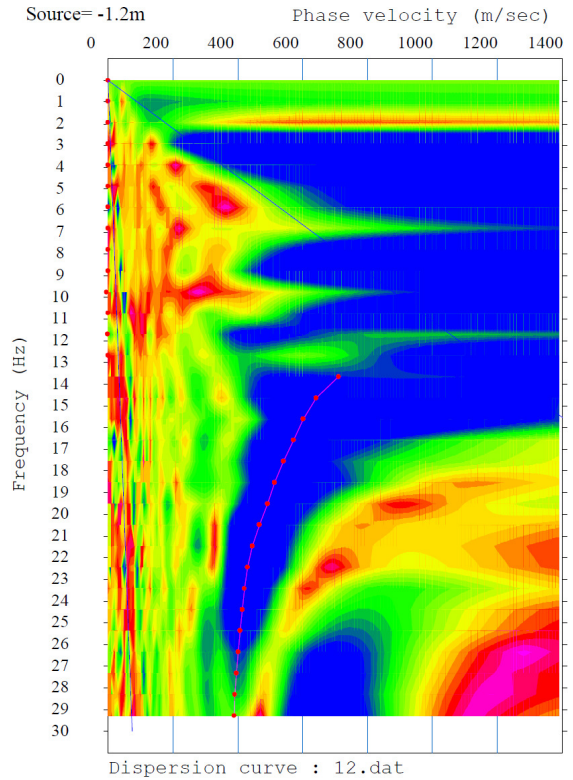


Vs30m = 600 m/s

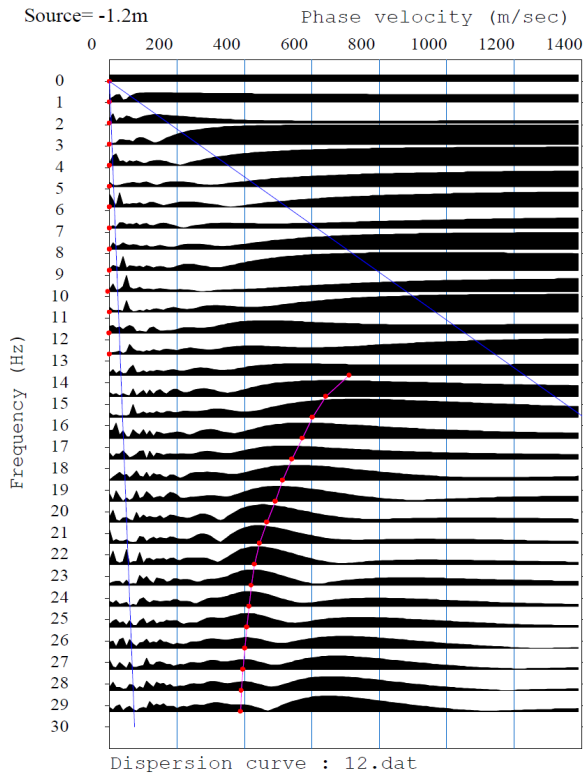
MASW - Referent Test Point #12



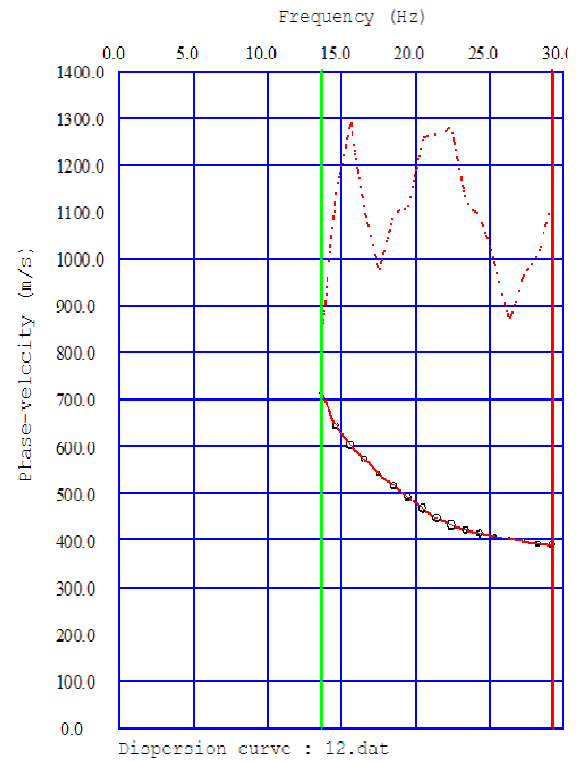
Test Point #12 MASW seismic waveforms



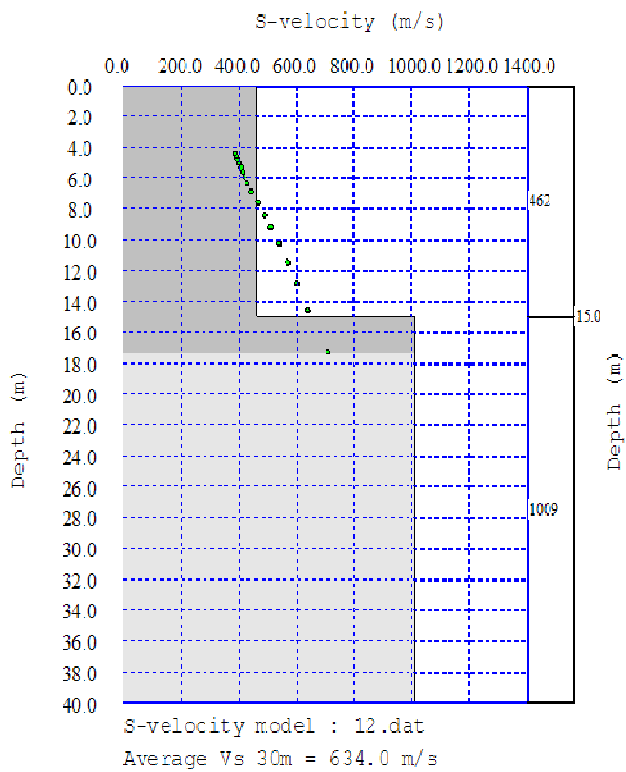
Surface Waves Dispersion - interpolated



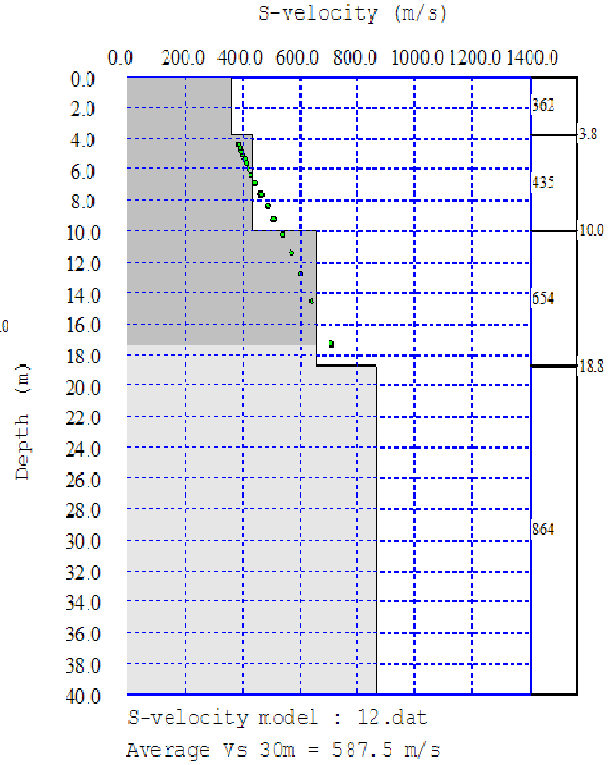
Surface Waves Dispersion



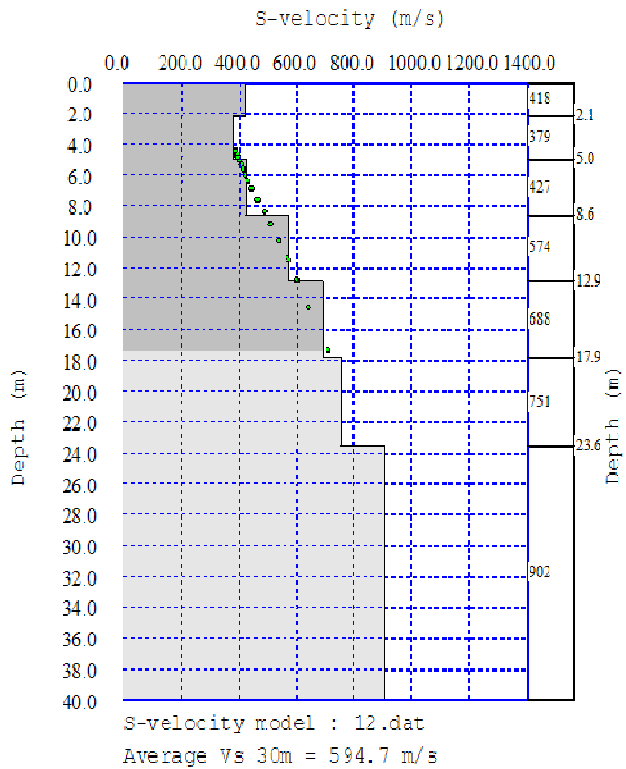
Phase velocity vs. frequency



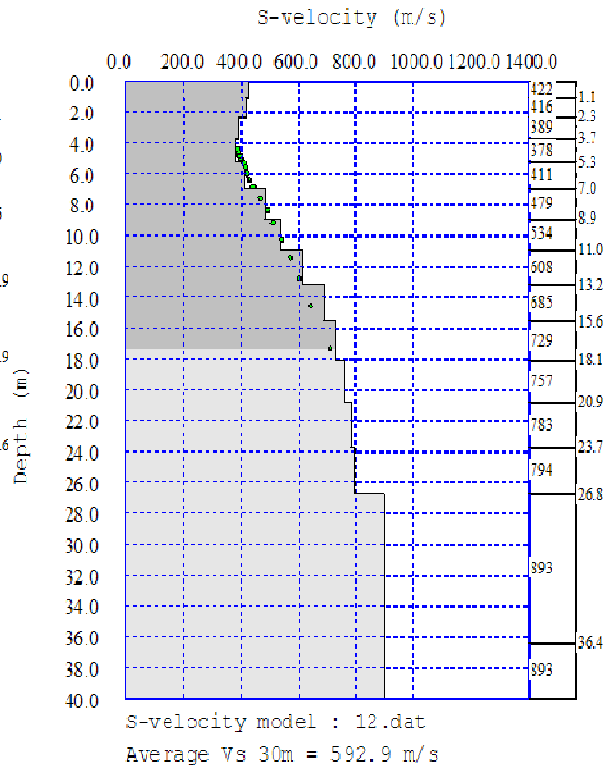
Test point #12 2-layers inversion



Test point #12 4-layers inversion

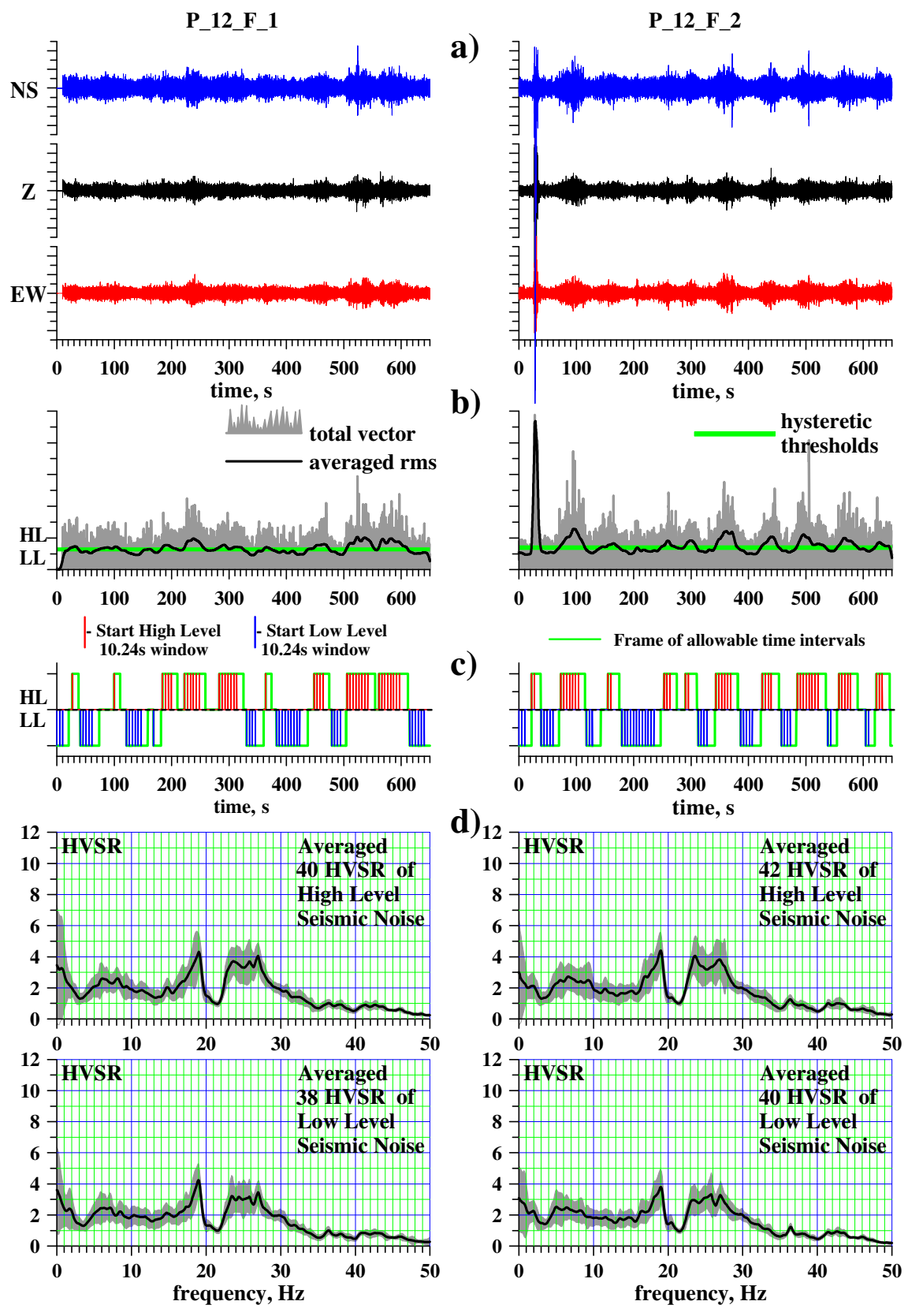


Test point #12 7-layers inversion



Test point #12 15-layers inversion

HVSR - Referent Test Point #12

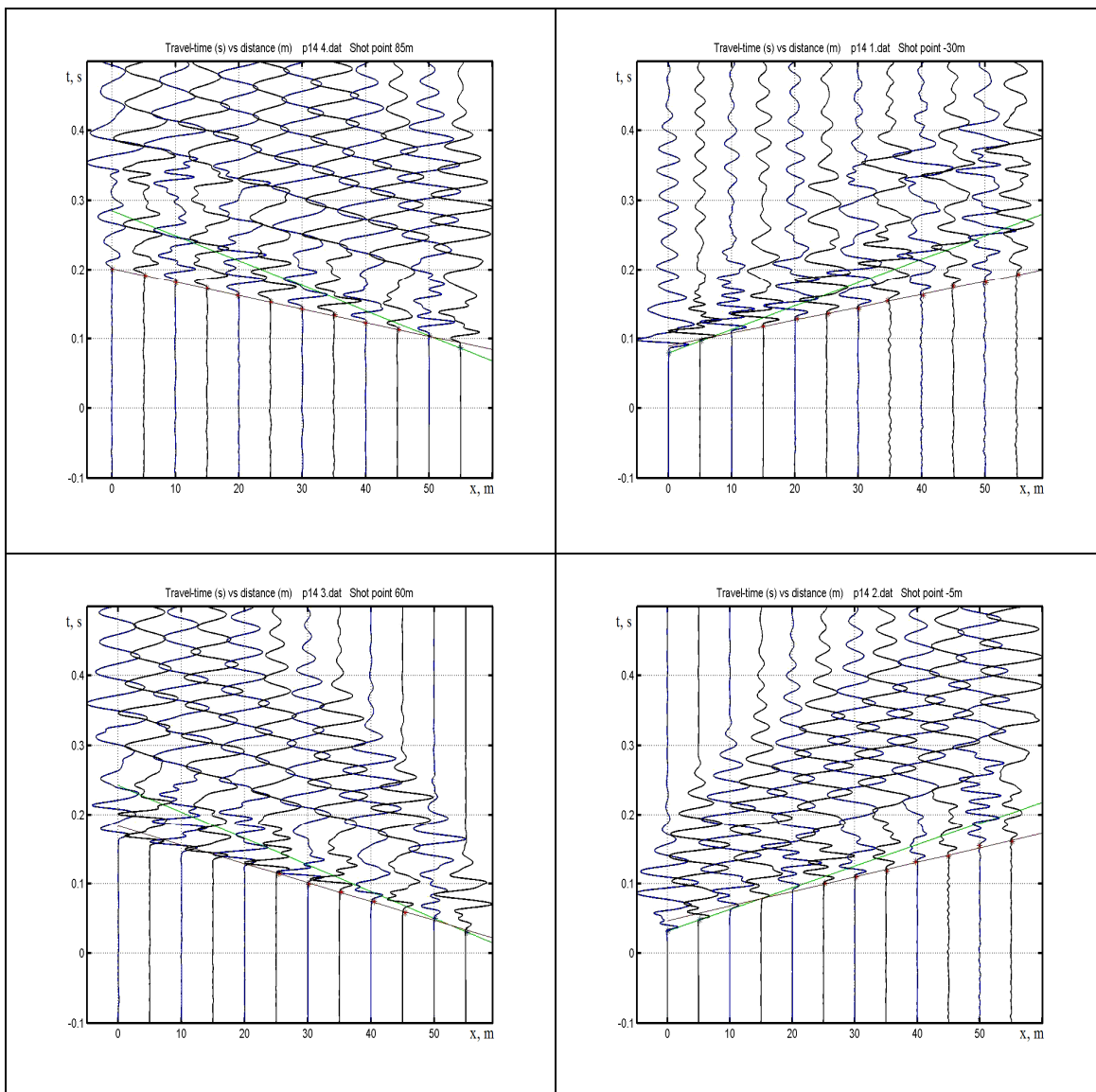


Results for Referent Test Point #14

Results for Vs30

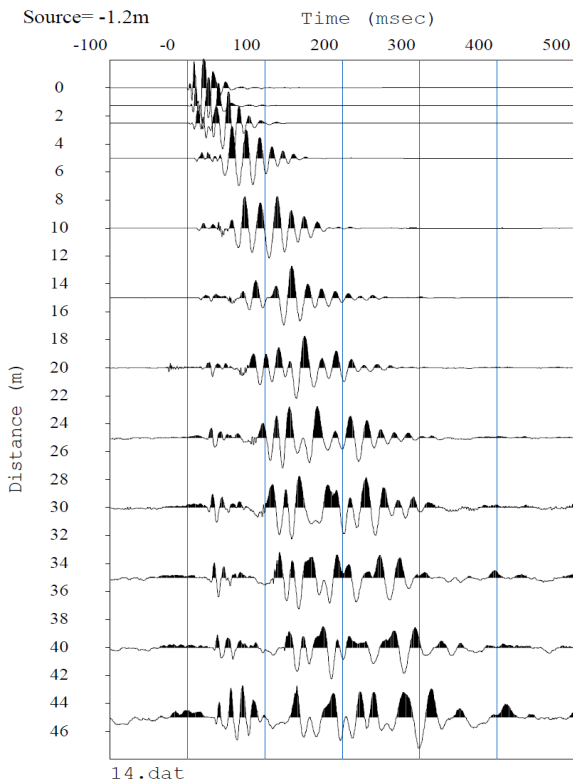
Vs30	SH-refraction	2-layer MASW	4-layer MASW	7-layer MASW	15-layer MASW
[m/s]	420	560	502	484	485

SH Refraction Profiles - Referent Test Point #14

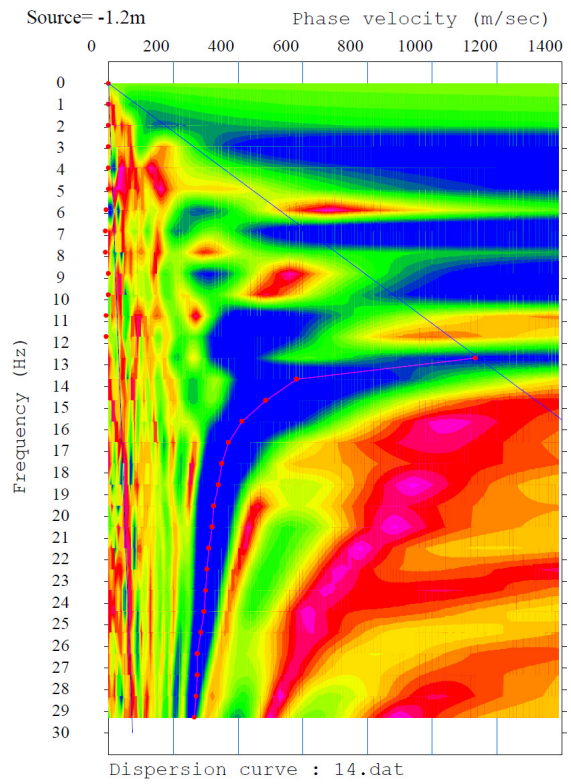


Vs30m = 420 m/s

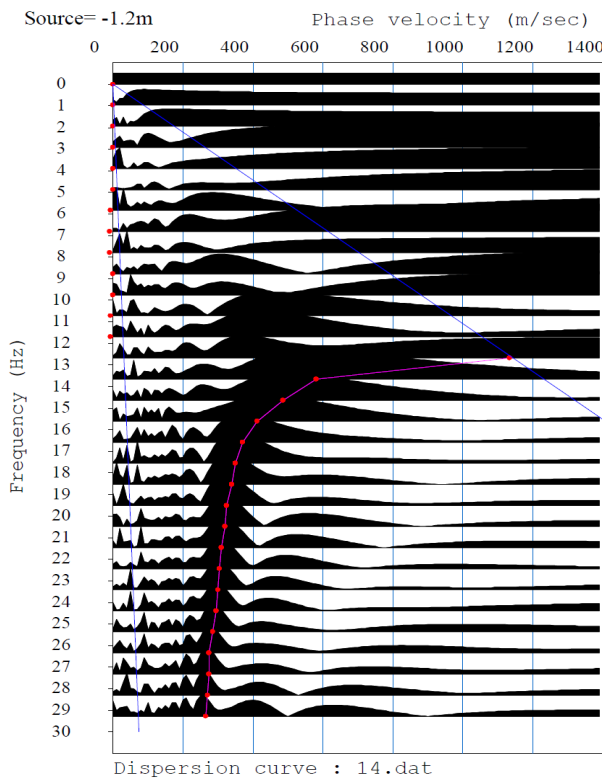
MASW - Referent Test Point #14



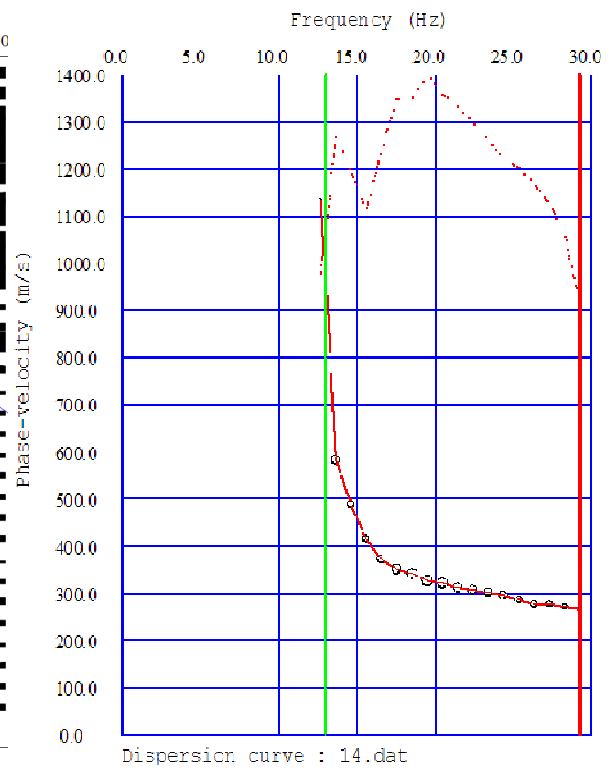
Test Point #14 MASW seismic waveforms



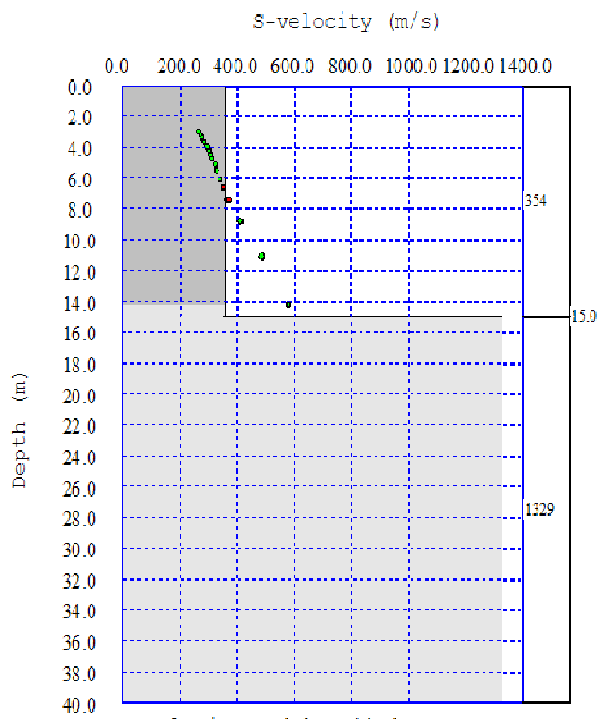
Surface Waves Dispersion - interpolated



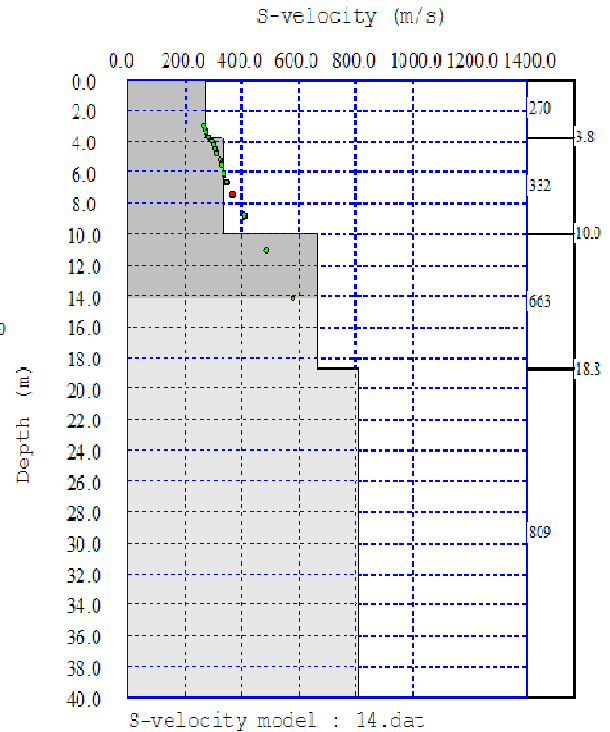
Surface Waves Dispersion



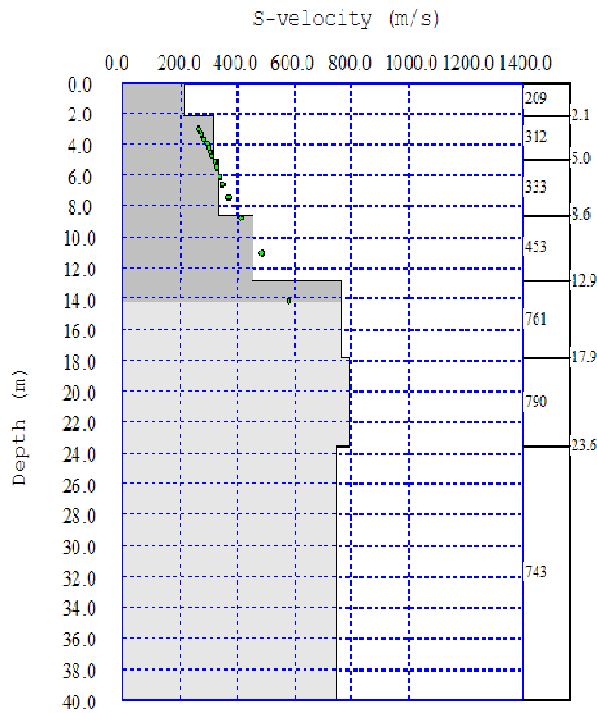
Phase velocity vs. frequency



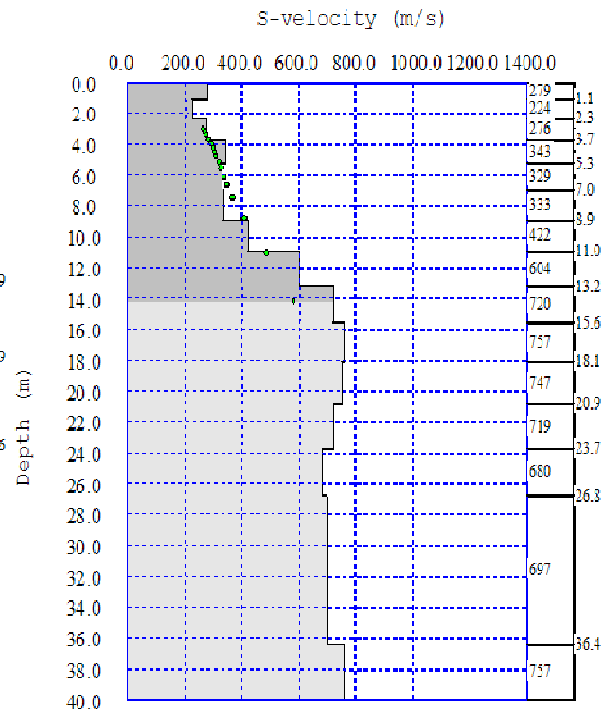
Test point #14 2-layers inversion



Test point #14 4-layers inversion

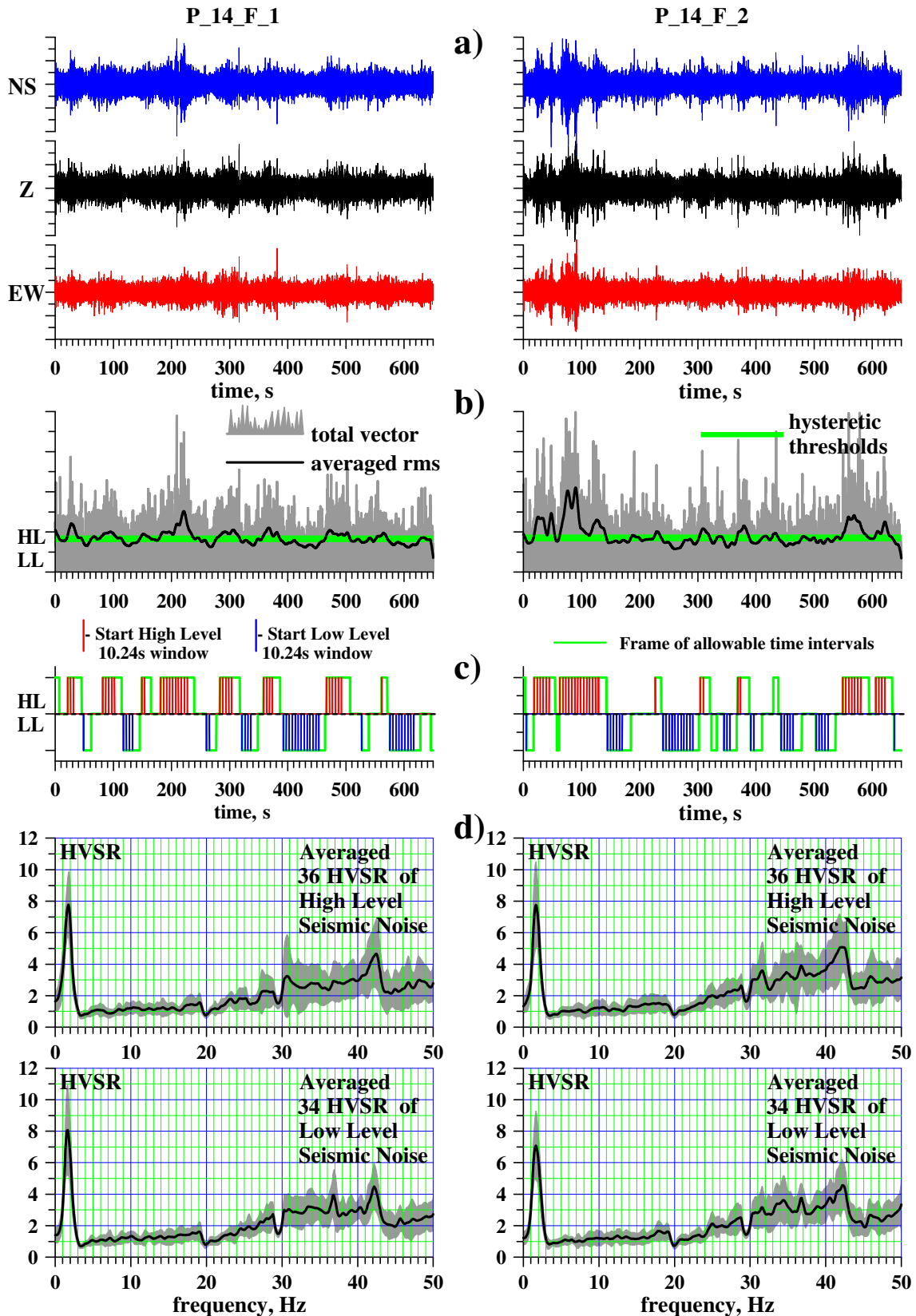


Test point #14 7-layers inversion



Test point #14 15-layers inversion

HVSR - Referent Test Point #14

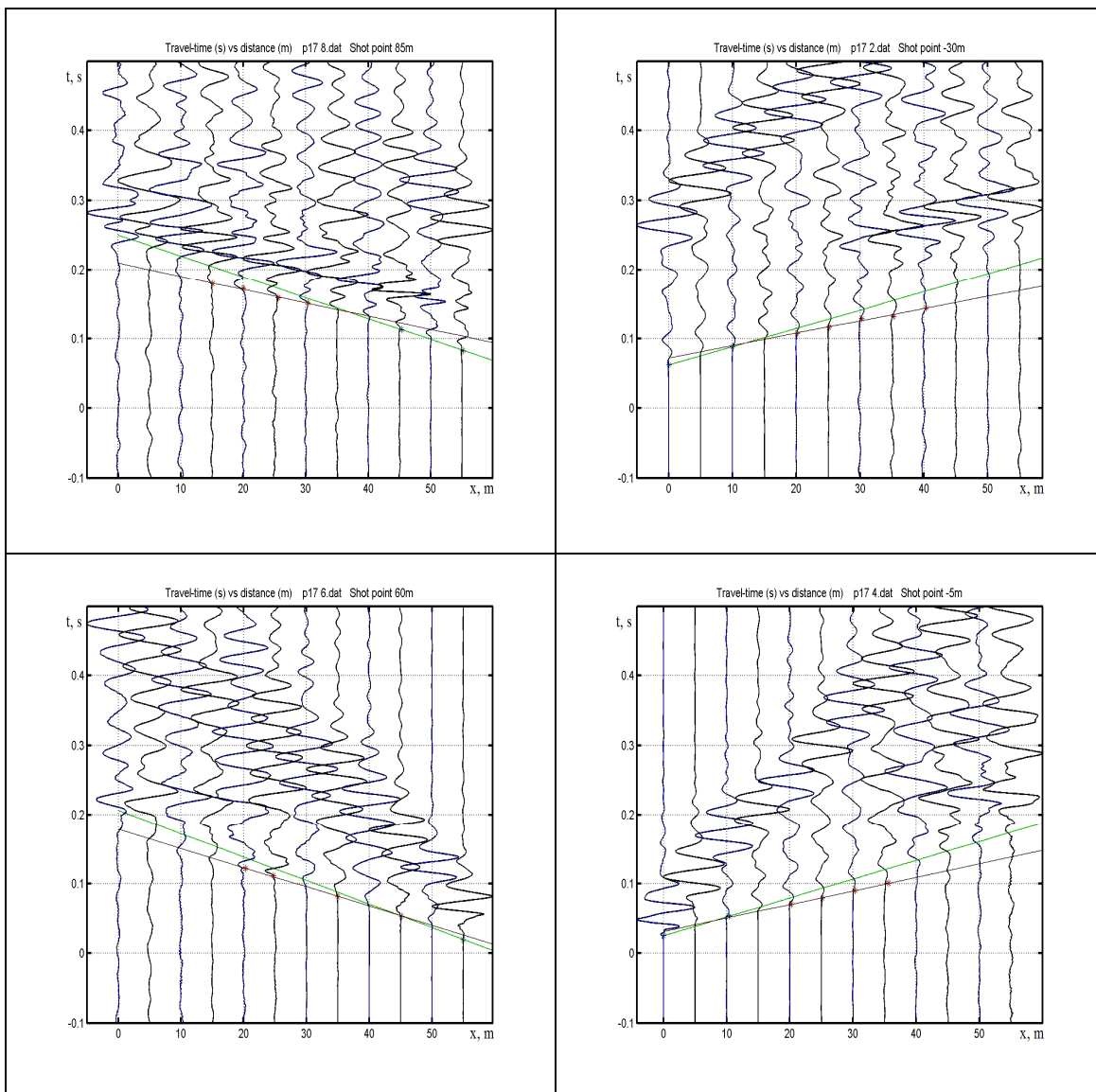


Results for Referent Test Point #17

Results for Vs30

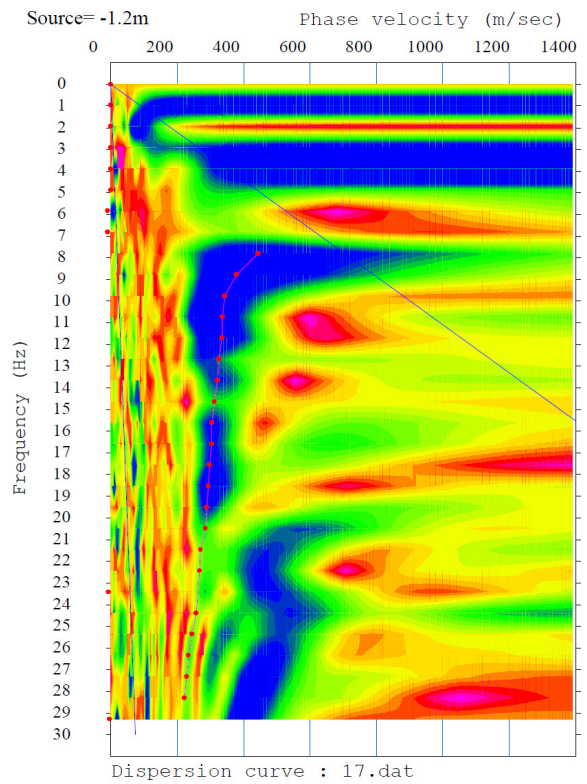
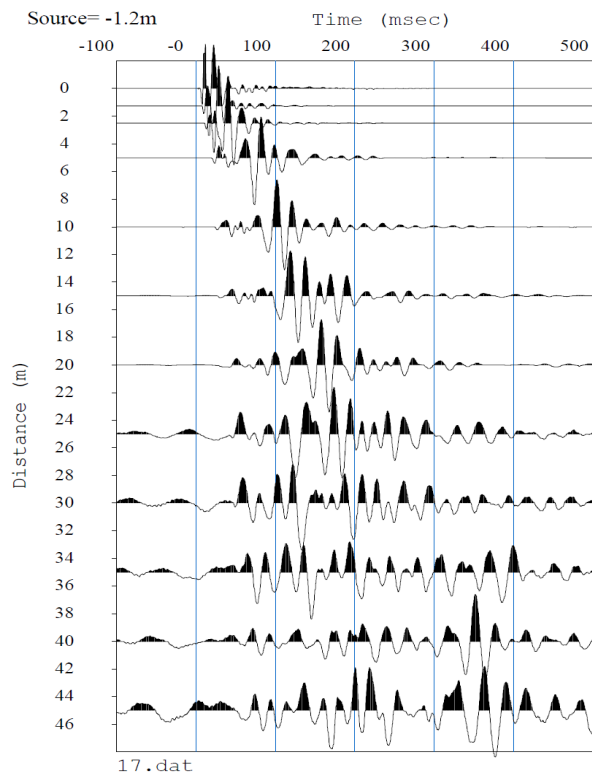
Vs30	SH-refraction	2-layer MASW	4-layer MASW	7-layer MASW	15-layer MASW
[m/s]	463	380	366	362	363

SH Refraction Profiles - Referent Test Point #17



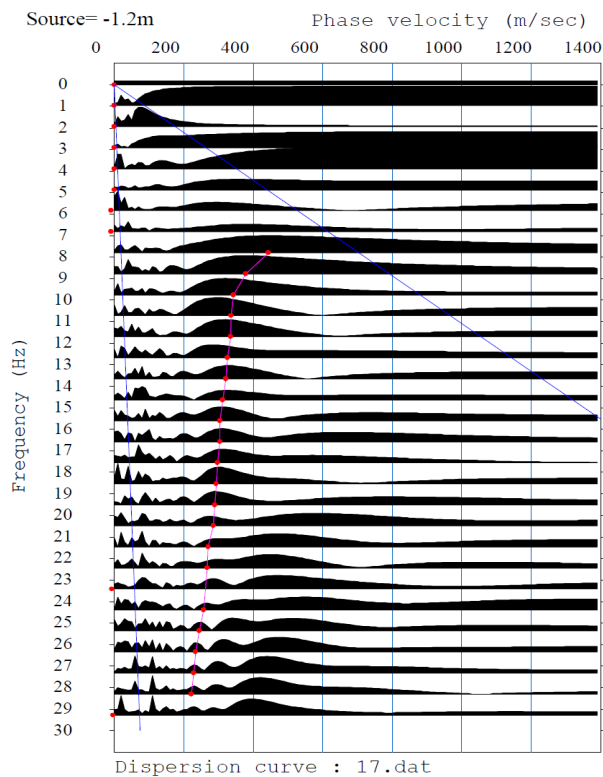
Vs30m = 463 m/s

MASW - Referent Test Point #17



Test Point #17 MASW seismic waveforms

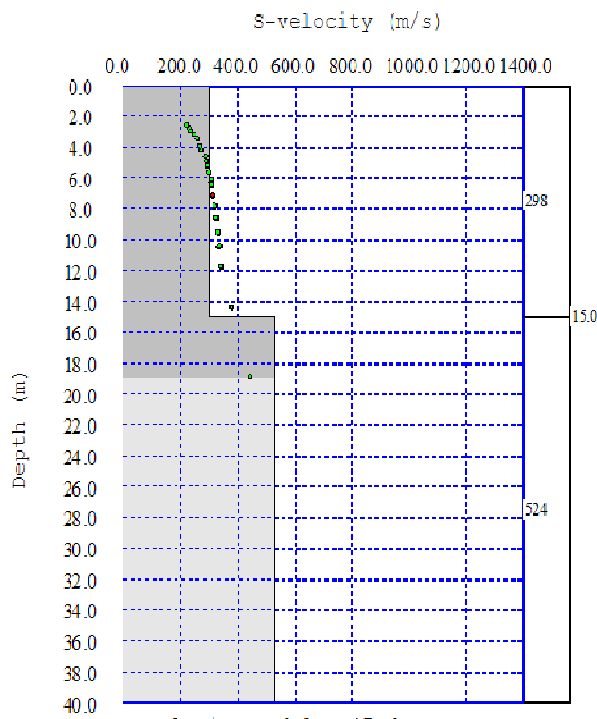
Surface Waves Dispersion - interpolated



Surface Waves Dispersion

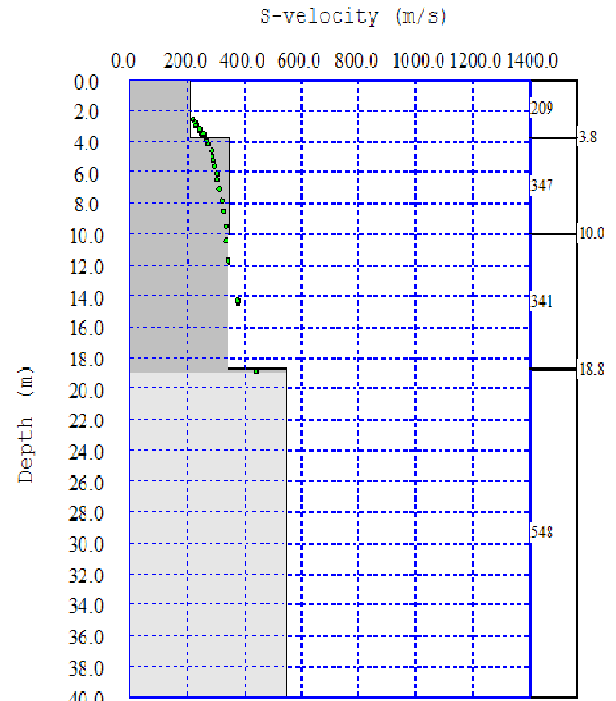


Phase velocity vs. frequency



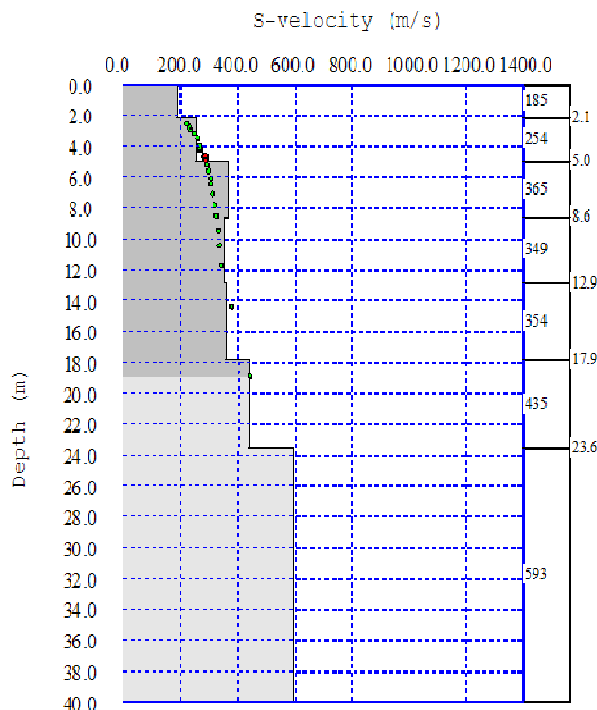
S-velocity model : 17.dat
Average Vs 30m = 380.3 m/s

Test point #17 2-layers inversion



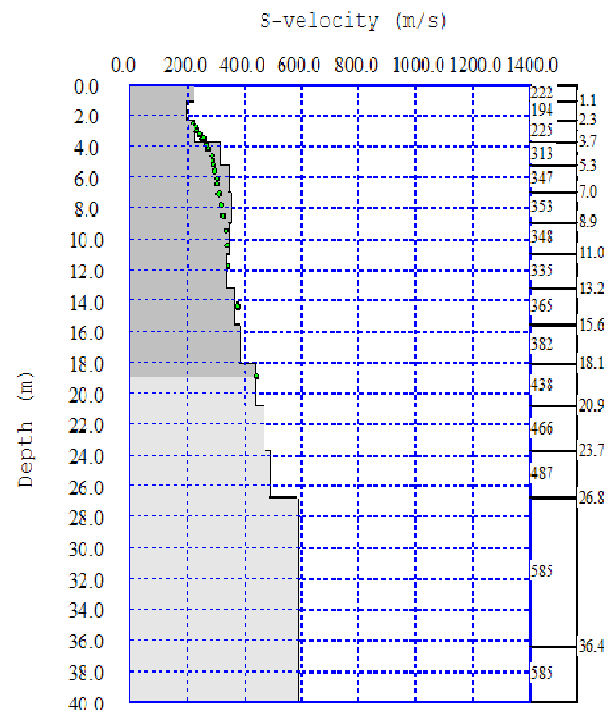
S-velocity model : 17.dat
Average Vs 30m = 365.7 m/s

Test point #17 4-layers inversion



S-velocity model : 17.dat
Average Vs 30m = 362.0 m/s

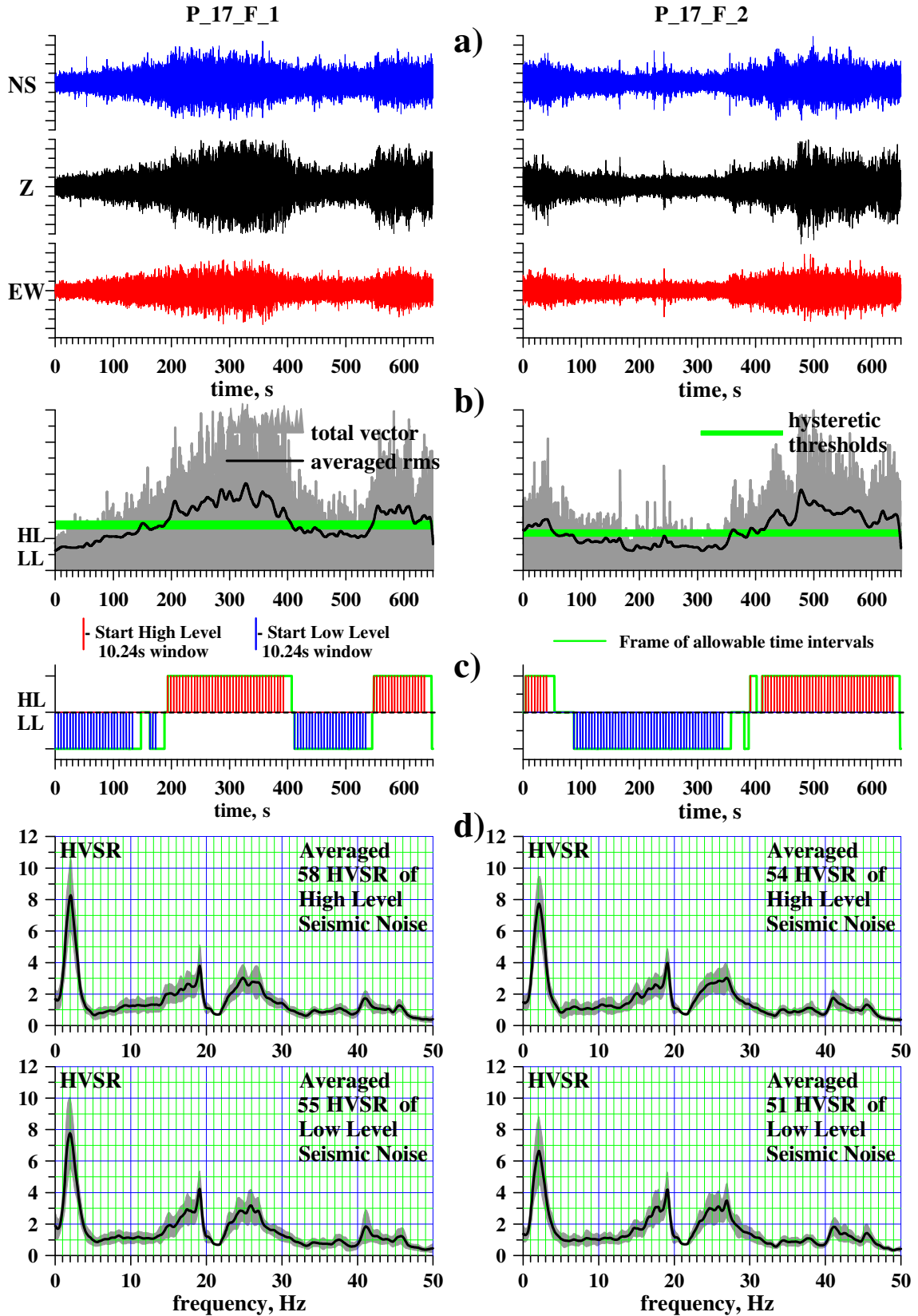
Test point #17 7-layers inversion



S-velocity model : 17.dat
Average Vs 30m = 362.9 m/s

Test point #17 15-layers inversion

HVSR - Referent Test Point #17

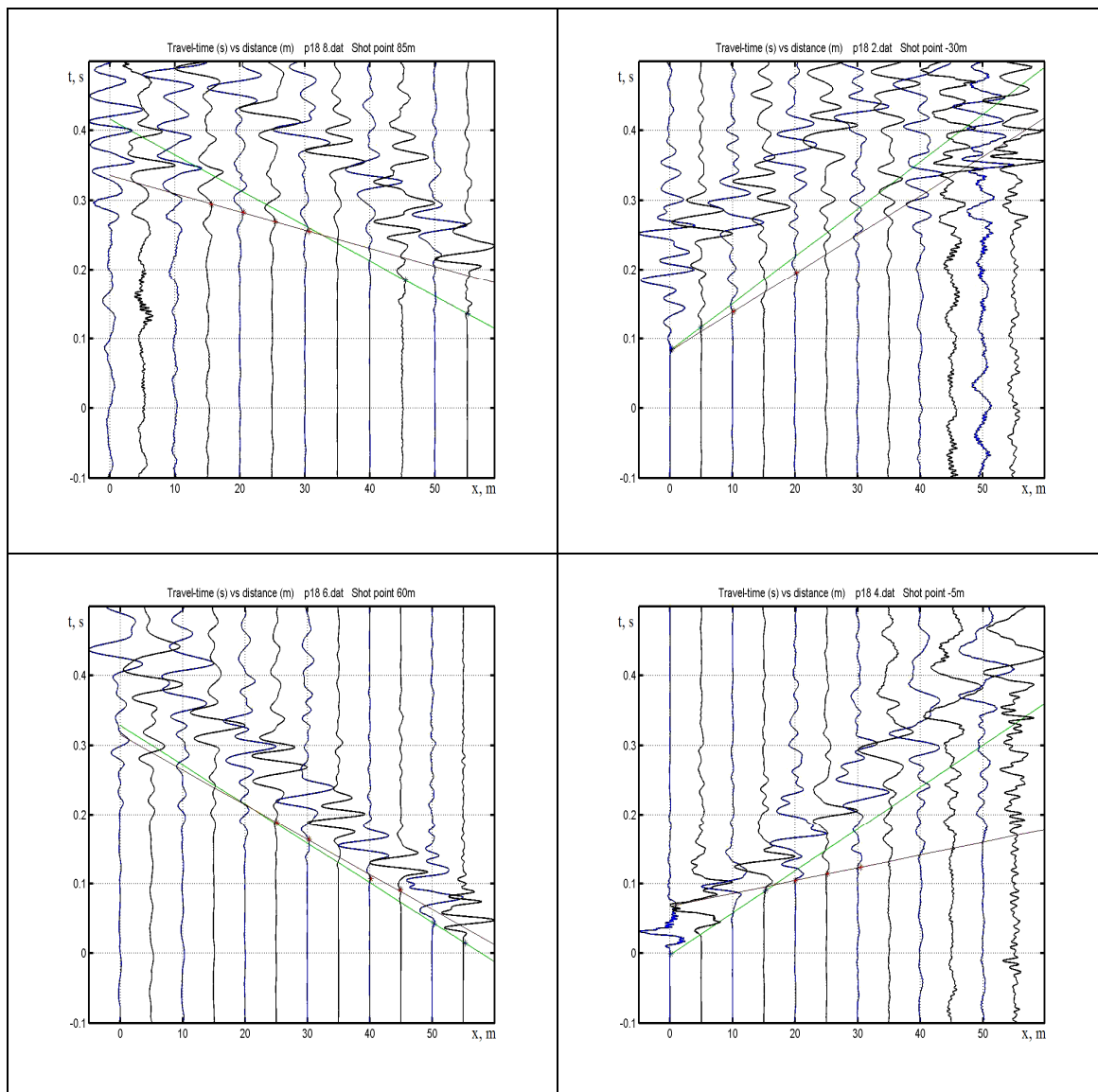


Results for Referent Test Point #18

Results for Vs30

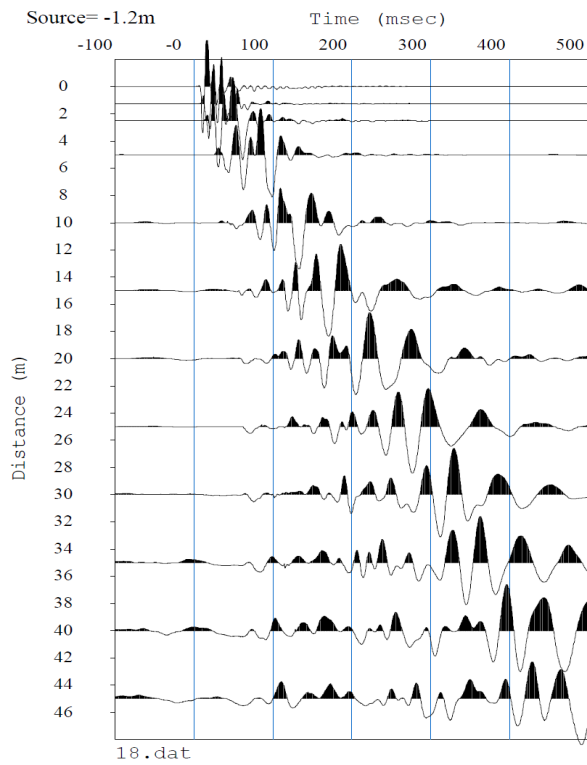
Vs30	SH-refraction	2-layer MASW	4-layer MASW	7-layer MASW	15-layer MASW
[m/s]	262	327	296	295	293

SH Refraction Profiles - Referent Test Point #18

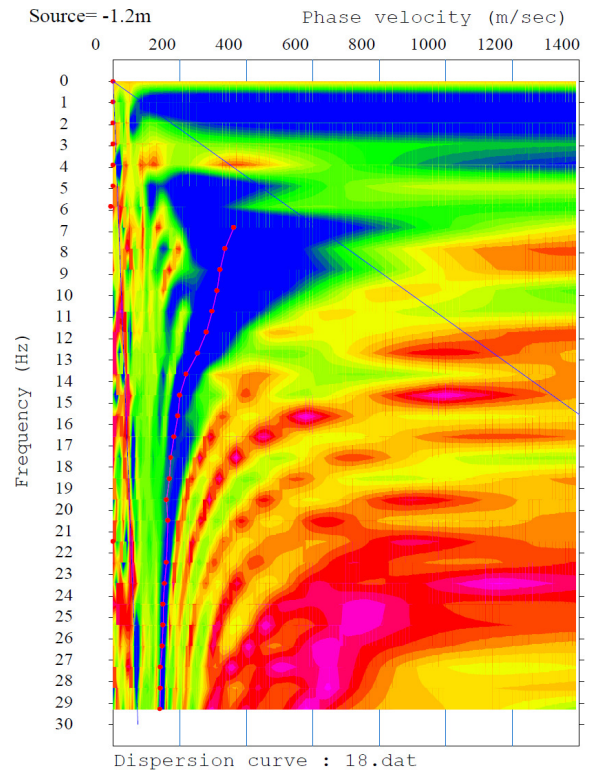


Vs30m = 262 m/s

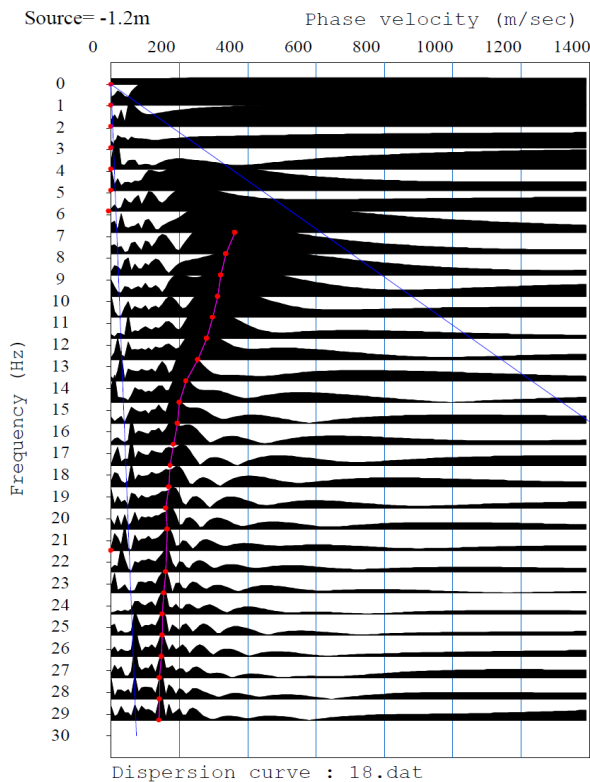
MASW - Referent Test Point #18



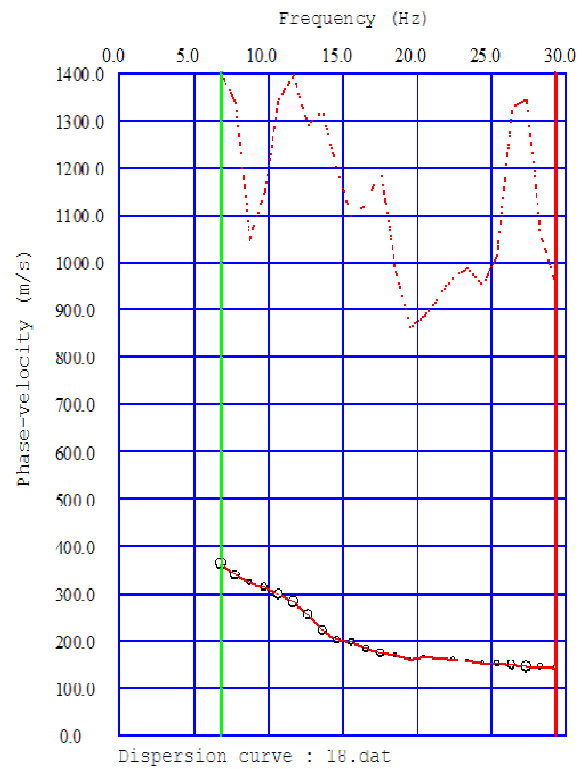
Test Point #18 MASW seismic waveforms



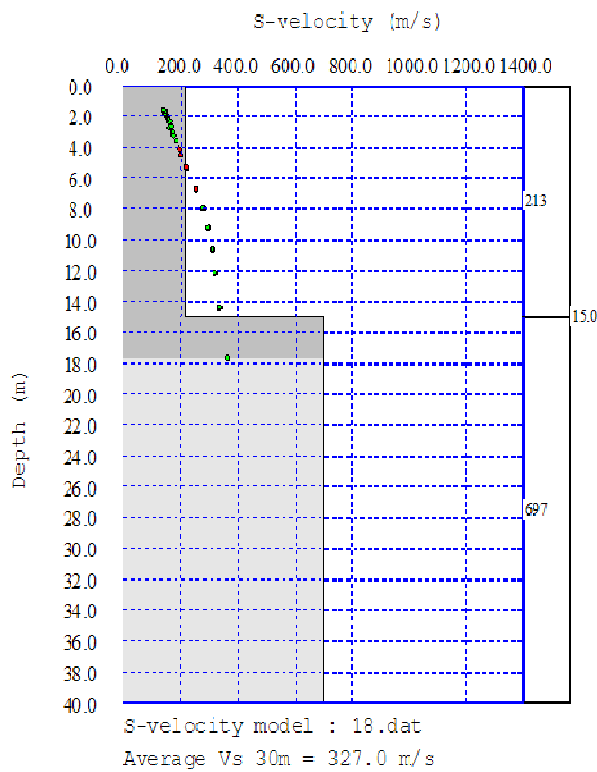
Surface Waves Dispersion - interpolated



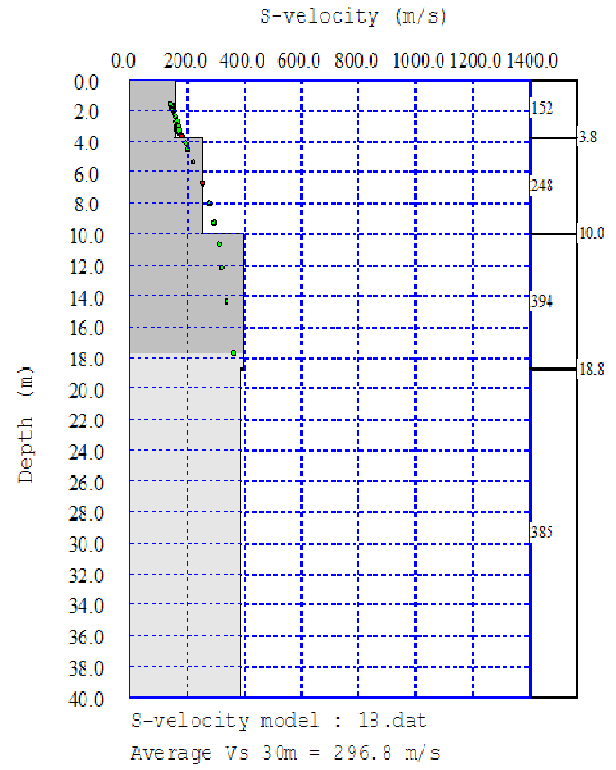
Surface Waves Dispersion



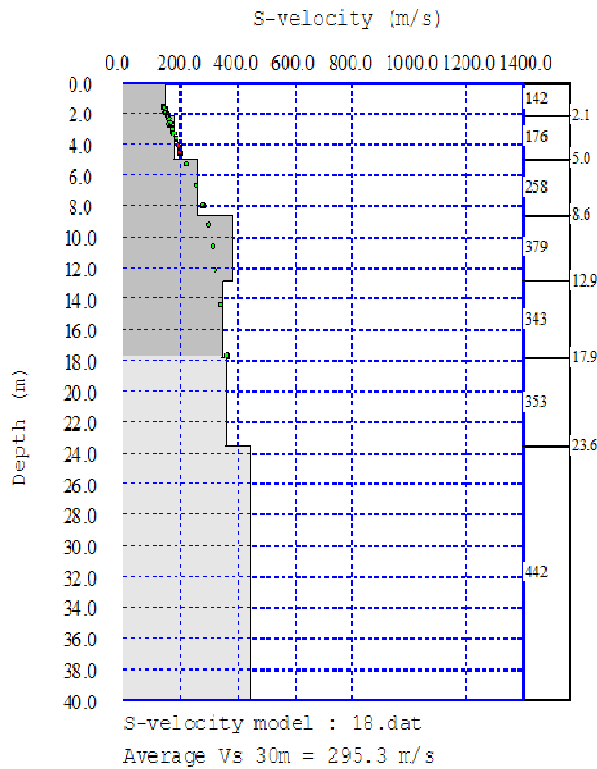
Phase velocity vs. frequency



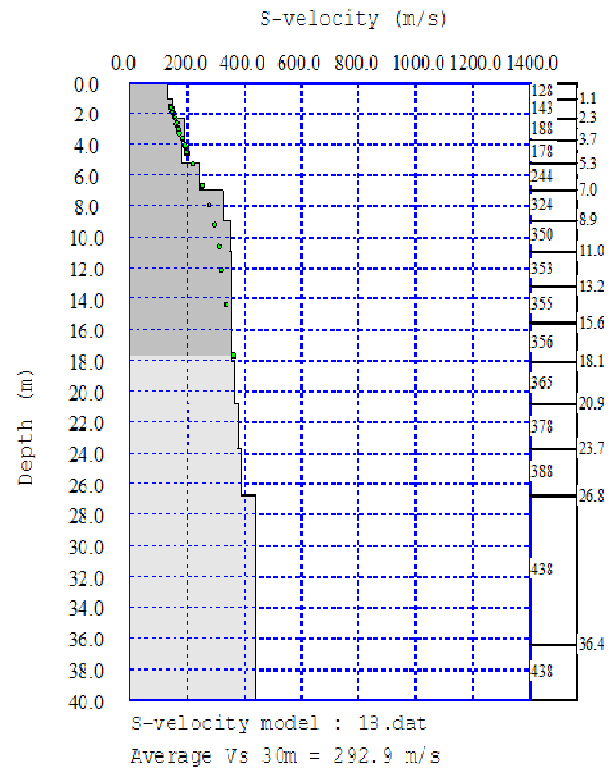
Test point #18 2-layers inversion



Test point #18 4-layers inversion

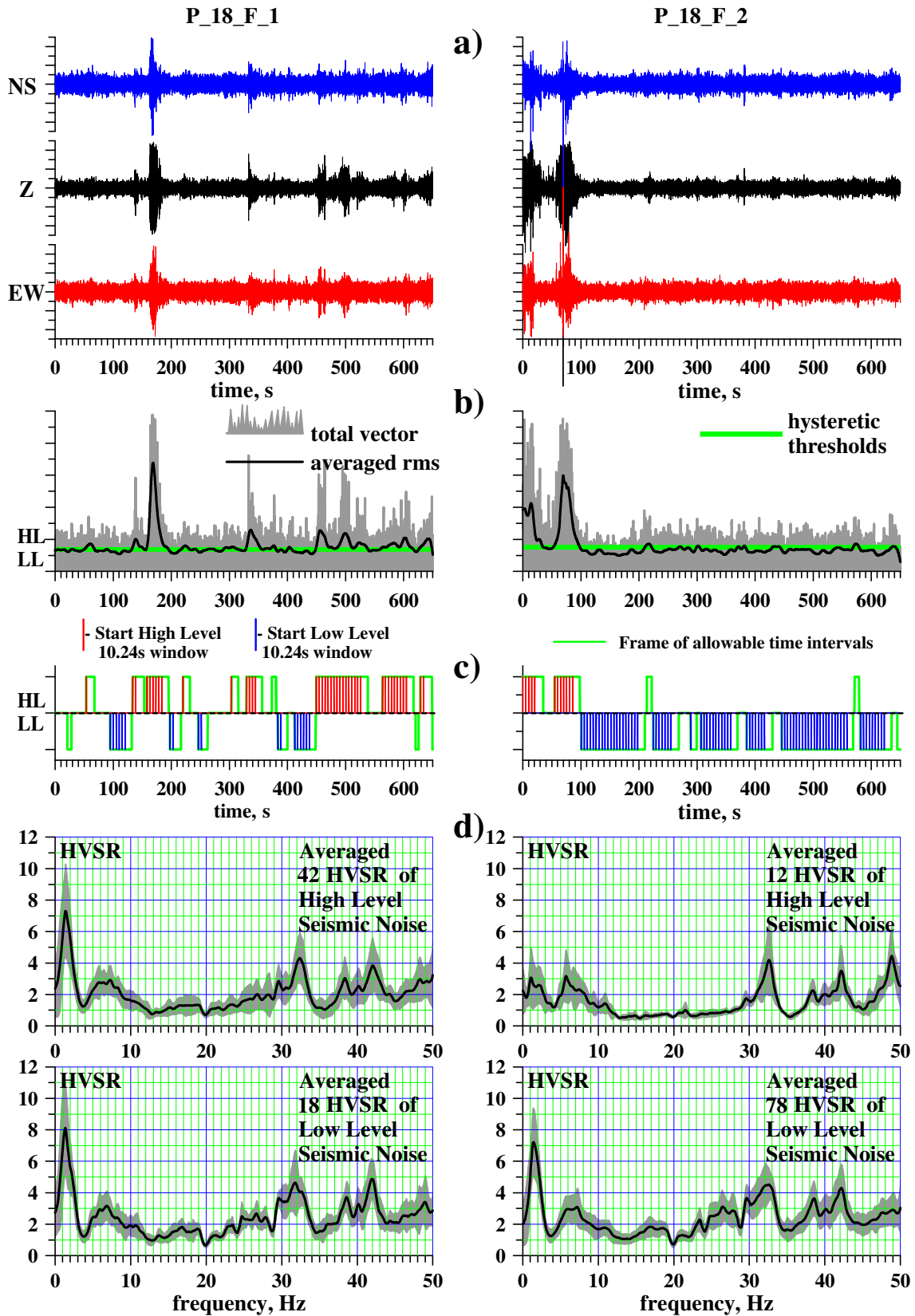


Test point #18 7-layers inversion



Test point #18 15-layers inversion

HVSR - Referent Test Point #18

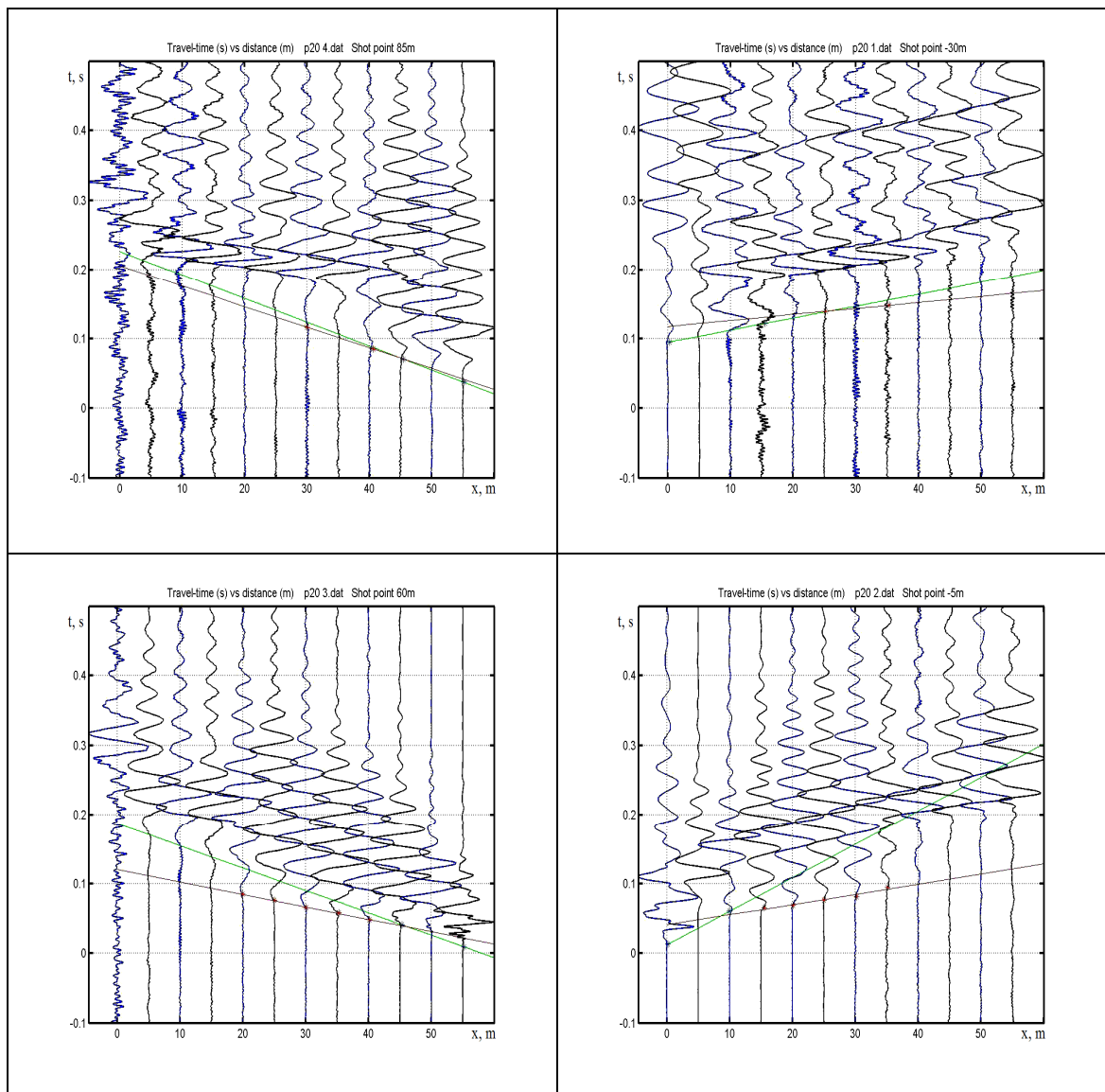


Results for Referent Test Point #20

Results for Vs30

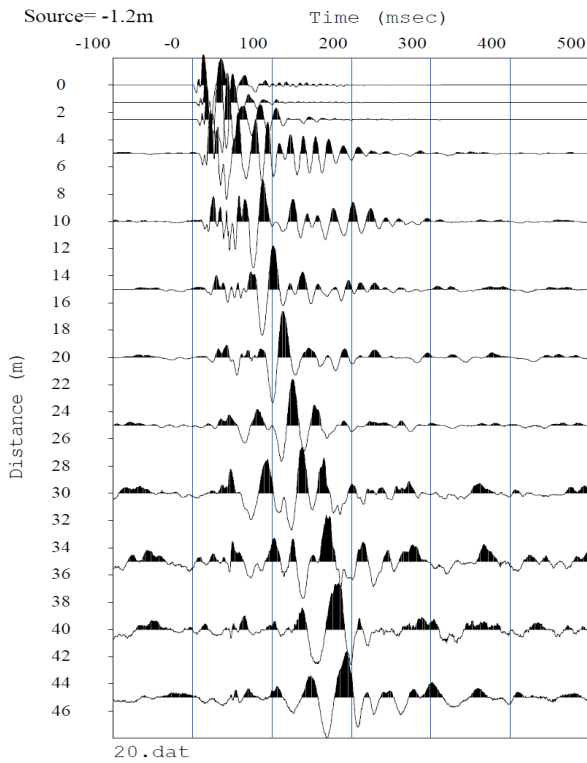
Vs30	SH-refraction	2-layer MASW	4-layer MASW	7-layer MASW	15-layer MASW
[m/s]	550	438	423	415	409

SH Refraction Profiles - Referent Test Point #20

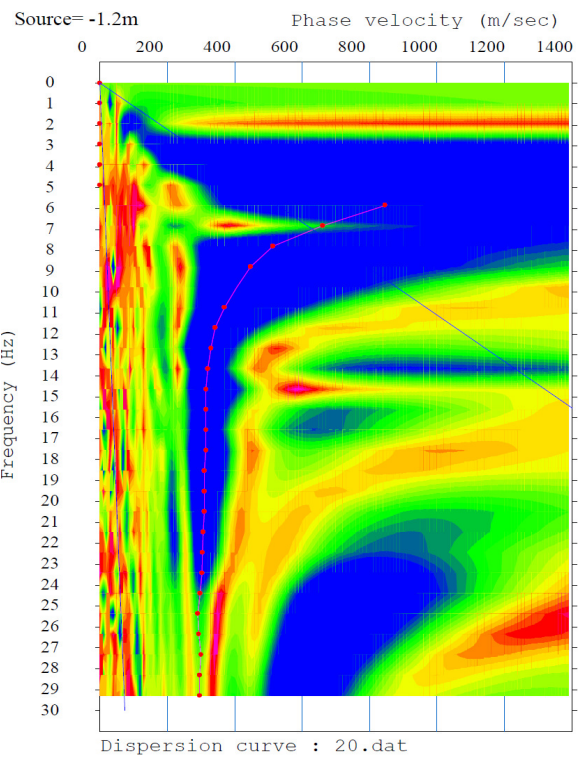


Vs30m = 550 m/s

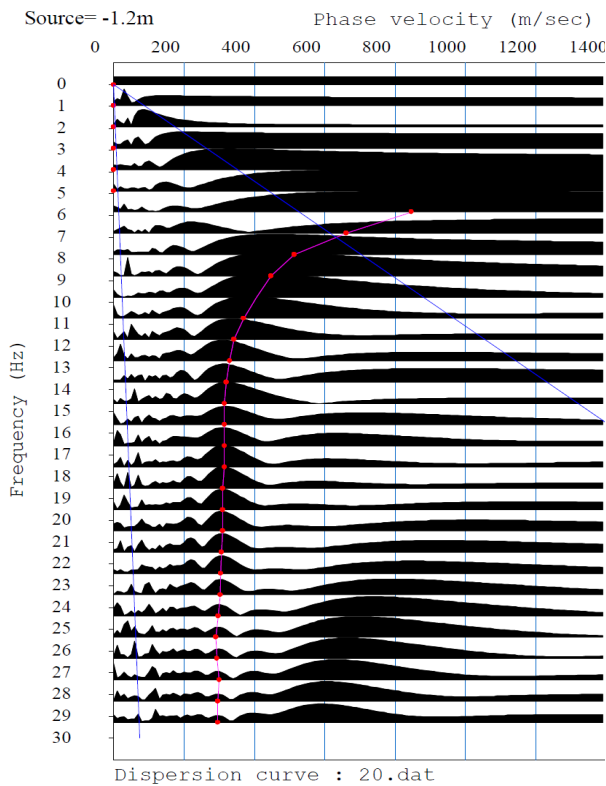
MASW - Referent Test Point #20



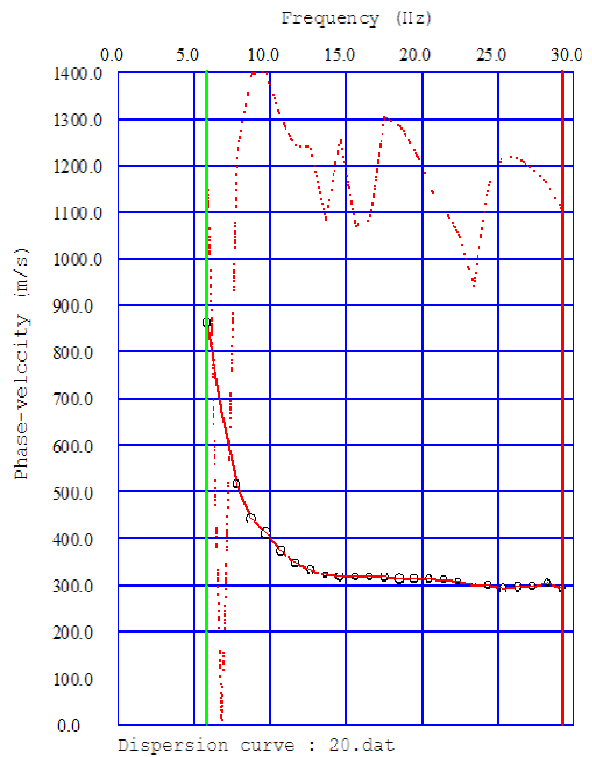
Test Point #20 MASW seismic waveforms



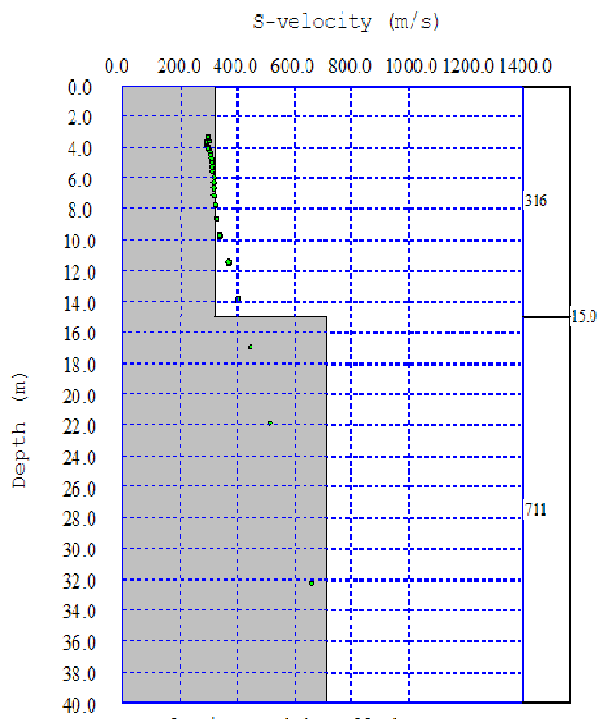
Surface Waves Dispersion - interpolated



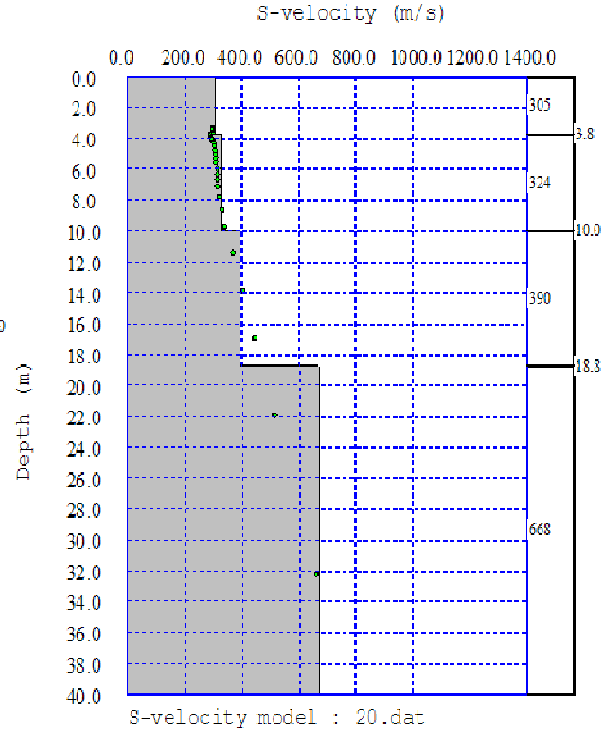
Surface Waves Dispersion



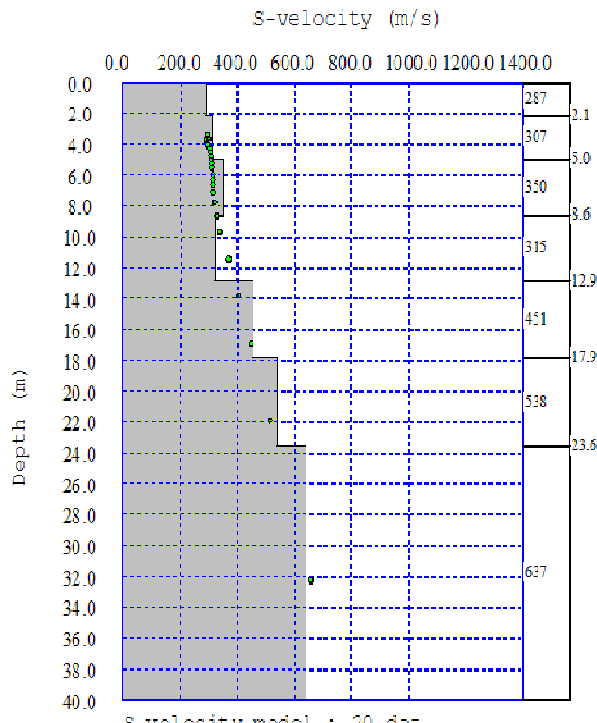
Phase velocity vs. frequency



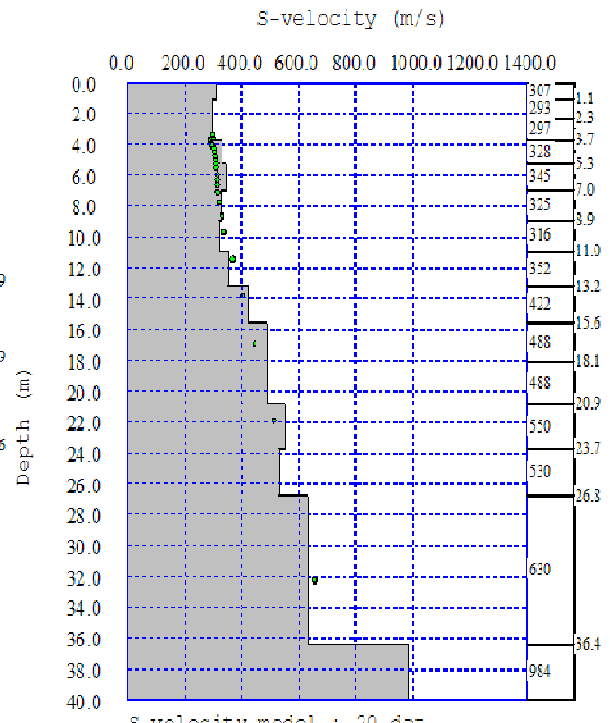
Test point #20 2-layers inversion



Test point #20 4-layers inversion

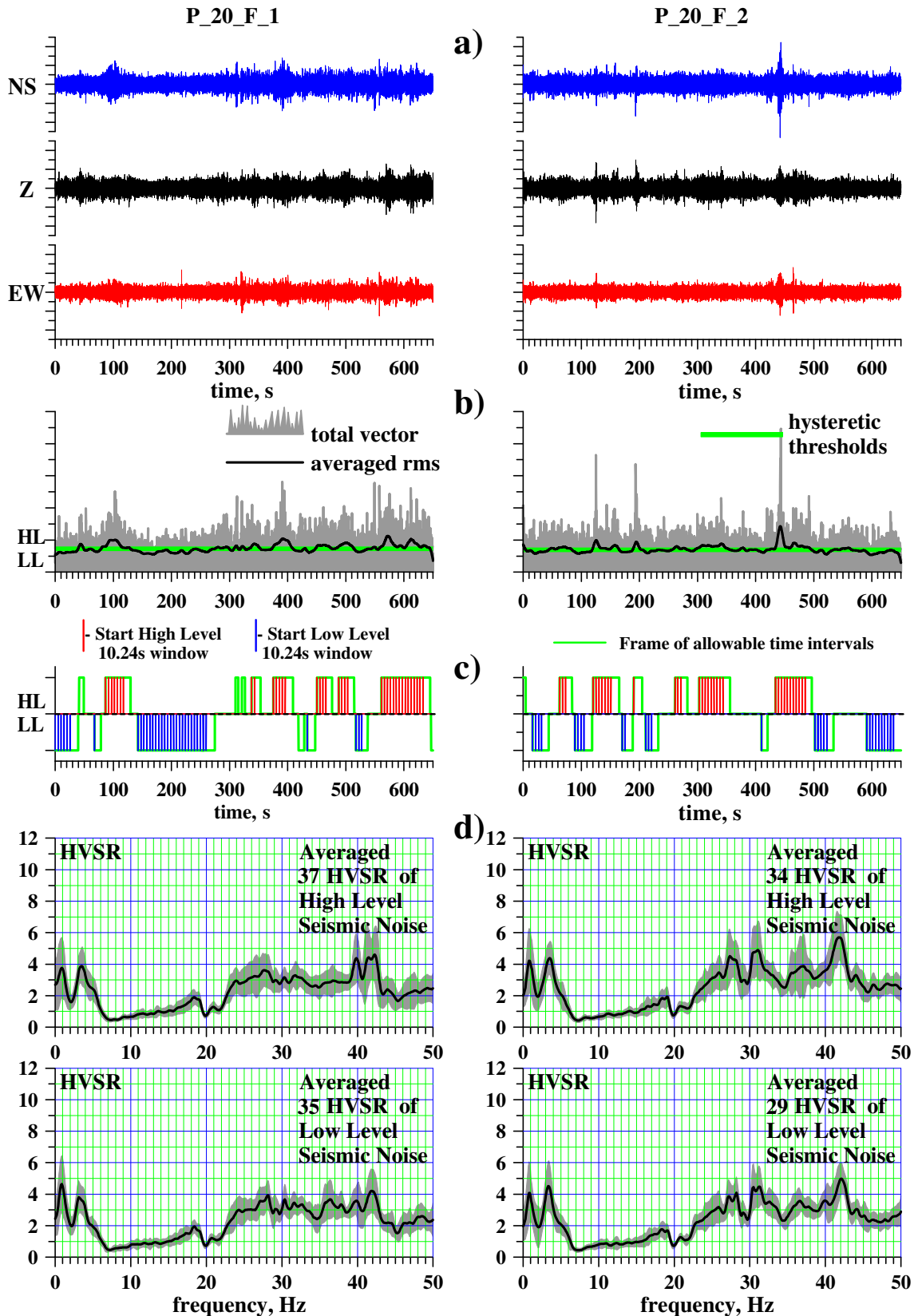


Test point #20 7-layers inversion



Test point #20 15-layers inversion

HVSR - Referent Test Point #20

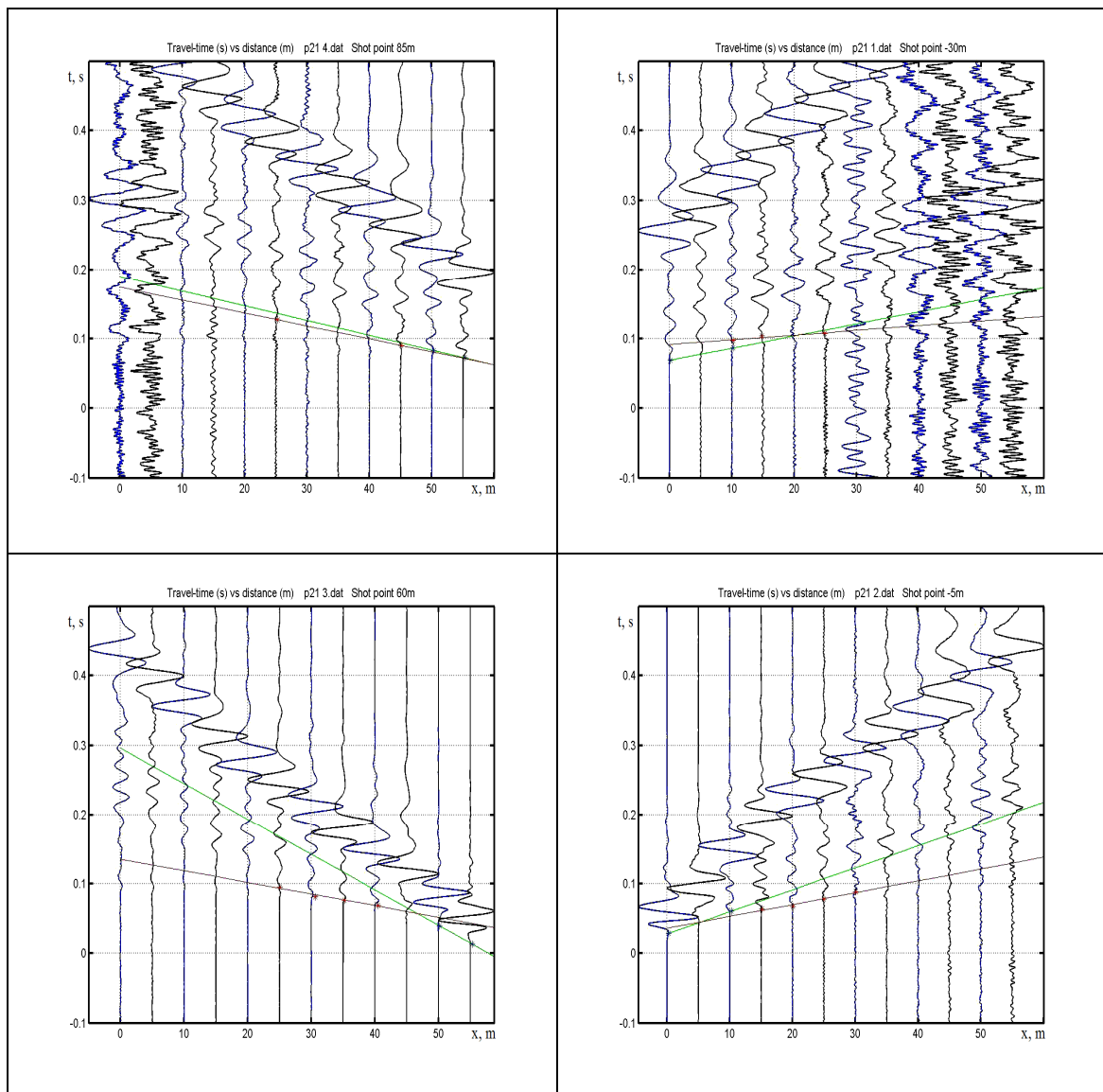


Results for Referent Test Point #21

Results for Vs30

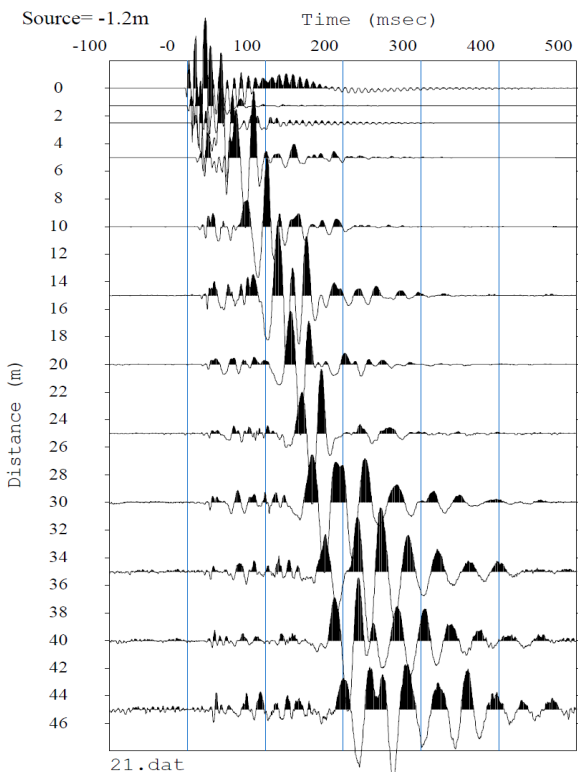
Vs30	SH-refraction	2-layer MASW	4-layer MASW	7-layer MASW	15-layer MASW
[m/s]	647	554	580	597	583

SH Refraction Profiles - Referent Test Point #21

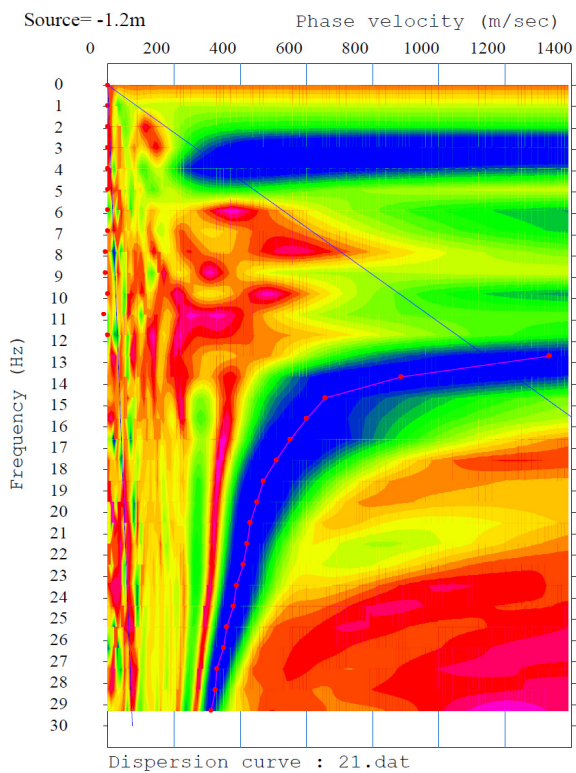


Vs30m =647 m/s

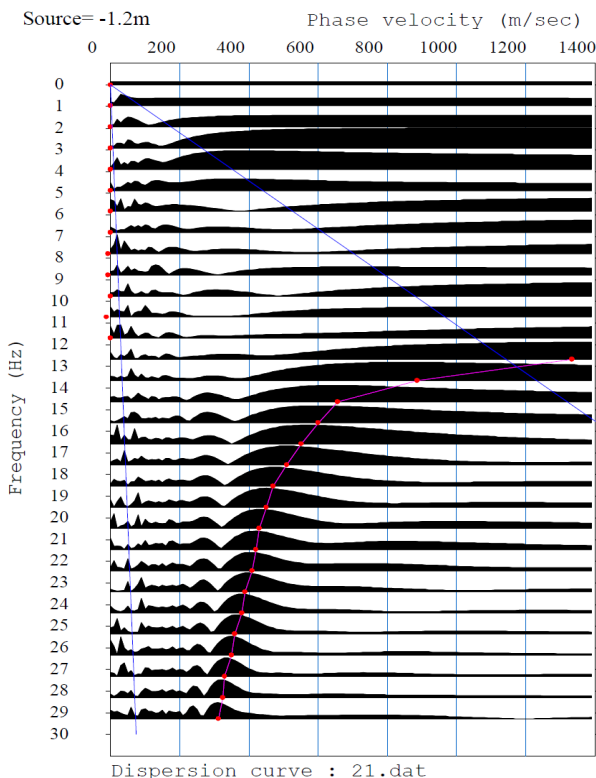
MASW - Referent Test Point #21



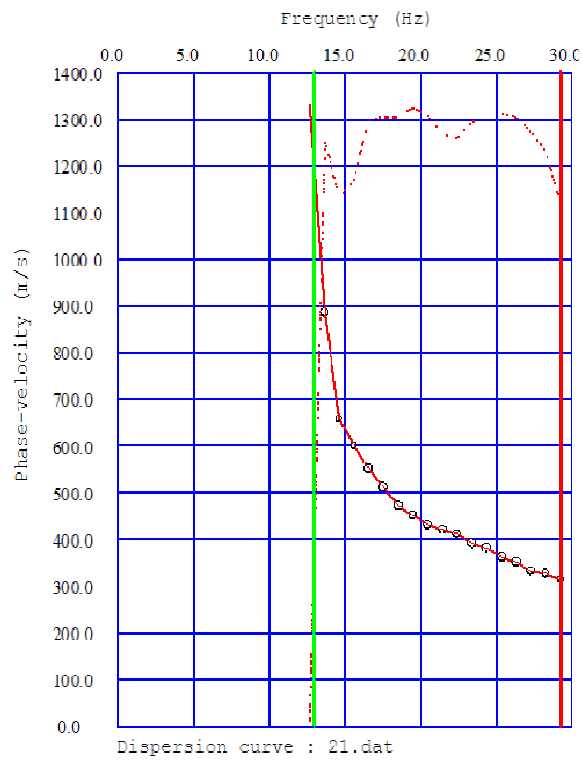
Test Point #21 MASW seismic waveforms



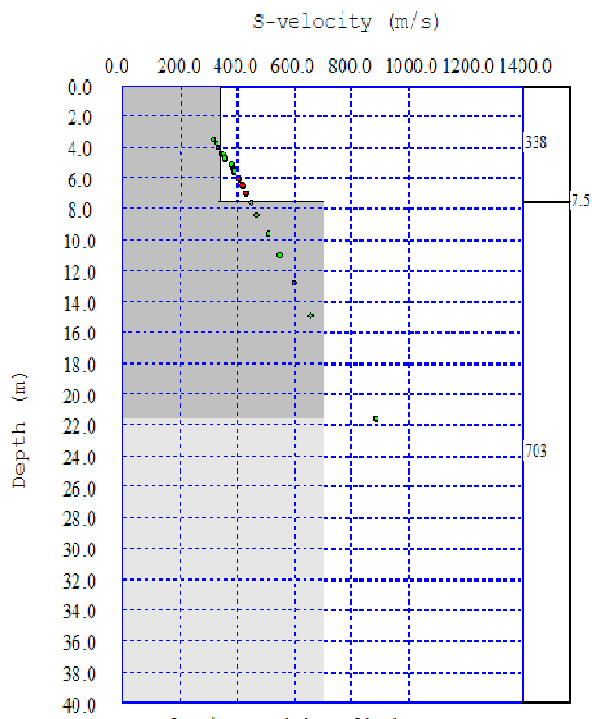
Surface Waves Dispersion - interpolated



Surface Waves Dispersion

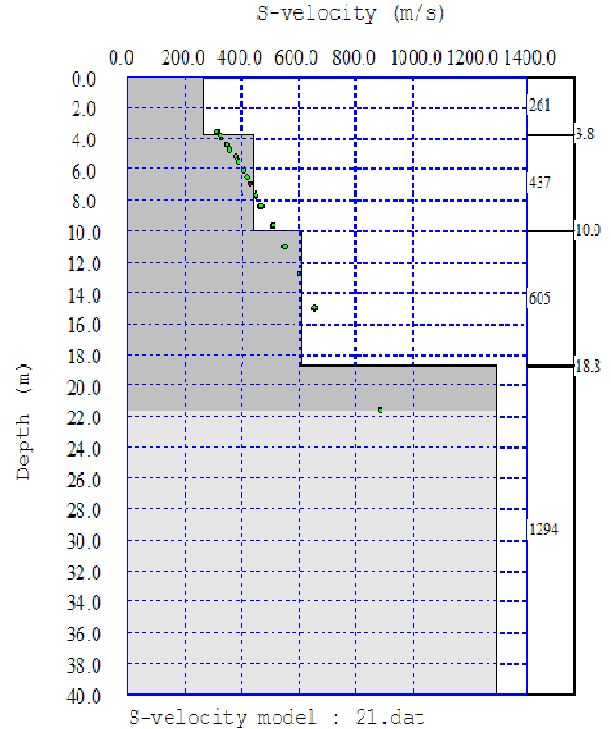


Phase velocity vs. frequency



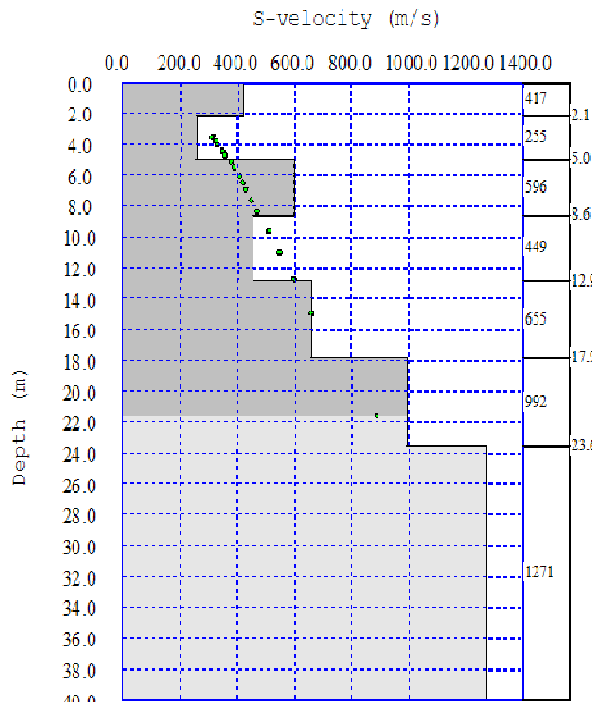
Average Vs 30m = 554.2 m/s

Test point #21 2-layers inversion



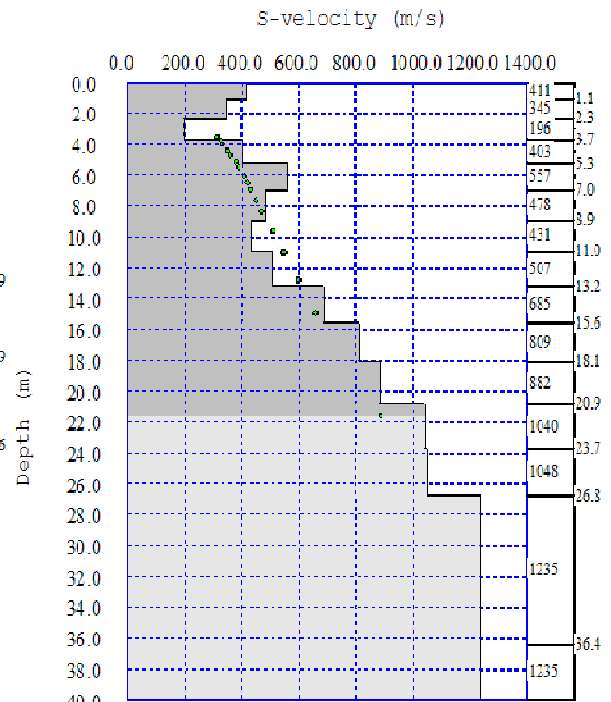
Average Vs 30m = 579.9 m/s

Test point #21 4-layers inversion



Average Vs 30m = 596.6 m/s

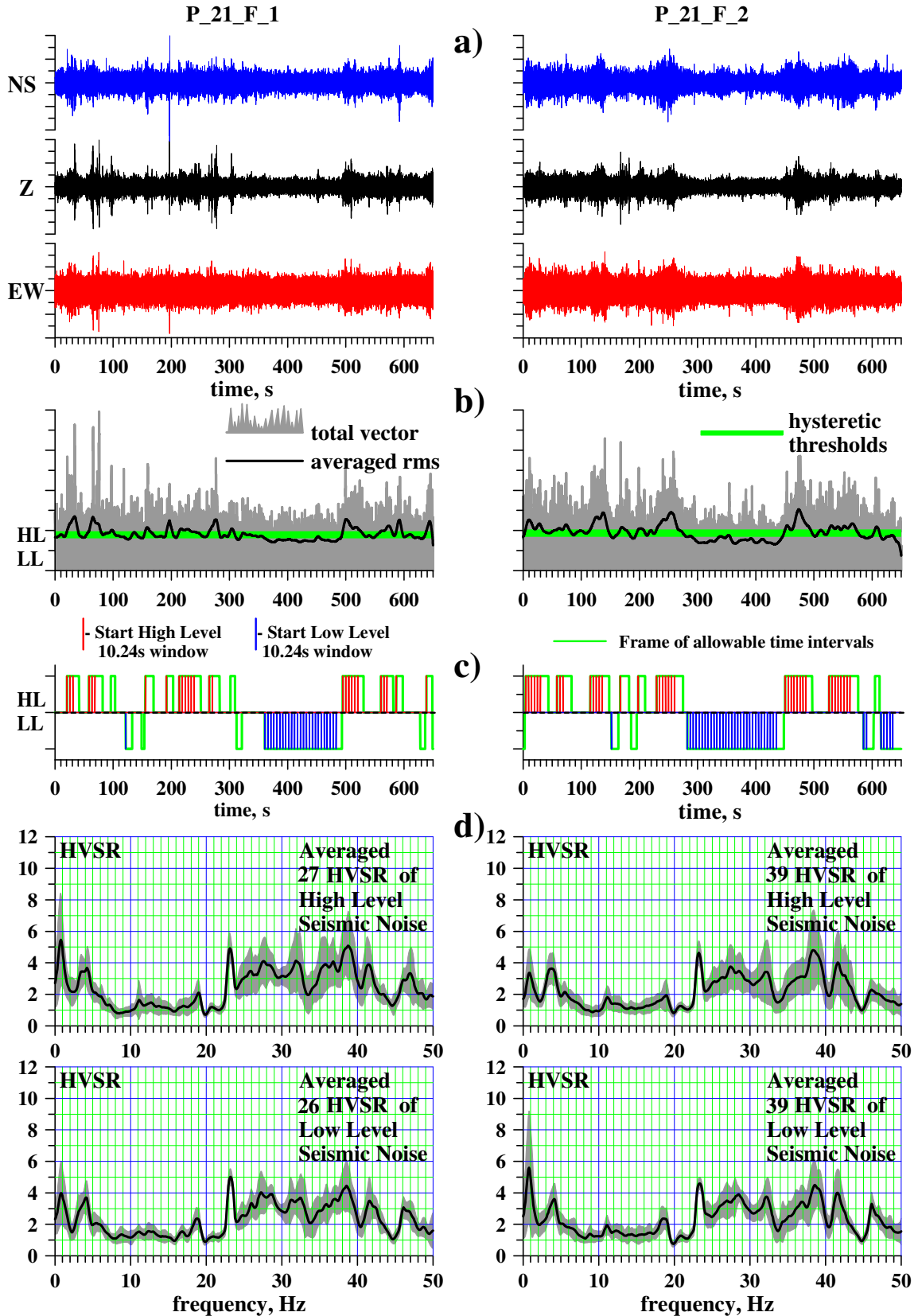
Test point #21 7-layers inversion



Average Vs 30m = 593.4 m/s

Test point #21 15-layers inversion

HVSR - Referent Test Point #21

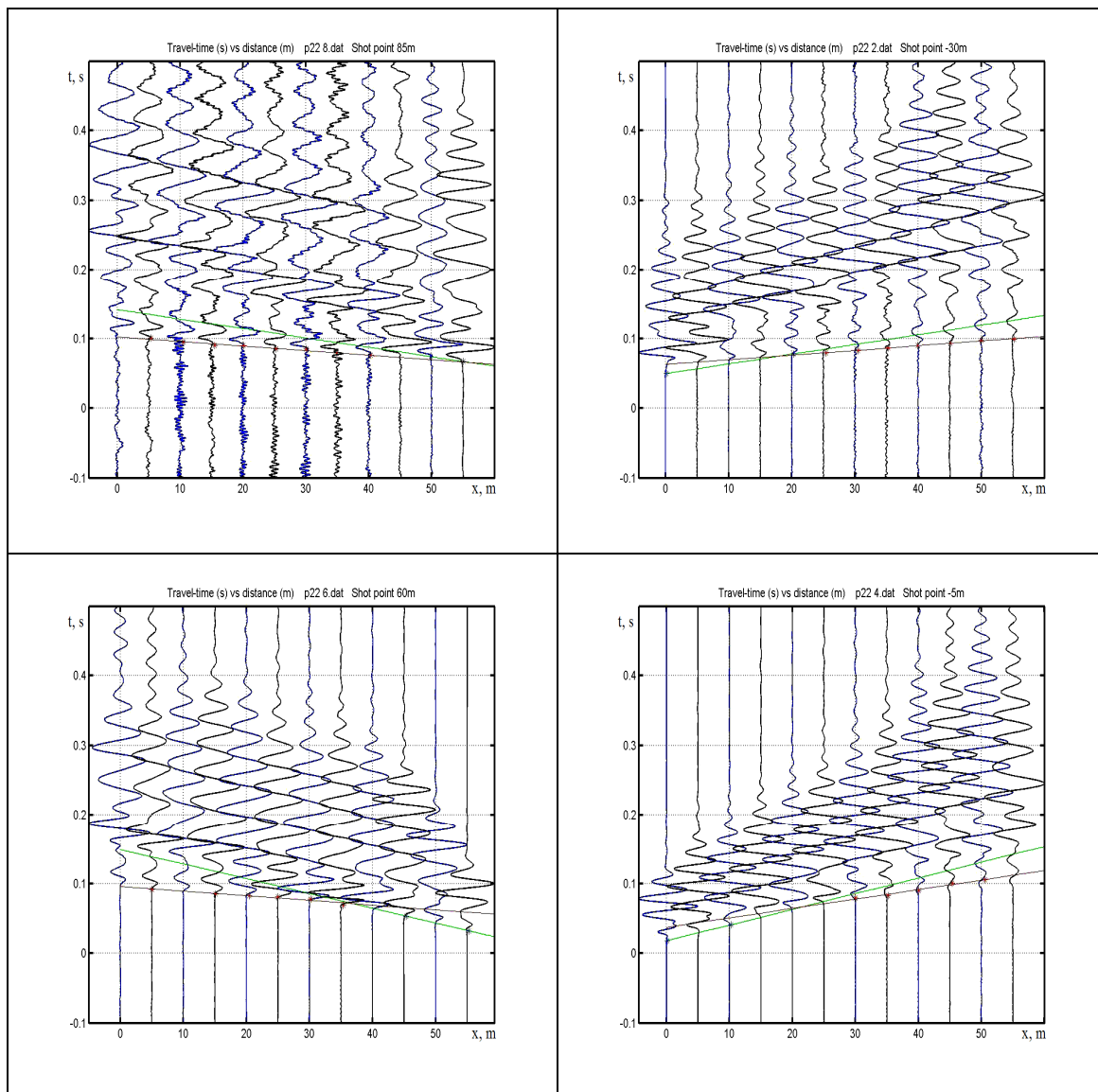


Results for Referent Test Point #22

Results for Vs30

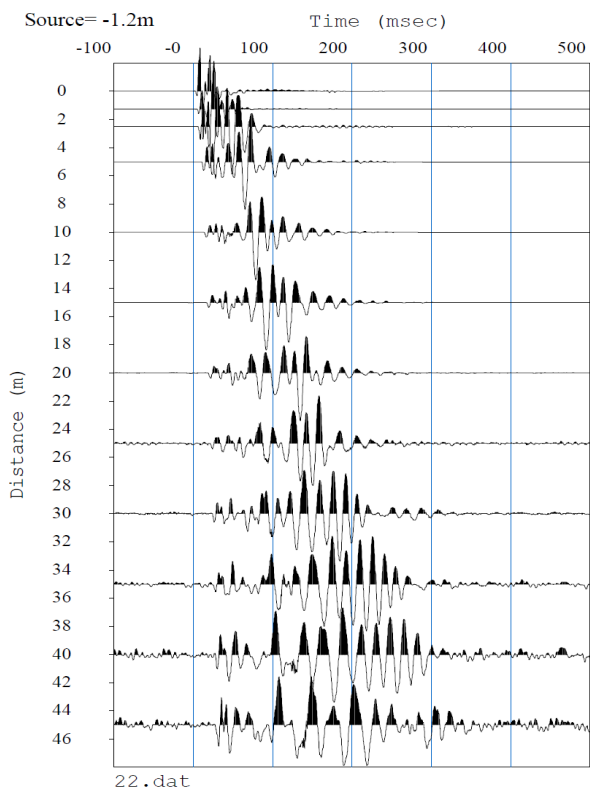
Vs30	SH-refraction	2-layer MASW	4-layer MASW	7-layer MASW	15-layer MASW
[m/s]	946	624	820	768	765

SH Refraction Profiles - Referent Test Point #22

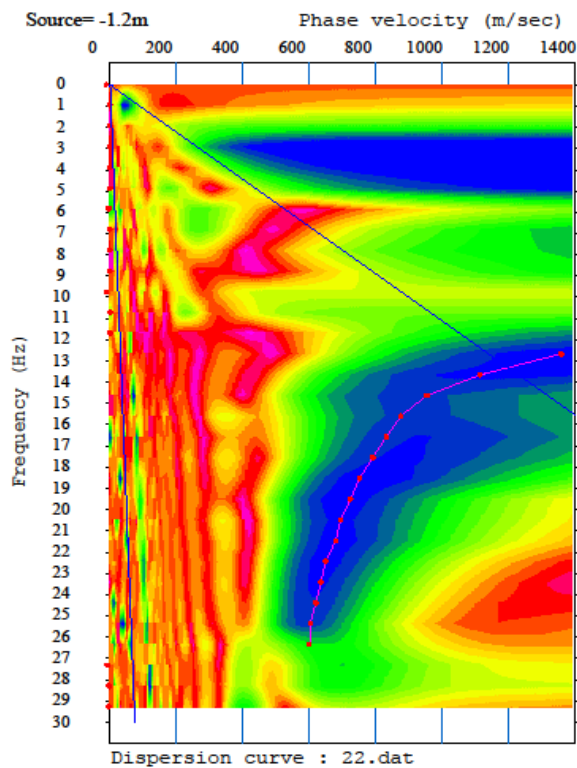


Vs30m = 946 m/s

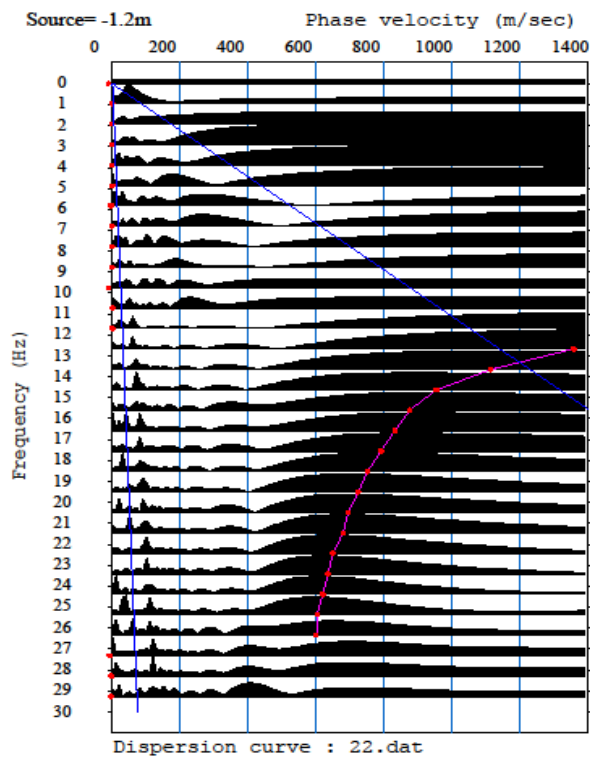
MASW - Referent Test Point #22



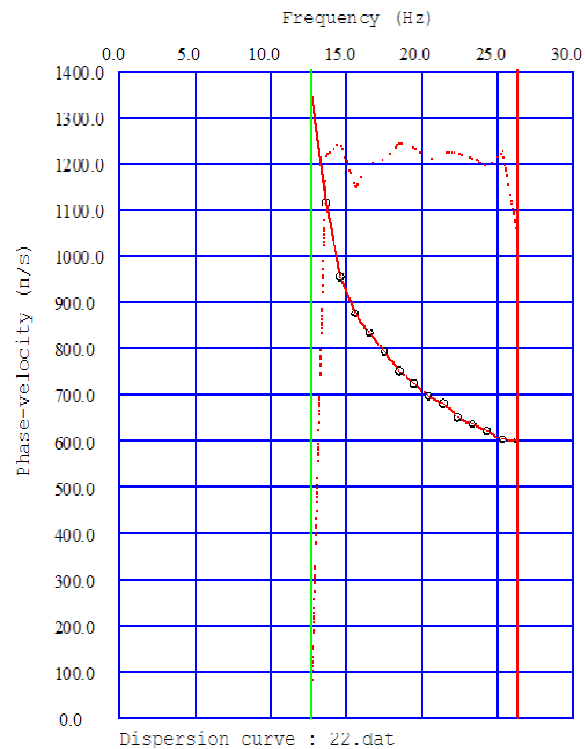
Test Point #22 MASW seismic waveforms



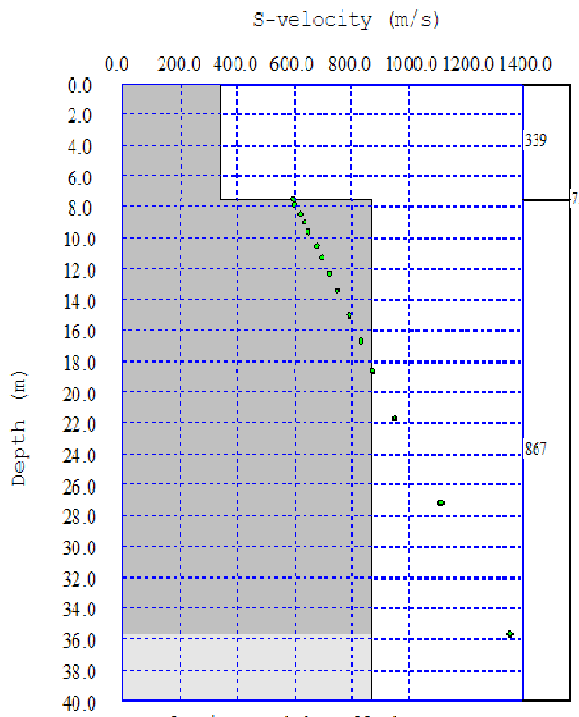
Surface Waves Dispersion - interpolated



Surface Waves Dispersion

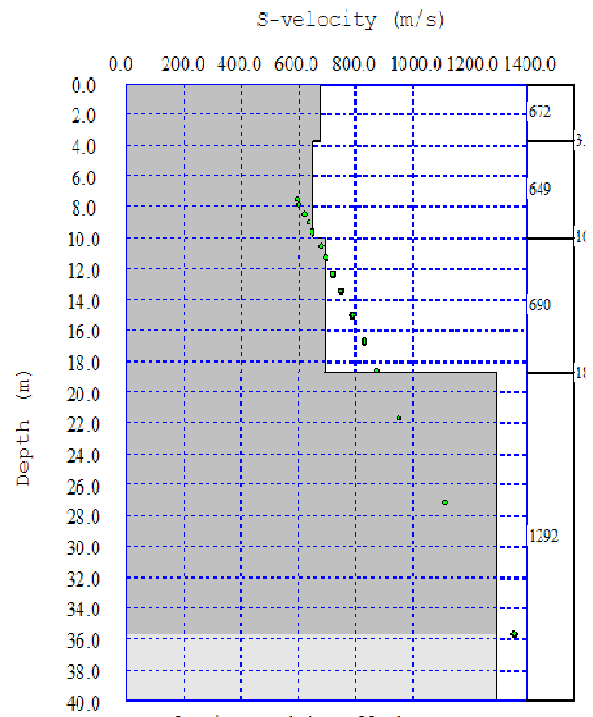


Phase velocity vs. frequency



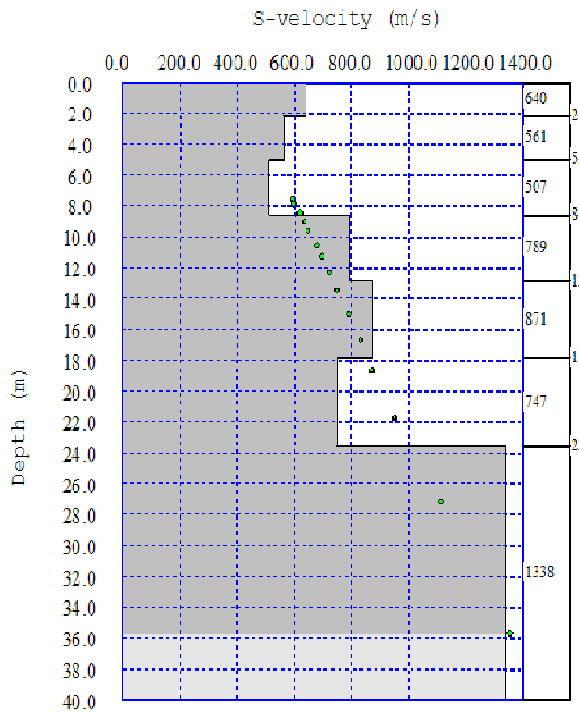
S-velocity model : 22.dat
Average Vs 30m = 624.7 m/s

Test point #22 2-layers inversion



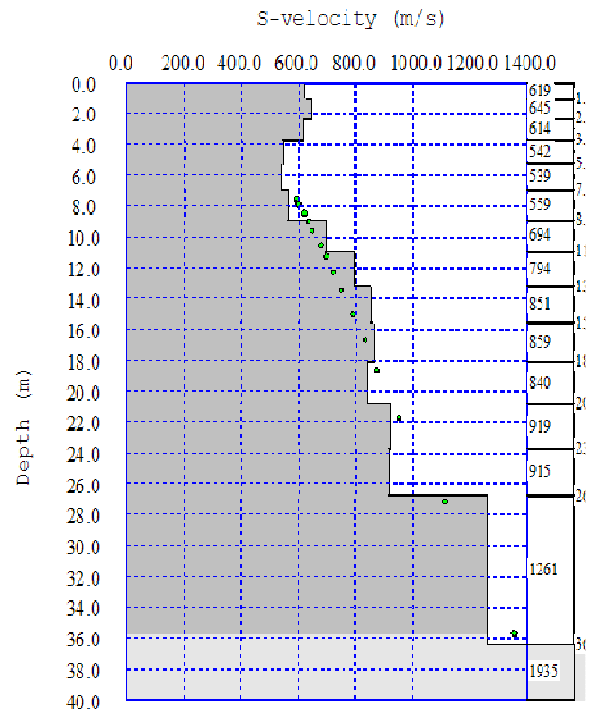
S-velocity model : 22.dat
Average Vs 30m = 820.2 m/s

Test point #22 4-layers inversion



S-velocity model : 22.dat
Average Vs 30m = 767.3 m/s

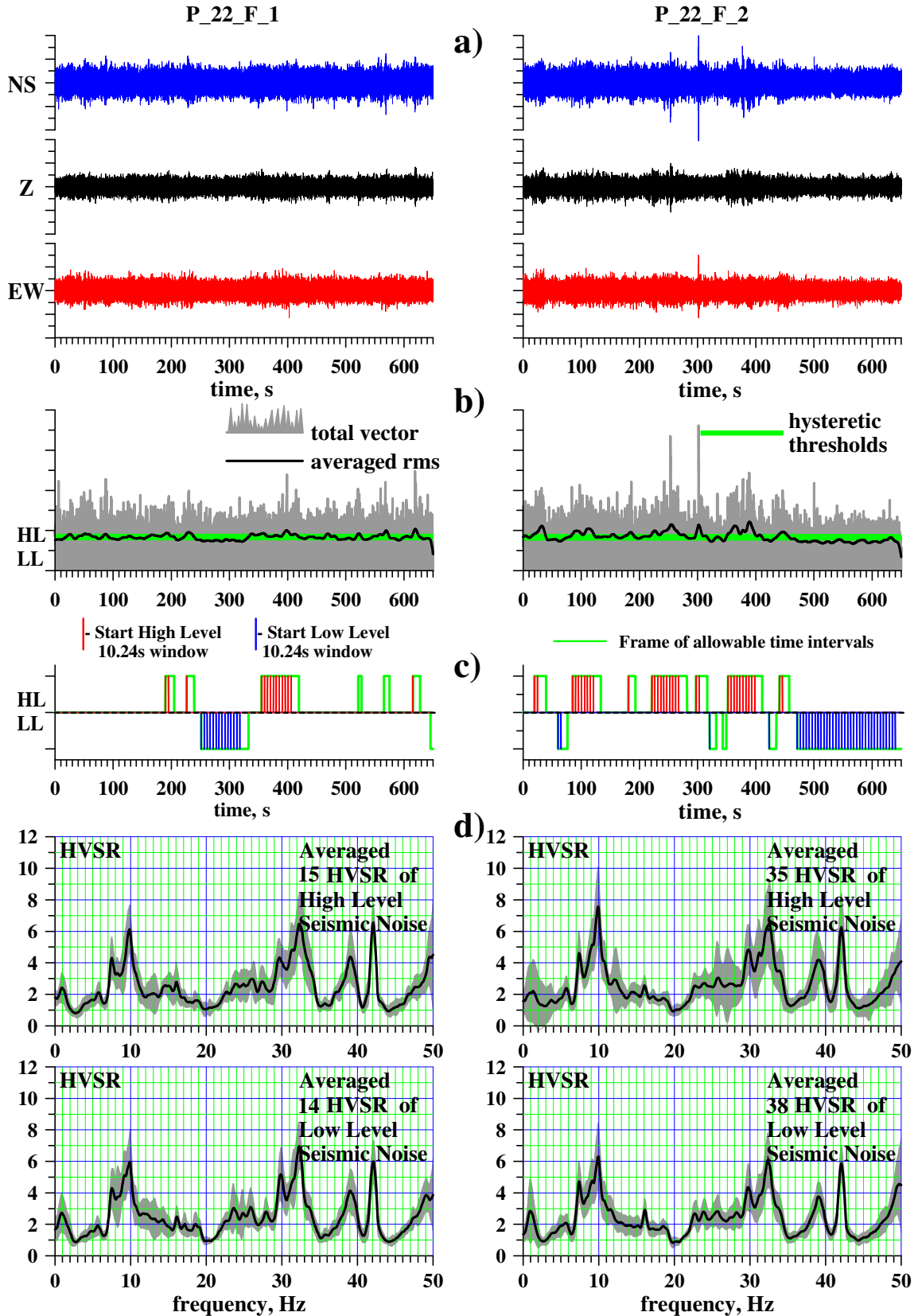
Test point #22 7-layers inversion



S-velocity model : 22.dat
Average Vs 30m = 765.3 m/s

Test point #22 15-layers inversion

HVSR - Referent Test Point #22

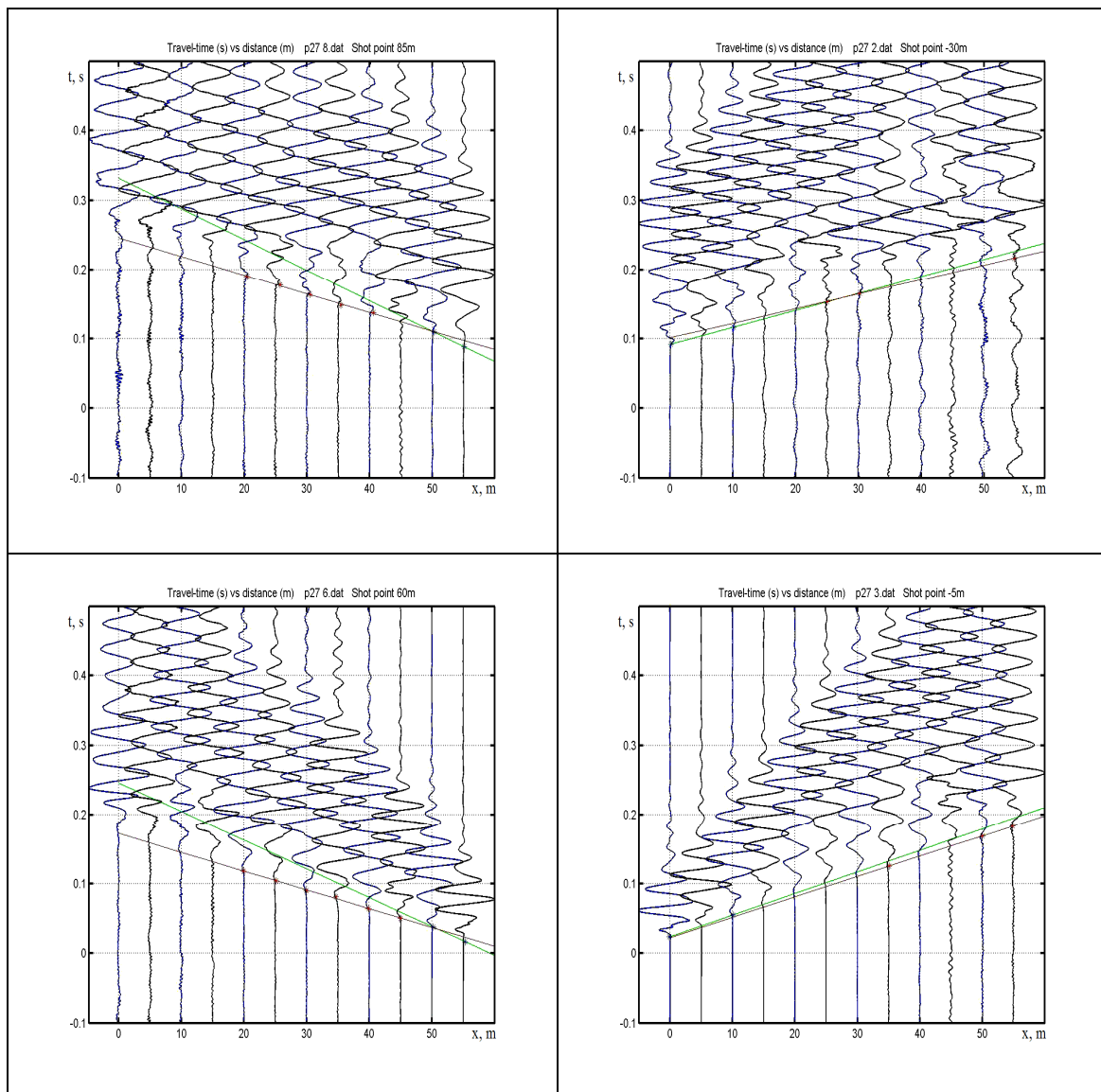


Results for Referent Test Point #27

Results for Vs30

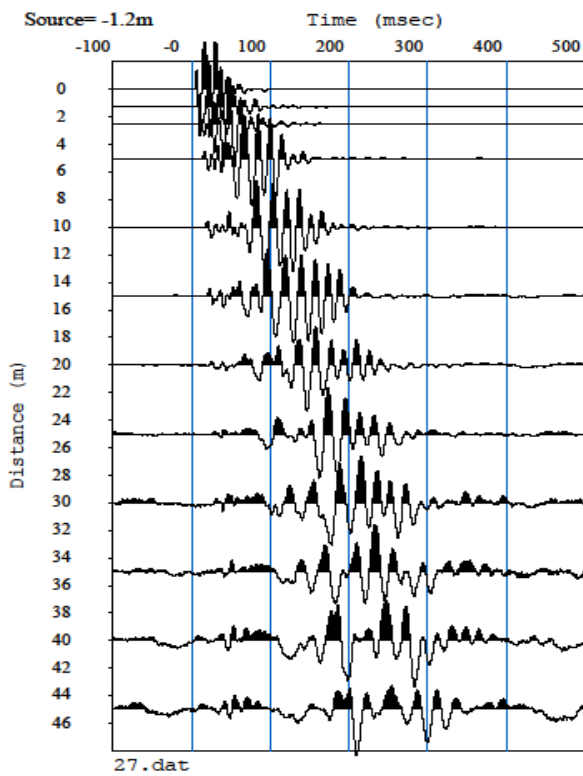
Vs30	SH-refraction	2-layer MASW	4-layer MASW	7-layer MASW	15-layer MASW
[m/s]	341	339	363	363	361

SH Refraction Profiles - Referent Test Point #27

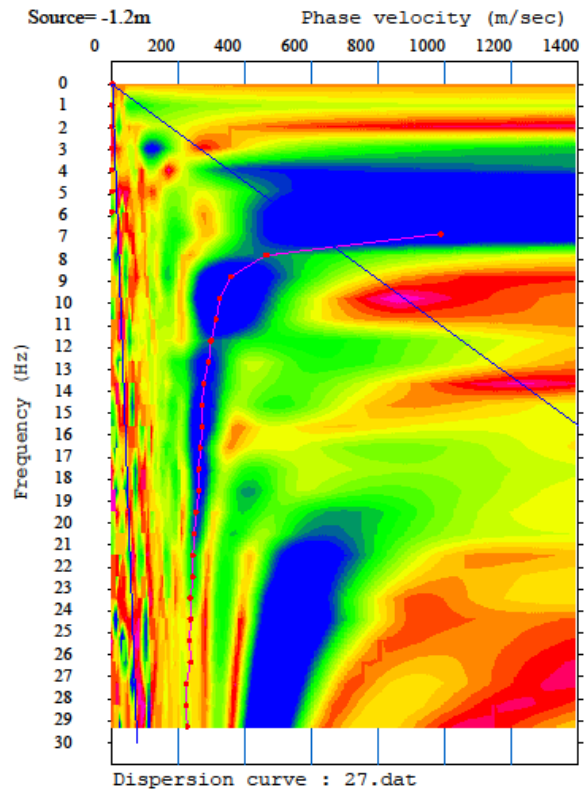


Vs30m = 341 m/s

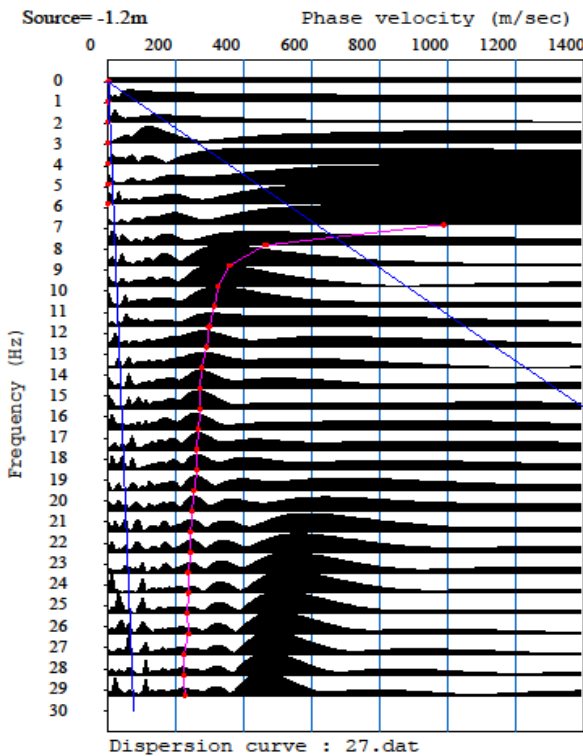
MASW - Referent Test Point #27



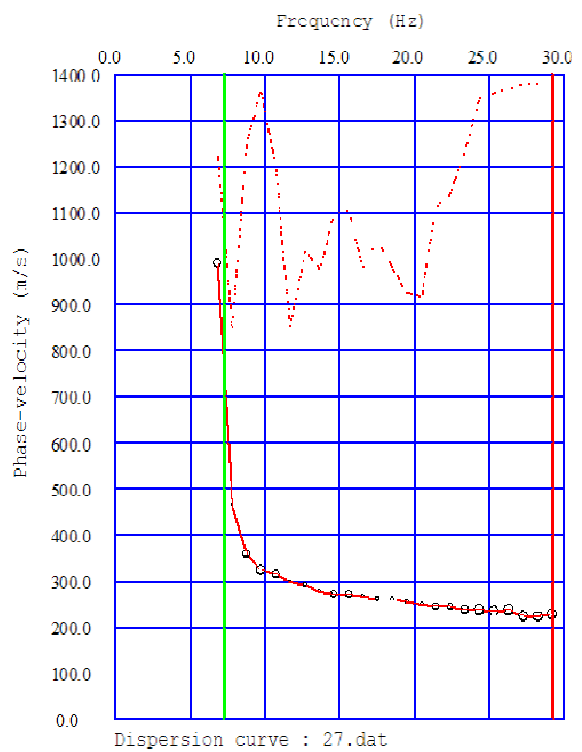
Test Point #27 MASW seismic waveforms



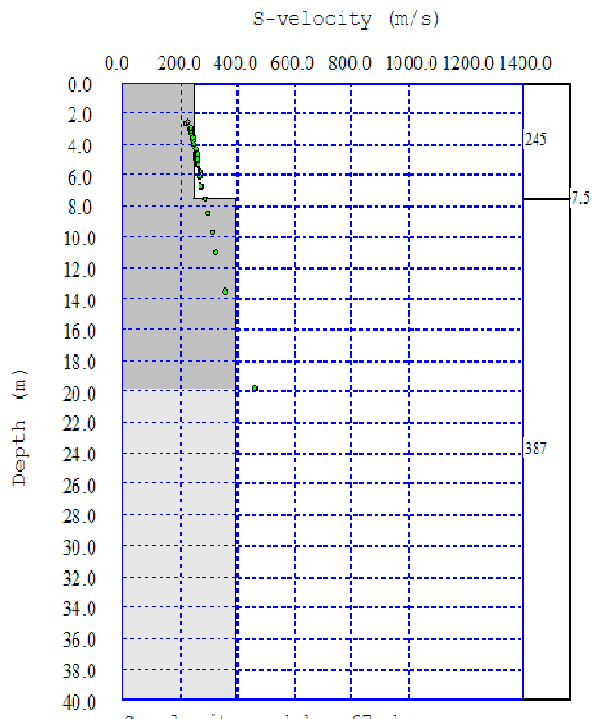
Surface Waves Dispersion - interpolated



Surface Waves Dispersion

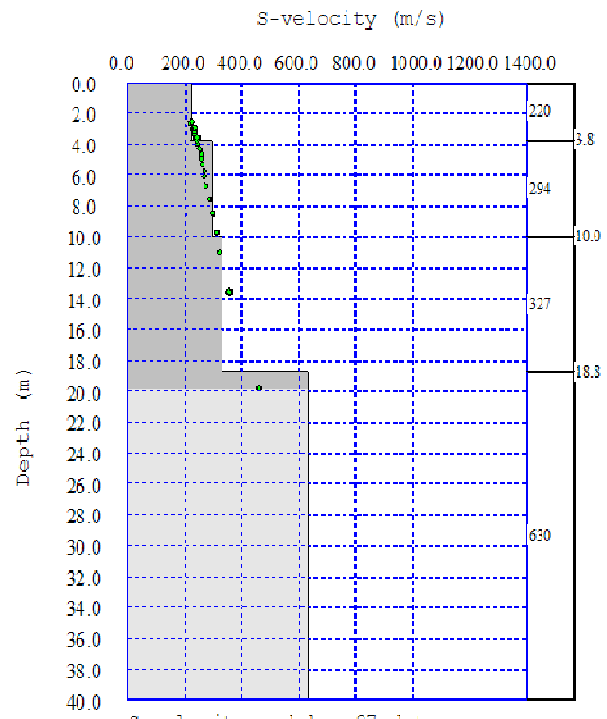


Phase velocity vs. frequency



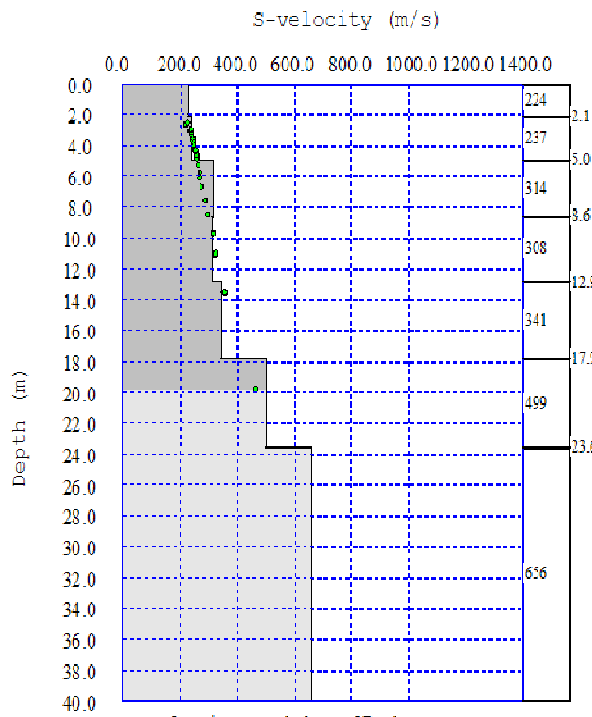
S-velocity model : 27.dat
Average Vs 30m = 338.6 m/s

Test point #27 2-layers inversion



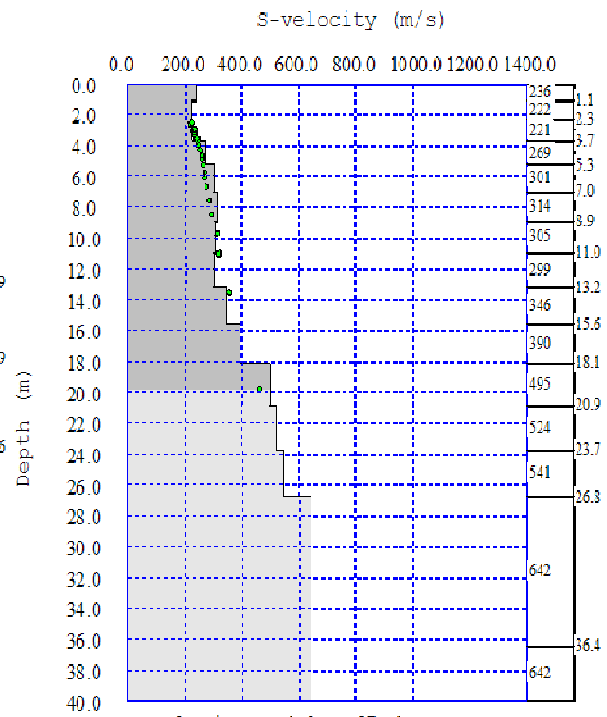
S-velocity model : 27.dat
Average Vs 30m = 362.6 m/s

Test point #27 4-layers inversion



S-velocity model : 27.dat
Average Vs 30m = 362.6 m/s

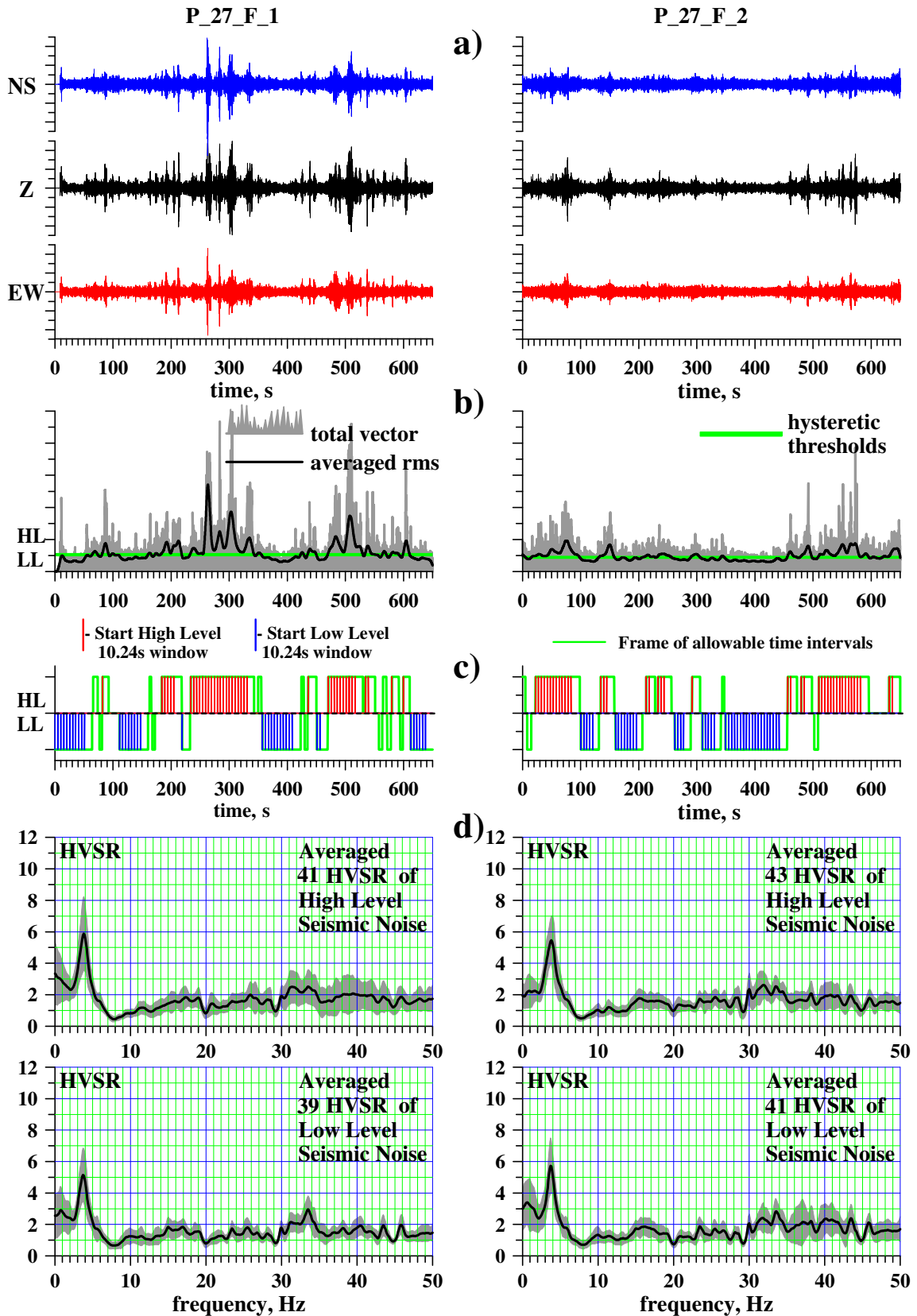
Test point #27 7-layers inversion



S-velocity model : 27.dat
Average Vs 30m = 360.6 m/s

Test point #27 15-layers inversion

HVSR - Referent Test Point #27

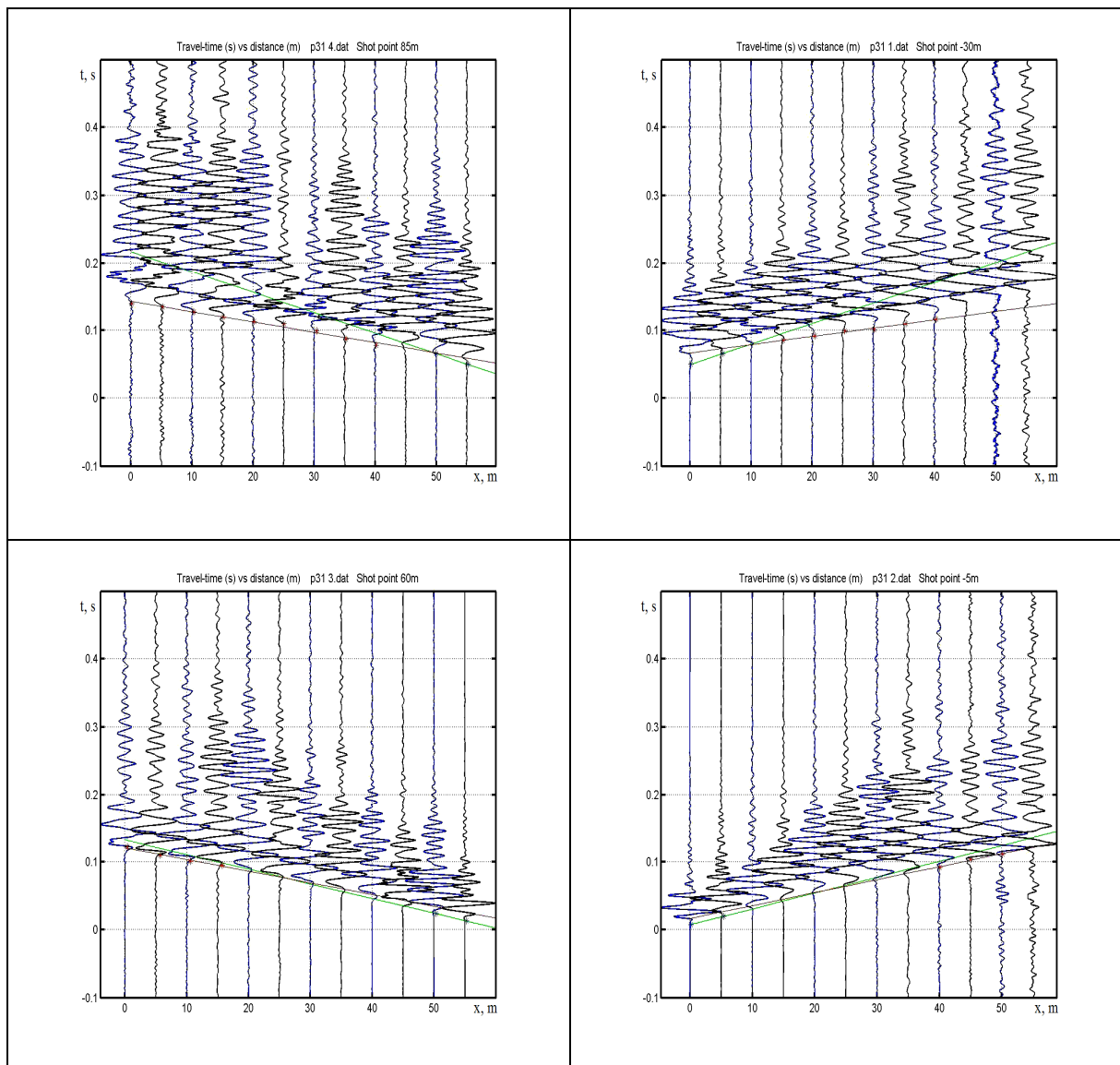


Results for Referent Test Point #31

Results for Vs30

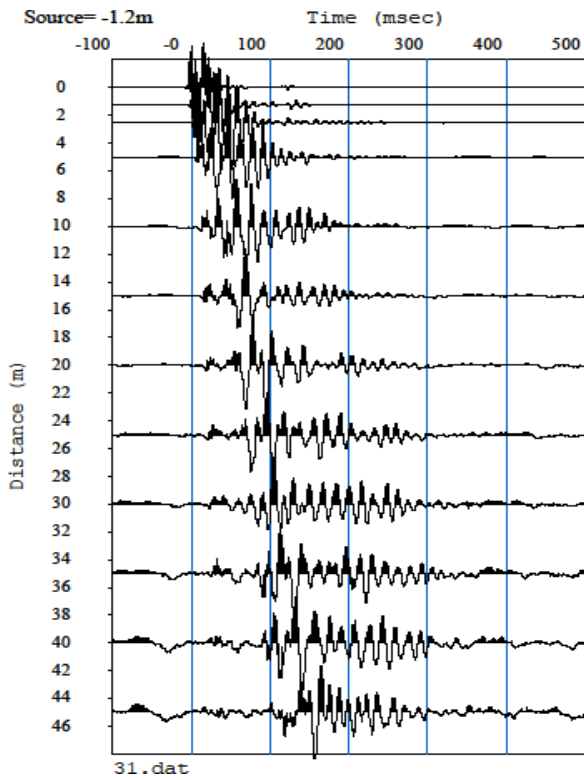
Vs30	SH-refraction	2-layer MASW	4-layer MASW	7-layer MASW	15-layer MASW
[m/s]	582	560	577	583	578

SH Refraction Profiles - Referent Test Point #31

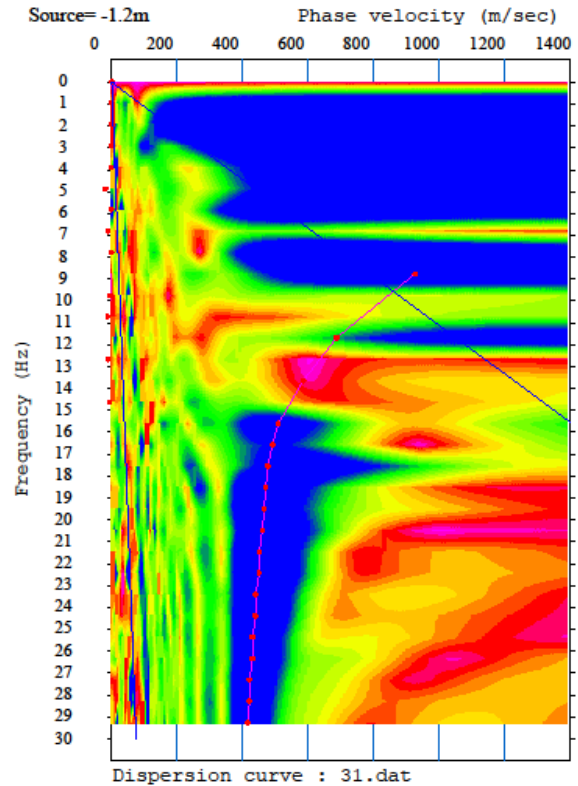


Vs30m = 582 m/s

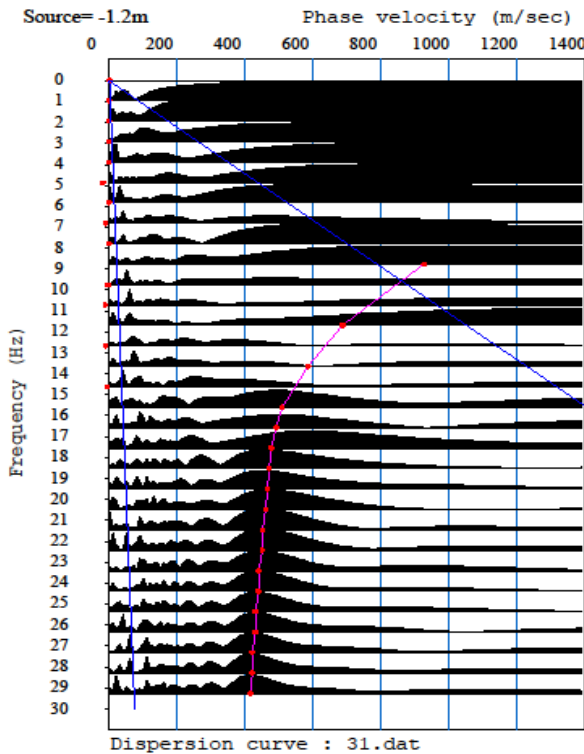
MASW - Referent Test Point #31



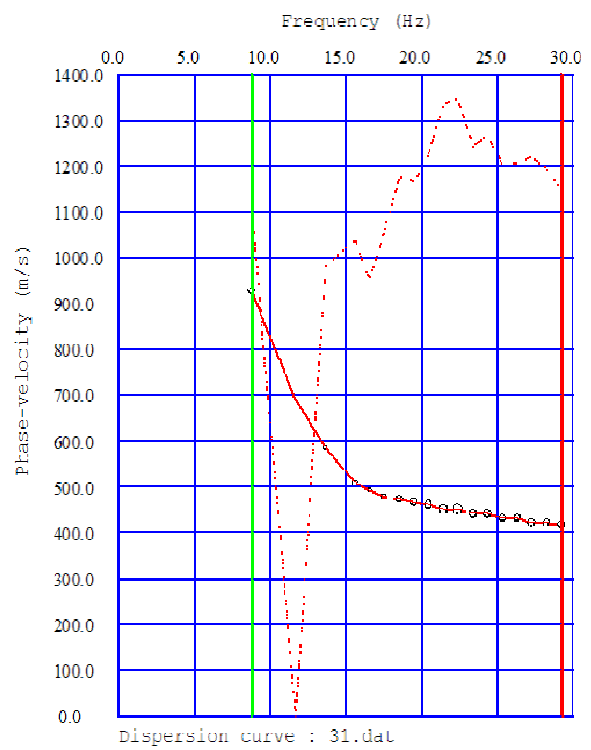
Test Point #31 MASW seismic waveforms



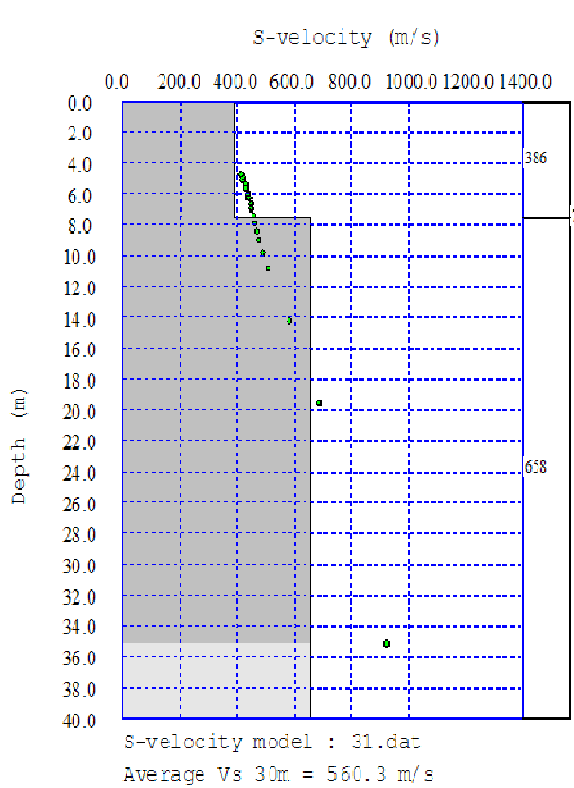
Surface Waves Dispersion - interpolated



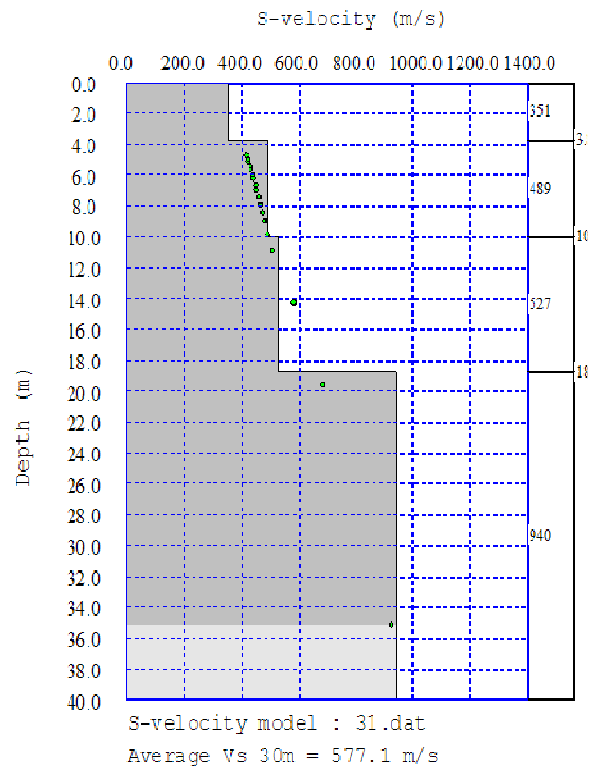
Surface Waves Dispersion



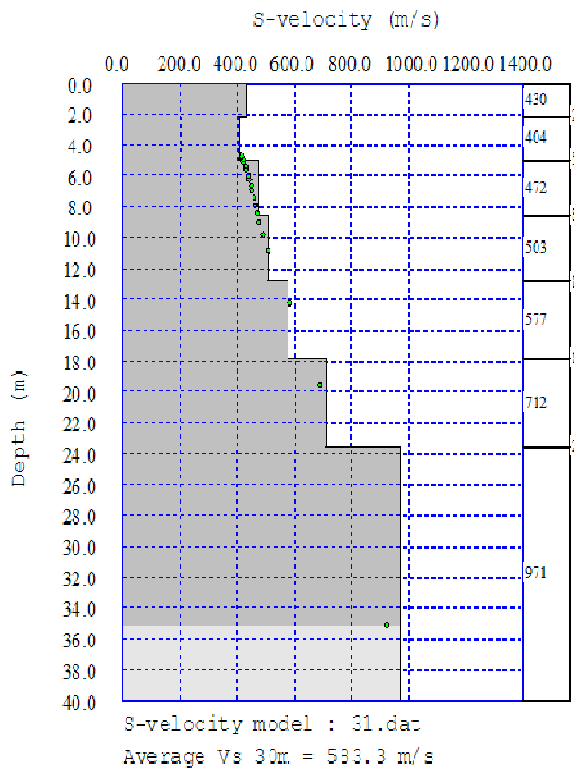
Phase velocity vs. frequency



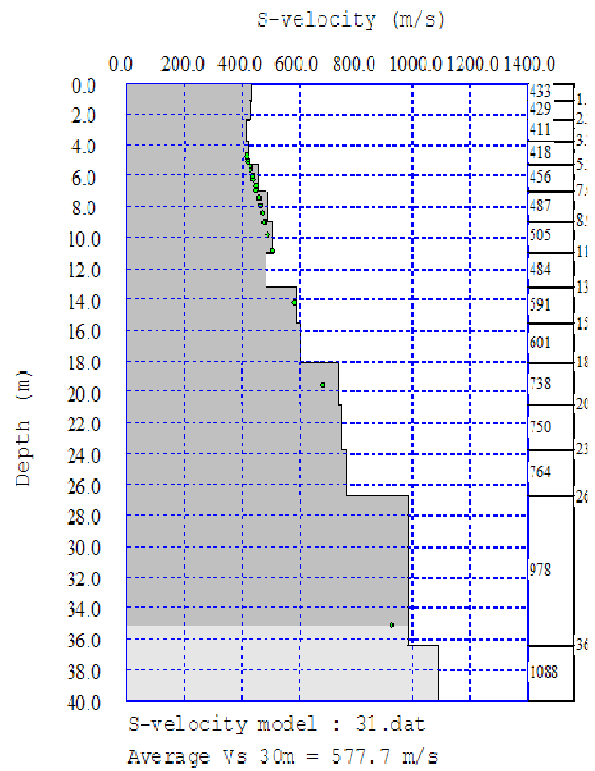
Test point #31 2-layers inversion



Test point #31 4-layers inversion

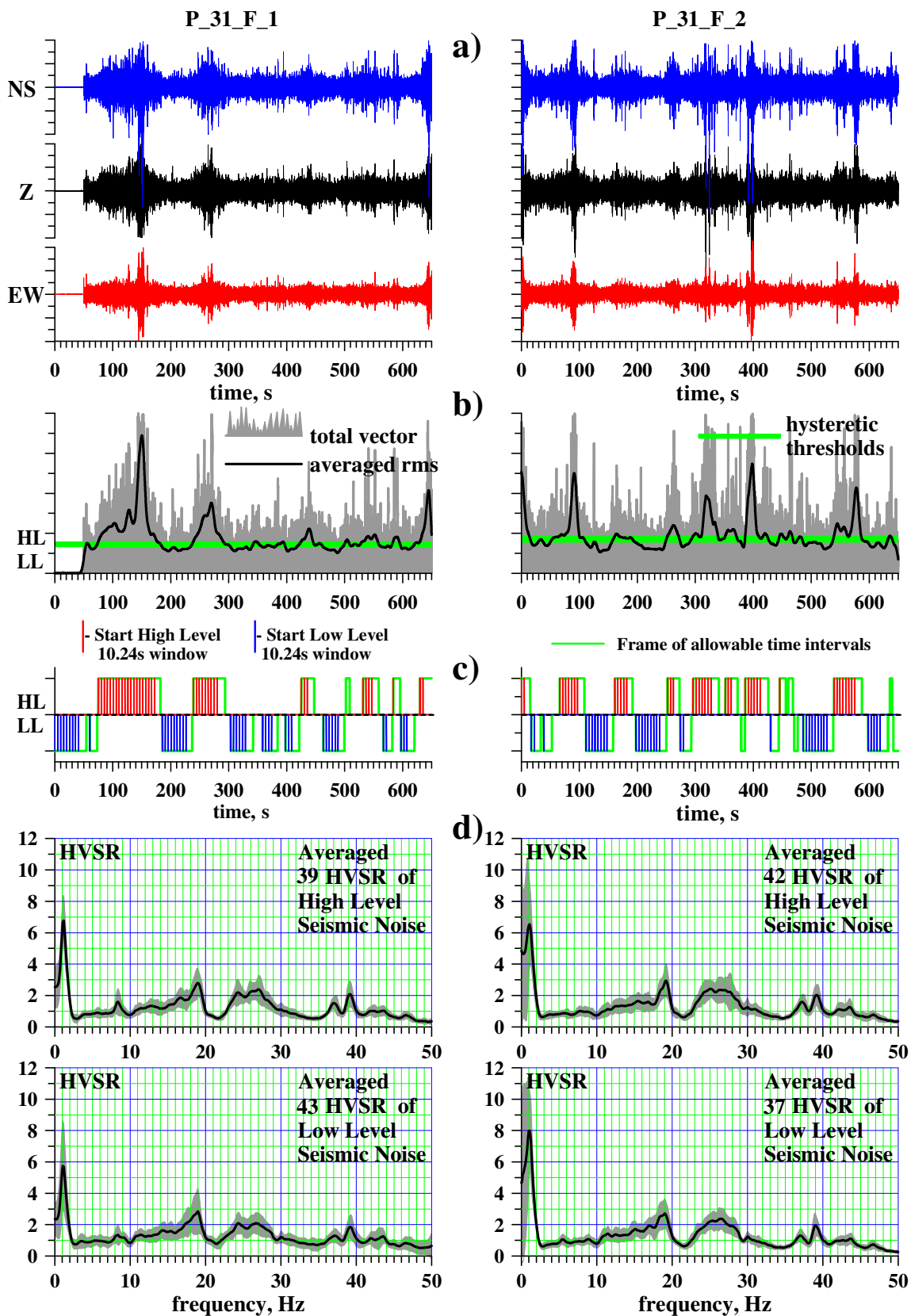


Test point #31 7-layers inversion



Test point #31 15-layers inversion

HVSR - Referent Test Point #31

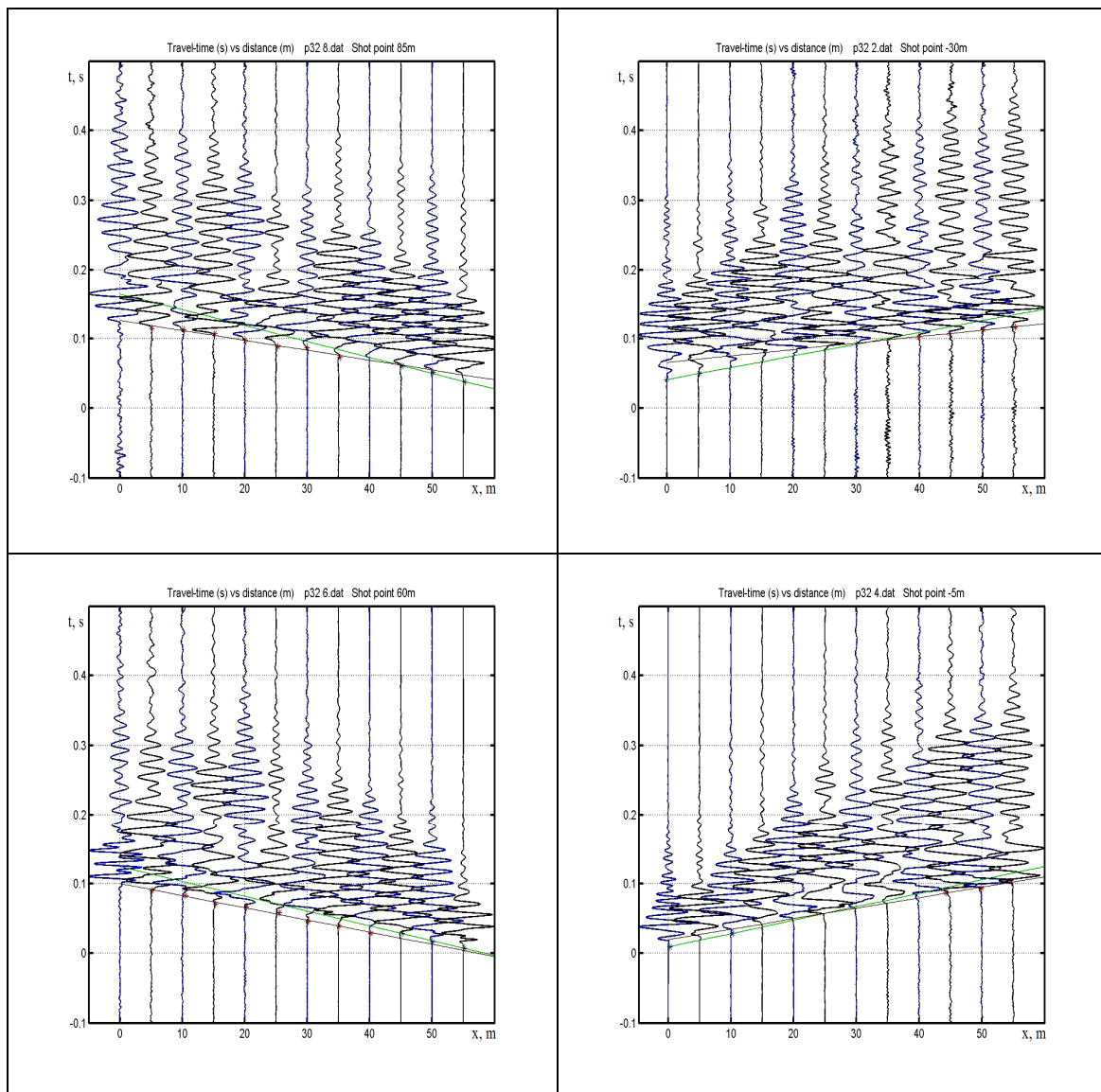


Results for Referent Test Point #32

Results for Vs30

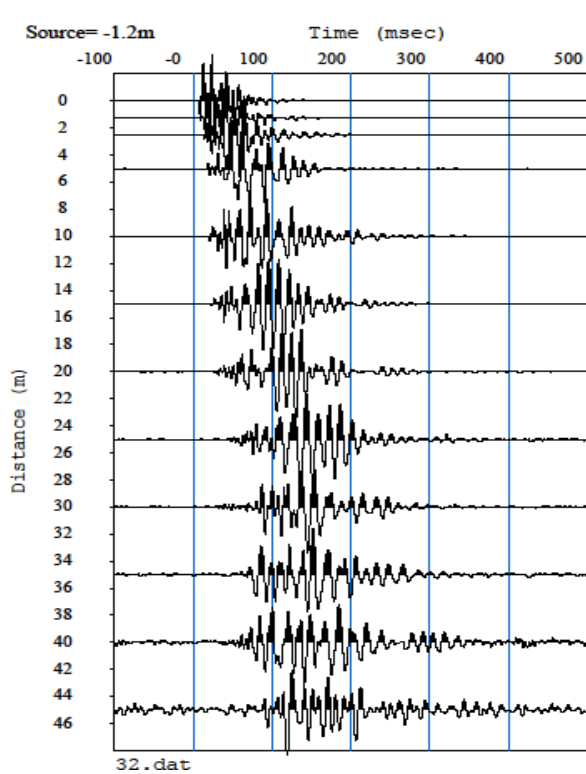
Vs30	SH-refraction	2-layer MASW	4-layer MASW	7-layer MASW	15-layer MASW
[m/s]	683	678	528	537	520

SH Refraction Profiles - Referent Test Point #32

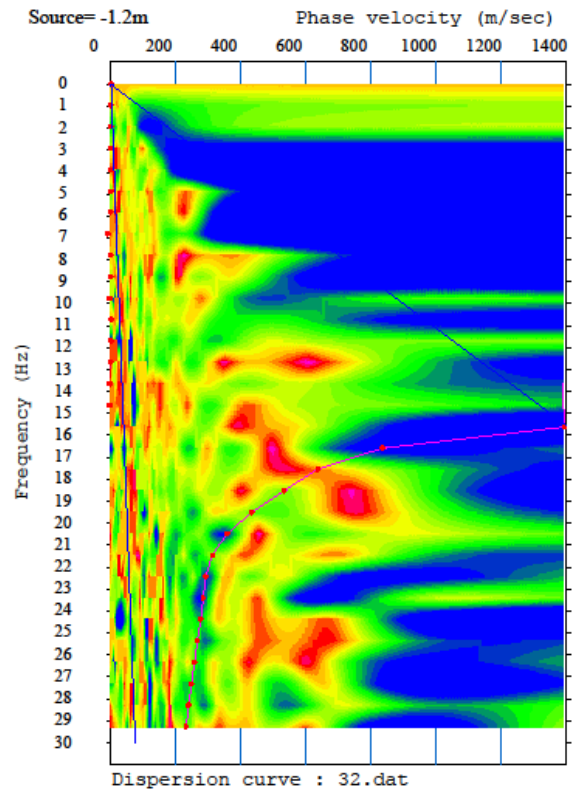


Vs30m = 683 m/s

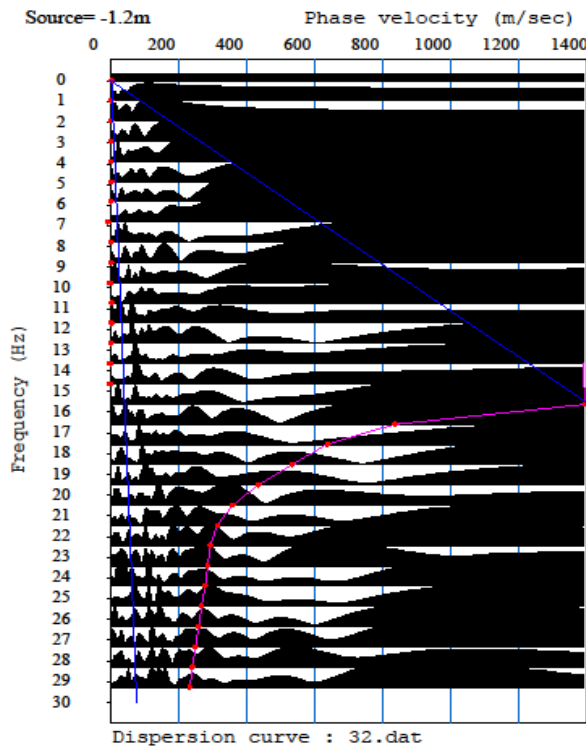
MASW - Referent Test Point #32



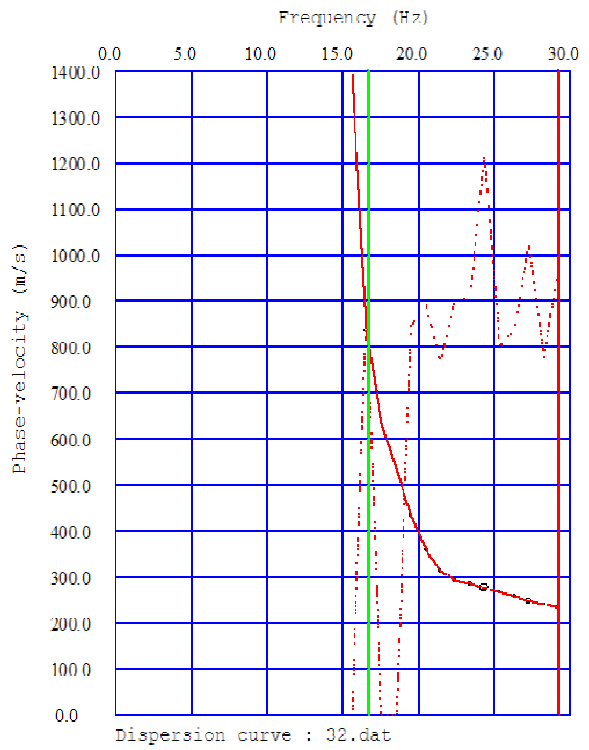
Test Point #32 MASW seismic waveforms



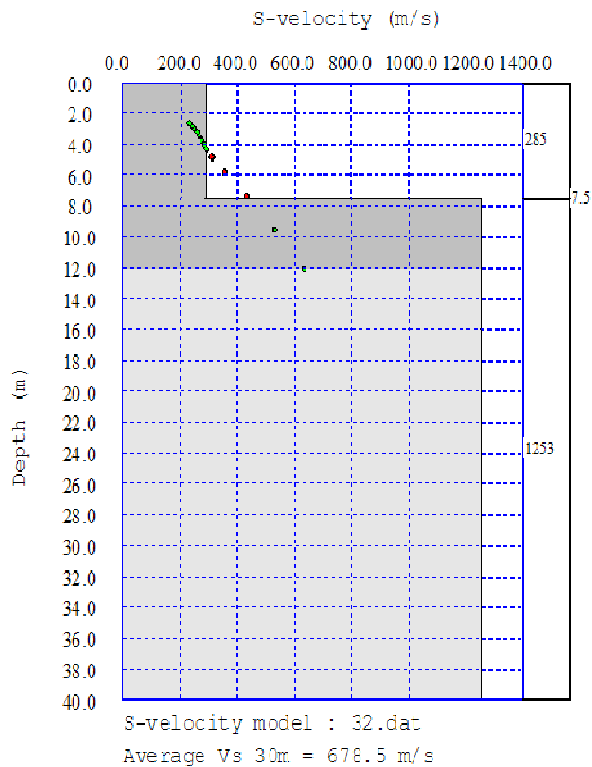
Surface Waves Dispersion - interpolated



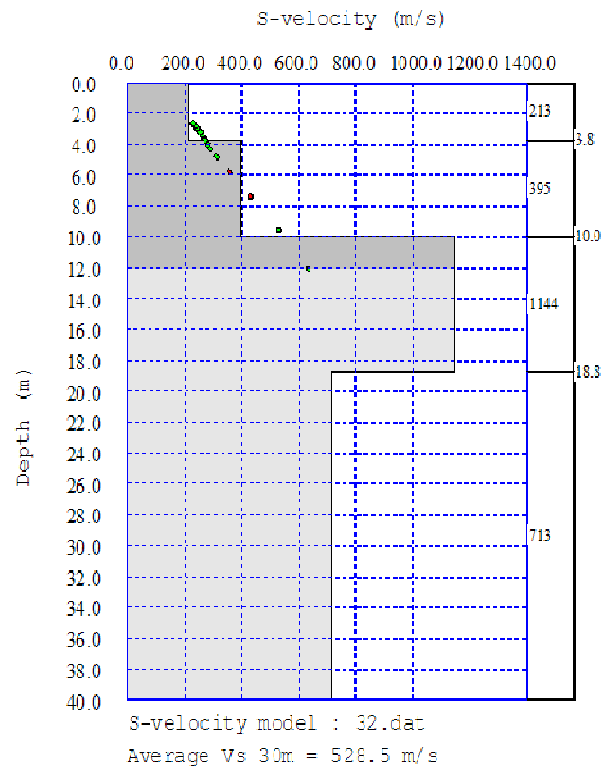
Surface Waves Dispersion



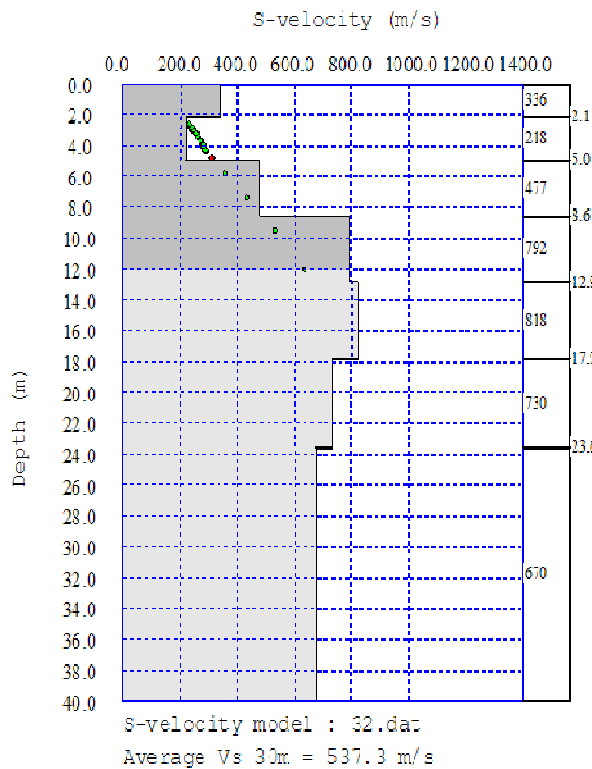
Phase velocity vs. frequency



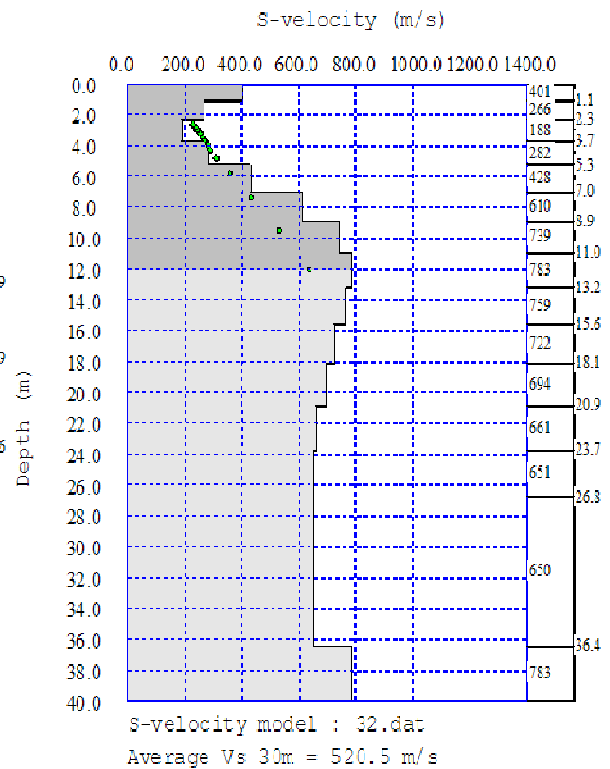
Test point #32 2-layers inversion



Test point #32 4-layers inversion

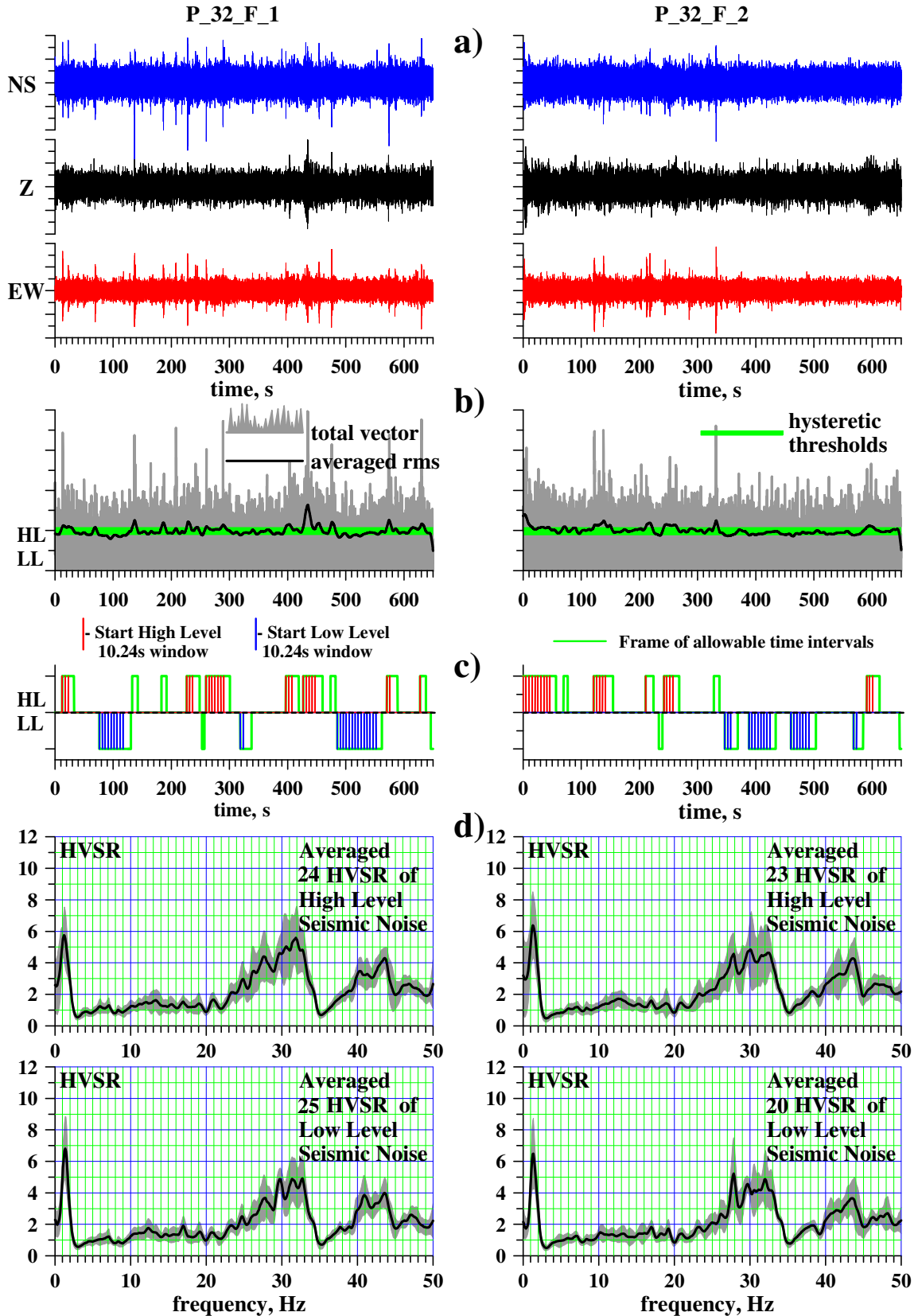


Test point #32 7-layers inversion



Test point #32 15-layers inversion

HVSR - Referent Test Point #32

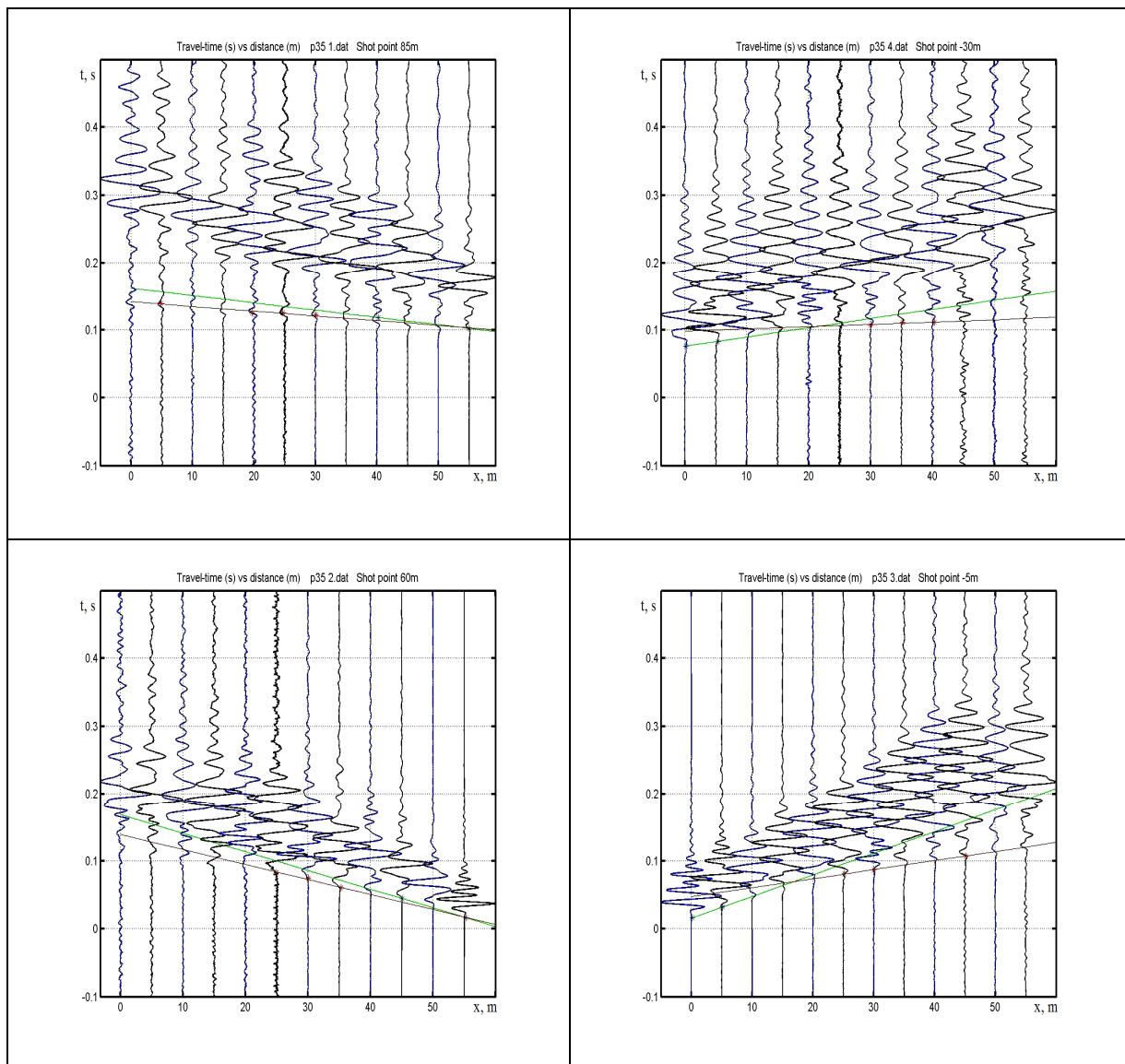


Results for Referent Test Point #35

Results for Vs30

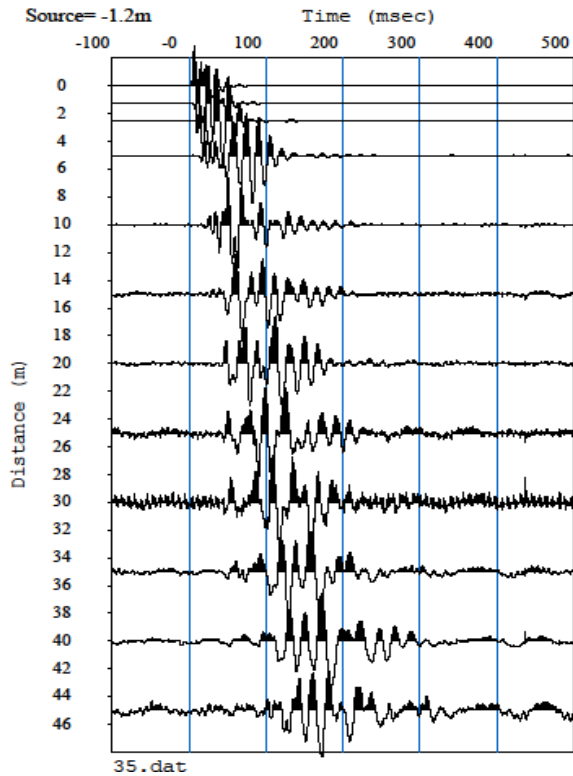
Vs30	SH-refraction	2-layer MASW	4-layer MASW	7-layer MASW	15-layer MASW
[m/s]	804	458	505	508	503

SH Refraction Profiles - Referent Test Point #35

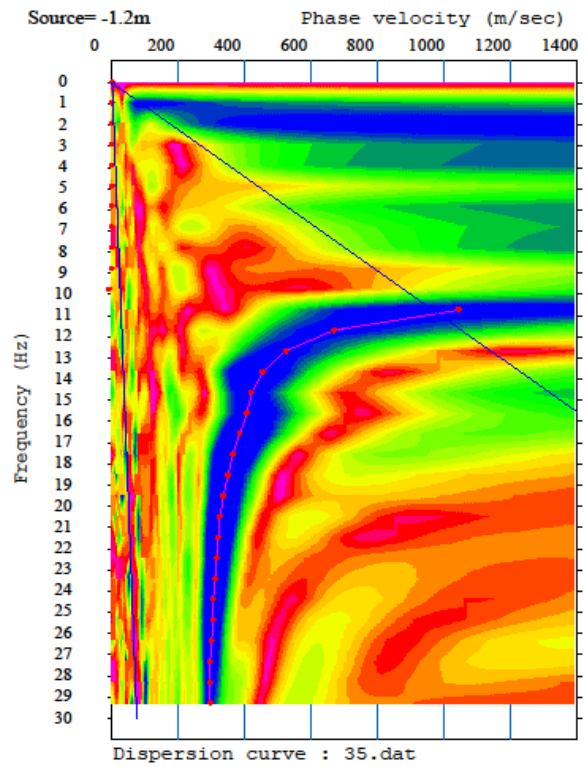


Vs30m = 804 m/s

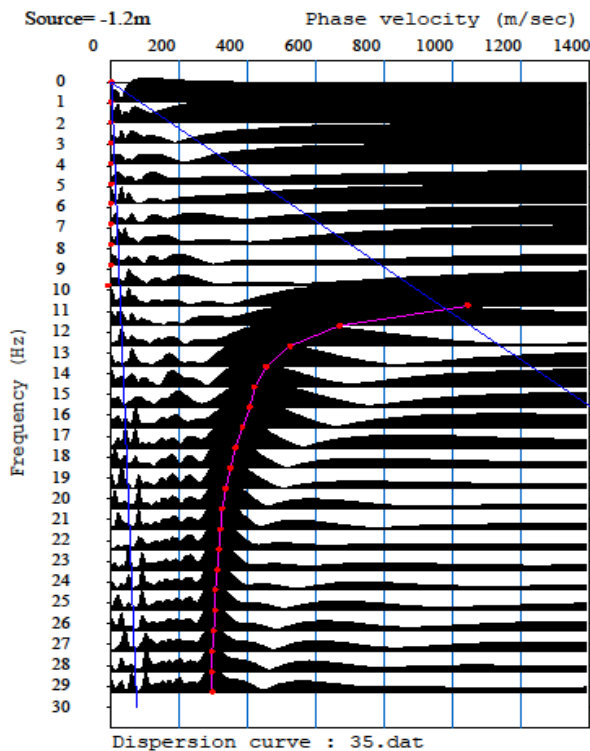
MASW - Referent Test Point #35



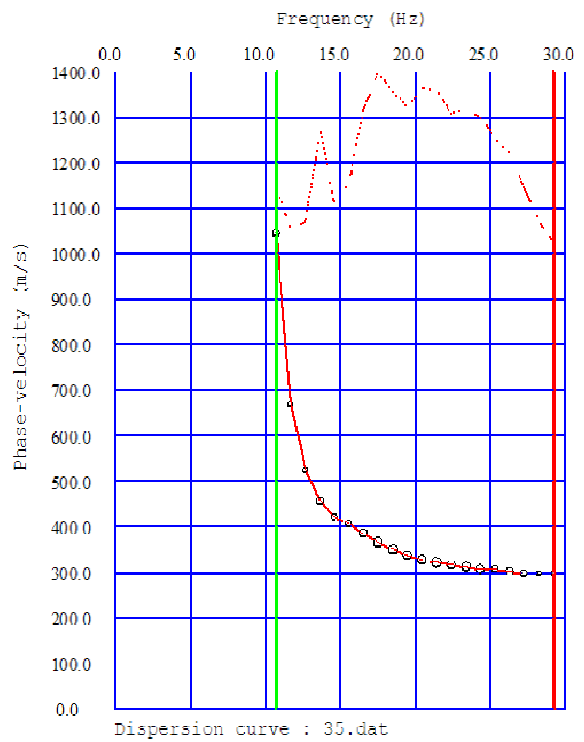
Test Point #35 MASW seismic waveforms



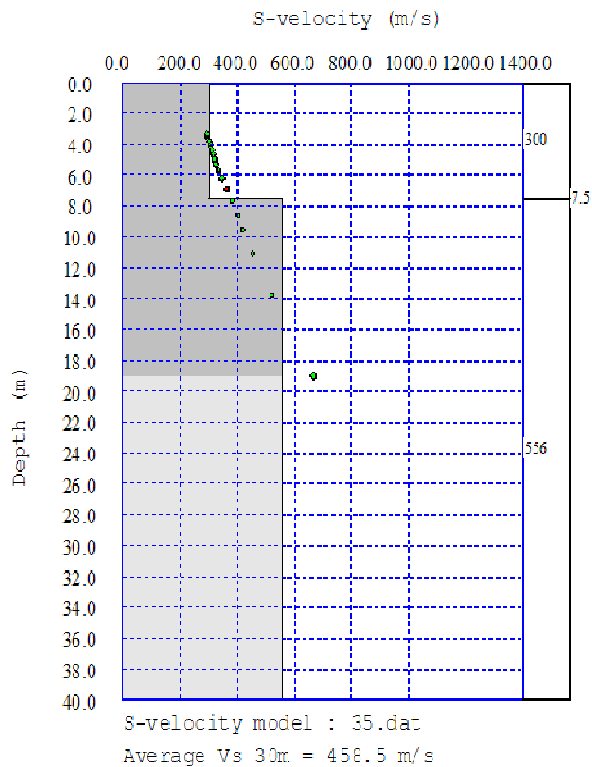
Surface Waves Dispersion - interpolated



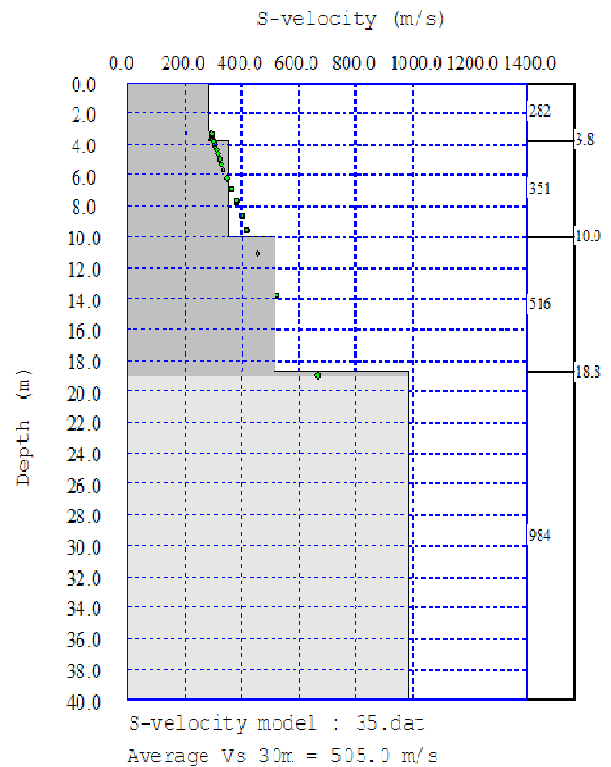
Surface Waves Dispersion



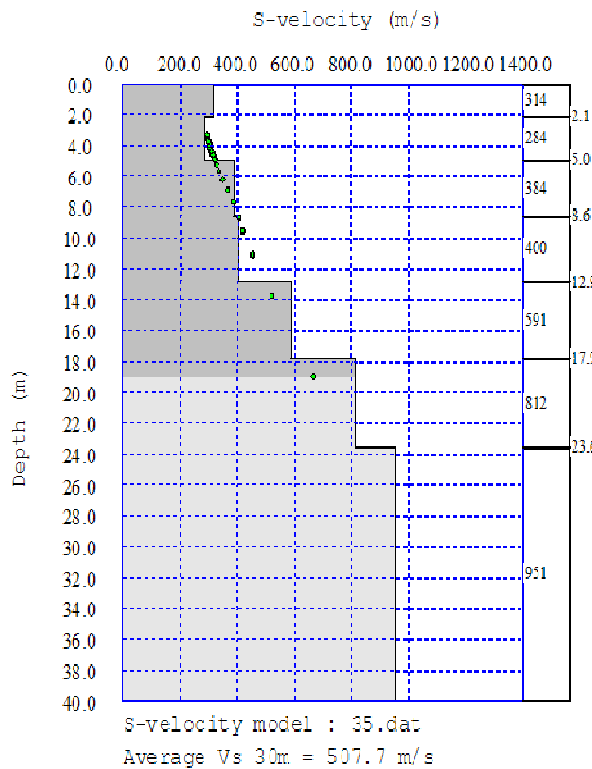
Phase velocity vs. frequency



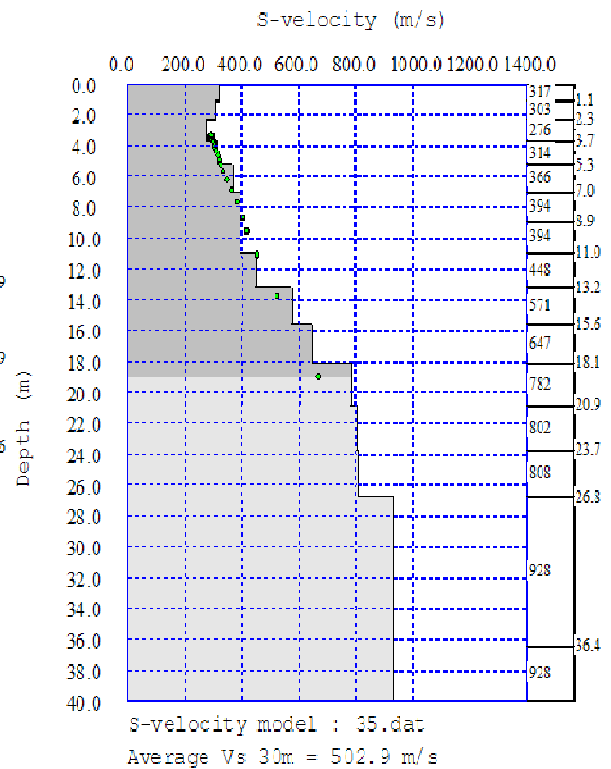
Test point #35 2-layers inversion



Test point #35 4-layers inversion

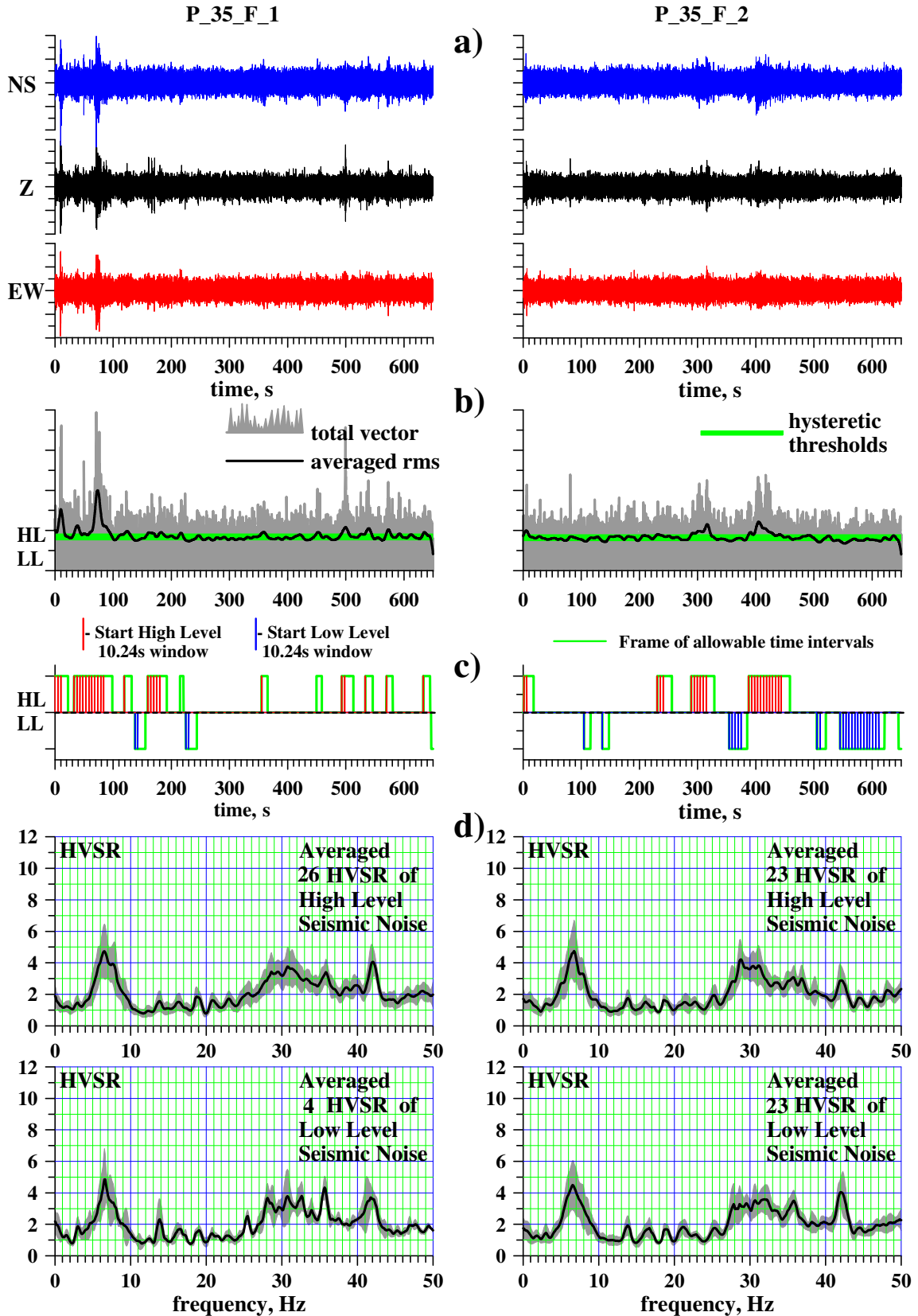


Test point #35 7-layers inversion



Test point #35 15-layers inversion

HVSR - Referent Test Point #35



Curriculum Vitae

Name: Dimitar Mihaylov

Post-secondary Education and Degrees: University of Mining and Geology,
Sofia, Bulgaria
1965-1970 M. Sc.

Honours and Awards: Scholarship for excellence in undergraduate/ M.Sc. studies
1969-1970

Award for graduation with excellence
1970

Related Work Experience

Technologist,
Department of Seismology.
Geophysical Institute of Bulgarian Academy of Sciences
1970-1973

Technologist,
Laboratory of Blasting Seismology
Geophysical Institute of Bulgarian Academy of Sciences
1973-1980

Research Associate,
Department of Seismology
Geophysical Institute of Bulgarian Academy of Sciences
1985-2004

Teaching Assistant,
Department of Civil and Environmental Engineering
The University of Western Ontario
2005-2009

Research Assistant
Department of Civil and Environmental Engineering
The University of Western Ontario
2005-2011

Publications:

Refereed journals:

1. Grigorova E., D. Mihaylov, N. Dachev (1976). Seismic events in the region of the "Iskar" dam, Bulgarian Geophysical Journal, 2,1, p. 65-66 (in Bulgarian)
2. Jordanov J., N. Ilev, D. Mihaylov (1977). Preservation of salt extraction boreholes in Provadia from the destroying impacts of quarry blasts in Ereka, Civil Engineering, Sofia, 24, 1 , p.28-29 (in Bulgarian)
3. Hvostov Y., D. Mihaylov (1978). A method for determination of detonation parameters of industrial explosives in natural conditions by electromagnetic method, Bulgarian Geophysical Journal, 4, 1, p. 88-92. (in Russian)
4. Jordanov I., N. Ilev, D. Mihaylov (1984). Determination of parameters of blasting works in quarry "Boaza" – Razgrad, securing the buildings and equipment of the factory for antibiotics, Journal for Civil engineering and Architecture, Sofia, 3, p. 66-70 (in Bulgarian)
5. Mihaylov D., K. Ischev, P Petrov, F. Filipov (1985). Physical and mechanical simulation of automatic control of engineering structures, Construction and Civil Engineering, 32, 7, p.26-28 (in Bulgarian)
6. Mihaylov D., S. Todorova (1989). Seismoacoustic Borehole Equipment. Compt. Rend. de l'Acad. Bulg. des Sciences. 42, 6, p.51-54.
7. Michailov, D., Glavcheva R., Dineva S., Elenkov S., Konstantinov B. (1990). Influence of local geological conditions on the macroseismic effects in the town of Strazhitza, Natural Hazards, v. 3, p.153-160.
8. Christoskov L., Glavcheva R., Georgiev C., Christova C., Donkova K., Simeonova S., Solakov D., Dineva D., Michajlov D., Dimitrov D., Spassov E. (1988). Seismological features of the space of earthquake sequences during 1986 in Gorna Orjahovica zone, Bulgarian Geophysical Journal, v.14, No.2, p.73-89 (in Bulgarian with English abstract).
9. Michailov, D., Glavcheva R., Dineva S., Elenkov S., Konstantinov B. (1990). Influence of local geological conditions on the macroseismic effects in the town of Strazhitza, Natural Hazards, v. 3, p.153-160.
10. Ouzounov, D., Dineva S., Michailov D., Petrov L. (1992). Investigation of spectral and spatial microseismic noise characteristics around Kozloduy NPP (Bulgaria), Proc. of the XXIII General Assembly of ESC, Prague, 1992, p.167-170.
11. Michajlov D., Dineva S., Petrov L., Yonchev R. (1995). Reduction of the surface microseismic noise by installing short-period seismometers in boreholes (For the local seismological network in the region of Kozloduy NPP), Bulgarian Geophysical Journal, v. 21, No. 2, p.31-39 (in Bulgarian with English abstract).
12. Dineva, S., Sokerova D., Michailov D. (1998). Seismicity of South-Western Bulgaria and border regions, Journal of Geodynamics, v.26, No. 2-4, p.309-325.

13. Dineva S., Sokerova D., Michajlov D. (1999). Present seismicity of South-Western Bulgaria and adjacent regions In "Geodynamics of SW Bulgaria" (Ed. G. Milev), p.49-64 (in Bulgarian).
14. Dineva S., Sokerova D., Mihaylov D. (2000). Seismic and seismotectonic features of South-Western Bulgaria and border regions, Reports on Geodesy, Warsaw Univ. of Technology, Inst. of Geodesy and Geodetic Astronomy, No. 4(49), p. 61-80.
15. Dineva S., Battlo J., Mihaylov D. and van Eck T. (2002). Source parameters of four strong earthquakes in Bulgaria and Portugal at the beginning of the 20th century, Journal of Seismology, 6, p. 99-123.

Other refereed contributions:

1. Grigорова E., D. Mihaylov, N. Dachev (1976). Seismic events in the region of the "Iskar" dam, Bulgarian Geophysical Journal, 2,1, p. 65-66 (in Bulgarian).
2. Jordanov J., N. Ilev, D. Mihaylov (1977). Preservation of salt extraction boreholes in Provadia from the destroying impacts of quarry blasts in Ereka, Civil Engineering, Sofia, 24, 1 , p.28-29 (in Bulgarian)
3. Mihaylov D. (1988). Seismoacoustic Borehole Equipment, Proc. of XXI General Assembly of ESC, Sofia, p. 362-367.
4. Dineva S., D. Michailov, D. Sokerova, E. Botev, D. Ouzounov, L. Petrov, L. Dimitrova, S. Popov (1994). Local seismicity in the Provadia region (NE Bulgaria) (Project for Local Earthquake monitoring) Proceedings of the XXIV Gen. Assembly of ESC, 19-24 September, 1994, Athens, Greece, p.1309-1318.
5. Michajlov D., Dineva S., Sokerova D., Botev E., Ouzounov D., Petrov L., Dimitrova L. (1994). Seismotectonic and seismological investigations for design of local seismic network in the region of Mirovo salt body, Proceedings of III Scientific-Practical Conference on protection of population against disasters and accidents, Sofia, 8-9 September 1994, v. 6 (Seismic hazard, Meteorological and hydrological aspects of the disasters and accidents), p.31-41 (in Bulgarian).
6. J. Batlló, R. Macià, S. Dineva, D. Mihaylov (2003). Source Parameters of two Large Earthquakes near Valandovo (Macedonia) - March 1931. In: Risk assessment of waste water re-use on groundwater quality, IAHS, p. A.456-A.457.

National/ International Conferences

1. Dineva S., D. Michailov, D. Sokerova, E. Botev, Ouzounov D., L. Petrov, L. Dimitrova, S. Popov (1994). Local seismicity in the Provadia region (NE Bulgaria) (Project for Local Earthquake monitoring) XXIV Gen. Assembly of ESC, 19-24 September, 1994, Athens, Greece.
2. Ouzounov D., S. Dineva, D. Michailov (1994). Spatial Analysis of the Microseismic Noise in the Provadia Region (NE Bulgaria), XXIV Gen. Assembly of ESC, 19-24 September, 1994, Athens, Greece.

3. Mihaylov D., Dineva S., Sokerova D., Botev E., Ouzounov D., Petrov L., Dimitrova L. (1994). Seismotectonic and seismological investigations for design of local seismological network around Mirovo salt deposit, Third scientific-practical conference for prevention of population of accidents and emergencies, v. VI - Seismic hazard, Sofia, December 8-9, 1994.
4. Dineva S., Sokerova D., Michajlov D., Botev E. (1997). Seismotectonics and geophysical features of the earth crust in SW Bulgaria and border regions, 29th General Assembly of IASPEI, August 18-28, 1997, Thessaloniki, Greece.
5. Dineva S., Mihaylov D., Nikolova L., Vlasakov V. (1997). Aftershocks of strong in 1986 in the region of Strazhitza town. Spatial-temporary and energetic characteristics, Forth scientific-practical conference for prevention of population of accidents and emergencies, Sofia, 1997.
6. Dineva S., Sokerova D., Mihaylov D. (1999). Temporary seismicity of South-Western Bulgaria and adjacent lands, Symposium "Geodynamic investigations, connected with earthquakes in 1904 in Krupnik-Kresna", Blagoevgrad, 27-28 April, 1999.
7. Dineva S., T van Eck, D. Mihaylov (1999). Between the Serbo-Macedonian and Rhodope Massifs: Seismotectonics of the Kresna region, XXIV Gen. Assembly EGS, Den Haag, 19-23 April, 1999.
8. Dineva S., Batllo J., Mihaylov D., van Eck T. (1999). Seismic parameters of strong earthquakes in Bulgaria and Spain during 20th century, IUGG 1999, Birmingham, 19-30 July 1999.
9. Dineva S., T. van Eck, D. Mihaylov (1999). Seismotectonic re-interpretations of the zone along the Struma lineament, IUGG 1999, Birmingham, 19-30 July 1999.
10. Dineva S., T. van Eck, D. Mihaylov (1999). Seismotectonic re-interpretations of the zone along the Struma lineament, Conference "Advances natural hazards mitigations experiences from Europe and Japan, Athens, 3-4 Nov. 1999, Greece.
11. Batlló J., Dineva S., Mihailov D. and Macia R. (2000). Source parameters of two large Iberian earthquakes (23 April and 16 June 1910) from instrumental data, XXVII ESC General Assembly, September 11-15, 2000. Lisbon, Portugal.
12. Dineva S., T. van Eck, D. Mihaylov (2001). Seismotectonic studies on the Krupnik Seismic Zone (SW Bulgaria-Northern Greece-Macedonia), 27th Annual Meeting of CGU, 14-17 May, 2001, Ottawa.
13. Battlo J., Dineva S., Mihaylov D. and R. Macia (2001). Source Parameters of two large Plovdiv (Bulgaria) earthquakes - April 1928. IAGA and IASPEI Joint Scientific Assembly 2001 in Hanoi, 19-31 August 2001. (Published in the Proceedings, p. 390).
14. Mihaylov, D., Macià, R., Dineva, S., y Batlló, J. (2002). Determinación de parámetros focales de los terremotos de Plovdiv de 1928 a partir de registros instrumentales, III Asamblea Hispano-Portuguesa de Geodesia y Geofísica, València, 4-8 February (Asamblea Hispano-Portuguesa de Geodesia y Geofísica 3: 149 (Abstract)).

15. Macià, R., Mihaylov, D., Batlló, J. y Dineva, S. (2002). Obtención de parámetros focales a partir de registros históricos instrumentales, Asamblea Hispano-Portuguesa de Geodesia y Geofísica, València, 4-8 February.
16. Dineva S., Batllo J., Macia R. and Michaylov D. (2002) Source parameters of selected large European earthquakes from the beginning of the 20th century, Seismological Society of America Meeting, Victoria, British Columbia, 17-19 April, 2002 (Seismological Research Letters 73 (2) : 224. (Abstract)).
17. Macià R., Mihaylov D., Batlló J., Dineva S. (2002). Waveform calculation and earthquake focal parameters determination from old seismographic records. Some case studies. In: European Seismological Commission (ESC). XXVIII General assembly. Book of Abstracts. European Seismological Commission, p. 182-182. (ISBN/ISSN: 88-7388-0088-8).
18. J. Batlló, S. Dineva, A. Bent, D. Mihaylov, R. Macià. (2002). Using modern techniques for historical data: Two Plovdiv (Bulgaria) events-1928, XXVIII General Assembly of ESC, 1-6 September 2002, Genoa, Italy. In: European Seismological Commission (ESC). XXVIII General assembly. Book of Abstracts. European Seismological Commission, p. 186-186. (ISBN/ISSN: 88-7388-0088-8).
19. Mihaylov D., Dineva S., Eaton D. (2003). Seismic Noise Characteristics and Recording Capabilities of the Ontario POLARIS Seismic Stations, 29th Annual Meeting of CGU, Banff, Alberta, May 10-14, 2003.
20. Dineva S., Mihaylov D. and Eaton D. (2003). Discriminating small local earthquakes from quarry blasts in southern Ontario, Seismological Society of America, Eastern Section Annual Meeting, 19-21 October 2003, Toronto, Ontario, Canada.
21. J. Batlló, R. Macià, S. Dineva, D. Mihaylov (2003). Source Parameters of two Large Earthquakes near Valandovo (Macedonia) - March 1931, IUGG meeting, June 30 – July 11, 2003, Sapporo, Japan.
22. J. Batlló, R. Macià, S. Dineva, D. Mihaylov (2003). Source Parameters of two Large Earthquakes near Valandovo (Macedonia) - March 1931. In: Risk assessment of waste water re-use on groundwater quality, IAHS, p. A.456-A.457.
23. Mihaylov ,D., and Dineva, S. (2004). Calibration of the southern Ontario POLARIS Seismic Stations, Joint CGU/AGU meeting, 17-21 May, 2004, Montreal, Quebec, Canada.
24. Mihaylov, D., Dineva, S., and Eaton, D. (2005). Noise characteristics of the combined southern Ontario seismic network: local and regional event detectability, 77th Annual Meeting of the Eastern Section of the Seismological Society of America, Memphis, Tennessee, October 3-4, 2005.
25. Dineva, S., Eaton, D., Mihaylov, D. (2006). Design of borehole seismograph network around Bruce Nuclear site (Ontario, Canada), Meeting of the Eastern Section of the Seismological Society of America/POLO, October 1-4, 2006, Ottawa, Canada.

26. Mihaylov, D., Naggar, H.M., Dineva, S., and Eaton, D. (2006). Microseismic noise measurements for microzonation of Great Toronto Area (GTA), Meeting of the Eastern Section of the Seismological Society of America/POLO, October 1-4, 2006, Ottawa, Canada. (PhD work).
27. Dineva, S., Eaton, D., Mihaylov, D., Lam, T. (2007). Borehole Seismograph network for microearthquake monitoring near Bruce Nuclear site (Ontario, Canada), Third POLARIS-POLO meeting, June 2-4, 2007, London, Ontario.
28. Mihaylov, D., El Naggar, H., Eaton, D., and Dineva, S. (2007). Microzonation of Great Toronto Area (GTA): Preliminary results, Third POLARIS-POLO meeting, June 2-4, 2007, London, Ontario. (PhD work)
29. Mihaylov, D., El Naggar, H., Dineva, S., Eaton, D. (2008). Application of GIS software for the seismic microzonation of Greater Toronto Area (GTA), 80th meeting of the Eastern Section of the SSA, Kingston, Ontario, Canada, October 5-7, 2008. (PhD work)
30. Mihaylov, D., and El Naggar, H.M. (2010). Technology and case study for analysis of vibrations and resonances of populated buildings, The 17th International Congress on Sound and Vibrations, Cairo, Egypt, 18-22 July, 2010. (PhD work)

Patent

1. G. Mardirossjan, D. Mihaylov. Galvanometric photorecorder with an automatic regulation of exposure. Patent number 40118. (in Bulgarian)

Some Technical Reports:

1. Seismological and engineering-seismological characteristics of the region Strazhica-Popovo-Vodica, affected by the earthquakes in 1986, Report for the government of Bulgaria, 1987.
2. Investigations for increase of the seismic safety of the Nuclear Power Plant Kozloduy, Preliminary investigations for Kozloduy NPP Near Site Local Seismological Monitoring Network, Contract with the National Electric Company - Bulgaria, 1991-1992.
3. Investigations for increase of the seismic safety of the Nuclear Power Plant Kozloduy, Preliminary investigations for Belene PNPP Near Site Local Seismological Monitoring Network, Contract with the National Electric Company - Bulgaria, 1991-1992.
4. Reevaluation of historical earthquakes, relation between seismicity in the regional and local areas of the Kozloduy NPP site, geophysical fields and the earth crust structure, Contract with the National Electric Company - Bulgaria, 1992.

5. Reevaluation of historical earthquakes, relation between seismicity in the regional and local areas of the Kozloduy NPP site, geophysical fields and the earth crust structure, Contract with the National Electric Company - Bulgaria, 1992.
6. Geomorphology, neotectonics, seismicity and seismotectonics of the NPP Kozloduy, Design of basic earthquake for seismic upgrading of NPP Kozloduy, Contract with the National Electric Company - Bulgaria, 1992.
7. Design and installation of Kozloduy NPP Near Site Local Seismological Monitoring Network, Contract with the National Electric Company and Kozloduy NPP LTD, 1994.
8. Seismicity and seismic regime on the territory of Bulgaria and adjacent areas, Contract with the Ministry of Education and Science - Bulgaria, 1991-1994.
9. Design, installation and exploitation of local seismic network in Provadia seismogenic zone, Contract with Geosalt LTD, 1993-1994.
10. Seismological characteristics of SW Bulgaria. Nature of Krupnik seismic source, Contract with the Ministry of Education and Science - Bulgaria, 1995-2000.
11. Seismic parameters of strong earthquakes ($M > 6$) in Bulgaria and Spain during 20th century (origin time, epicentre location, magnitude, scalar seismic moment from analysis of instrumental records and bulletin data) - joint project between Bulgarian Academy of Sciences and CSIC - Spain, 1997-1999.

Publications under preparation:

1. Mihaylov, D., El Naggar H., Dineva, S. Pilot seismic microzonation of Great Toronto Area.
2. Mihaylov, D., El Naggar H., Oskirko, R. Assessment of building resonances and their influence on the HVSR results using output only identification of vibration modes (case study).
3. Mihaylov, D., and El Naggar H. Interaction between soil and building non-linear responses during cyclic load and strong earthquake.